CHAPTER NINE

CHARACTERIZATION OF MATERIAL PROPERTIES BASED ON INVERSE FINITE ELEMENT MODELLING WITH DIFFERENT INDENTERS AND EXPERIMENTAL RESULTS

9.1 Introduction

In this chapter, the application of indentation processes with different indenter geometries has been studied to predict the elastic plastic material properties of various material systems to develop an accurate method for specific applications. Many researchers suggested that a non-unique set of mechanical properties can be predicted for strain hardening elastic plastic material from a single indentation test. However, most proposed methods in literature have been characterised by parameters of load displacement curves using two or more indenters to determine a unique set of material properties (Chollacoop, Dao et al. 2003, Swaddiwudhipong, Tho et al. 2005, Luo, Lin et al. 2006).

This chapter is mainly focused on alternative approaches of using inverse FEM accompanied by an optimization algorithm to obtain and optimize the elastic plastic properties (E, σ_y, n, ν) and Drucker-Prager material properties (E, σ_{yc}, β) .The framework established would help to develop an approach for characterising complex material systems such as thermally treated glass. The main objective of this chapter is to develop a computational method based on FEM and an optimization algorithm to extract unique and accurate mechanical properties of elastic plastic and Drucker-Prager materials from full indentation loading unloading curves using single and dual indenter geometry. The second objective is to examine the accuracy of the proposed inverse program FEM with optimization algorithm technique when the target load-displacement data comes from real experimental data.

This chapter consists of three main parts. In the first part, an inverse FEM of continuous indentation of axisymmetric and 3-D commonly used indenter geometries (Vickers, Berkovich, Spherical indenter, and axisymmetric conical) was developed.

In the second part, an inverse program FEM interfaced with a non-linear MATLAB optimization algorithm was developed based on the load displacement results of single and dual indentation data of predefined material properties. The effect of initial guess material properties and indenter geometry were examined. The optimization method was then used to predict material properties, which produce an indentation curve(s) matching the input experimental data. In the third part, after a feasibility study and validation of combined FEM and optimisation algorithm, the proposed method will be applied to actual experimental load displacement curves of a range of thermally treated recycled glass material.

9.2 FEM Based on the indentation process

FEM algorithms using single and multiple indenters have been proposed by other researchers to determine the mechanical properties of different engineering material systems. This approach has been used on some complex or non-standard materials or surfaces, such as in vivo tension, and brittle indentation (Meuwissen, Oomens et al. 1998, Shan and Gokhale 2003, Ren X. J. 2005).

In this chapter, different types of indenter geometries were comparatively studied to develop an accurate, non-dependent of initial guess material properties approach. Two different approaches were established to investigate and predict the elastic plastic material properties and other complex material constitutive laws. The first one was performed to predict the material properties based on the single indentation test, examined separately, all indenters sharing the same initial start value. The applications of such an approach by many researchers have failed to achieve high accuracy, because the range of tested material properties produced identical load displacement curves. In some cases the accuracy of this approach will improve depending on the previous knowledge about the material (Giannakopoulos and Suresh 1999, Dao, Chollacoop et al. 2001, Bucaille, Stauss et al. 2003).

The second approach was implemented to predict the material properties based on the dual indentation test. In this approach two types of indenter with different shapes and dimensions were employed resulting in different plastic strain profiles i:e: different load displacement curves; such a condition may potentially help to predict multiple material parameters. Chollacoop, Dao et al. (2003) applied a modified single indenter algorithm to two and more indenter shapes. Dao, Chollacoop et al. (2001) developed forward analysis which considered that the representative stress and strain and the loading curvature are functions of the face angle of the conical indenter. The inverse algorithm then uses the second pair of representative stress and strain in order to obtain the unknown mechanical properties.

The algorithm shows significant improvements in the predicted Yield stress, σ_y and strain hardening exponent, *n* compared to single indenters. Yan, Karlsson et al. 2007) have used dual indenter geometries to determine the mechanical properties in engineering materials.

The Elastic modulus and initial residual stress were assumed to be known material properties. Forward FEM simulations with dual indenters were performed to predict the Yield stress and strain hardening. The results show that the load displacement curves are predict better yield strength compared with single indenter geometry with an error of less than 5%.

9.3 FEM automated algorithm for material characterization

The main objective of the FEM automation algorithm for material characterization was to enable the user easily to determine the mechanical properties of the complex material system based on indentation data; those which are difficult to characterize using a conventional tensile or compression test such as soft, brittle and non-linear materials. The material property investigation is conducted in three steps: Firstly, the creation of FEM based on the experimental input data (inp.) file. Secondly, generate output database (odb.) file by post processing the (inp.) file through the FEM solver. Thirdly, inverse analyses by iterative optimization of the numerical simulation to fit with the experimental data.

The input file is a text file within the ABAQUS software which contains the necessary information about the computer aided engineering model (cae.) such as dimensions, material properties and constitutive law, kinematic contact , boundary conditions, the applied load (displacement controlled or force controlled), and mesh design. In this work, the inp files of different indenter geometries were imported into the automated algorithm MATLAB code, which gives the users ability to select a specific type of tip geometry based on the input experimental data.

The selected input file can be called for post processing by the FE solver through the execution of a job file. This process was carried out within the automated algorithm MATLAB code to produced odb files, which contain the output results of the numerical simulations. The results of load displacement curves can be extracted from the odb files by using a separate python script file, which is responsible also for transferring these specific data into text files (rpt. files) used in the final stage of the optimization process.

Figure 9.1 shows the optimization arrangement of material characterization. In this arrangement, the processing of input files was created, post processing to odb files, and then extracting the data to the rpt. files.

The whole process was implemented into the automated algorithm for the final stage of inverse FEM analysis by a non-linear least square data fitting optimization tool.

As stated before, the main objective of the automated algorithm is to extract the mechanical properties of non-standard specimens or surface loading conditions. Such parameters can be determined by conducting an inverse FEM approach based on the indentation test. This approach consists of fitting the experimental load displacement data of material to FEM simulations by an iterative process relating to a material constitutive law within the input file previously introduced in the automated algorithm, based on the geometry and experimental boundary conditions. The material parameters in a particular constitutive law were adjusted by the development optimisation method to solve the parameter estimation problem. In order to evaluate the quality of the parameter set, an objective function is created based on the mathematical model; however these parameters are iteratively refined until the objective function achieved the convergence criterion

A range of optimization approaches and indentation techniques have been developed by various researchers (Gu, Nakamura et al. 2003, Bolzon, Maier et al. 2004, Chen, Ogasawara et al. 2007, Nakamura and Gu 2007), however, the uniqueness and accuracy of their solutions cannot be guaranteed, because the inverse problems was in ill-condition. This may be attributed to a large number of points needed to reconstruct the models which produce a large number of degrees of freedom after each iterative solution resulting in the non-uniqueness of the inverse modelling, i:e many different materials can explain the output results equally well (Snieder 1998).

The ill-conditional inverse analyses can be overcome if an appropriate initial guess parameter value for the optimization algorithm is known. However, a typical method was established in this study based on the evaluation of a new search procedure with different initial guess parameters. Such a development allows the initial step to be repeated, exploring a large solution space until the convergence conditions are satisfied.

9.3.1 Optimization method development

Many optimization methods have been used by researchers to predict the best parameters using single- or multi- objective functions, for example Gérard, Ohayon et al. (2005), and Kang, Becker et al. (2012). The main purpose of optimization techniques involves

iteratively changing the material parameters by re-running the FEM until it achieves a best fit between the load displacement curve obtained from real measurement results and the curve obtained from numerical analysis. In this approach, an optimisation algorithm is coupled with the FE method in order to find the optimal values (minimum objective function) for a set of target material parameters to be determined.

In this study an optimization algorithm has been developed to determine the material properties for a given set of indentation data using an iterative procedure with Math Works computing software (MATLAB, The Math Works Inc.). The non-linear least-squares optimization function (LSQNONLIN) has been developed in the MATLAB code based on the Levenberg–Marquardt algorithm (Matlab). A special code was written in MATLAB including the optimisation function and commands to read input files, write output files and execute ABAQUS. The optimisation process started by selecting arbitrary initial values for each parameter and then running the ABAQUS input file using these values for the particular material model. A python script was then used to extract the history of force and displacement which is read in MATLAB to compute the objective function. The optimization model for a single indenter is given by the following objective function:

$$minF(x) = \frac{1}{2}\sum_{i=1}^{n}\left[\left(F_{num-l}^{i} - F_{exp-l}^{i}\right)^2 + \left(F_{num-ul}^{i} - F_{exp-ul}^{i}\right)^2\right] \qquad (9.1)$$

$$x \in D^n \qquad (9.2)$$

$$LS \leq x \leq US \qquad (9.3)$$

-where, $x = \left(E, v, \sigma_y, and\ n\right)$ for Elastic-Plastic material law

$x = \left(E, v, \sigma_{yc}, and\ \beta\right)$ for Linear Drucker-Prager material law

Where $min\ F(x)$ is the minimum objective function, x is the optimization parameter set in the n dimensional space D^n, $LS\&US$ are the lower and upper simulation space of the x parameter during the optimization. $F_{exp-l}^{i}$is the measured Force applied in loading at a particular depth, F_{num-l}^{i} is the value of Force obtained from theory for the loading section of the curve at the same depth predicted by FEM, F_{exp-ul}^{i} is the measured Force in unloading at a particular depth, F_{num-ul}^{i} is the value of Force obtained from theory for the unloading section of the curve at the same depth predicted by FEM, and n is the number of sampling points in each test.

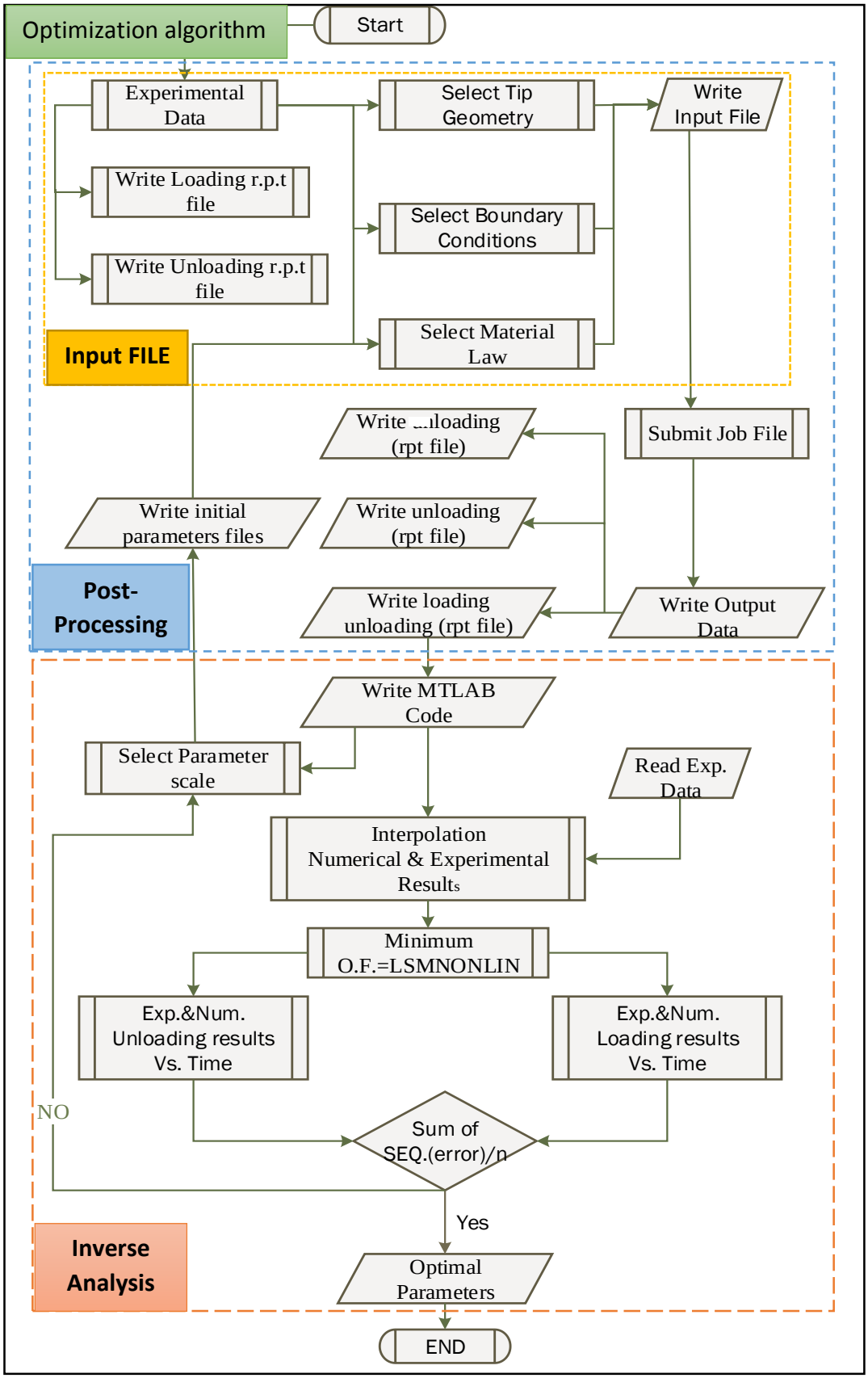

Figure 9-1 Optimization arrangements for material characterization

9.3.2 Optimization algorithm and inverse analysis setup

The MATLAB optimization algorithm consists of three main parts: experimental (target) loading unloading curves, interfaced FEM code to predict loading unloading curves, and an inverse programme based on the objective function. In the inverse program, the input experimental data was transformed into a separate form (csv.) file with uniformly spaced points against the indentation depth. At each indentation depth, the objective function values were automatically calculated within the algorithm. The overall objective function was determined by the summation objective function over the whole indentation curve. The mechanical properties which give minimum objective function value were defined as the optimum solution.

The typical optimization algorithm used in this work is demonstrated in Figure 9-1. The optimization procedure was carried out using a set of initial guess material properties based on several steps in MATLAB code coupled with numerical simulations developed by commercial ABAQUS software. The inverse analysis starts with the pre-processing stage, which involves control script languages (C and Python), and (EXE) files in order to automatically generate and update the current material properties in the ABAQUS inp files by the new estimated material properties. In the post processing stage, the MATLAB programme reads the data and extracts load history results from the ABAQUS odb files using python script, and then iteratively runs the objective function of least square errors between the experimental and simulated load curves at the same intervals of displacement values. The final stage of the inverse optimization algorithm is, to copy the final results in the separate history txt file.

9.4 Finite element indentation models

Three-dimensional numerical simulations of three different axisymmetric indenter geometries (Berkovich, Vickers, and Spherical) were developed to validate the optimization technique for various material systems. Figure 9-2 (a, and b) shows 3-D Berkovich and Vickers indenter geometries, only1:6and 1:4 of symmetric specimens and indenters were performed, respectively. The planes of symmetric geometries are concentrated in the y and x direction.

All specimens and indenters were modelled with 8-node element type reduced integration (C3D8R), and 4-node element type rigid quadrilateral (R3D4) respectively, both elements types are used for stress and displacement analysis. Figure 9-2 (c) shows 3-D spherical indenter, 1:4 of the specimen and indenter were modelled; as a result symmetric surfaces are concentrated on both x and y direction along symmetry planes. The specimens and indenters were analyzed with 8-node element type reduced integration (C3D8R) for the stress analysis approach. Figure 9-2 (a-, b-, and c-) shows The details of a created 2-D axisymmetric conical equivalent to 3-D Berkovich and 3-D Vickers, and 2-D axisymmetric spherical equivalent to 3-D Spherical indenter geometries which were covered in the earlier [Chapter 6, and 7]. All specimens and indenters were modelled with 4-node bilinear axisymmetric quadrilateral, reduced integration (CAX4R).

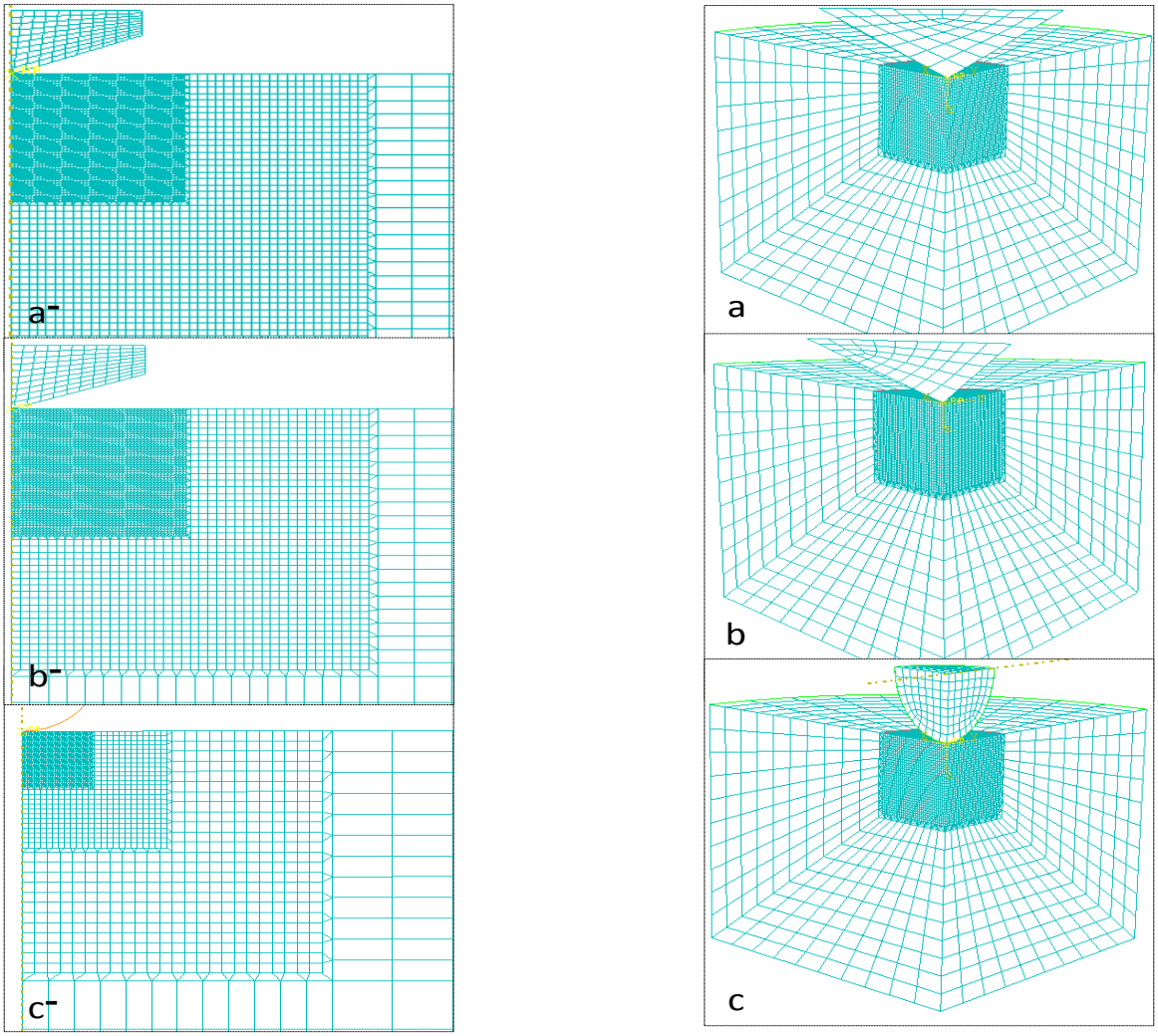

Figure 9-2 3-D & 2-D equivalent FEM models of Vickers, Berkovich, and Spherical indentation test

Table 9.1 shows the area functions of the Berkovich and Vickers tip geometries used in the numerical simulations based on the area function results obtained from experimental work presented in Chapter 6, and Chapter 7

Table 9-1 Area functions of the Vickers and Berkovich indenters

Indenter Geometries	***Area Function (μm^2)***
Vickers	$A_P = 33.1(h + 0.06)^2$
Berkovich	$A_P = 30.5(h + 0.0125)^2$

A manual adaptive re-meshing technique was used in the area below the indenter contact in order to achieve larger deformation and stress gradients during indentation, thus a single mesh can be employed without excessive distortion. The indentation method was simulated in two alternating steps, during the loading step the indenter was moved along in the z-direction in ramp mode and penetrated the specimen until the maximum depth of 1.25 μm is achieved. The reaction force was recorded at a reference point representing the overall load on the specimen. During the unloading step, the indenter was returned to the initial position and to the same reference point. Based on the results of the indentation size effect determined in chapter 8, the specimen sizes used in the simulations were greater than or equal to 100 times the maximum indentation depth, which is satisfactorily large, in order to avoid any specimen size effect and boundary effects. The lower surface of the specimens was fixed for all degrees of freedom, free surface modelled at the top and sides of the specimen. The contact and simulation mechanism are the same in all types of indenters geometries, which can be described by: The contact constraint between the indenter and material was defined as the 'master surface (indenter)' and 'slave surface (material)' interaction with a normal contact, to allow the master surface to move and contact the material at all times during the simulation. The contact direction is then obtained in relation to the master surface.

9.5 Characterization of elastic plastic material properties

9.5.1 Elastic plastic material constitutive model

Two sets (elastic plastic and elastic perfectly plastic) material constitutive law were created in the ABAQUS input files in order to represent a wide range of material properties.

The constitutive law has been used to simulate the indentation process, was for an isentropic elastic plastic material with power law strain hardening determined by the tensile behaviour (stress, σ, and strain,ϵ) given by Eq. (9.4). This is commonly used in the numerical simulation of metallic alloys (Swaddiwudhipong, Hua et al. 2006).

$$\sigma = \begin{cases} E\varepsilon\,, for: \sigma \leq \sigma_y \\ R\varepsilon^n, for: \sigma \geq \sigma_y \end{cases} \tag{9.4}$$

However, in the true stress-true strain behaviour, Swaddiwudhipong, Hua et al. (2006) proposed Eq. (9.5) to calculate the plastic stress in the ABAQUS input file

$$\sigma_p = R(\frac{\sigma_y}{E} + \varepsilon_p)^n \tag{9.5}$$

The material coefficient, *R* is given by:

$$R = E^n {\sigma_y}^{1-n} \tag{9.6}$$

Four parameters $(E,\ \sigma_y, v, n)$ have been used to optimize the elastic plastic material properties. The Poisson's ratio and strain hardening exponent values are placed between 0 and 0.5 for most engineering materials. However, in this study no lower and upper boundaries have been specified for the values of Young modulus and Yield stress in order to represent a wide range of metallic and ceramics material properties. A fixed set of plastic strain values of $0 > \varepsilon_p \geq 0.3$ with 0.05 interval step has been used in the ABAQUS input file, therefore the stress value can be updated for a given plastic strain value using Eq. (9.5).

9.6 Optimization analysis of elastic plastic material properties based on single indenter geometry

The optimisation algorithm based on the single indentation method was evaluated using blind test numerical data (numerical simulation with known material properties). Such an approach is commonly used to investigate the accuracy and sensitivity of the inverse FE methods using the optimization process (Delalleau, Josse et al. 2006). In order to evaluate the uniqueness of the single indenter optimization algorithm, a set of initially assumed material properties were selected and employed in the optimization algorithm.

This process allowed the MATLAB code to automatically run the ABAQUS input file and iteratively determine the error between the target and predicted load displacement data using non-linear least-squares optimization function (LSQNONLIN).

The optimization algorithm was carried out using 3-D, and 2-D indenter geometries (Berkovich, Vickers and Spherical) to predict the material properties of the elastic plastic target material. Various ranges of initial guess were used to investigate the effect of starting point on the convergence of results. Figure 9.3 (a, and b) shows the target numerical load displacement curve for pure Aluminium material with known mechanical properties ($\sigma_y = 550MPa\,, E = 72GPa\,, v = 0.22, n = 0.1$) (Chollacoop, Dao et al. 2003), which is used as blind test numerical data based on the indentation process of three different tip geometries (Berkovich, Vickers, and Spherical). The numerical load displacement data was divided into 50 equally spaced points against the indentation force, transformed into a separate excel file form and saved into the MATLAB programme. This data will be used in the post-processing stage at each iteration to determine the objective function. The objective function value was calculated at each indentation point (displacement step) using a non-linear least-squares objective function (LSQNONLIN) in MATLAB code then the sum of the objective functions integrated over the whole indentation curve was determined.

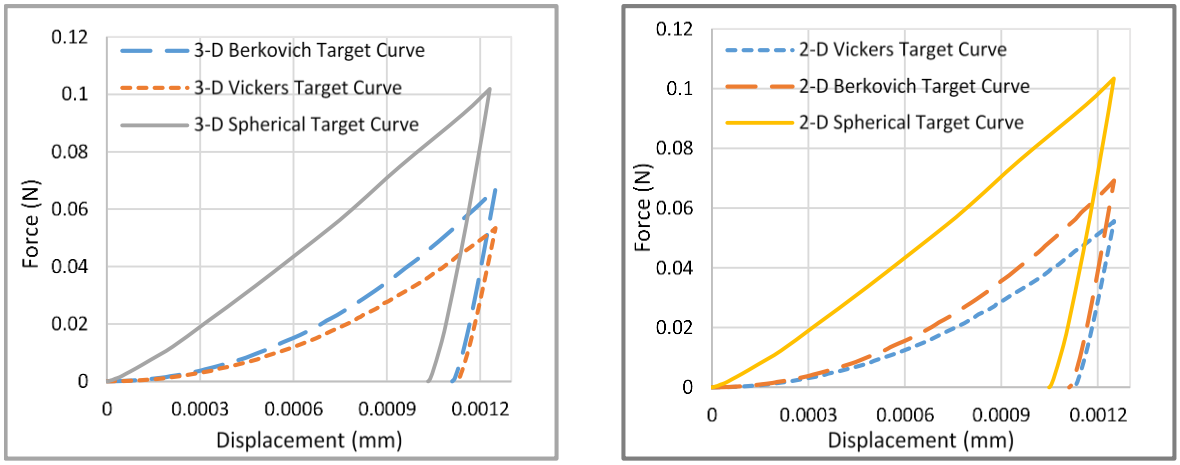

(a) (b)

Figure 9-3 Target numerical load displacement curves determined from 3-D and 2-D FEM simulations for Berkovich indentation, Vickers indentation, and Spherical indentation

The numerical simulations of the target material show discrepancy in the loading unloading curves for different indentation processes. These differences in the load displacement curves give a good boundary to test the sensitivity and accuracy of the optimization algorithm of elastic plastic materials. However, in order to validate the optimization algorithm in more depth, indentation hardness H_{IT}, effective elastic modulus, E_{eff} and indentation depth ratio (final indentation depth to the maximum indentation depth) which represents the depth ratio of target material $(h_{max}/h_f)_T$ divided by the depth ratio of optimized material/$(h_{max}/h_f)_O$, can be calculated from the optimal loading unloading curve using the Oliver and Pharr method and compared with results obtained from target loading unloading curves.

Indentation hardness $$H_{IT} = \frac{F}{A_P} \quad (9.7)$$

Effective elastic modulus $$E_{eff} = \frac{\sqrt{\pi}}{2\beta}\frac{S}{\sqrt{A_P}} \quad (9.8)$$

Depth ratio $$(h_{max}/(h_f)_t/(h_{max}/(h_f)_{opt} \quad (9.10)$$

In this case, the sensitivity of this algorithm was examined by changing four material parameters (σ_y , E , $v, and\ n$). Other parameters related to the specimen geometry and size , boundary conditions and applied load are fixed for all numerical simulations. The Young's modulus, Yield stress, Poisson's ratio, and strain hardening values were selected within the range of $(10 \leq E \leq 150)$ GPa, 100 MPa $\leq \sigma_y \leq$10 GPa, $0.05 \leq v \leq 0.5$, and $0 \leq n \leq 0.5$, respectively. The optimization results are summarised in Table 9-2. The intial guess set was selected randomly from a range of material properties for various types of single indenter numerical simulations. However, the percentage errors between the predicted results for a particular parameter and the target results for the same parameters can be calculated using the following expression:

$$Residual\ error\ \% = \left|\left[1 - \frac{predicted\ result - target\ result}{target\ result}\right] \times 100\right| \% \quad (9.11)$$

The results of six indenter geometries in Table 9-2 shows that all parameters achieve convergence to within about 3 % of the target results regardless of the intial guess values.

The results also show that the objective function between target and predicted load displacement curves are in excellent agreement. This suggests that the material properties of an unknown elastic plastic material can be accurately predicted using the proposed optimaization algorithm method based on a single indentation test.

Figure 9-4 shows the optimization ratio (optimal value / target value) at each iteration of material parameters based on different indentation geometries. It clearly demonstrates that all selected parameters can converge to the target values despite different indenter geometries and variation in the initial guess values. The number of iterations required to achieve the target values is subject to the type of indenter geometry. The 3-D and 2-D models exhibit similar trends for the four parameters (σ_y , E , v, n) and optimize towards the target values when the same initial numbers were employed, while the number of iterations are different. Three different 3-D, and 2-D indentation processes were established, the Berkovich convergence history (a), and (b) shows the four parameters can achieve the target values after 18, and 33 iterations respectively, the Vickers indentations (c), and (d) shows the convergence can be achieved after 22, and 45 iterations respectively, and the Spherical indentation (e), and (f) shows the convergence can be achieved after 14, and 23 iterations respectively. This suggested that the 3-D model needs more computational time compared with the 2-D model, but fewer iterations to achieve convergence. It is interesting to note that the Poisson's ratio and strain hardening achieved convergence faster than the other parameters, but with less agreement with the target value , the Young modulus agreed well with the target value, but required a large number of iterations. Yield stress stay in the middle of parameters regarding the number of iterations required for convergence. In summary the optimal results were achieved in about 14-22 iterations for three different 3-D models and about 23-45 iterations for the same geometries of 2-D models where all the material parameters converge from initial guess to the target values to within 3% error regardless of the start points. In order to examine the accuracy of the proposed method Table 9-2 presents the calculation of the normalized hardness ratio H_T/H_O (target indentation hardness / optimized indentation hardness), and normalized Reduced modulus ratio $(Er)_T/(Er)_O$ (target reduced modulus / optimized reduced modulus). The results show that the maxium percentage error was about 5% in the Reduced modulus ratio, and 2% in the hardness ratio over indentation techniques.

The 3-D simulations exhibit overestimation of the target value results, whereas 2-D underestimates the target value results.

These differences may be attributed to the fact that the mesh density of the 2-D simultions is much finer in the area around the indenter resulting in lower reaction forces.

Table 9-2 Single indenter optimaization results of elastic perfictly plastic material

Indenter	*Parameter*	*Target value*	*Initial value*	*Predicted value*	*Error %*	H_T/H_O	$(Er)_T/(Er)_O$	*Depth ratio*
3-D Berkovich	E(GPa)	72	10	73.23	1.71	0.984	0.989	0.98
	σ_y(MPa)	550	260	535	2.72			
	v	0.22	0.14	0.223	1.5			
	n	0.1	0.01	0.0972	2.2			
3-D Vickers	E(GPa)	72	90	73.86	2.58	0.977	0.982	0.978
	σ_y(MPa)	550	260	533	2.54			
	v	0.22	0.35	0.217	1.2			
	n	0.1	0.05	0.0975	2.5			
3-D Spherical	E(GPa)	72	50	73.08	1.5	0.989	0.99	0.986
	σ_y(MPa)	550	440	539	2.0			
	v	0.22	0.2	0.223	1.45			
	n	0.1	0.01	0.098	2.0			
2-D Eq. Berkovich	E(GPa)	72	10	70.31	2.34	1.028	1.03	1.03
	σ_y(MPa)	550	260	563	2.36			
	v	0.22	0.14	0.222	0.95			
	n	0.1	0.01	0.1023	2.3			
2-D Eq. Vickers	E(GPa)	72	90	69.9	2.92	1.03	1.043	1.03
	σ_y(MPa)	550	260	565	2.73			
	v	0.22	0.35	0.218	1.1			
	n	0.1	0.05	0.1011	1.1			
2-D Eq. Spherical	E(GPa)	72	50	70.7	1.8	1.013	1.015	1.02
	σ_y(MPa)	550	440	560	1.8			
	v	0.22	0.2	0.222	1.01			
	n	0.1	0.01	0.1045	0.45			

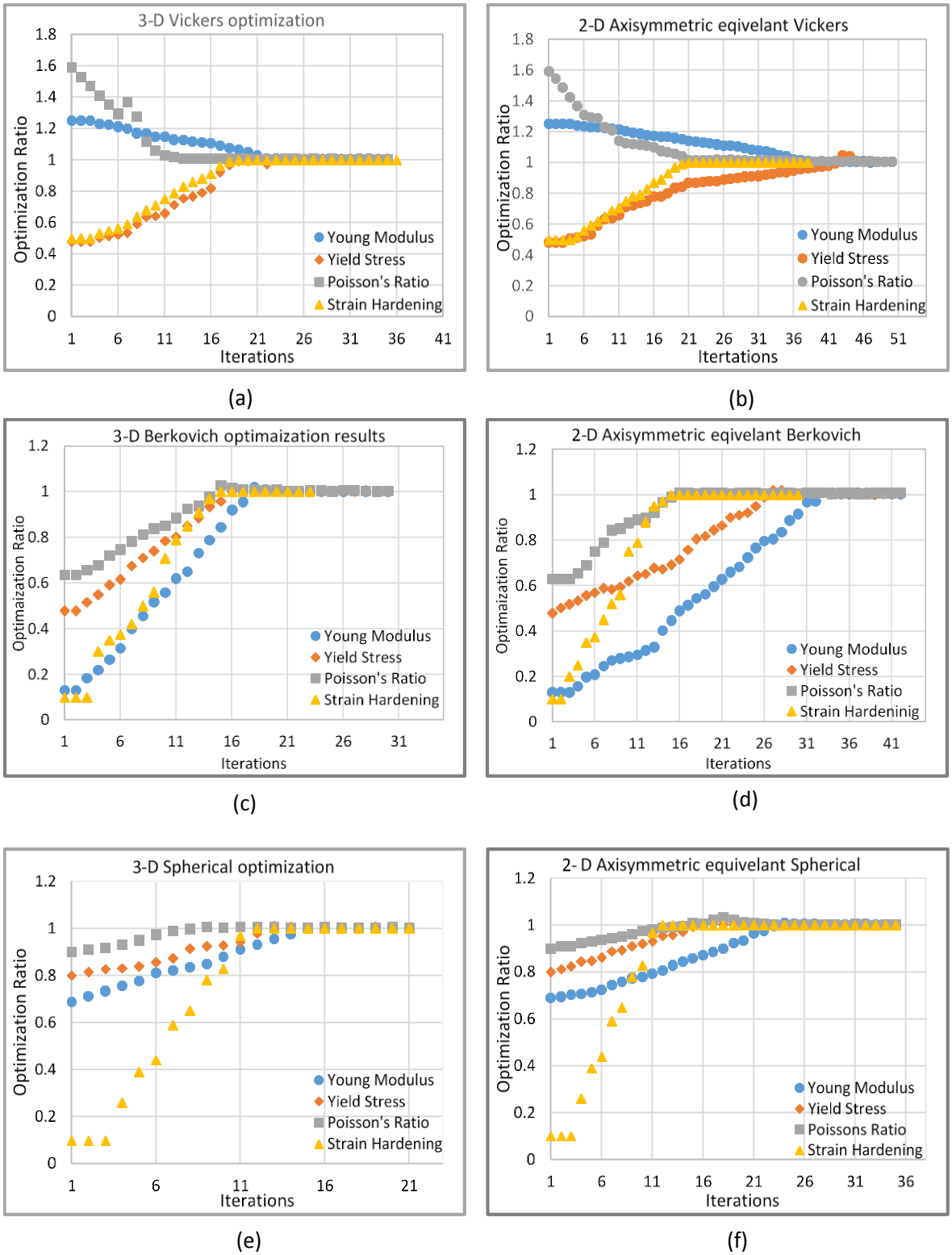

Figure 9-4 Optimization ratio at each iteration of different indentation techniques a)3-D Berkovich indenter , b) 2-D axisymmetric equivalent Berkovich c) 3-D Vickers indenter , d) 2-D axisymmetric equivalent Vickers , e) 3-D Spherical indenter , and f) 2-D axisymmetric equivalent Spherical

The divergence in the load displacement curves during the iterations for different indentation geometries are displayed in Figure 9-5. The optimization process tends to reduce the variance of numerical material properties with respect to the target values until the optimal results are achieved where the best fit the numerical load displacement curves with the experimental data. It is interesting to note that the Spherical indenter required fewer iterations compared with other shapes to predict the optimal material properties regardless of initial start. The results also proposed that in spite of large variations between the initial guess and target values used in Vickers indentation, the convergence results in this simulation are achieved with fewer iterations compared with the Berkovich indentation. However, the proposed results suggest that the single indenter could be used to predict elastic plastic material properties with an accurate stress-strain curve.

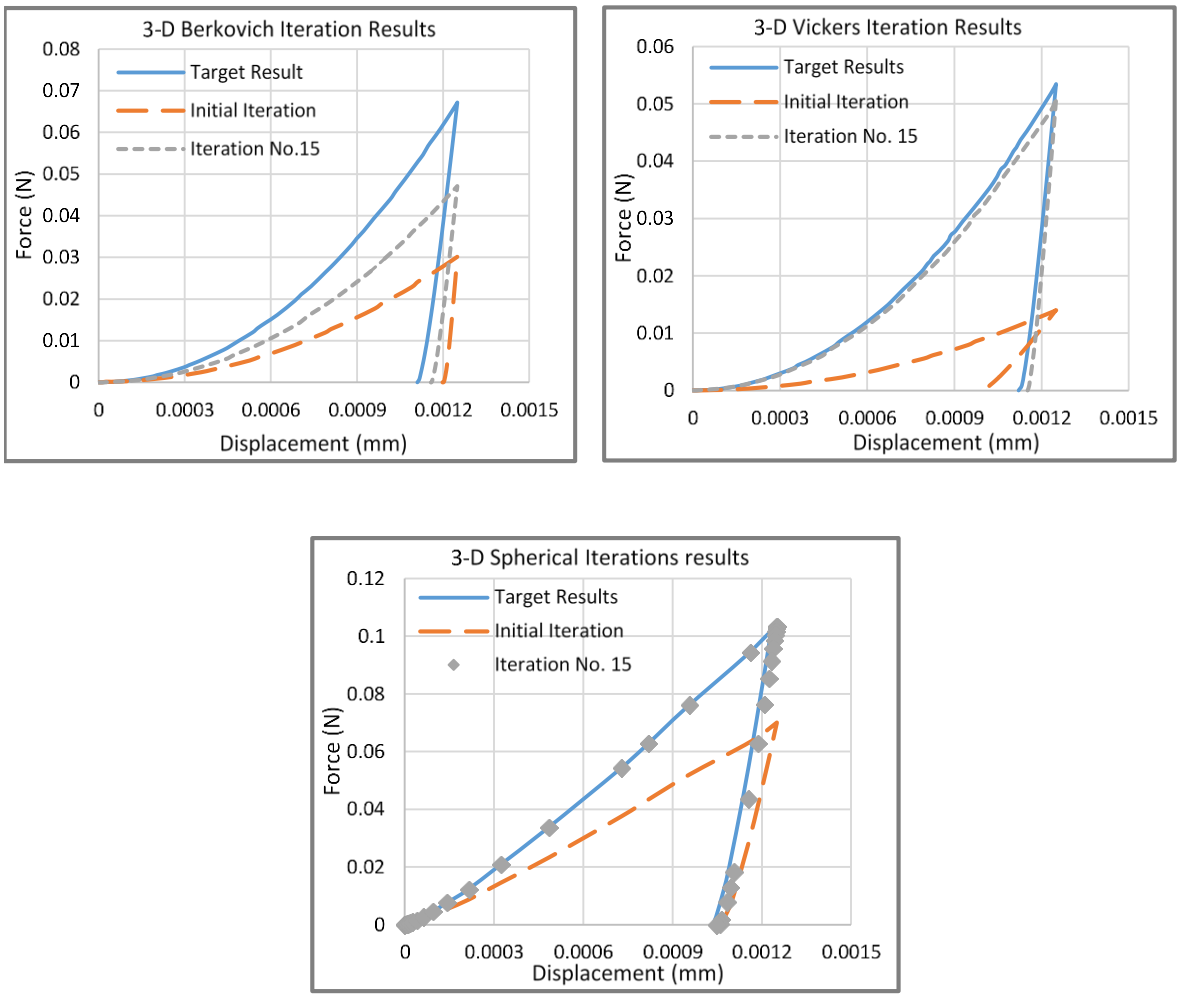

Figure 9-5 Loading unloading curves deviation during iterations history of three different indentation processes of 3-D Berkovich, 3-D Vickers, and Spherical

9.6.1 Optimization analysis of elastic plastic material properties based on dual indenter geometries

The optimization algorithm based on the dual indentation method was also assessed to predict the elastic plastic material properties. In this case the new optimization algorithm was developed to allow two experimental input data with different indenter types or size were used. Then the MATLAB code used for automatically running two ABAQUS input files and iteratively determined the residual error between input and optimized load displacement curves using the objective function. The objective function of dual indenters is defined by:

$$minF(x) = \frac{1}{2}\sum_{i=1}^{n}\left\{\left[\left(F_{num-l}^{i} - F_{exp-l}^{i}\right)^2 + \left(F_{num-ul}^{i} - F_{exp-ul}^{i}\right)^2\right]_{indenter1} + \left[\left(F_{num-l}^{i} - F_{exp-l}^{i}\right)^2 + \left(F_{num-ul}^{i} - F_{exp-ul}^{i}\right)^2\right]_{indenter2}\right\} \quad (9.12)$$

In this method the objective function value was calculated at each indentation point (displacement step) using non-linear least-squares objective function (LSQNONLIN) in MATLAB code then the sum of the objective functions integrated over the whole indentation curve was determined. The total objective function value for a given set of material parameters (σ_y , E , v, n) was calculated by the summation the objective function of dual indenters at each iteration in the optimization algorithm. The optimization algorithm was carried out using the same process and principles used in the single indenter optimization algorithm of 3-D, and 2-D indenter geometries such as: boundary conditions, initial guess material properties, material properties range, and target input numerical load displacement curves.

The initial guess mechanical properties of elastic plastic hardening material (σ_y , E , v, n) were changed randomly in order to examine the sensitivity of this method. Table 9-3 summarised the optimization results of three different dual indenter geometries Berkovich and Vickers (*B&V),* Vickers and Spherical *(V&S),* and Spherical and Berkovich *(S&B*).

The initial guesses were selected from a wide range of material property sets for various dual numerical simulations.

The optimization analysis based on dual indenter geometries suggested that the four parameters (σ_y , E , v, n) were achieved convergence at different iteration numbers to within 2% of the target values regardless of the starting point. The result also shows that the objective function between the target and predicted load displacement curves was less than 1%. The optimized reduced modulus and hardness values are in excellent agreement with the target values. This suggests that the elastic plastic material properties can be accurately obtained by the proposed optimization technique of dual indenter geometries.

Figure 9-6 shows the convergence trends of the five initial guess values of elastic plastic materials. The results clearly illustrate that the initial guess values of elastic plastic hardening materials and elastic perfectly plastic materials can converge to their target values by the dual indentation optimization algorithm, but with different iteration numbers. The hardening material always required more iteration numbers to converge. It is interesting to note that additional analyses were also investigated using a wide range of initial guess values. It was found that the application of the proposed algorithm was more reliable for any initial guess values within the defined database i:e , (1≤ E ≤220) GPa, 100MPa≤ σ_y ≤7GPa, 0≤ n ≤6, $0.05 \leq v \leq 5$.

Table 9-3 Dual indenter optimization results of elastic plastic material

Indenter	*Parameter*	*Target value*	*Initial value*	*Predicted value*	*Error %*	H_T/H_O	$(Er)_T/(Er)_O$	*Depth ratio*
(3-D)	E(GPa)	72	10	72.71	0.99	0.992	0.996	0.98
Berkovich	σ_y(MPa)	550	260	540	1.85			
&	v	0.22	0.14	0.222	1.2			
Vickers	n	0.1	0.01	0.099	0.99			
(3-D)	E(GPa)	72	90	72.43	0.59	0.997	0.992	0.978
Vickers	σ_y(MPa)	550	260	543	1.28			
&	v	0.22	0.35	0.222	1.25			
Spherical	n	0.1	0.05	0.099	0.87			
(3-D)	E(GPa)	72	50	72.22	0.30	0.990	0.994	0.986
Spherical	σ_y(MPa)	550	440	546	0.47			
&	v	0.22	0.2	0.222	1.11			
Berkovich	n	0.1	0.01	0.101	1.01			

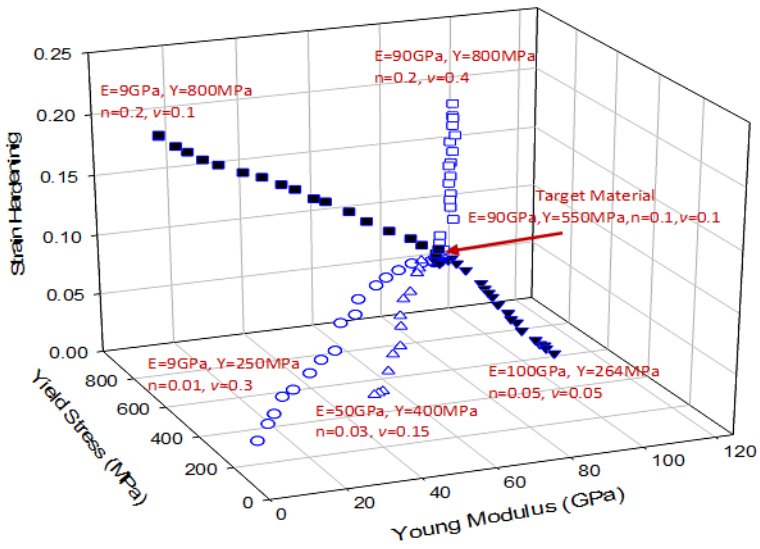

(a)Elastic plastic hardening target material

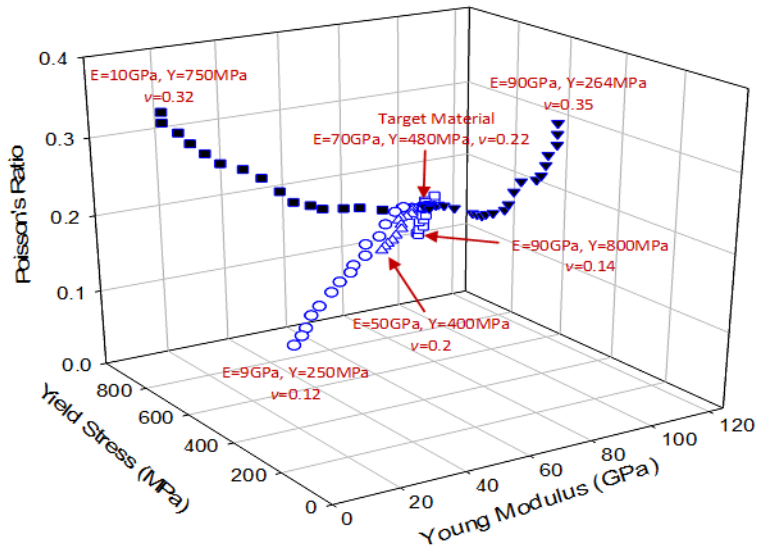

(b) Elastic perfectly plastic material

Figure 9-6 Converging trends of five initial guess values using *S&B* dual indenter for a) elastic plastic hardening target material, b) elastic perfectly plastic material

Figure 9-7 shows the optimization history of the material properties from initial guess values to their target values (with 0.01 residual error) based on three different dual indentation tests (*B&V), (V&S),* and *(S&B*). The average convergence history of the indentation tests shows that the four parameters achieved the target values after 19, 17, and 14 iterations respectively over a range of initial guess material properties. The error bar presented in each column explains the material properties can reach their target values at different iteration numbers, these variations depending on initial guess values.

The optimization process based on the *S&B* indentation test provides the best solution, because fewer iterations are required for the main parameters (σ_y , E , and n) to achieve convergence. It is clearly noticed that the Poisson's ratio required less iteration to achieve convergence; however the results are not affected due to less influence of this parameter on the load displacement curve, whereas, the Young modulus required high iteration numbers to achieve convergence followed by Yield stress and then strain hardening.

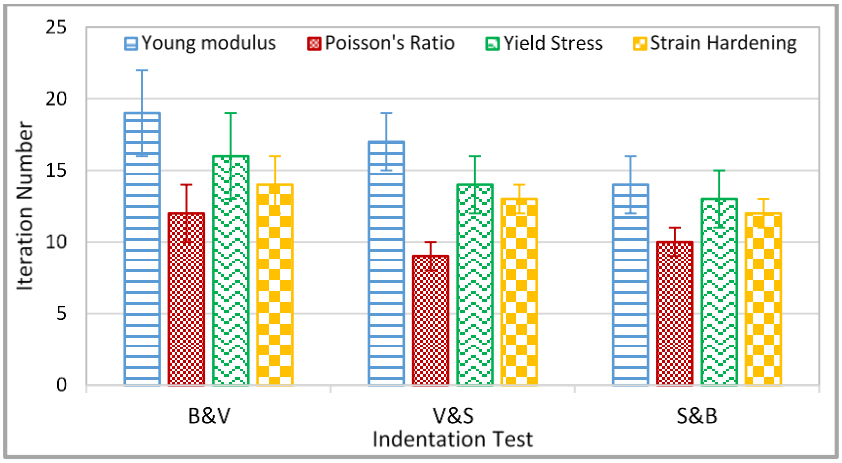

Figure 9-7 Optimization histories of elastic plastic material properties based on s (*B&V), (V&S), (S&B*) indentation test

9.7 Comparison between single and dual indentation optimization process

Figure 9-8 shows the optimization history comparison between single and dual indenter geometries within the accuracy of ≤0.01(objective function). A range of indentation tests was conducted to establish the differences in the results and evaluate the accuracy of both methodologies. The single indentation method required more iterations to achieve the target results, while the dual indentation method required fewer iteration numbers but more computational time in order to run two inp files within the optimization algorithm. The results also show that the Elastic modulus and Yield stress required more iterations (i:e more computational time) to reach convergence compared with other parameters, however the computational time can be reduced to about 18% when a pre-knowledge of the material being studied was known.

The optimization history of the full set of material properties for different indentation techniques clearly demonstrates that the optimal convergence values can be achieved despite a large variation in the starting values.

The error bars also prove that the dual indentation optimization algorithms required less numbers of iteration to predict material properties compared with single indentation. The results presented in Table 9-2 show that maximum percentage error in elastic plastic material properties (σ_y , E , ν, n) was about 2.72, 2.58, 1.5, and 2.5 % respectively and the results presented in Table 9-3 show that the maximum percentage error in elastic plastic material properties (σ_y , E , ν, n) was about 1.85, 0.99, 1.25, and 1.01%, respectively. This suggests that the dual indentation method is more accurate than single indentation method to predict the elastic plastic material properties and stress strain curves. The results also show that the accuracy and computational effort associated with the *S&B* indentation is significantly better than the other methods.

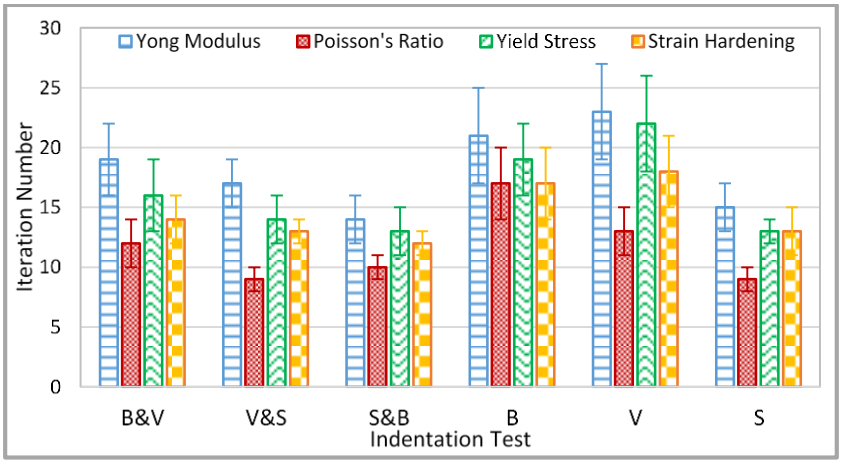

Figure 9-8 comparisons of optimization histories between single and dual indentation test

9.8 Sensitivity analysis of elastic plastic optimization algorithms

The sensitivity of the optimization process to predicted elastic plastic material properties as a result of continuous changing the input parameters until the best match between the predicted and experimental data is achieved is a major difficulty in using inverse or reverse method (T.A. Venkatesh 2000). In this study, the input indentation data were taken from the numerical simulations. However, in the actual experimental work, there are many factors which potentially cause systematic and random error. These errors may relate to indenter deformation and tip blunting during indentation, and the accuracy of the indentation measurements (Dao, Chollacoop et al. 2001). A series of input target materials was employed (Table 9-4) to investigate the sensitivity and accuracy of the optimization algorithm based on *S&B, B&V,* and *V&S* indentation methods.

Figure 9-9 shows the sensitivity analysis of three optimization methods with five different sets of material properties which have been used as input data to evaluate the accuracy and sensitivity of the approaches. In each approach, there are only a few material properties sets that match the target data and all parameters are focused in a small boundary region. As displayed the results achieved by the *S&B* approach is significantly better than the other methods (B&V, and V&S). A small deviation in the predicted mechanical properties (σ_y , E , and n) produces a very limited material range with identical load displacement curves (same objective function); such behaviour reflects the uniqueness of the method in solving complex material systems.

Table 9-4 summarizes the sensitivity analysis of the *S&B* optimization method. The results from each set of parameters represent the residual error between the target and predicted load displacement curves to within $\leq$ 2% determined by a non-linear least-squares objective function (LSQNONLIN) in MATLAB code. The previous analysis shows that the Poisson's ratio has less influence on the predicted load displacement curves, therefore the three parameters (σ_y , E , and n) have been used in the optimization algorithm.

In the case of the *S&B* approach, the deviation and percentage error of E measured during the sensitivity analyses of a range of materials were within 2.6 GPa, and 1.6% respectively. The deviation and percentage error of σ_y were within 6.5 MPa, and 1.1% respectively, while the percentage error of *n* was within 0.001, and 1.2% respectively. This suggests that the Elastic modulus, Yield stress, and strain hardening can be extracted using the proposed method within 1.6%, 1.1%, and 1.2% relative error respectively. All the proposed parameters can be determined with a specific percentage of errors if the load displacement curves are measured with accuracies greater than 98%. The accuracy achieved is significantly better than some stated methods in the previous works (Giannakopoulos and Suresh 1999, Dao, Chollacoop et al. 2001).

The true stress-strain curves with optimal predicted material properties (minimum objective function) were plotted in Figure 9-10, which shows that these stress-strain curves are identical. Figure 9-11 compares the load displacement curves of optimal material property sets with the input target data ($\sigma_y = 550\ MPa$, $E = 80GPa, v = 0.2, n = 0.09$). The load displacement curves of the predicted material properties agree very well with the target material, all parameters bieng focused in a small boundary region to within $\leq$ 2% residual errors.

This suggests the optimization algorithm based on the pair of Spherical and Berkovich` indentations can accurately predict the elastic plastic material properties with unique stress-strain curves.

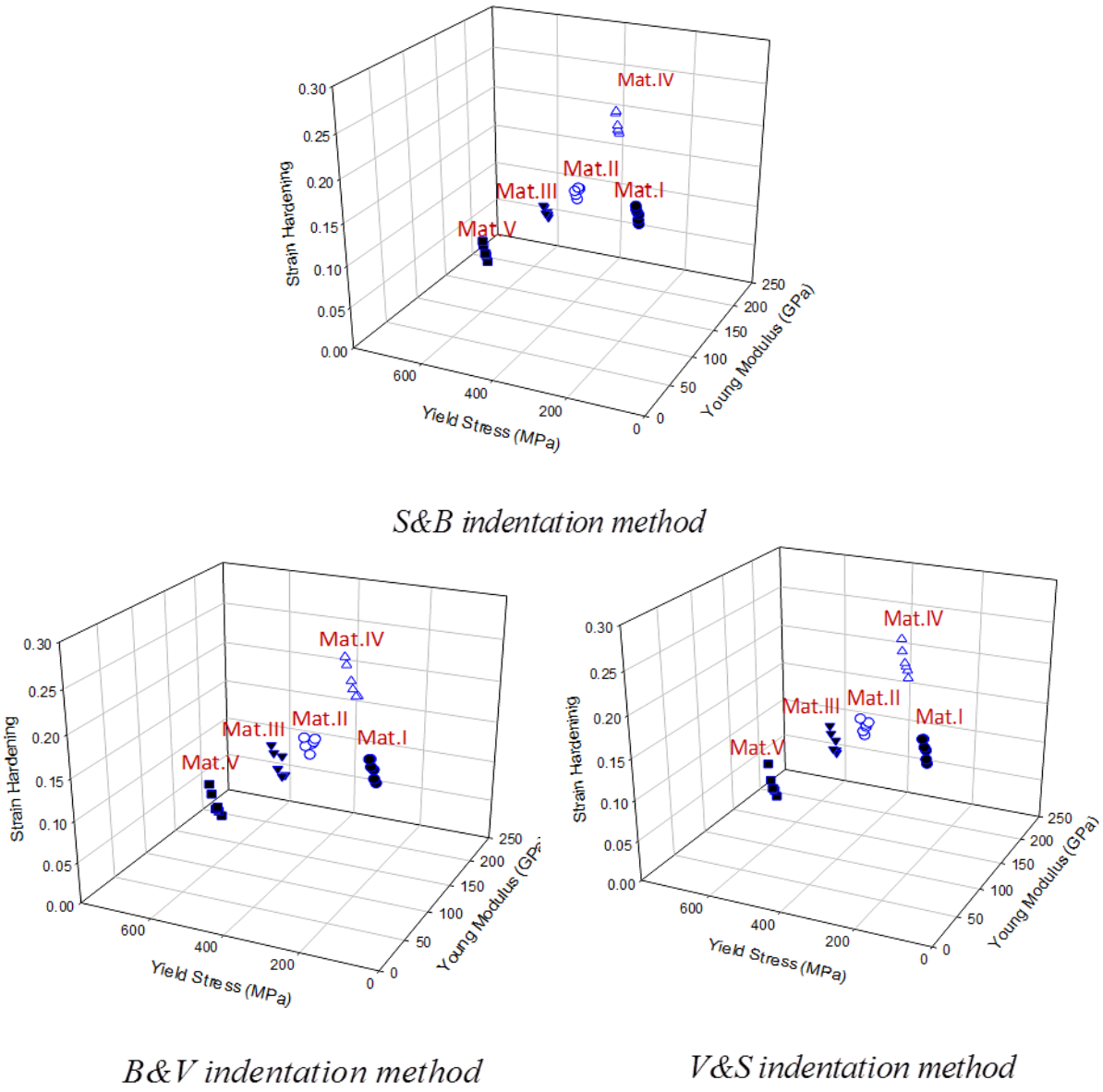

Figure 9-9 Sensitivity and accuracy results of elastic plastic optimization algorithms (*S&B*, *B&V*, and *V&S*)

Table 9-4 Sensitivity and accuracy analysis of *S&B* optimization method

Material	*Parameter*	*Target value*	*Initial value*	*Predicted value*	*Error %*
Mat.I	E(GPa)	100	40	100.9	0.82
	σ_y(MPa)	160	100	161.2	0.71
	v	0.2	0.2	0.2	0
	n	0.16	0.1	0.16	0.99
Mat.II	E(GPa)	120	60	121.4	1.1
	σ_y(MPa)	350	175	346.6	0.98
	v	0.2	0.2	0.2	0
	n	0.15	0.05	0.15	0.87
Mat.III	E(GPa)	160	70	157.4	1.6
	σ_y(MPa)	500	250	544.5	1.1
	v	0.2	0.2	0.2	0
	n	0.1	0.01	0.09	1.11
Mat.IV	E(GPa)	200	110	202.4	1.2
	σ_y(MPa)	350	150	353.4	0.98
	v	0.2	0.2	0.2	0
	n	0.2	0.05	0.202	1.2
Mat.V	E(GPa)	80	10	79.2	1.0
	σ_y(MPa)	550	100	556.5	1.1
	v	0.2	0.2	0.2	0
	n	0.09	0.01	0.089	0.99

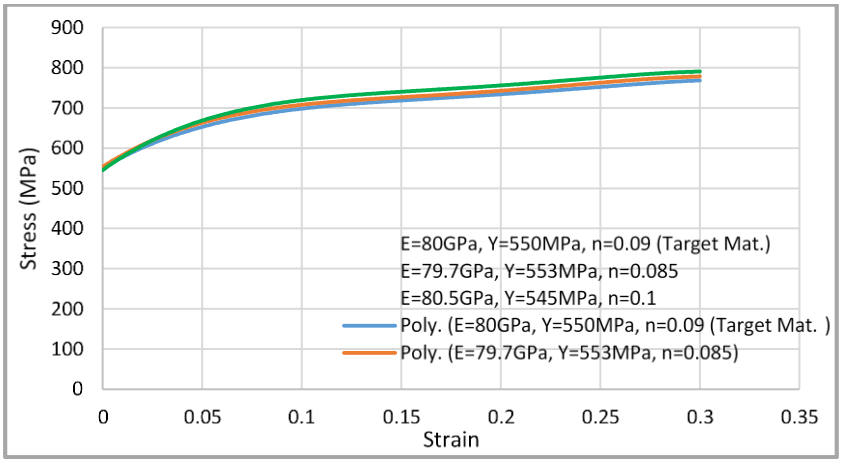

Figure 9-10 True stress-strain curves of target material and other data with objective function ≤ 0.01

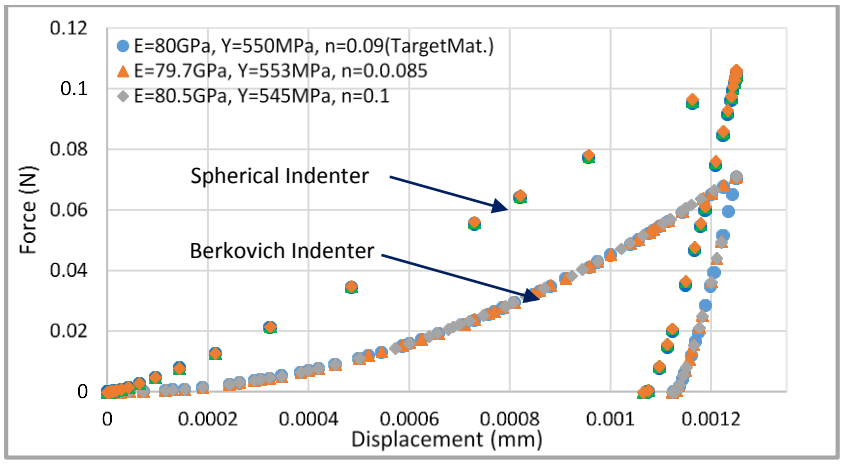

Figure 9-11 Comparison between the predicted load displacement curves using the optimal and target material properties for S&B approach

9.9 Characterization of Drucker-Prager material properties

The conventional indentation elastic plastic FEM models assume highly uniform stress fields which made these models particularly important when extracting the fracture toughness values. The application of such FEM models based on the Von-Mises criterion are more compatible and valid in applications of the homogeneous and isentropic materials (e.g. metallic material, glasses, and single crystal materials) but are not suitable for anisotropic, inhomogeneous and polycrystalline, materials (e.g. granular material, metallic glasses, ceramics, and silicon nitride). Keryvin (2007) applied the new constitutive Drucker-Prager model which takes into account the influence of hydrostatic pressure on the metallic glass material in order to validate the experimental physical phenomena in the FEM simulations. Giannakopoulos and Larsson (1997, and Larsson and E Giannakopoulos (1998) studied the pressure-sensitivity of hard metals and ceramics using the linear Drucker-Prager model.

The plasticity in the brittle material (e.g. viscoplastic and amorphous silica) cannot be accurately described by shear flow theories such as tri-axial, tensile and uni-axial damage for two reasons. Firstly, there is no equivalence to the dislocation based deformation, and secondly it has an open structural arrangement, more than the crystalline materials making it more liable to densification (volume change), (Perriot, Vandembroucq et al. 2006).

The densification behaviour of such materials can be defined by means of a linear Drucker–Prager model. Gadelrab, Bonilla et al. (2012) used the linear Drucker–Prager model to describe the densification of fused silica material, the estimated parameters from the experimental and numerical analysis are in agreement with the values published in the literature such as by Kermouche, Barthel et al. (2008). Patnaik, Narasimhan et al. (2004) developed an analytical solution to calculate the stress field and displacement of indentation on material exhibiting hydrostatic pressure-sensitive plastic behaviour using Drucker-Prager yield criterion.

Despite the above stated researches, there is a yet no established method to determine the mechanical properties of hydrostatic pressure-sensitive plastic materials from the experimental load displacement curves. In the present work the optimization algorithms were created using the Drucker-Prager constitutive model in order to establish an automated predictive tool for characterization of a wide range of engineering material systems based on numerical and experimental indentation data. However, in order to validate the optimization algorithm special attention is given to the unloading curves of the indentation. As a result H_{IT}, E_{eff} and indentation depth ratio can be calculated from the optimal loading unloading curve using the Oliver and Pharr method and compared with results obtained from target loading unloading curves.

9.9.1 Drucker-Prager material constitutive model

The Linear Drucker-Prager hardening constitutive material law has been developed to describe the indentation response of material exhibiting hydrostatic pressure-sensitive plastic behaviour as is shown in Figure 9-12, where p is the hydrostatic pressure, and it flow direction which is defined by Eq. (9.13). Such a model can be used to describe the deformation behaviour of soil and granular material, metallic glass, and polymer material (Keryvin 2007). The linear plastic Drucker-Prager model is given by Eq. (9.14):

$$t = \frac{1}{2} q \left[1 + \frac{1}{k} - \left(1 - \frac{1}{k} \right) \left(\frac{S_{ij}}{q} \right) \right] \tag{9.13}$$

$$\sigma_e + \mu \, \sigma_m - \sqrt{3} \, \sigma_S = 0 \tag{9.14}$$

Where: $\sigma_e = \sqrt{\frac{3}{2} S_{ij} S_{ij}}$ is the Von Mises equivalent stress, and $S_{ij} = \sigma_{ij} - \sigma_m \varepsilon_{ij}$ is the stress deviator, $\sigma_m = \sigma_{kk}/3 = -p$, σ_S is the shear stress, μ is the hydrostatic stress sensitivity parameter, and β is friction angle. In the ABAQUS input file, the Drucker-Prager material model is defined using the angle of friction β, dilatation angle ψ , and flow stress ratio *K*, and hardening curves for different strain rates.

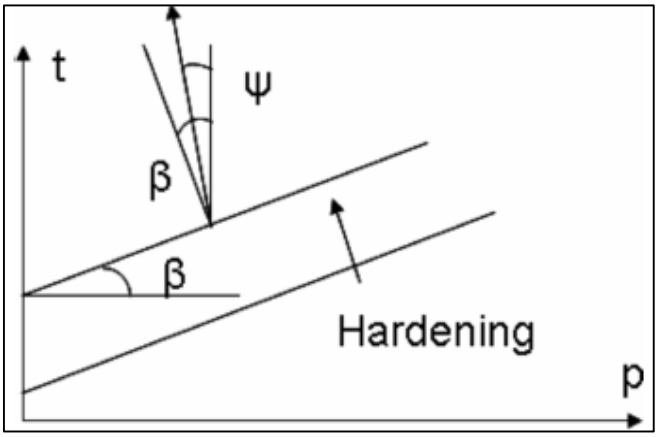

Figure 9-12 Linear Drucker-Prager model: yield surface and flow direction in the *p*–*t* plane (ABAQUS, 2010)

The angle of friction β can be determined from the hydrostatic stress sensitivity parameter, μ which is dependent on the adhesive material and characterises the sensitivity of yielding to hydrostatic stress. A value of μ is determined from tests under two different stress states given by Eq. (9.15), using yield stress from shear and tensile tests. The dilatation angle ψ can be determined from the flow parameter μ^* Eq. (9.16). If the calculated value of parameter μ^* is not equal to μ then flow is called non-associated; associated flow is found by setting μ^* equal to μ. For simplicity, the associated flow can be assumed by setting μ^* equal to μ but the resulting loss in the accuracy of stress and strain calculations will be uncertain (ABAQUS).

$$tan\,\beta = \mu = 3\left[\left(\sqrt{3}\,\sigma_s/\sigma_T\right) - 1\right] \tag{9.15}$$

$$\mu^* = \tan\psi = 3(1 - 2\,v^p)/2(1 + v^p) \tag{9.16}$$

Where v^p is a plastic component of Poisson's ratio.

The third parameter required by the ABAQUS input file is the flow stress ratio *K*, which defines the differences in material behaviour under tension and compression. Park, Xia et al. (2001) considered that the parameter *k*, changes within the range of $0.788 \leq k \leq 1$ in order to ensure the convexity of the yield stress. However, the flow stress ratio used for the material model has been set to 1 which associates equivalent behaviour under tension and compression.

Since the plastic strain is too small, perfect plasticity was developed in conjunction with associated plastic flow. Three parameters (E, σ_{yc}, β) have been used to optimize the Linear Drucker-Prager hardening material properties. In this study no lower and upper limits have been specified for the values of Young modulus and compressive Yield stress. The friction angle values were selected to be in the range of $0^o \geq \beta \leq 30^o$, with 0.1^o space interval in order represent a wide range of material properties.

9.9.2 Optimization analysis of Drucker-Prager material properties based on dual indenter geometries

The optimization algorithms based on the dual indentation method were developed to predict the Linear Drucker-Prager material properties. The optimization algorithms were carried out using the same procedure and principles used in the dual indenter geometries of elastic plastic materials. Combinations of 3-D indenter geometries (Berkovich, Vickers and Spherical) were performed to predict the Drucker- Prager material behaviour. Various ranges of initial guess have been used to investigate the accuracy and sensitivity analysis of the proposed approaches. Figure 9-13 shows the target numerical load displacement curves to Bulk Metallic Glasses (BMG) with known mechanical properties ($\sigma_{yc} = 1640\ MP\ , E = 72GP\ , v = 0.22,\ \beta = 30, \psi = 30, and\ k = 1$) (Seltzer, Cisilino et al. 2011) , which is used as a blind test for numerical data.

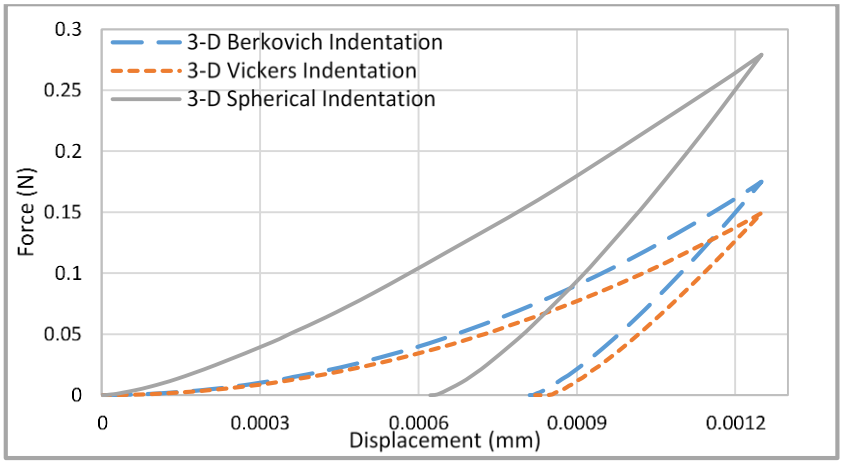

Figure 9-13 Target Drucker-Prager numerical load displacement curves determined from 3-D FEM simulations for a) Berkovich b) Vickers and c) Spherical indentations

The optimization processes include three different pairs of indenter geometries (*B&V), (V&S),* and *(S&B*). The initial guess mechanical properties of Linear Drucker-Prager hardening material (E, σ_{yc}, β) were changed a few times in each process in order to investigate the sensitivity of this method. Table 9-5 summarised the optimization results of three different indentation tests based on the dual indentation methods on BMG material.

The initial guess material properties were selected from a range of material property sets for various dual numerical simulations. The optimization algorithms were carried out by automatically changing the material properties in the (inp.) file of each iteration until the objective function between the target and predicted load displacement curves achieved the minimum convergence value within the range of $0.001 \leq minF(x) \leq 0.02$. Despite using a range of initial guess parameters, the variables (E, σ_{yc}, β) can converge to their target values at different iteration numbers to within 2% percentage error. The optimized reduced modulus and hardness values are in good agreement with the target values. This suggests that the linear Drucker-Prager material properties can be accurately obtained by the proposed optimization techniques of dual indenter geometries.

Table 9-5 Dual indenter optimization results of hydrostatic pressure sensitive (BMG) material

Indenter	*parameter*	*Target value*	*Initial value*	*Predicted value*	*Error %*	H_T/H_O	$(Er)_T/(Er)_O$	*Depth ratio*
3-D	E(GPa)	72	50	73.39	1.89	0.97	0.96	0.97
(B&V)	σ_{yc}(GPa)	1.64	1	1.61	1.82			
	β^0	30^0	15^0	30.4	1.31			
3-D	E(GPa)	72	90	73.26	1.72	0.98	0.97	0.98
(V&S)	σ_{yc}(GPa)	1.64	1	1.62	1.23			
	β^0	30^0	40^0	29.8	0.6			
3-D	E(GPa)	72	10	72.94	1.28	0.985	0.99	0.984
(S&B)	σ_{yc}(GPa)	1.64	1	1.62	1.23			
	β^0	30^0	0.05^0	30.2	0.7			

Figure 9-14 shows the convergence trends of five initial guess values of hydrostatic pressure-sensitive plastic to their target material using S&B indentation technique. The results demonstrated that the initial guess values could converge to their target values by the dual indentation optimization algorithm with different iteration numbers. The materials with less difference between the initial and target values (i:e availability of prior knowledge) will require a fewer iterations to achieve convergence. It is interesting to note additional analyses were also investigated using a wide range of initial guess values. It was found that the application of the proposed algorithm is more reliable for any initial guess values within the defined database i:e , 1GPa$\leq$ E $\leq$150GPa, 100MPa$\leq \sigma_y \leq$5GPa, $0^0 \leq \beta \leq 30^0$, and $0.05 \leq \nu \leq 0.5$.

It is also interesting to note that the most important challenge of such an optimization algorithm is how to clarify the accuracy of the final predicted values in real experimental tests where target values are unknown. However, the solution of repeating the process several times with different initial guess values can overcome this problem and ensure the repeatability of numerical simulations.

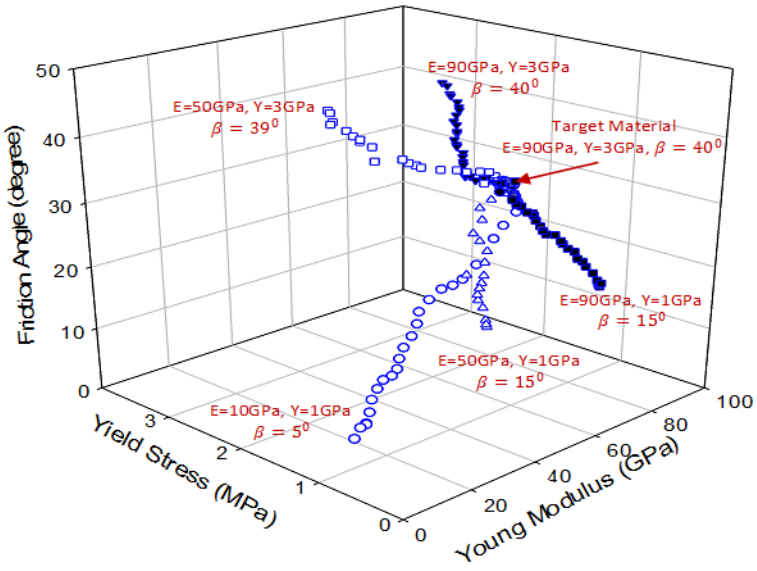

Figure 9-14 Converging trends of five initial guess values using *S&B* dual indenter for pressure-sensitive plastic material properties

Figure 9-15 shows a comparison between three dual indentation methods concerning the optimization history of the initial guess material properties to their target values. The average convergence history of the *B&V*, *V&S*, and *S&B* indentation tests shows that the three parameters achieved their target values after 49, 45, and 38 iterations, respectively over a range of initial guess material properties. The error bar presented in each column explains the material properties can reach their target values at a different iteration numbers, these variations depending on initial guess values. The optimization process based on the S&B indentation test provide the best solution, because fewer iterations are required for the main parameters (E, σ_{yc}, β) to achieve convergence.

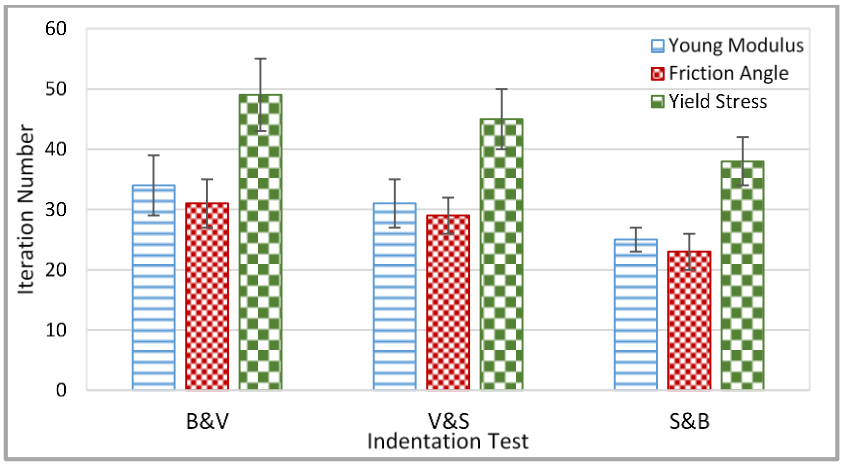

Figure 9-15 Optimization history of (E,σ_{yc},β) based on *(B&V)*, *(V&S)*, and *(S&B)* indentation test

9.10 Sensitivity analysis of Drucker-Prager optimization algorithms

A series of FEM simulations were developed to examine the accuracy and sensitivity of the optimization algorithms based on *S&B, B&V,* and *V&S* indentation methods using a range of hydrostatic pressure-sensitive plastic material properties. Table 9-6 presents the material properties of bulk metallic glass BMG material used in the numerical simulations. The material sets were employed as an input target data (blind test data) to evaluate the accuracy and sensitivity of the methods

Figure 9-16 shows the sensitivity analysis of three optimization methods with four different sets of BMG material properties presented in Table 9-6. As presented, there are few material property sets that match the target data with minimum objective function, and all parameters are concentrated in a small boundary region. The residual errors between target values and optimized parameters are various according to the optimization algorithm type, however the results achieved by *S&B* method are significantly better compared with the other methods. The maximum relative errors were estimated of 7.5%, 6%, and 3.5% in the *B&V, V&S, and S&B* respectively. Consequently, the predicted properties (E,σ_{yc},β) produce a very limited material range having identical load displacement curves (same objective function); such behaviour reflects the uniqueness of the method in solving complex material systems. However, the satisfactory existence of uniqueness, and stability will lead us to consider the proposed method as a well-posed optimization solution.

Table 9-6 Bulk metallic glass material properties

Material	*E (GPa)*	$\boldsymbol{\sigma_{yc}}$ *(GPa)*	$\boldsymbol{\beta}$ *(degree)*	*v*	*k*	$\boldsymbol{\psi}$ *(degree)*	*References*
BMG I	*124*	2.01	40	0.25	1	40	(Inoue, Zhang et al. 2001)
BMG II	*92*	1.34	36	0.23	1	36	(Saida, Kato et al. 2007)
BMG III	74	1.78	35	0.23	1	35	(Yuan, Zhang et al. 2003)
BMG IV	52	1.08	32	0.22	1	30	(Inoue, Zhang et al. 1989)

In the case of the *S&B* optimization algorithm, the convergence of Elastic modulus E, Yield stress σ_{yc} and Friction angle β for the examined materials was within 4%, 3.65%, and 4.2%, respectively.

This demonstrated that the material properties $E, \sigma_{yc},$ and β can be extracted using the proposed method to within 4%, 3.65%, and 4.2% relative error, respectively. All the proposed parameters can be determined with a specific percentage of errors if the load displacement curves are measured with accuracies greater than 97%.

The sensitivity analysis of dual indentation *S&B* optimization algorithm has been expanded to include other material systems such as ceramics, polymers, concrete and BMG. Table 9-7 summarized several material properties (E, σ_{yc}, β) have been used as input data to numerical simulations. The relative error for each parameter was measured at the best match between the predicted and target load displacement curves to within accuracy of $\leq$ 3% determined by a non-linear least-squares objective function (LSQNONLIN) in MATLAB code

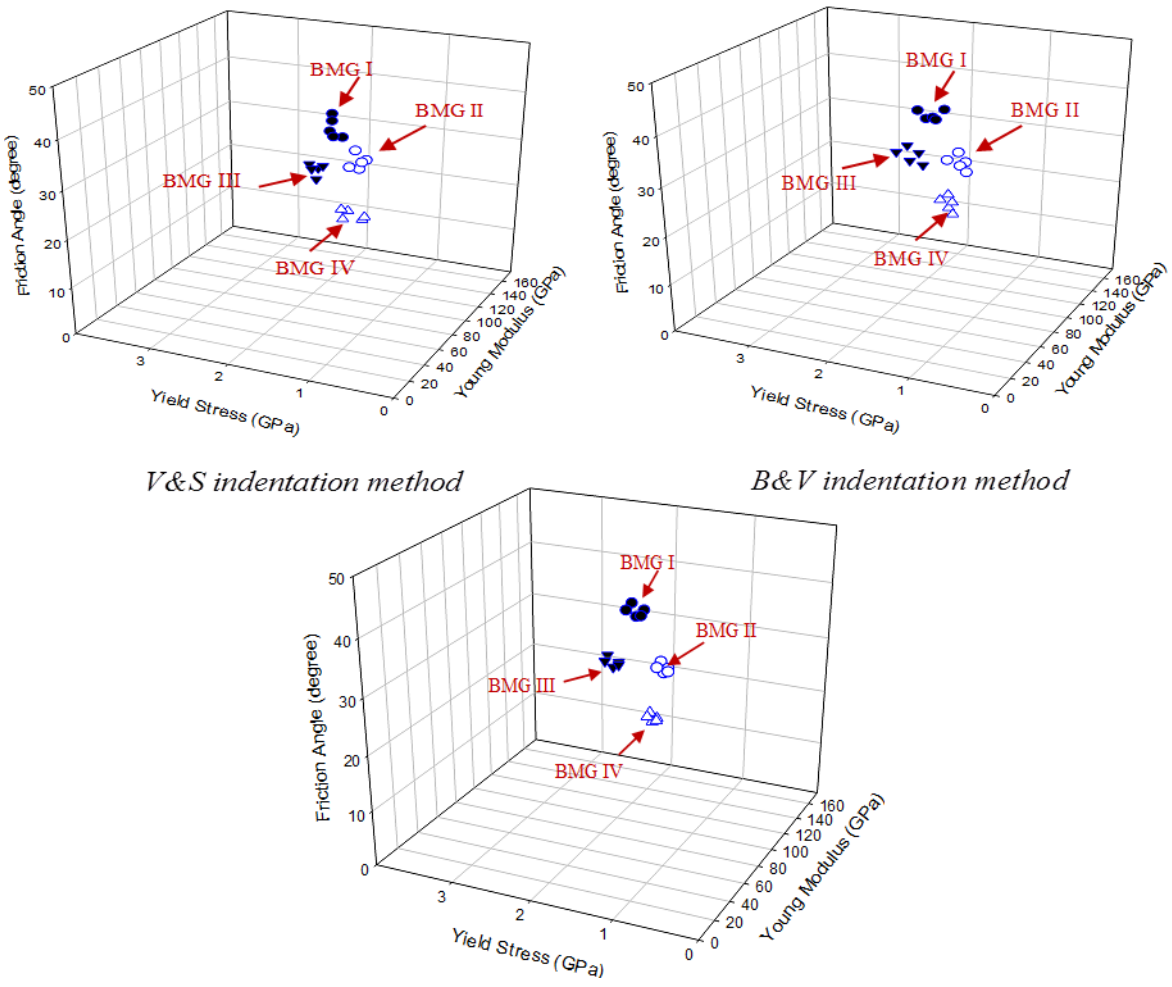

Figure 9-16 Sensitivity and accuracy results of Drucker-Prager optimization algorithms (*S&B, B&V*, and *V&S*)

Figure 9-17 illustrates that there are a few material data sets over a small region matching the input data. This suggests that the combination of Spherical and Berkovich indenters could produce unique results.

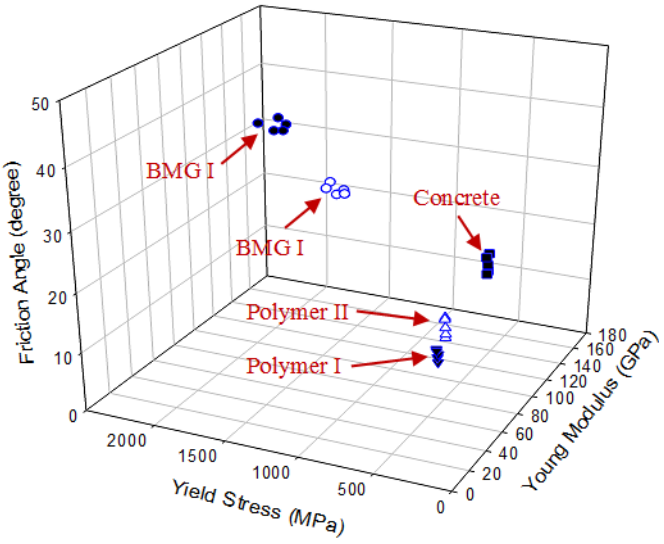

S&B indentation method

Figure 9-17 Sensitivity and accuracy results of *S&B* optimization algorithms

Table 9-7 sensitivity and accuracy analysis of *S&B* optimization method

Material	*Parameter*	*Target value*	*Initial value*	*Predicted value*	*Error %*
Polymer I	E(GPa)	5	0.5	5.18	3.4
(Seltzer, Cisilino et al. 2011)	σ_{yc}(MPa)	140	10	144.5	3.2
	β^0	20^0	0.05^0	22^0	9
Polymer II	E(GPa)	3.5	0.25	3.65	4.2
(Seltzer, Cisilino et al. 2011)	σ_{yc}(MPa)	90	10	92.61	2.9
	β^0	25^0	2^0	23^0	8.6
Concrete	E(GPa)	40	3	38.2	4.5
(Mokhatar and Abdullah 2012)	σ_{yc}(MPa)	40	5	41.56	3.9
	β^0	30^0	5^0	31.5^0	5
BMG I	E(GPa)	124	10	127.72	3
(Inoue, Zhang et al. 2001)	σ_{yc}(MPa)	2010	300	2076	3.3
	β^0	35^0	1^0	32.9^0	4.7
BMG II	E(GPa)	92	5	89.5	2.7
(Saida, Kato et al. 2007)	σ_{yc}(MPa)	1340	200	1380	3
	β^0	30^0	1^0	28.65^0	4.5

Figure 9-18 Shows comparison of load displacement curves between the predicted and input target data ($\sigma_y = 1.76\,GPa\,, E = 74\,GPa, \nu = 0.22, \beta = 32^0$). It is clearly demonstrated that the load displacement curves using the predicted material properties agree very well with the input numerical target data. This suggests that the optimization algorithm based on dual of Spherical and Berkovich indentations can be accurately predict the pressure-sensitive plastic material properties.

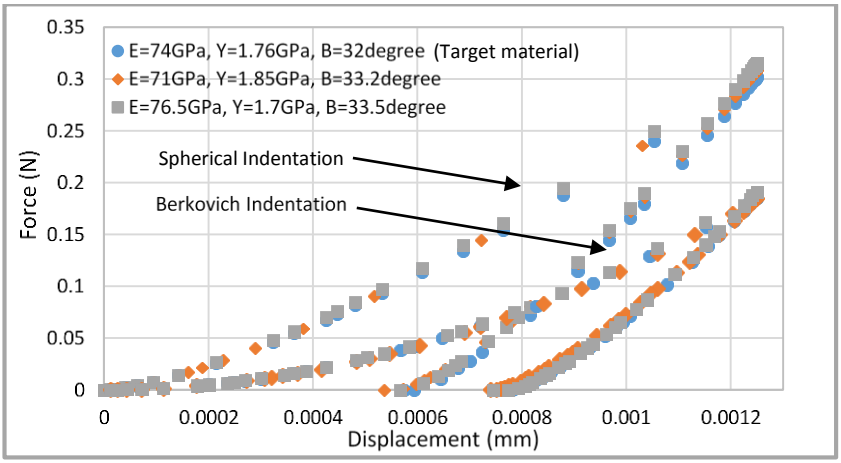

Figure 9-18 Comparison of load displacement curves between the predicted and target pressure-sensitive plastic material properties using S&B approach

9.11 Determining plastic properties of material with residual stress

9.12 Dimensional analysis of mechanical properties and residual stress

This work focuses on determining the elastic plastic properties of heat-treated specimens when the residual stresses are known in a prior study based on the previous numerical and experimental analysis. Incorporating the effect of residual stress in the material can accurately lead to assessing the plastic properties of heat treated specimens. A common method for considering the effect of residual stress is to compare the load displacement curves, or contact area, and/ or contact depth of the material specimens with and without residual stress (Carlsson and Larsson 2001, Lee and Kwon 2004). Other researchers explain the relation between the residual stress level and plastic strain associated at the indentation zone during the loading and unloading cycle. Carlsson and Larsson (2001) Proposed that the compressive residual stress enhances the pile-up, whereas tensile residual stress reduces the plastic strain. Consequently, the projected contact area was calculated as a function of σ_{res} using FEM analysis.

This suggest that the accuracy of σ_{res} increases if the plastic strain can be calculated accurately for a given material. Chen, Yan et al. (2006) investigate the effect of residual stress on the plastic zone. It is found that the indentation compressive stress reduces when applied on the tensile stress area, causing a larger plastic field and lower hardness while the indentation compressive stress increases on the compressive stress area resulting in a smaller plastic field and higher hardness.

In order to investigate the effect of residual stress on the indentation results a comprehensive study of numerical analysis was performed using the dimensional analysis relationships of hardness and reduced modulus. The hardness values were normalized by yield stress, and reduced modulus normalized by the square of contact radius and contact stiffness. By changing the normalized stress ratio σ_{res}/σ_y, and yield strain ratio E/σ_y, the functional forms $f, and\ g$ can be determined from the numerical simulations using the dimensional analysis approach given by Eq.(9.17), and (9.18). The Hardness, H and contact stiffness, S are calculated from the experimental load displacement curve using the Oliver and Pharr method. However, the mechanical properties (E, σ_y, σ_{res}, and n) of the elastic plastic material can then be obtained from reverse analysis.

$$\frac{\mathrm{H}}{\sigma_y} = f\left[\frac{\sigma_{res}}{\sigma_y}, \frac{E}{\sigma_y}, n\right] \tag{9.17}$$

$$\frac{2aE_r}{S} = g\left[\frac{\sigma_{res}}{\sigma_y}, \frac{E}{\sigma_y}, n\right] \tag{9.18}$$

9.12.1 FE indentation with residual stress

FEM calculations were performed using ABAQUS finite element code. The equivalent 2-D axisymmetric conical to Vickers and Spherical geometries were used to simulate the rigid indenter, and the option of displacement control and the reaction force measured along the direction of indentation depth was employed. The specimen was modelled as isentropic homogeneous elastic plastic hardening material. The coulomb's friction law was used between the contact geometries, and the friction coefficient was taken to be 0.15. The residual stress was applied to the region of interest beneath the tip geometry. The projected contact area can be calculated directly from numerical simulations by measuring the nodes in contact with the indenter at maximum indentation depth.

The material parameters (E, σ_y, σ_{res}, and n) are varied over a wide range, such that the normalized residual stress was selected to be in the range ($-1 \leq \sigma_{res}/\sigma_y \leq 1$), and the yield strain ratio range was $10 \leq E/\sigma y \leq 250$, such ranges will cover almost all combinations of residual stress and mechanical properties found in engineering materials. A parametric study was undertaken to determine the effect of residual stress on the indentation results and also to calculate the functional forms ($f, or\ H/\sigma_y$), and (g, or $2aE_r/S$) by regression analysis for a given set of indentation data using script programming language (python) interfaced with ABAQUS FEM. In this arrangement, the programme automatically searches for a range of material properties and residual stress. In the searching process, the input data was transformed to a discrete form with equally spaced points at each indentation depth (indentation points). The numerical simulation results were then recorded and saved into a database to form a simulation range. The results over the numerical simulation range were arranged into a predefined an excel program, which allows easy interpretation.

9.12.2 The effect of residual stress on the indentation test

FEM analyses were employed to investigate the effect of residual stress on indentation stress, plastic zone, and surface profile. Soda lime silicate glass was selected as a target material in these analyses. Figure 9-19 shows the effect of residual stress ratio (normalized residual stress with Yield stress) on the load displacement curves of elastic plastic material with a strain hardening property. As illustrative for given elastic plastic properties (σ_y, E, v, n) and maximum indentation depth, the compressive indentation stress causing a higher indentation force and gives increase to the hardness, whereas the tensile residual stress will result in lower indentation force and clearly gives a lower hardness.

The effect of residual stress on hardness can be explained from shear plasticity. Since the indentation load generates compressive stress perpendicular to the applied surface, then the existence of tensile residual stress at the specimen surface increases the magnitude of the shear stresses underneath the indenter compared with an unstressed specimen. Consequently, the plastic deformation in the specimen is enhanced, causing reduction of contact hardness and pile-up when residual tensile stress present. These results are in agreement with the results obtained by Chen, Yan et al. (2006).

However, the mechanics behind this phenomenon can be gained by analysis of the plane residual stress component, $\boldsymbol{\sigma_{33}}$ after unloading stage for various residual stress ratios $\boldsymbol{\sigma_{res}/\sigma_y}$. Figure 9-20 shows the counter plot distribution of plane stress component $\boldsymbol{\sigma_{xx}}$ with different residual stress levels of Vickers, and Spherical indentation processes.

As displayed, when the residual stress is tensile, σ_{res}/σ_y = 0.5, the region of indentation compressive stress is smaller than for the initial case of stress free, σ_{res}/σ_y = 0. This increases the opportunity for lower hardness material. In the opposite case when the specimen holds residual compression stress σ_{res}/σ_y = -0.5 , the maximum compressive stress will be higher than that in the stress free sample, and the resulting overall compression zone is much larger. These results are in agreement with the results obtained by Yan, Karlsson et al. (2007).

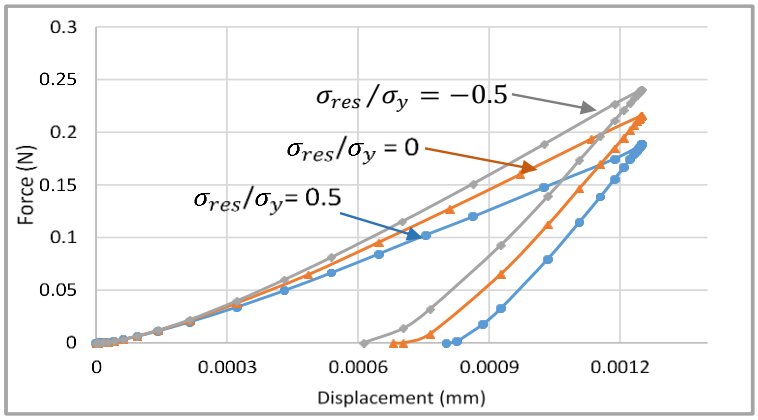

(a)

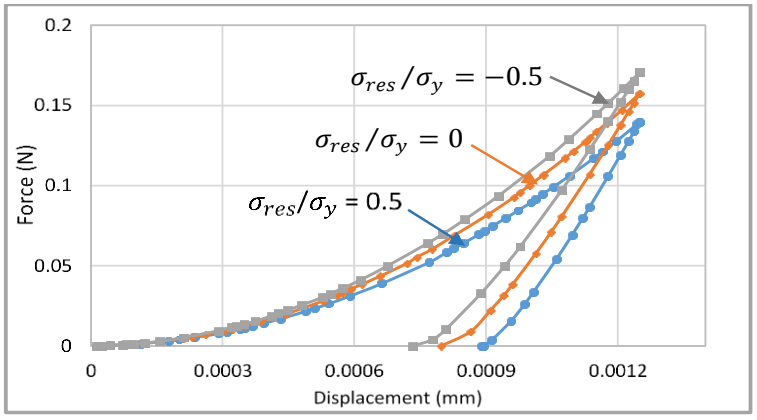

(b)

Figure 9-19 Effect of stress ratio on the numerical load displacement curves of strain hardening elastic plastic material of a) Spherical and, b) Vickers indentations

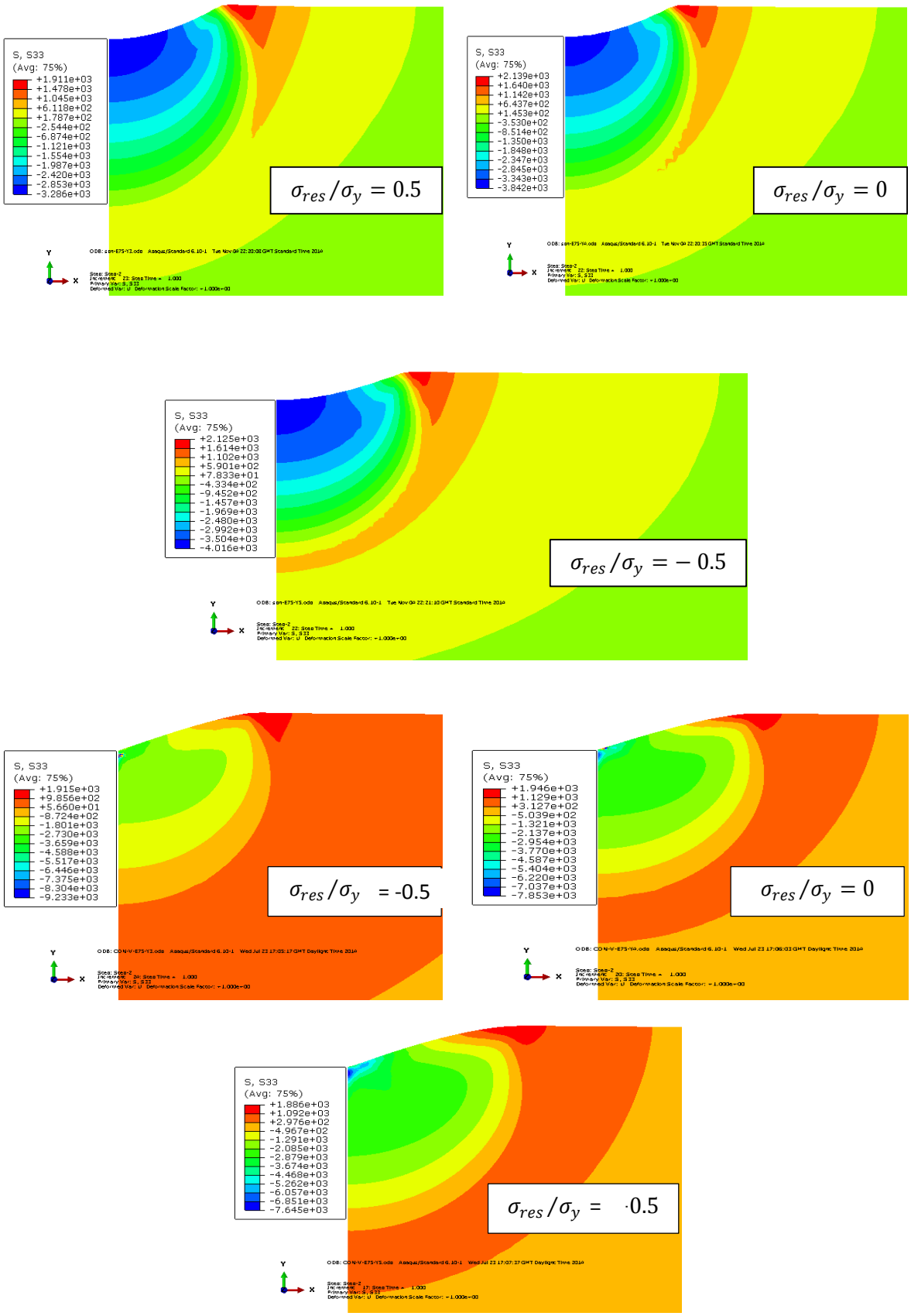

Figure 9-20 Counter plot distribution of plane stress component $\boldsymbol{\sigma_{xx}}$ with different residual stress level at Vickers, and Spherical indentation processes

Figure 9-21 shows the parametric study analysis of mechanical properties and residual stress with reference to Eq. (9.17). Regression analysis can be used to determine, f the normalized hardness H/σ_y as a function of elastic plastic mechanical properties and normalized residual stress ($E/\sigma_y, n, \sigma_{res}/\sigma_y$). It is clearly noticed that for a given residual stress and maximum indentation depth, the indentation force increases with the increasing strain hardening, resulting in increasing H/σ_y. The results also show that the normalized hardness value increases with increasing of the residual compressive stress, whereas it decreases with the increases of tensile residual stress for material properties in the range$10 \leq \mathrm{E}/\sigma\mathrm{y} \leq 100,$ and $0 \leq n \leq 0.3$. Based on the numerical simulations results, the residual stress achieved a constant value when the normalized hardness>3 and $E/\sigma_y >$70. This suggests that for hard material the residual stress significantly increases the plastic flow in the specimen, which produces normalized hardness more sensitive to residual stress variation. In case of soft material, due to the finite plastic deformation, H/σ_y is essentially insensitive to residual stress.

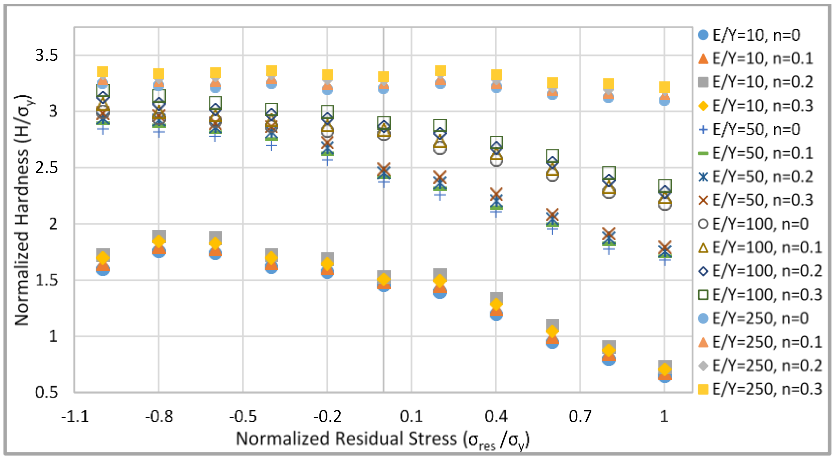

Figure 9-21 Normalized hardness as a function of yield strain and normalized residual stress

Figure 9-22 shows the parametric study analysis of mechanical properties and residual stress with reference to Eq. (9.18). Regression analysis can be used to determine, g the normalized reduced modulus, $2aE_r/S$ as a function of elastic plastic mechanical properties and normalized residual stress ($E/\sigma_y, n, \sigma_{res}/\sigma_y$).The results show that for a given residual stress and maximum indentation depth, $2aE_r/S$ increases with the decreasing strain hardening values.

The results also show that the normalized reduced modulus decreases with decreased residual compressive stress, whereas it is decreases with the increased tension residual stress for material properties range $0 \leq E/\sigma y \leq 20, \text{and } 0 \leq n \leq 0.3$. Based on the numerical simulations results, the residual stress achieved a constant value when the normalize reduced modulus achieved a constant value of about 0.88 and $E/\sigma_y > 20$.

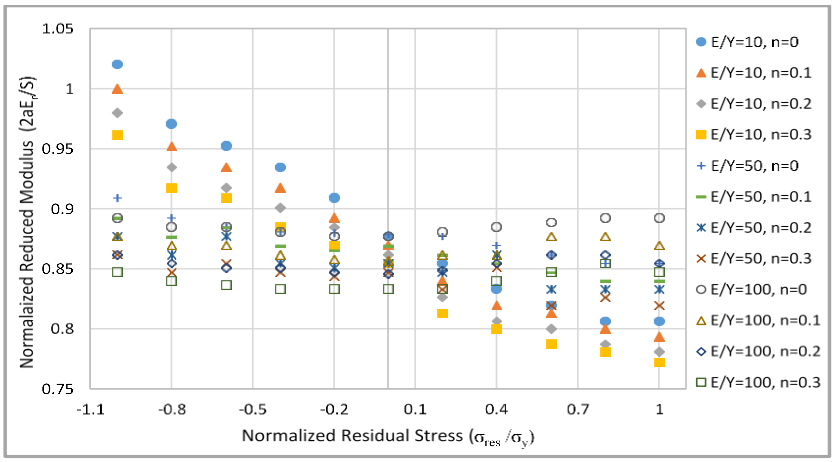

Figure 9-22 Normalized reduced modulus as a function of yield strain and normalized residual stress

9.13 Optimization analysis of thermally treated recycled glass

The results presented in previous sections have established that the dual indenters could give more accurate and robust results compared with a single indentation process. The complete study of different optimization algorithms based on load displacement curves suggested that the combined spherical and Berkovich indenter geometries is an accurate method used to determine the elastic plastic and pressure sensitive hardening properties. However, in order to explore the robustness and feasibility of this approach in real-life applications, the S&B optimization algorithm has been extended to characterize the material properties of thermally treated recycled glass media used for finishing and super-finishing applications.

9.14 Experimental work

Specimens of thermally treated recycled glass media were prepared for standard metallographic and indentation tests by cold mounting and subsequent wet grinding and polishing operations using a Metaserv Rotary Grinder machine. Abrasive papers of grade P120 to fine abrasive grade P1200A were used to remove surface asperities and to achieve the required surface roughness for instrumented indentation tests. A range of glass media samples produced under different heat treatment cycles were used in this investigation.

A series of instrumented indentation experiments were performed at room temperature with the CSM nano-indentation instrument. The experiments were carried out with Berkovich and Spherical indenters using a continuous stiffness measurement to different peak loads of 150mN, 200mN, and 250mN. The loading and unloading rate speed was 2000nm/min. Three indentation test were performed at each load, the average of the group results are presented in this study with thermal drift neglected.

The experimental works were carried out with three different (Vibraglaz) media grades manufactured by three different levels of heat treatment cycles. Figure 9-23 (a, b, and c) shows the experimental load displacement curves of three different glass media grades Finishing media (VT+60), Cutting media (VT-70), and General purpose media (VT-10), respectively. The indentation load displacement curves demonstrate that the three grades of thermally treated glass media show both elastic and plastic deformation during the nano-indentation tests and prove that the unloading period marked elastic recovery occurs. However, for the same indentation force, the elastic recovery of Berkovich and spherical indenters were 45%∓3%, and 69%∓2%, respectively. This may be attributed to the fact that the residual area increases with the increased tip radius, while the residual depth decreased.

It is clearly observed that there are small differences in the load displacement curves over various media samples particularly for the unloading stage, causing small differences in the Hardness and Elastic modulus. This difference is used as a quality control tool to distinguish the grade type. Based on the above assumptions the elastic plastic hardening material constitutive law was developed through the optimization algorithm to obtain the unknown material properties (σ_y , E , v, n).

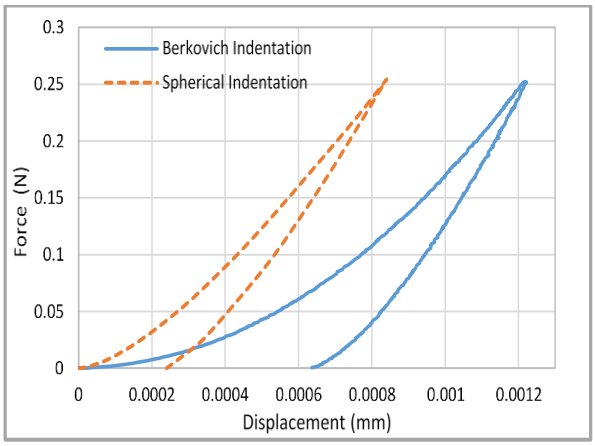

(a)

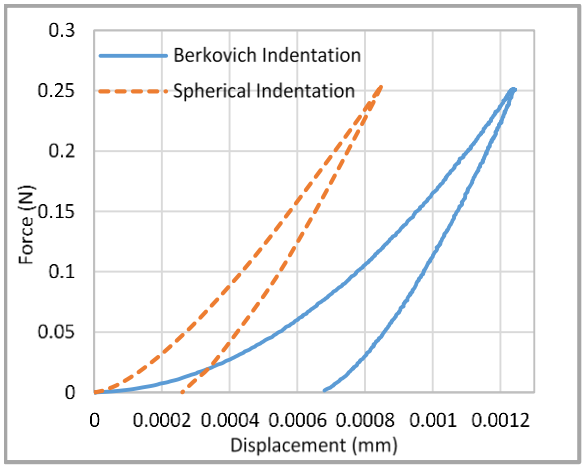

(b)

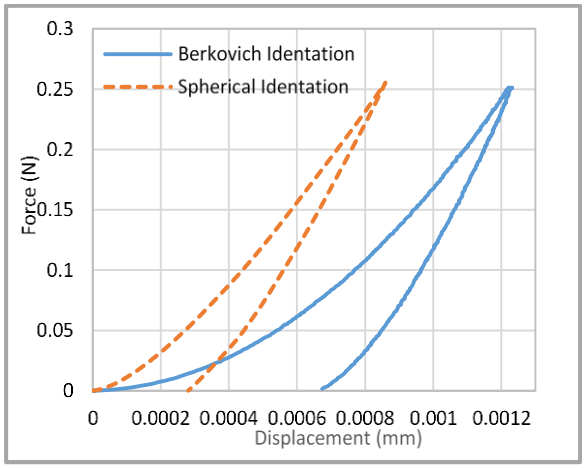

(c)

Figure 9-23Experimental load displacement curves of dual indentation S&B method for: a) VT+60, b) VT-70, and c) VT-10

9.15 Optimization analysis of thermally treated recycled glass based on dual indenter geometries

In this section, the method of *S&B* optimization algorithm developed in the previous section was applied to extract the detailed material properties of the three various grades of thermally treated recycled glass obtained from different heat treatment cycles.

A similar procedure has been followed as detailed in section (9.6.1) to determine the unknown four material parameters (σ_y , E , v, n), but in this case for a given residual stress value obtained from previous numerical and experimental results presented in [Chapter 5]. The target experimental load displacement curves illustrated in Figure 9-23 were used as input data to the optimization algorithm of the three different specimens' grades VT+60, VT-70, and VT-10.

The indentation hardness H_{IT}, effective elastic modulus, E_{eff} and indentation depth ratio values for each case can be calculated from the optimal loading unloading curve using the Oliver and Pharr method. Table 9-8 presents the optimization results of glass media grades based on the dual *S&B* indentation method.

The optimization algorithms were carried out with three different initial guess parameters to ensure the uniqueness of each approach to converge sets of initial guess values to the same actual values. Python script was interfaced with FEM simulation, in order to allow the programme to automatically change the material properties in the (inp.) file of iteration until the objective function between the experimental and predicted load displacement curves achieved the minimum convergence value in the range $0.001 \leq minF(x) \leq 0.01$. Although using a range of initial guess parameters, the variables (σ_y , E , v, n) can converge to the experimental material properties at different iteration numbers. The results show the convergence is achieved in about 15-30 iterations. Figure 9-24 shows the predicted hardness values are in a good agreement with the experimental results. It has been observed that the indentation hardness of thermally treated recycled glass increases with decreasing indentation depth or indentation load resulting in a decrease in the elastic properties due to the indentation size effect (ISE). The results also suggested that the heat treatment cycles have an influence on the Hardness values, which is used as a quality control tool to differentiate the media grades. Consequently, the experimental and numerical results demonstrated that the hardness values of VG+60, VG-10, and VG-70 were about (6.2, 5.9, and 5.6) GPa respectively.

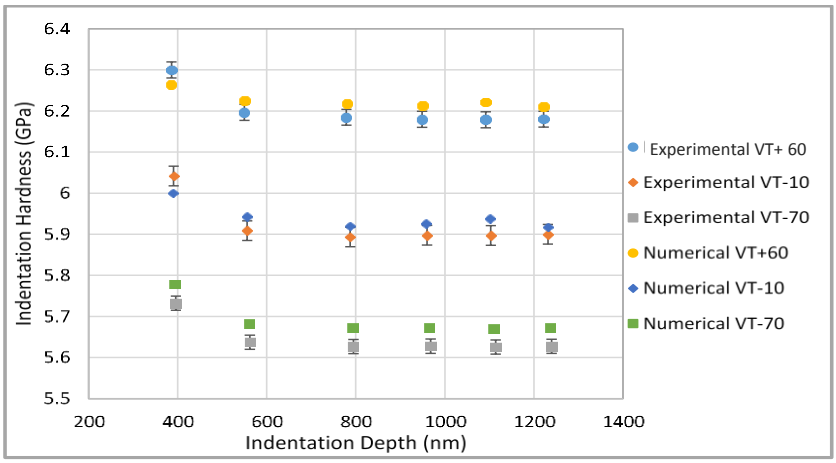

Figure 9-24 Numerical and experimental indentation hardness of different indentation load for thermally treated glass media, VT+60, VT-10, and VT-70

Table 9-8 Optimization results of glass media grades based on *S&B* algorithm

material	*parameter*	*Initial 1*	*Initial 2*	*Initial 3*	*Optimal value*	$(H_{IT})_O/(H_{IT})_{exp}$	$(Er)_O/(Er)_{exp}$	*Depth ratio*
VT+70	E(GPa)	10	120	30	83.35	1.02	0.996	0.97
	σ_y(GPa)	1	7	8	5.5			
	v	0.1	0.4	0.1	0.24			
	n	0.01	0.2	0.04	0.085			
VT-10	E(GPa)	10	120	30	82.5	1.03	0.992	0.968
	σ_y(GPa)	1	7	8	4.85			
	v	0.1	0.4	0.1	0.24			
	n	0.01	0.2	0.04	0.1			
VT-60	E(GPa)	10	120	30	82.9	1.035	0.994	0.96
	σ_y(GPa)	1	7	8	5.15			
	v	0.1	0.4	0.1	0.24			
	n	0.01	0.2	0.04	0.09			

Figure 9-25 shows the convergence trends of the three initial guess values of thermally treated recycled glass grades VT+60, VT-70, and VT-10 . The results demonstrated that the initial guess values can converge to their target values by dual indentation optimization algorithm with different iteration numbers. The materials with fewer differences between the initial and experimental values (i:e availability of prior knowledge) will require fewer iteration numbers to achieve convergence such as in initial guess 2.

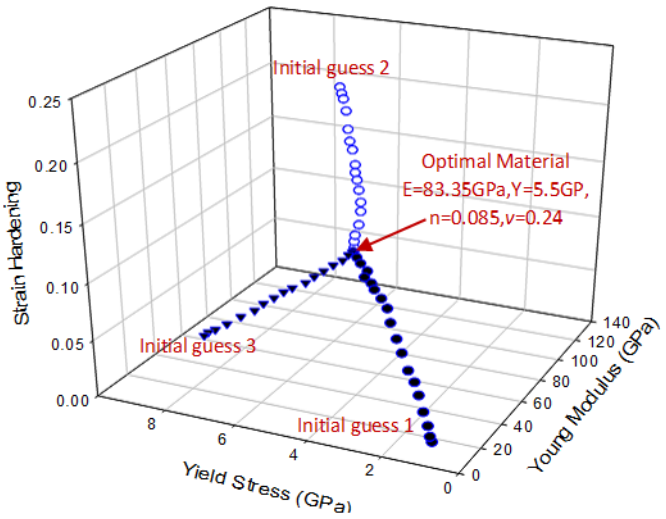

(a) VT+60

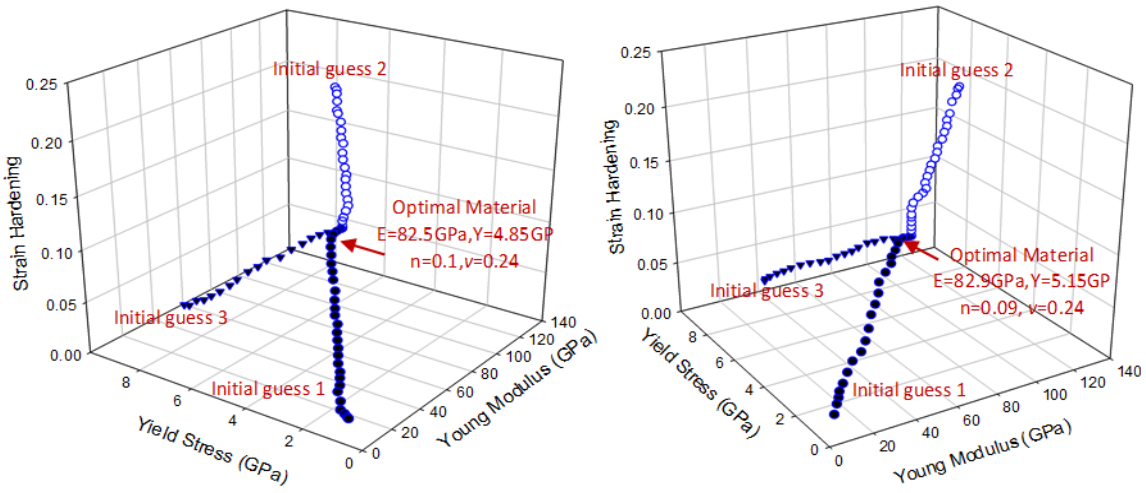

(b) VT-70 (c) VT-10

Figure 9-25 Converging trends of three initial guess values using *S&B* dual indenter for Vibraglaz mediaVT+60, VT-70, and VT-10,

Figure 9-26 shows the comparison of load displacement curves between the predicted and input experimental target data of Vibraglaz media. It is clearly demonstrated that the load displacement curves using the predicted material properties agree very well with the input experimental target data. The analysis also illustrated that there are a few material data sets over a small region matching the input data. This suggests that the combination of Spherical and Berkovich indenters could produce unique results and accurately predict the elastic plastic properties of thermally treated glass materials.

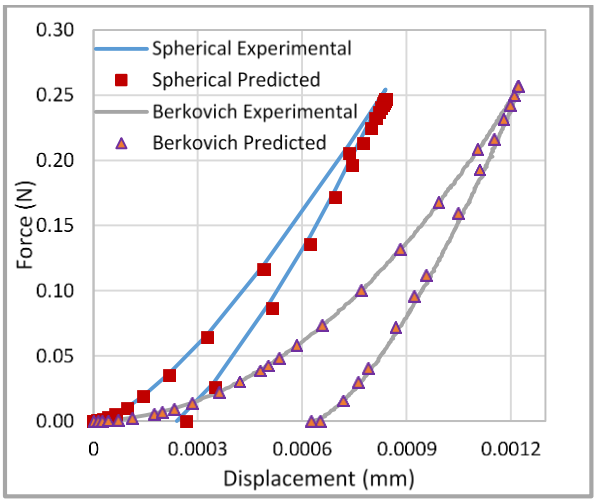

VT+60

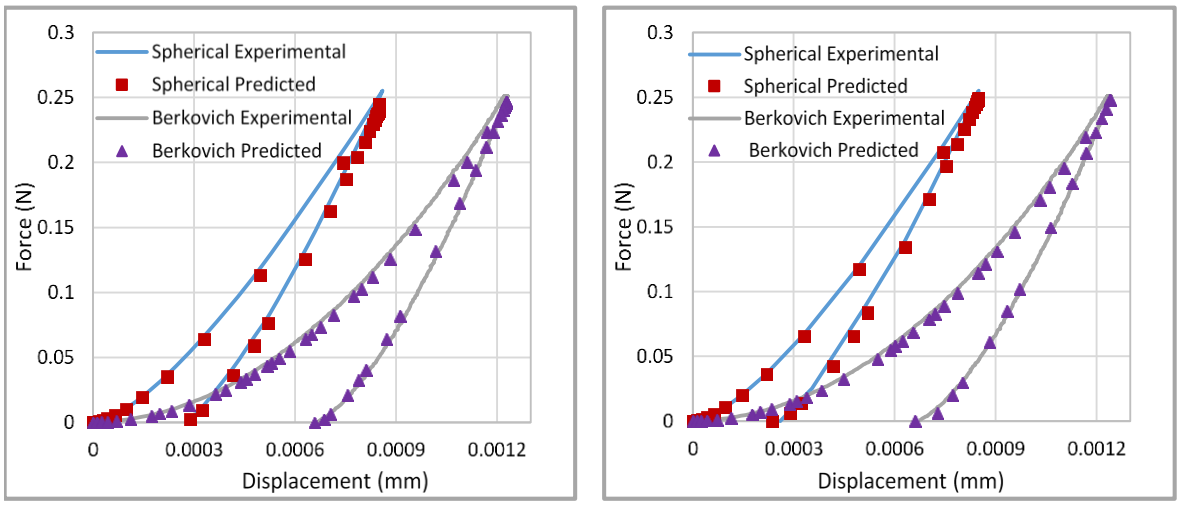

VT-70 VT-10

Figure 9-26 Comparison of load displacement curves between the predicted and input experimental target data for VT+60, VT-70, and VT-10 using S&B approach.

Figure 9-27 shows the relationship between the hardness values normalized by yield stress, and reduced modulus normalized by square contact radius and contact stiffness. The mechanical properties results suggests that the heat treatment cycle has a major influence on the Hardness, Yield stress and Young modulus and less effect on the strain hardening . It is interesting to observe that despite different heat treatment cycles the Poisson's ratio does not have a strong effect on the indentation results and it converges to the same value in the products under investigation. However, the presented results can be used as a quality control tool to classify the products according to the values of mechanical properties. Increasing temperature and holding time through the heat treatment cycle enhances the mechanical properties and crystallization tendency of glass media. This effect was observed in VT+60, which is considered as Finishing media, as a result of large crystal growth and higher hardness compared with VT-70, Cutting media, while VT-10, a General-purpose media was in between according to crystal size and hardness value.

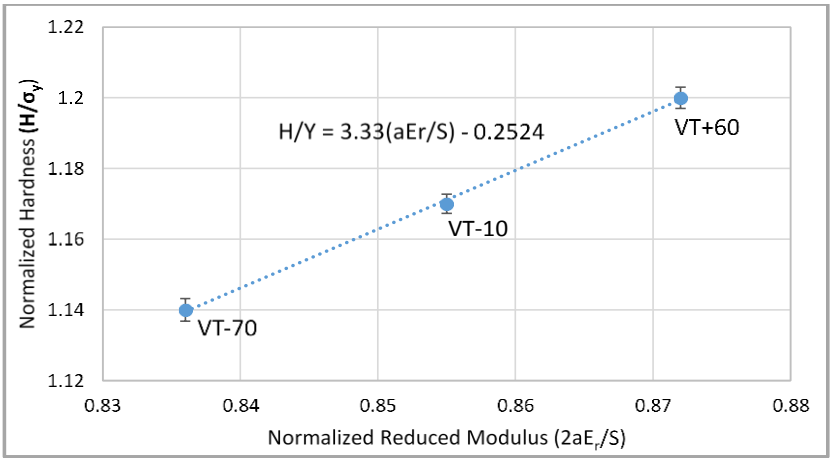

Figure 9-27 Relationship between normalized hardness with yield stress, and normalized reduced modulus with square contact radius and contact stiffness

9.16 Conclusion

In this study an optimization algorithm has been developed to extract the mechanical properties of the unknown materials for a given set of indentation data using non-linear least-squares curve fitting function (LSQNONLIN) within the optimization toolbox of MATLAB based on the Levenberg–Marquardt algorithm. A special code was written in MATLAB including the optimization function and command to read input files, write output files and execute ABAQUS. The optimization process started by selecting arbitrary initial values for each parameter and then running the input file using these values of the selected material model. A python script was then used to extract the history of load displacement data which is used to compute the objective function. The process runs iteratively until the best fit is achieved between the predicted and experimental load displacement curves (when the objective function reaches its minimum set by the convergence criteria). The optimum values of the parametrs are selected to give the best fit numerical experimental data.

Single and dual indentation optimization process were established to predict the mechanical properties over a wide range of material constitutive laws (elastic perfectly plastic material model, elastic plastic material, and Drucker-Prager material model) to investigate the effectiveness of the optimization techniques for a wide range of materials. A comparison between single and dual indenter geometries within the accuracy of ≤ 0.01 convergence criteria in the load displacement curves between the optimized and target values over a range of indentation tests was conducted to establish the differences in the

results and evaluate the accuracy of both methodologies. This study demonstrated that the single indentation approach required more iteration to achieve the target results, while the dual indentation method required less iteration but more computational time. The results also show that the Elastic modulus and Yield stress are required more iteration to reach convergence compared with other parameters. The optimization history of the full set of material properties for different indentation technique clearly demonstrates that the dual indentation method provides better optimal convergence values can be achieved despite a large variation in the starting parameter values and / or material constitutive model.

The proposed algorithms have been also applied to actual indentation experimental data of a range of thermally treated recycled glass materials to determine the unknown four material parameters (σ_y , E , v, n) rather than numerical simulation FE target curves. In this case, S&B dual indentation approach and different initial guess material properties values were also used to investigate the robustness of the proposed optimization algorithm. The results shows that an accurate Young modulus, Yield stress, and strain hardening were obtained and compared with the traditional technique of the Oliver and Pharr method based on experimental load displacement curve analysis.

In summary, this study has shown that a robust optimization method based on a non-linear least-squares curve fitting function (LSQNONLIN) through a combined MATLAB and ABAQUS fully automated solution can be used to accurately predict a unique set of elastic plastic material properties (σ_y , E , v, n) and Drucker-Prager(E,σ_{yc}, β) material properties.

9.17 Refrences

ABAQUS, T. m. v., Pawtucket: Hibbitt, Karlsson and Sorensen, Inc.

Bolzon, G., G. Maier and M. Panico (2004). "Material model calibration by indentation, imprint mapping and inverse analysis." International Journal of Solids and Structures **41**(11): 2957-2975.

Bucaille, J.-L., S. Stauss, E. Felder and J. Michler (2003). "Determination of plastic properties of metals by instrumented indentation using different sharp indenters." Acta materialia **51**(6): 1663-1678.

Carlsson, S. and P. L. Larsson (2001). "On the determination of residual stress and strain fields by sharp indentation testing.: Part I: theoretical and numerical analysis." Acta Materialia **49**(12): 2179-2191.

Carlsson, S. and P. L. Larsson (2001). "On the determination of residual stress and strain fields by sharp indentation testing.: Part II: experimental investigation." Acta Materialia **49**(12): 2193-2203.

Chen, X., N. Ogasawara, M. Zhao and N. Chiba (2007). "On the uniqueness of measuring elastoplastic properties from indentation: the indistinguishable mystical materials." Journal of the Mechanics and Physics of Solids **55**(8): 1618-1660.

Chen, X., J. Yan and A. M. Karlsson (2006). "On the determination of residual stress and mechanical properties by indentation." Materials Science and Engineering: A **416**(1): 139-149.

Chollacoop, N., M. Dao and S. Suresh (2003). "Depth-sensing instrumented indentation with dual sharp indenters." Acta materialia **51**(13): 3713-3729.

Dao, M., N. Chollacoop, K. Van Vliet, T. Venkatesh and S. Suresh (2001). "Computational modeling of the forward and reverse problems in instrumented sharp indentation." Acta materialia **49**(19): 3899-3918.

Delalleau, A., G. Josse, J.-M. Lagarde, H. Zahouani and J.-M. Bergheau (2006). "Characterization of the mechanical properties of skin by inverse analysis combined with the indentation test." Journal of biomechanics **39**(9): 1603-1610.

Gadelrab, K., F. Bonilla and M. Chiesa (2012). "Densification modeling of fused silica under nanoindentation." Journal of Non-Crystalline Solids **358**(2): 392-398.

Gérard, J.-M., J. Ohayon, V. Luboz, P. Perrier and Y. Payan (2005). "Non-linear elastic properties of the lingual and facial tissues assessed by indentation technique: Application to the biomechanics of speech production." Medical engineering & physics **27**(10): 884-892.

Giannakopoulos, A. E. and P. L. Larsson (1997). "Analysis of pyramid indentation of pressure-sensitive hard metals and ceramics." Mechanics of Materials **25**(1): 1-35.

Giannakopoulos, A. E. and S. Suresh (1999). "Determination of elastoplastic properties by instrumented sharp indentation." Scripta Materialia **40**(10): 1191-1198.

Gu, Y., T. Nakamura, L. Prchlik, S. Sampath and J. Wallace (2003). "Micro-indentation and inverse analysis to characterize elastic–plastic graded materials." Materials Science and Engineering: A **345**(1): 223-233.

Inoue, A., T. Zhang and T. Masumoto (1989). "Al–La–Ni amorphous alloys with a wide supercooled liquid region." Materials Transactions, JIM **30**(12): 965-972.

Inoue, A., W. Zhang, T. Zhang and K. Kurosaka (2001). "High-strength Cu-based bulk glassy alloys in Cu–Zr–Ti and Cu–Hf–Ti ternary systems." Acta materialia **49**(14): 2645-2652.

Kang, J., A. Becker and W. Sun (2012). "Determining elastic–plastic properties from indentation data obtained from finite element simulations and experimental results." International Journal of Mechanical Sciences **62**(1): 34-46.

Kermouche, G., E. Barthel, D. Vandembroucq and P. Dubujet (2008). "Mechanical modelling of indentation-induced densification in amorphous silica." Acta Materialia **56**(13): 3222-3228.

Keryvin, V. (2007). "Indentation of bulk metallic glasses: Relationships between shear bands observed around the prints and hardness." Acta materialia **55**(8): 2565-2578.

Larsson, P.-L. and A. E Giannakopoulos (1998). "Tensile stresses and their implication to cracking at pyramid indentation of pressure-sensitive hard metals and ceramics." Materials Science and Engineering: A **254**(1): 268-281.

Lee, Y.-H. and D. Kwon (2004). "Estimation of biaxial surface stress by instrumented indentation with sharp indenters." Acta Materialia **52**(6): 1555-1563.

Luo, J., J. Lin and T. Dean (2006). "A study on the determination of mechanical properties of a power law material by its indentation force–depth curve." Philosophical magazine **86**(19): 2881-2905.

Matlab, O. t. T. u. g., (T.M.Inc.).

Meuwissen, M., C. Oomens, F. Baaijens, R. Petterson and J. Janssen (1998). "Determination of the elasto-plastic properties of aluminium using a mixed numerical–experimental method." Journal of Materials Processing Technology **75**(1): 204-211.

Mokhatar, S. N. and R. Abdullah (2012). "Computational analysis of reinforced concrete slabs subjected to impact loads." International Journal of Integrated Engineering **4**(2): 70-76.

Nakamura, T. and Y. Gu (2007). "Identification of elastic–plastic anisotropic parameters using instrumented indentation and inverse analysis." Mechanics of materials **39**(4): 340-356.

Park, S., Q. Xia and M. Zhou (2001). "Dynamic behavior of concrete at high strain rates and pressures: II. Numerical simulation." International journal of impact engineering **25**(9): 887-910.

Patnaik, M. N. M., R. Narasimhan and U. Ramamurty (2004). "Spherical indentation response of metallic glasses." Acta Materialia **52**(11): 3335-3345.

Perriot, A., D. Vandembroucq, E. Barthel, V. Martinez, L. Grosvalet, C. Martinet and B. Champagnon (2006). "Raman microspectroscopic characterization of amorphous silica plastic behavior." Journal of the American Ceramic Society **89**(2): 596-601.

Ren X. J., S. C. W., Evans K. E., Dooling P. J., Burgess A. and Wiechers J. W. (2005). "Experimental testing and numerical modelling of mechanical properties of the human skin." International Foundation of Society of Cosmetic Chemists (IFSCC), **1** 95-98.

Saida, J., H. Kato, A. D. H. Setyawan, K. Yoshimi and A. Inoue (2007). "Deformation-induced nanoscale dynamic transformation studies in Zr-Al-Ni-Pd and Zr-Al-Ni-Cu bulk metallic glasses." Materials transactions **48**(6): 1327-1335.

Seltzer, R., A. P. Cisilino, P. M. Frontini and Y.-W. Mai (2011). "Determination of the Drucker–Prager parameters of polymers exhibiting pressure-sensitive plastic behaviour by depth-sensing indentation." International Journal of Mechanical Sciences **53**(6): 471-478.

Shan, Z. and A. M. Gokhale (2003). "Utility of micro-indentation technique for characterization of the constitutive behavior of skin and interior microstructures of die-cast magnesium alloys." Materials Science and Engineering: A **361**(1): 267-274.

Snieder, R. (1998). "The role of nonlinearity in inverse problems." Inverse Problems **14**(3): 387.

Swaddiwudhipong, S., J. Hua, K. Tho and Z. Liu (2006). "Equivalency of Berkovich and conical load-indentation curves." Modelling and Simulation in Materials Science and Engineering **14**(1): 71.

Swaddiwudhipong, S., K. Tho, Z. Liu and K. Zeng (2005). "Material characterization based on dual indenters." International journal of solids and structures **42**(1): 69-83.

T.A. Venkatesh, K. J. V. V., A.E. Giannakopoulos and S. Suresh (2000). "Determination of elasto-plastic properties by instrumented sharp indentation: Guidelines for property extraction." Scripta mater. **42**: 833–839.

Yan, J., A. M. Karlsson and X. Chen (2007). "Determining plastic properties of a material with residual stress by using conical indentation." International journal of solids and structures **44**(11): 3720-3737.

Yuan, G., T. Zhang and A. Inoue (2003). "Thermal stability, glass-forming ability and mechanical properties of Mg-Y-Zn-Cu glassy alloys." Materials Transactions **44**(11): 2271-2275.

CHAPTER TEN

FEM INDENTATION-BASED METHODS TO ASSESS FRACTURE TOUGHNESS FOR THERMALLY TREATED RECYCLED GLASS

10.1 Introduction

Instrumented indentation compared with conventional testing techniques (e.g. tension, compression, etc.) is widely used to characterize the mechanical properties of complex materials, since it requires minimum sample preparation (Chen, Ogasawara et al. 2007). Sharp indentation techniques can be employed to determine the material properties, residual stress, and fracture toughness of brittle materials (Chen, Yan et al. 2006, Yan, Karlsson et al. 2007). The indentation results analysis is often more complicated than conventional methods due to the compressive and tensile stress field associated with crack initiation and propagation during loading and unloading cycles (Lawn and Evans 1977, Arora, Marshall et al. 1979, Lawn, Evans et al. 1980). The morphology and size of such crack is dependent on material properties, indenter geometry and the applied indentation load. For example, the median and radial crack system is often observed during indentation with the Vickers, Berkovich and cube-corner pyramidal indenters, although median cracking is observed in materials such as glasses, radial or lateral cracking is seen in other materials such as tungsten carbide (Perrott 1977, Evans 1979). Thus, the fracture toughness measurements relating to indentation crack length is further complicated due to lack of knowledge of the crack development from material to material (Lawn, Evans et al. 1980). Such complexities will limit the accuracy and applicability of current indentation methods for measuring fracture toughness, due to the elastic plastic material behaviour occurring at different deformation scales causing a problem in the description of the complex stress and strain fields in adequate detail. The application of FEM to such difficulties can enhance the capabilities of understanding and development of current characterization techniques. Moreover, the numerical simulation techniques for solving cracking problems can help for understanding the physical methods of controlling indentation crack processes and improving modelling performance (Chiang, Marshall et al. 1982).

Finite element modelling of indentation processes has been widely used in the determination of the elastic plastic properties of metals and ceramic materials (Giannakopoulos, Larsson et al. 1994, Larsson, Giannakopoulos et al. 1996, Zhang and Mahdi 1996). Some of these studies look at fracture characterization of brittle material. Such models failed to recognize the crack development at the loading unloading stage due to lack of information about the plastic zone beneath the indentation tip. The above studies are focused on stress field development and estimation of stress intensity factor which

predicts the crack initiation, not crack propagation during the indentation process. Asundi (1993) developed an elastic plastic theory coupled with an anisotropic damage model to analyses the fracture of brittle material, such a model is a good representative of isentropic brittle material and simple to use by finite element code, but the damage constitutive law is difficult to find from an experimental test. However, the elastic –plastic –cracking constitutive model developed by Zhang and Subhash (2001) is a more reliable tool for isotropic brittle materials such as ceramic and glass, to take into account tensile cracking and compressive yielding. The indentation elastic plastic behaviour of the material is followed by a different type of cracking process based on many variables such as material types, indentation geometry, and indentation load.

The aim of this study is to establish an FEM method for detailed analyses of the stress intensity fields coupled with fracture toughness of both median and Palmqvist cracks during the Vickers indentation of the brittle materials (thermally treated recycled glass parts). The superposition technique was employed to determine the stress intensity factor (K) using dimensional analysis in order to establish the relationship between the material properties and different crack geometries and polar coordinates during the fracture. The results are also compared with the experimental cracking models developed by previous researchers such as Lawn, Evans et al. 1980, Laugier (1987).

10.2 Elastic plastic cracking model formulation and implementation for finite element analysis

The Elastic plastic crack model was considered by many researchers as a reliable tool to control the propagation of median crack development normal to the loading surface during the loading phase, and the propagation of lateral crack development parallel to the loading surface during the unloading phase of a Vickers indentation test. Figure 10-1, shows the elastic plastic cracking constitutive model proposed by Cook and Pharr (1990) ; this model suggested that the uniaxial tensile behaviour of a brittle material can be represented by a linear elastic response of AB. The tensile stress is increased to a maximum value achieving fracture stress at point D, then the crack is initiated and the stress release will develop nonlinearly along BD line. ,

During the loading phase of indentation processes, compressive loading is associated with the material exhibiting elastic plastic responses. Compressive deformation is developed when the remaining stress greater is than the flow stress σ_e at point E. The plastic deformation during the loading phase of the sharp indentation cycle is responsible for the development of lateral cracks during the unloading phase (Cook and Pharr, 1990) .The unloading phase is shown by DC, the crack can start from a random point along the stress release path DC, which is represented by GE.

The equivalent flow stress during plastic deformation is given by Eq. (10.1):

$$\sigma_e=\sigma_y + E_p\varepsilon_e^p \tag{10.1}$$

Where, E_p is the plastic hardening modulus and ε_e^p is the equivalent plastic strain Eq. (10.2).

$$\varepsilon_e^p = \int_0^1 \sqrt{\frac{2}{3}}\dot{\varepsilon}^p . dt \tag{10.2}$$

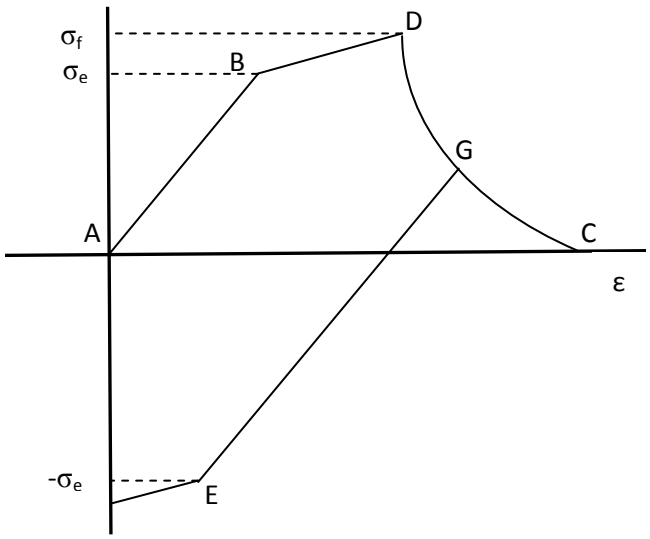

Figure 10-1 Schematic of elastic plastic cracking constitutive model (Zhang and Subhash 2001)

Inoue, Zhang et al. (2001) reported that the crack initiation in the Elastic plastic crack model is assumed to follow Rankine theory (maximum stress theory), which states that failure will take place when the maximum principal stress at any point achieves a value equal to or exceeding the tensile strength. Such a theory is suitable for brittle material and not appropriate to ductile materials.

Three orthogonal cracks were developed at the same material point, which represents in total the strength of damage. The first crack could occur when the maximum principal stress is greater than the predefined fracture stress σ_f resulting in (mode I), a crack propagated in the direction normal to that of the maximum principal stress axis. The second crack (mode II) could happen when the maximum tensile stress at the same material point of mode I crack is greater than, σ_f , and the third crack (Mode III) is developed when the perpendicular tensile stress of both crack I, and II exceeds σ_f

The normal stress σ_{ni} is calculated across each crack *i*, which is updated when achieving a value greater than predefined fracture stress as a function of power law crack opining displacement, u_i is given by Eq. (10.4) :

$$\sigma_{ni} = \sigma_f f_i \ , (i = 1,2,3, \dots, n) \tag{10.4}$$

$$f_i = (1 - u_i/u_0)^n \tag{10.5}$$

where u_0 is maximum crack opening displacement, and n represents the shape of post cracking (stress release) curve, CD path. The crack opening displacement u_i is given by Eq. (10.6), can be calculated for different crack type at a given material point by multiplying the incremental strain between two adjustment time steps during the cracking process by cube root of the equivalent element volume, h , (ABAQUS) .

$$u_i = h\, \varepsilon_i = h \int \varepsilon_i \tag{10.6}$$

Therefore, the total damage magnitude, u_t at a selected material point for a given stress is calculated by measuring the effective crack opening displacement along the three different cracks orthogonal directions given by Eq. (10.7):

$$u_t = \sqrt{u_1^2 + u_2^2 + u_3^2} \tag{10.7}$$

Based on the assumption of shear stress reduced to zero at crack opening displacement ,Zhang and Subhash (2001) simplify the current model by assuming the Shear modulus, *S* is a function of power law crack opening displacement f_i, f_j in two orthogonal directions given by Eq. (10.8)

$$S = \frac{G\, fi\, fj}{fi + fj - fi\, fj} \tag{10.8}$$

where G, is the shear modulus of the un-cracked material. Shear stress,τ_{ij} can be defined as a function of the sum of elastic and cracking strain, given by Eq. (10.9):

$$\tau_{ij} = 2S\left(\varepsilon_{ij}^{e} + \varepsilon_{ij}^{c}\right) = 2S\left(\varepsilon_{ij} - \varepsilon_{ij}^{p}\right) \tag{10.9}$$

where $\varepsilon_{ij}$is the total strain, $\varepsilon_{ij}^{e}, \varepsilon_{ij}^{p}, \varepsilon_{ij}^{c}$are the strains due to elastic, plastic and cracking response respectively.

The above model was successfully integrated into the finite element package ABAQUS/Explicit. This model can be used for brittle material subjected to a single tensile-compressive loading cycle and simulate indentation cracking during a Vickers indentation. This model differs from the models built in ABAQUS software such as elastic cracking and fracture mechanics; this model analysed the crack tip stress field in brittle material using a stress intensity factor parameter. Accurate calculation of stress intensity factors should be achieved in order to reduce errors in the fatigue life predictions Eq. (10.10):

$$\sigma_{ij}(r,\theta) = \frac{K_I}{\sqrt{2\pi r}} f_{ij}^{I}(\theta) + \frac{K_{II}}{\sqrt{2\pi r}} f_{ij}^{II}(\theta) + \frac{K_{III}}{\sqrt{2\pi r}} f_{ij}^{II}(\theta) \tag{10.10}$$

Where K_I is the mode *I* opening stress intensity factor, K_{II} is the mode *II* in plane shear stress intensity factor, K_{III} is the mode *III* transverse shear stress intensity factor, *r* is the distance from crack tip, f_{ij}^{x} is the angular variation of the stress at mode *x*.

The model proposed by Zhang and Subhash (2001) differs from the elastic cracking model implemented in ABAQUS in a number of points. Firstly, the crack strain is a part of the total strain, therefore there is no need to define the relationship between stress and crack strain. Secondly, the residual stress and lateral crack development upon the unloading phase is due to the plasticity flow during the loading phase. Thirdly, the crack strain is accompanied by the crack development even if the crack is completely closed.

The elastic plastic fracture mechanics in ABAQUS are based on a nonlinear elastic material, not on the elastic plastic material constitutive law. For such a model, Hutchinson (1968) shows that the stress field near the crack tip is given by Eq. (10.11) :

$$\sigma_{ij} = \sigma_o \left[\frac{J}{\alpha\sigma_o\varepsilon_o I_n r}\right]^{\frac{1}{n+1}} \tag{10.11}$$

$$\varepsilon_{ij} = \varepsilon_o \left[\frac{J}{\alpha\sigma_o\varepsilon_o I_n r}\right]^{\frac{n}{n+1}} \tag{10.12}$$

$$J = \frac{1-v^2}{E} K_I \tag{10.13}$$

Where J is the energy release associated with crack growth, $\sigma_o$is the effective yield stress, ε_o is the effective strain, I_n mass inertia, $n\ and\ \alpha$ is material constant.

However, in case of elastic plastic deformation, ABAQUS use a J integral instead of K_I to analyse the fracture behaviour of the material having a particular crack length. The value of the J integral is related to the strain energy concentrated in the high intensity stress field (crack area) and can be used to predict the stress strain value for crack initiation in the loading stage.

10.3 Indentation crack model and stress field of brittle material

Static indentation fracture mechanic approaches have been developed by many researchers to evaluate the fracture characteristics of brittle materials (Lawn, Evans et al. 1980, Chiang, Marshall et al. 1982, Ponton and Rawlings 1989, Cook and Pharr 1990, Zeng, Söderlund et al. 1996). It has been established that the Palmqvist, and median crack can nucleate normally to the specimen surface during the loading stage, and lateral crack can develop parallel to the specimen surface during the unloading stage as demonstrated schematically in Figure 10-2. The typical indentation mechanism in brittle material such as ceramics and glasses can be described as plastic flow under hydrostatic stress, causing large compressive stress which start below the indenter tip. This produces plastic deformation resulting in Palmqvist and median crack initiating and propagating during the loading phase, and residual stress is developed after the indenter is released from the workpiece during the unloading phase resulting in propagation of lateral cracks.

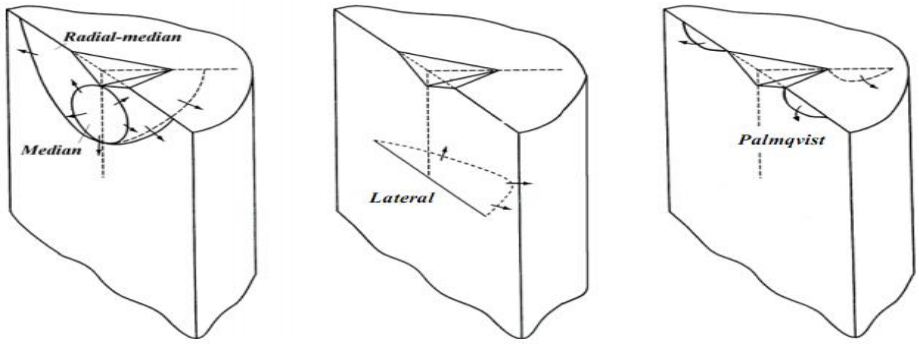

Figure 10-2 Mechanism of crack nucleation during indentation test(Dias, Modenesi et al. 2006)

Many researchers have studied and analysed the complex elastic plastic cracking system and stress field development when a sharp indenter contacts brittle material such as glass (Johnson 1970, Lawn and Evans 1977, Lawn, Evans et al. 1980, Chiang, Marshall et al. 1982, Yoffe 1982, Cook and Pharr 1990). Upon the loading phase into the glass specimen, a hemispherical plastic deformation zone is developed beneath the indentation contact, the zone size being dependent on the contact radius of the indentation imprint (Arora, Marshall et al. 1979, Hagan and Van Der Zwaag 1984)

Figure 10-3 (a), shows elastic and plastic stress fields generated during the loading phase in brittle materials; as is shown, the elastic field is active outside the plastic zone. For sharp indentation systems such as Vickers, Berkovich, and Conical indenters, the residual stress component generated during the loading phase is tensile at the surface, but the elastic stresses are compressive, therefore the net stress is compressive (Anstis, Chantikul et al. 1981). The residual stress field developed, reaches a maximum intensity factor after completing the loading phase due to generating incompatible strain on the inelastic and plastic deformation zones , resulting in median crack initiation, and when the load is sufficiently high, the crack may be propagated beneath the surface in the tensile region along the elastic-plastic periphery. Lawn and Evans (1977) observed that the median crack is developed at the end of the plastic zone, where the tension is supposed to be very high.

Figure 10.3 (b), shows the plastic zone is in compression at the end of the unloading phase , while in the remaining indentation zone there is tension, so initiation and propagation of median, Palmqvist and/or lateral cracks may take place after the indenter is removed from the material. During the unloading phase compressive stress is reduced at the surface, resulting in the net tensile stress from the residual field increasing. If the median and Palmqvist cracks are generated during the loading phase, the crack will be a little below the surface as the load is removed, then break through specimen surface which causes in increasing tensile stress. If no median cracks are generated on the loading phase and the residual stress field is strong enough, the median and Palmqvist cracks may be initiated during the unloading phase. Lateral cracks may also develop at the interface between the elastic and plastic boundaries after completing the unloading phase (Lawn, Evans et al. 1980). However, the crack initiation and propagation during the loading phase is due to the residual stress field developed by elastic and plastic zones, while during the unloading phase, the elastic field decreases to zero, the crack initiation and propagation is due to the residual stress generation which reaches a maximum value (Lawn and Wilshaw 1975).

The indentation hardness has a great effect on the intensity of the residual stress field, and elastic stress field. Since the indentation hardness should be independent of indentation force, therefore the residual stress intensity should be independent of indentation force.

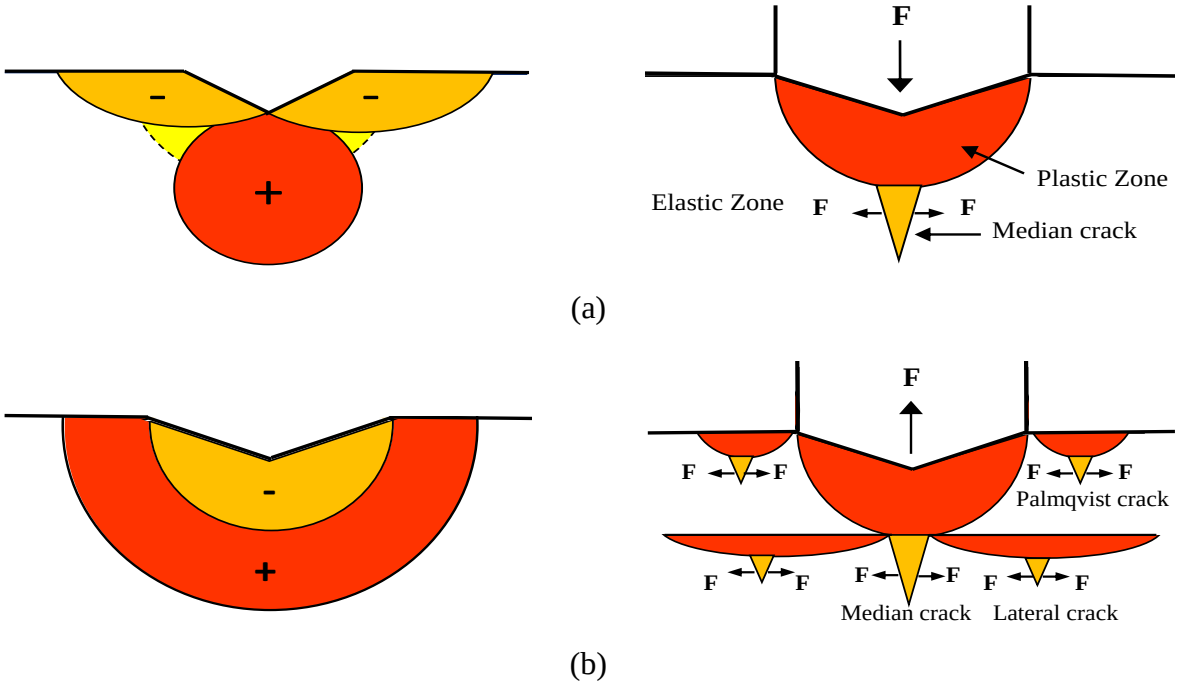

Figure 10-3 Schematic diagram of elastic plastic field development by: a) Loading phase, b) Unloading phase

(Cook and Pharr 1990) proposed that for a given material property the Palmqvist cracks initiate at lower loads whereas median cracks initiate at higher loads; both crack types propagate to full length after completing the unloading phase, and they are independent crack systems (i.e. the Palmqvist crack is not the initiator of the median cracks above a critical load). It is therefore valuable to study the two crack systems separately. The results also demonstrated that the crack systems were found to be dependent on the ratio between elastic modulus and hardness. FEM analyses of the stress field have been developed by many other researchers and they did not interface the fracture analyses with the stress fields (Zhang and Subhash 2001, Muchtar, Lim et al. 2003, Pachler, Souza et al. 2007).

Since the indentation effect is coupled with the stress field developed from finite deformation, it is indirectly related to the elastic plastic material properties and fracture toughness; therefore, in this study the analytical solution based on the stress intensity factor SIF must be established to correlate the indentation reaction with the fracture toughness, crack behaviour and material properties.

10.4 Experimental procedure

10.4.1 Numerical analysis of the Vickers indentation fracture test

The aim of the FEM analyses in this study is to reproduce the residual stress fields developed during the indentation loading stage; consequently, Palmqvist and median cracks systems have been modelled. Figure 10-4 shows the schematic details of Vickers indentation cracking mechanism. The Vickers indenter has an apex angle of 136◦ between opposite faces. The diagonal length of impression *a*, is measured at the maximum indentation depth δ; the median and Palmqvist crack systems are assumed as a semi-circular geometry to simplify the analysis. The radius of the Palmqvist crack is *l/2* starting from the impression corner and propagating in one direction outward radially with maximum depth PC_{depth}. The median crack radius is *c*, which is propagated uniformly in all directions with maximum depth MC_{depth}. For simplicity, the assumption of Palmqvist crack, and median crack propagation with a constant angle relative to the surface has been made; the polar coordinates of $r_1 - \theta$, and $r_2 - \beta$ respectively. Both types of crack are located in the X_2-X_2 plane and considered independently, the characteristic crack lengths *a* and *l*, and the crack depths PC_{depth}, and MC_{depth} will help the assessment effect of the crack front geometry on SIF.

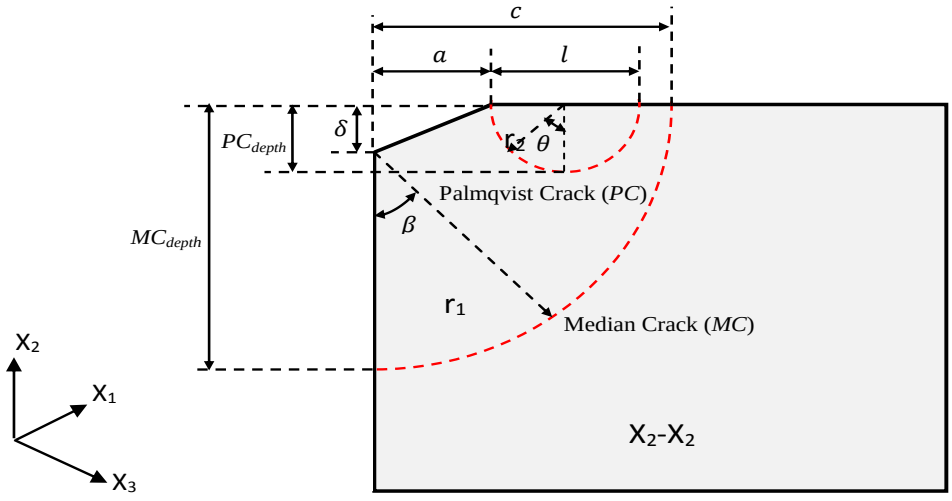

Figure 10-4 Schematic of Palmqvist crack system and Median crack system by Vickers indentation

10.4.2 Superposition technique

The common superposition technique (Anderson 2005, Yan, Karlsson et al. 2007) was employed to determine the stress intensity of the thermally treated glass material which is suitable to use when the crack tip plasticity can be ignored. The general concept of this technique illustrated in Figure 10-5, the stress field of case A is equal to the summation stress fields of case B, and C. Both cases A (with crack), and B (crack free) are assumed an elastic body subjected to prescribed traction T_u, and displacement u_i, over the boundaries S_T , and S_u, respectively. A negative residual stress field, -σ(x) can be applied over the crack faces in case B, in order to close the crack position and efficiently eliminate the presence of the crack. Based on superposition technique, a residual opening stress σ(x) was extracted from case, (A) and imposed over the crack face in case,(C).

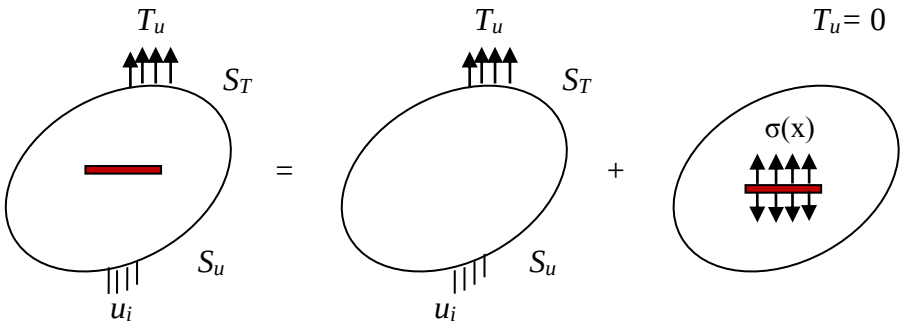

Where

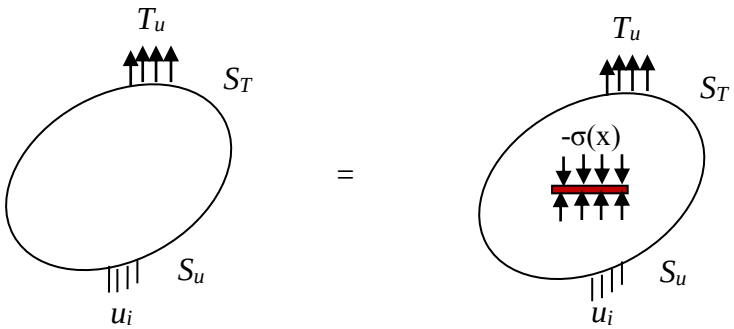

Figure 10-5 Schematic of superposition technique

Therefore, the indentation fracture analysis can be divided into three steps as described in Figure 10-6 : First step, determine the residual stress field of elastic plastic indentation material systems without crack (Figure 10-6 step one) after the unloading stage where both

Palmqvist and median cracks reach the maximum length as proposed by the previous study. Second stage, a Palmqvist crack or median crack is then introduced into the deformed model when the maximum indentation depth is achieved (Figure 10-6 step two). Third stage, the residual stress field σ(x) estimated from the first step (step one) is then imposed on the nodes and elements along the crack surface in step three ; as a result the stress intensity factor (SIF) can be calculated through the computation of the J-integral around the crack tip. The results of the J-integral are taken from the averaged values of three counters around the crack tip.

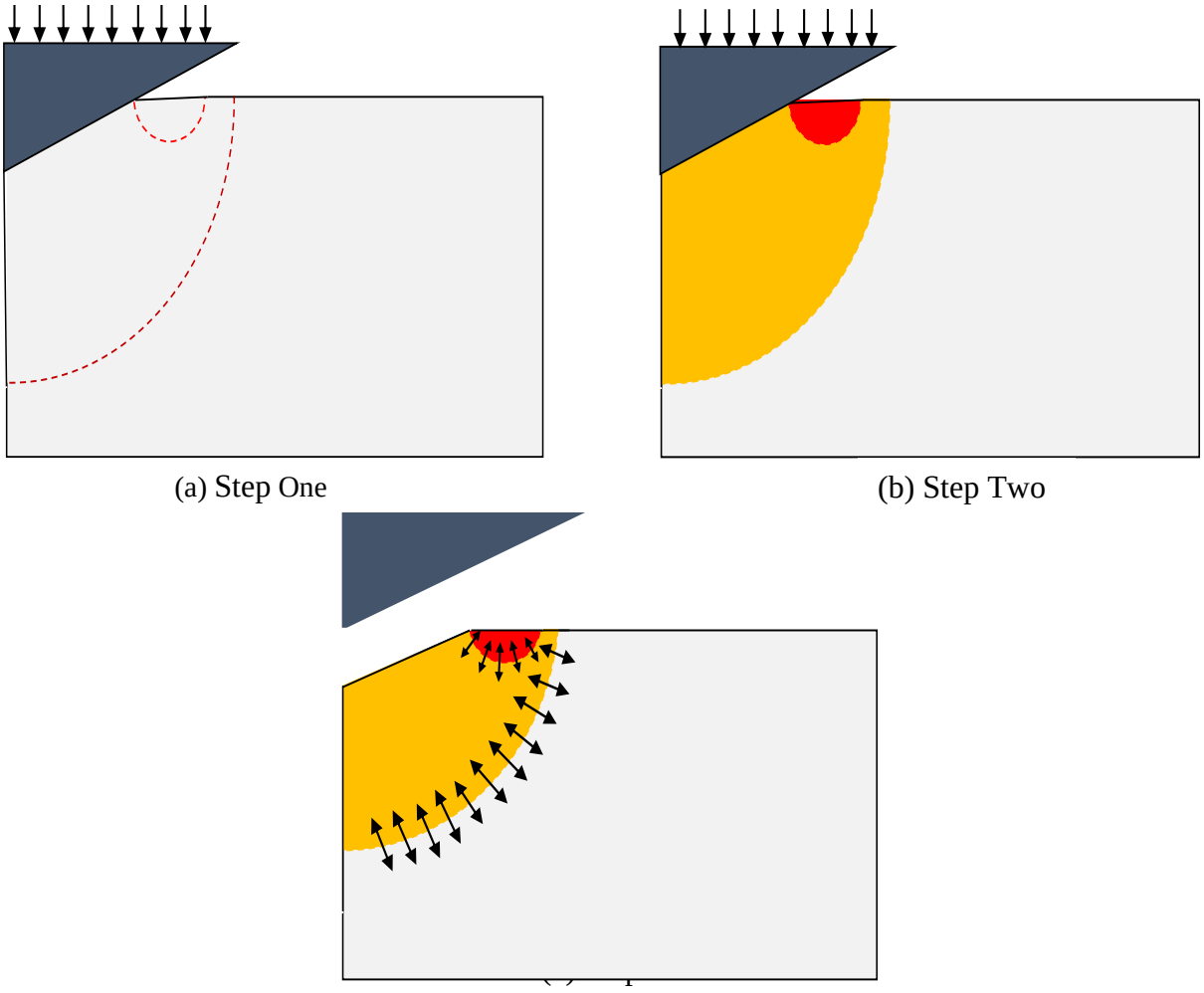

(a) Step One (b) Step Two

Figure 10-6 Schematic of the superposition principles for indentation fracture analysis, a) elastic body without crack at maximum indentation load, b) elastic body with crack at maximum indentation load, c)residual stress field σ(x) is imposed on the crack surface.

10.5 FEM Dimensional analysis of Vickers indentation cracking system

Dimensional analyses were employed to investigate the effect of elastic plastic material properties and crack geometry on the fracture toughness. The dimensional analysis is an approach which reduces the complexity and minimizes the experimental parameters that cause a physical problem through the use of simple and basic techniques (Barenblatt 1996). In general, the researchers has been given a great attention to the stress intensity factor (*SIF*) induced by the Vickers crack systems in the determination of the fracture toughness. The *SIF* magnitude depends on the material properties ($E,$ and σ_y), crack geometry ($l,$ and c), the polar coordinate position of the crack front (θ, and β) and the indentation size, a. The Poisson's ratio is considered a minor factor during the Vickers indentation cracking (Chen, Hutchinson et al. 2005, Yan, Karlsson et al. 2007), however, it is set as a typical value of 0.22 for brittle materials.

The fracture toughness will calculated when the *SIF* reaches the maximum value. In case of crack propagation on the material surface, the *SIF* needs to exceed the material fracture toughness. Therefore, the dependent parameter *SIF*, must be a function of all relevant independent parameters. Thus for given Palmqvist and median crack systems the *SIF* is given in Eq. (10.14) and Eq. (10.15), respectively.

$$K = f\left(E, \sigma_y, l, a, \theta\right) \tag{10.14}$$

$$K = g\left(E, \sigma_y, c, a, \beta\right) \tag{10.15}$$

According to the work established by E.Vans and Charles (1976), and Niihara (1983), the SIF is normalized by the square root of the half diagonal impression length and the yield stress. The crack length l and c, should normalize by half of the diagonal length, and the Young's Modulus will be normalized by the Yield stress.

Therefore, K can be expressed by Eq. (10.16), and Eq. (10.17):

$$\frac{K}{\sigma_y\sqrt{a}} = f\left(\frac{E}{\sigma_y}, \frac{l}{a}, \theta\right) \tag{10.16}$$

$$\frac{K}{\sigma_y\sqrt{a}} = g\left(\frac{E}{\sigma_y}, \frac{c}{a}, \beta\right) \tag{10.17}$$

A series of FEM simulations were performed using a three dimensional Vickers indentation cracking model to investigate the dimensionless analysis effect on the *SIF*. The dimensionless functional values of f and g can be determined during the forward analysis over a wide range of crack lengths and material properties. Figure 10-7 shows the schematic diagram of the crack front geometry for the Palmqvist and Median crack systems.

Upon each simulation the SIF was evaluated at each node of the crack fronts for a given set of material properties and crack geometries. Due to the symmetry of the Vickers indentation process, only the results of mode I *SIF* (K_I) of the cracks in the normal plane (X_2-X_2) plane were created by this study. The position of nodes along the crack front of Palmqvist crack was identified according to the polar coordinate of $r_1 - \theta$ with the centre of the crack θ = 0, as illustrated by surface node A in Figure 10-7. Whereas, the position of nodes along the crack front of median crack was identified according to the polar coordinate $r_2 - \beta$ with the start point at the centre of crack β= 0, as illustrated by surface node B in Figure 10-7.

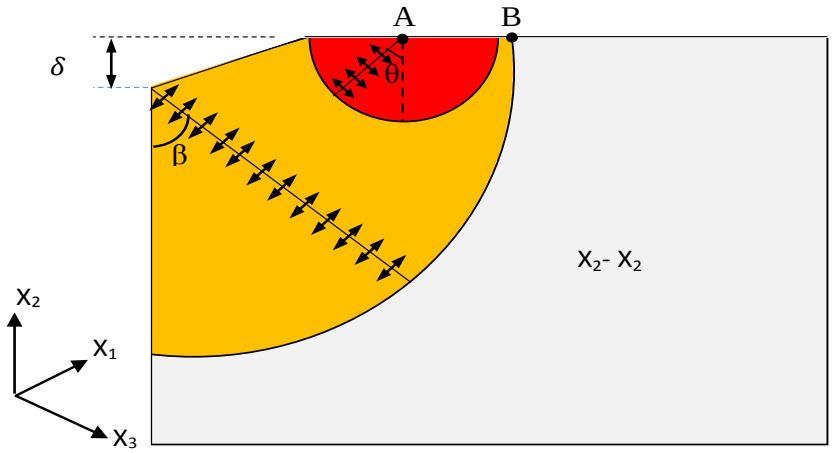

Figure 10-7 Schematic diagram of the crack front geometry for the Palmqvist and Median crack systems

Niihara (1983) reported that the dimensionless crack length *l/a*, for Palmqvist crack is varied between 0.25 and 2.5, while for a median crack system Gong, Wang et al. (2002) reported that the dimensionless crack length is valid when $c/a > 2.5$. Thus, the maximum indentation depth δ for particular Palmqvist, l or median c crack, can be calculated from the relation between penetration and indentation size.

Consequently, the minimum criteria of l/a= 0.25, and c/a=2.5 are satisfied according to the following equation (10.18) given by Leonardi, Furgiuele et al. (2010)

$$a = \sqrt{2}\tan(\theta)\,\delta \tag{10.18}$$

In this study, the dimensionless parameter range of Palmqvist and median crack systems were selected according to the condition of $0.25 \leq l/a \leq 2.5$ and $2.5 \leq c/a \leq 5$, respectively. Table 10-1 presents the dimensionless parameters range used in numerical simulations to investigate the influence of Palmqvist (*PC*) and Median (*MC*) crack systems on a wide range of elastic plastic constitutive models.

Table 10-1 Dimensionless parameters range used for (*PC*), and (*MC*) Numerical simulations

Dimensionless parameter	Crack System	Range
$\boldsymbol{E/\sigma_y}$	*PC*	20, 30, 40, 60, 80, 120,200
$\boldsymbol{l/a}$	*PC*	$0.5 \leq l/a \leq 2.5$ (0.5 interval rate)
$\boldsymbol{E/\sigma_y}$	*MC*	20, 30, 40, 60, 80, 120,200
$\boldsymbol{c/a}$	*MC*	$2.5 \leq c/a \leq 6$ (0.5 interval rate)

10.6 FEM for microindentation fracture test

Three-dimensional Vickers FEM simulations were performed to evaluate the fracture toughness K_{IC} of the brittle materials. The ABAQUS 6.12 program was employed to develop the numerical simulations of non-dimensional analysis obtained from Eq. (10.16), and Eq. (10.17). The ABAQUS program showed many advantages since it provides a numerical solution for assessing the SIFs using the counter integral method. The Vickers indentation exhibits eightfold pyramidal deformation surfaces with a semi-angle between the vertical and each face of 68^0. For simplicity and less computational time only on quarter of the Vickers indenter and specimen was modelled as is shown in Figure 10-8. As a consequence symmetric surfaces are concentrated on both y and x sides along the symmetry planes. The models were also constrained vertically over their base face and left freely to move over their horizontal cylindrical surfaces.

The resulting FEM of the Vickers indentation process is shown in Figure 10-9. Figure 10-9 (a) shows the 3-D FEM Vickers indentation of the Palmqvist crack system and Figure 10-9 (b) shows the 3-D FEM Vickers indentation of the median crack system. As displayed in both models a non-uniform mesh density was employed. The mesh density under the indenter tip was refined in order to model the deformation and residual stress field gradients during indentation to high accuracy, and a coarse mesh away from these critical zones Figure 10-9 (c, and d). The specimen and indenter are modelled with 8-node elements of reduced integration type (C3D8R element), and 4-node element type rigid quadrilateral (R3D4 element) respectively, both element types are used for stress and displacement analysis. The indenter is assumed to be a rigid body, therefore only the results of its interface with the specimen were considered.

The contact constraint between the indenter and material was defined as the ‘master surface (indenter)’ and ‘slave surface (material)’ interaction with a normal contact, to allow the master surface to move and contact the material at all times during the simulation. The contact direction is then obtained in relation to the master surface. The friction was considered through the classical isotropic Coulomb friction model, which requires the input of an appropriate value for the static friction coefficient. The Coulomb friction coefficient value of 0.16 is considered in the literature (Kobe 1951), thus the friction coefficient was assumed between the indenter and specimen was assumed to be equal to 0.16.

Contact and the consequent indentation are simulated as shown in Figure 10-9 , that is by applying a negative quasi-static displacement along the vertical direction. The vertical displacement of the indenter is specified as an input value corresponding to total indentation depth. The reaction force was measured along the direction of indentation depth, which is equal to the summation of forces at a set reference point on the rigid indenter. The area function of the Vickers tip geometries was used in the numerical simulations based on the area function results obtained from experimental and numerical work presented in [Chapter 7].

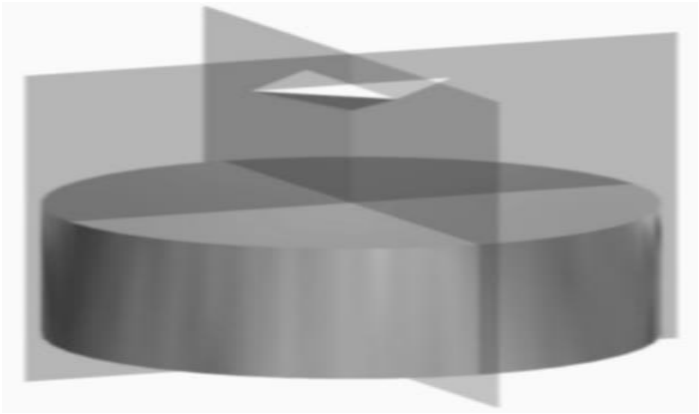

Figure 10-8 Isometric view of Vickers indentation test

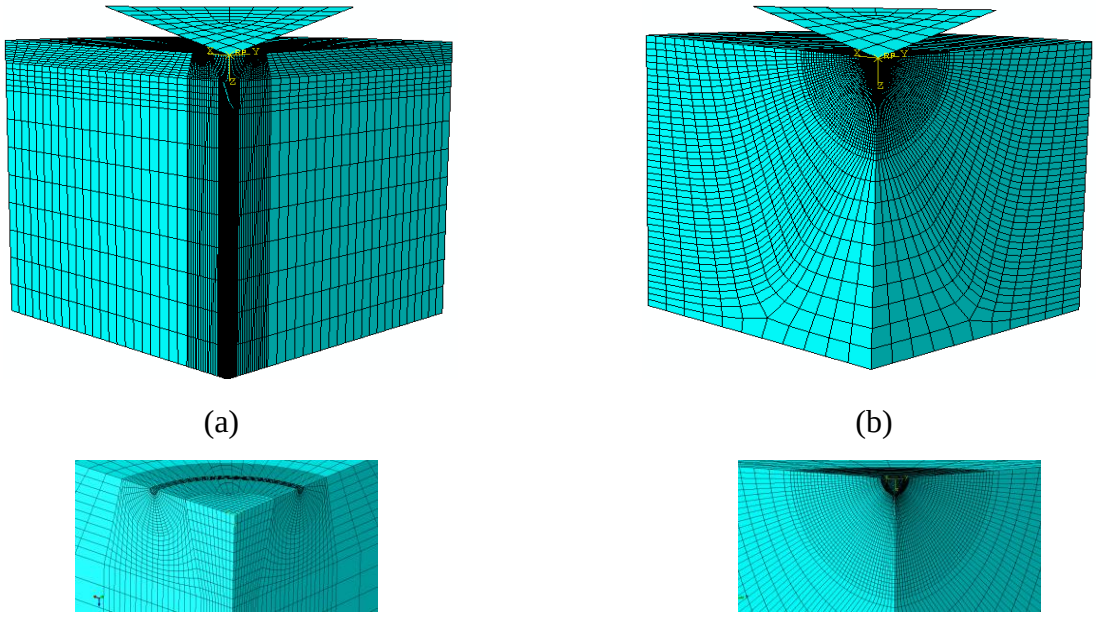

Figure 10-9 3-D FEM Vickers indentation cracking system of a) Palmqvist crack systems, b) Median crack systems c) Mesh density of Palmqvist crack front, d) Mesh density of median crack front

In this study, the specimen material was assumed homogeneous and isotropic following the elastic perfectly plastic material constitutive law. However, the indentation tests on many brittle materials such as most ceramics and glass show that these materials are isentropic and homogenous and can be approximated by the elastic perfectly plastic as presented by Rabier and Demenet (2000), Gei, Bigoni et al. (2004), Yao, Ruan et al. (2006), and Jiang, Qiu et al. (2007).

In order to increase the accuracy of indentation fracture analysis, the residual stress in the specimen was considered prior to the indentation process according to the results obtained from [Chapter 5].

However, to ensure convergence results of the counter integral as well as SIF, specimen geometries partitioned based on the crack system types, resulting in a multi block structural meshing technique were employed, thus the physical domain was divided into a sub-domain of structural blocks joined together along their common boundaries. Such an arrangement provides 80 equally spaced nodes along each crack front, as is shown in Figure 10-9 (c, and d). This will lead to an increased capability to introduce a wide range of crack length and orientation and also increase the accuracy and sensitivity of the predicted SIF at the nodes along the different crack fronts, sizes and geometries.

The models' convergence analyses were also established relating to sample size, mesh density and friction coefficient as demonstrated in [Chapter 8]. The numerical load displacement data and residual stress field were then validated against published experimental data; the maximum relative differences were about 2-4%.

10.7 FEM numerical results and discussion

10.7.1 Stress Field analysis during Vickers indentation test

The simulations of the Vickers indentation cracking on brittle materials were performed over a wide range of Palmqvist and median crack system lengths and indentation depths. The stress field component σ_{22} perpendicular on the crack front is responsible for evaluation of both Palmqvist and median cracks as described in Figure 10-4. The counter plots of the residual stress σ_{22} during the loading and unloading phase are given in Figure 10-10 at two maximum indentation depth , δ(1.25, and 2) µm for given non-dimensional material properties $E/\sigma_y = 20, and\ E/\sigma_y = 60$. As displayed the plastic zone radius increases with E/σ_y and is about the twice the indentation impression diagonal. The maximum residual stress is concentrated at the end of the impression diagonal.

The residual stress development histories at median and radial directions outside the impression zone demonstrated that the stress grows to its maximum values after the unloading stage, which indicated that the Palmqvist and median cracks can increase to their final lengths as the restraining elastic field is removed during the unloading stage. This result is consistent with experimental results obtained by Cook and Pharr (1990).

The FEM simulation analysis gives reasonable results for the Vickers indentation test behaviour. During the loading stage, Figure 10.10 (a, b, c, and d), high tensile residual stress was developed along the indenter diagonal contact with the specimen. Surface plastic strain appeared at the end of loading stage with the result that Palmqvist and median crack systems can nucleate when their SIF are higher than the material fracture toughness. The indentation region shows a high elastic stress profile due to the effect of the compression force. This hydrostatic stress created is less critical for the crack nucleation. During the unloading stage, Figure 10.10 (e, f, g, and h), the tensile residual stress increases and reaches maximum value resulting in crack nucleation in the radial and median coordinates. This is due to residual stress at the interface between the elastic and plastic regions, which is formed due to the relaxation of elastic strains and surface material failures that can act as stress concentrator; therefore, the particular residual profile of the impression zone is taken into account in the 3-D FEM fracture analysis. Thus the residual stress field obtained after the unloading stage is applied to a given crack length to determine the SIF as reported in the superposition technique in Figure 10-6.

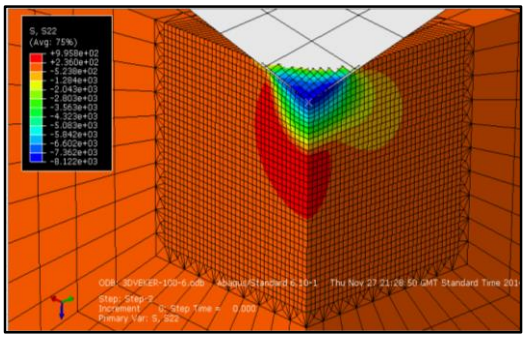

(a)

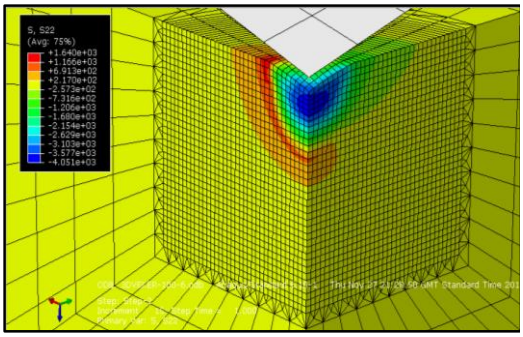

(e)

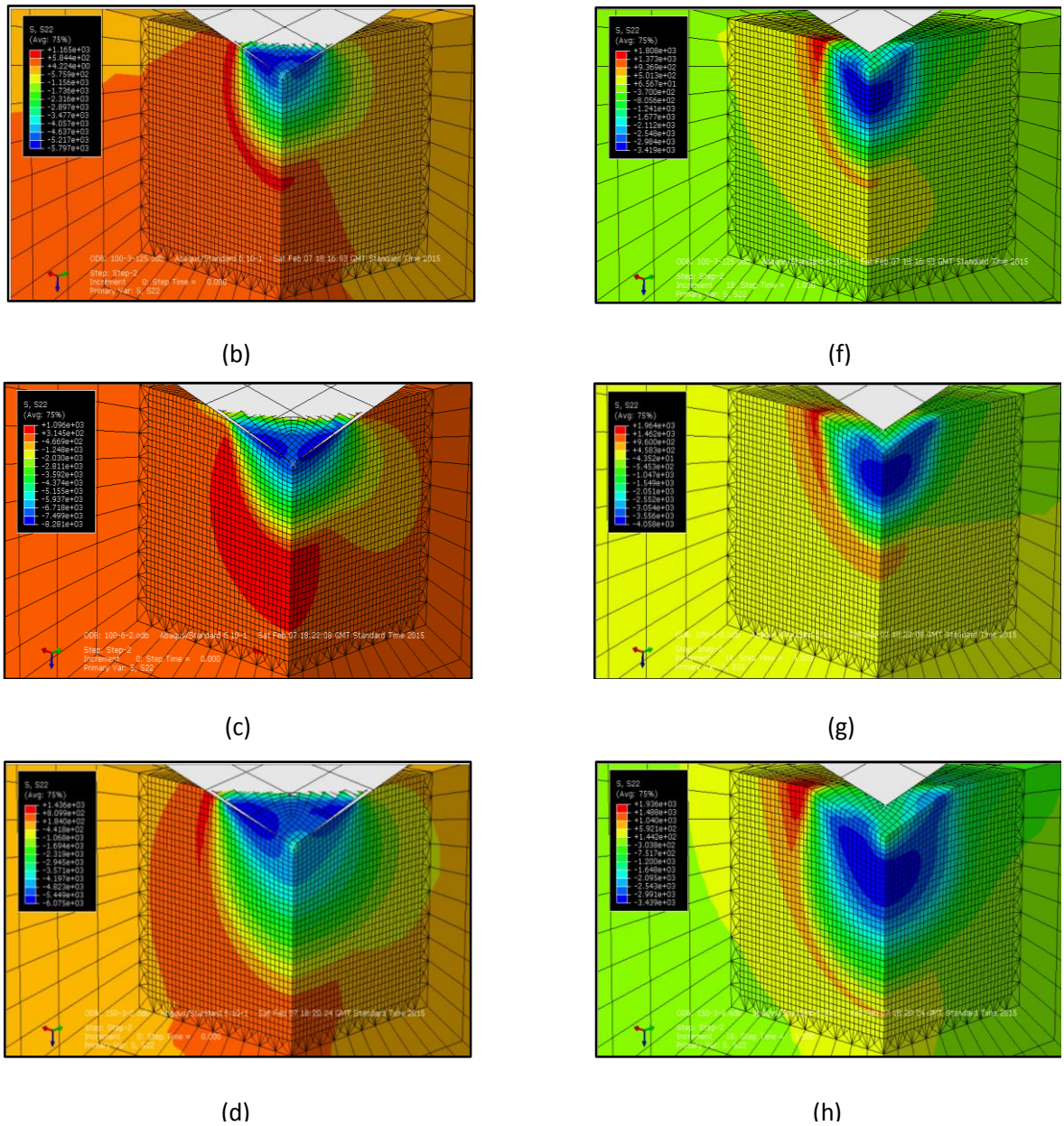

Figure 10-10 Residual stress field σ_{22} during loading and unloading cycles (a, e)$E/\sigma_y = 20$, δ=1.25µm, (b, f)$E/\sigma_y = 60$, δ=1.25µm, (c, g) $E/\sigma_y = 20$, δ=2µm, (d, h)$E/\sigma_y = 60$, δ=2µm.

10.7.1.1 Numerical Stress intensity factor analysis of Palmqvist crack

The residual stress field during loading and unloading cycles provides an insight into the development of stress intensity factor until critical conditions are achieved resulting in indentation cracks. In all cases, it is predicted that a small Palmqvist crack system will be initiated and propagate in the radial direction.

This is consistent with experimental determinations of material fracture toughness when only the surface crack tip of the specimen is considered. The normalized *SIF* along the circular crack front was measured as a function of polar coordinates angles (- 90 $\leq \theta \leq$ 90) for a given Palmqvist crack length range 0.5 $\leq l/a \leq$ 2.5 and material ratio range 20 $\leq E/\sigma_y \leq 120$. Figure 10-11 shows the results of normalized SIF for five different normalized crack lengths l/a values (0.5, 1, 1.5, 2, and 2.5) and three different material properties ratios E/σ_y (30, 60, and 120). Since, only the crack length at the specimen surface at 90^0 is considered as a final length of the Palmqvist crack system in the experimental measurement, therefore *SIF* at a polar coordinates angle of $90^0$is considered as a material fracture toughness K_{IC} in the numerical simulation analyses.

As illustrated in Figure 10-11 for brittle material properties range 20 $\leq E/\sigma_y \leq 80$, the SIF reached its maximum value at the contact edge between the indenter face angle and specimen at (-90^0) and then reduces gradually until approaching the fracure toughnes value at (90^0). However, the critical SIF decreases with an increasing crack length and/or a decreasing material ratio. For more ductile material properties in the range 100 $\leq E/\sigma_y \leq 200$, the *SIF* fluctuation along the crack front is more noticeable. This may be attributed to the complex stress field that can develop below the specimen surface resulting in high SIF generated in this region.

The *SIF* fluctuation increases with further growth of the normalized crack length l/a. Such variation in performance is due to the high residual stress σ_{22} occuring under the indentation suurface which affects the *SIF* at the surface. The magnitude of *SIF* is compatible to the residual stress value obtained from step two of the superposition technique.

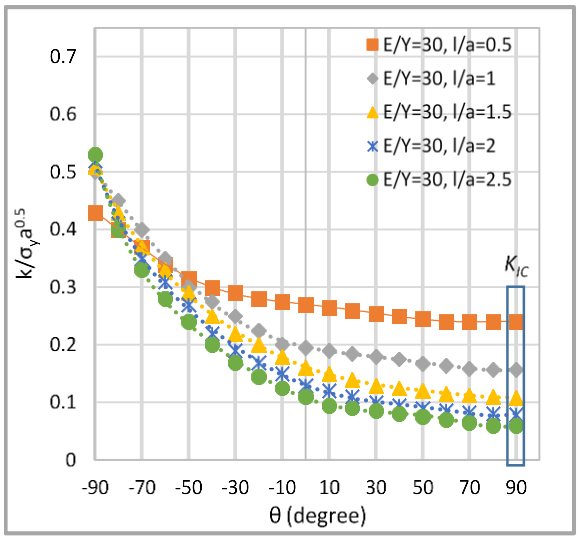

(a)

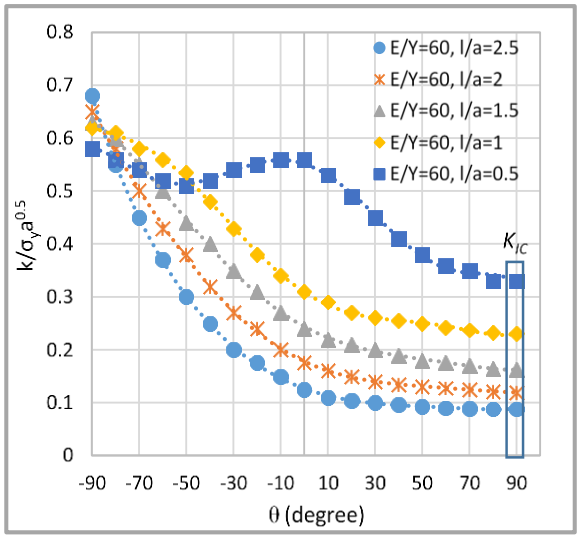

(b)

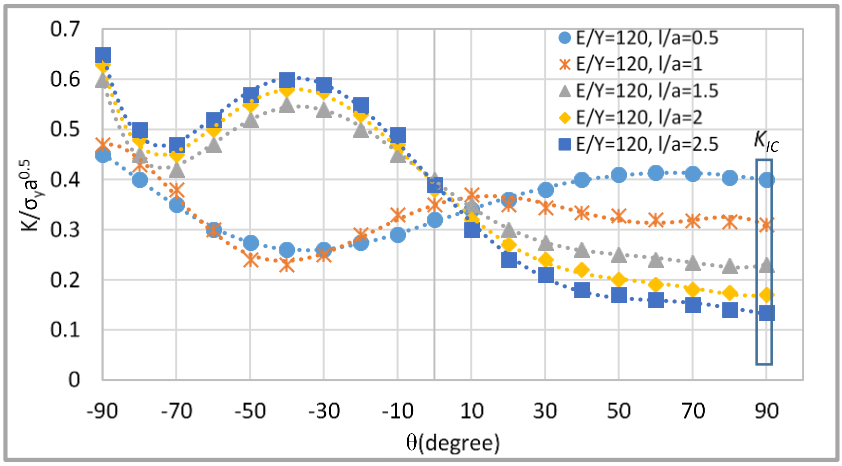

(c)

Figure 10-11 The normalized stress intensity factor $K/\sigma_y a^{0.5}$along the circular Palmqvist crack front for a selected crack length l/a= (0.5, 1, 1.5, 2, and 2.5) and material properties: a) E/σ_y = 30, b) E/σ_y = 60, and c) E/σ_y = 120

A series of numerical simulations were carried out using the dimensionless analysis approach to investigate the normalized critical *SIF*, $K_{IC}/\sigma_y a^{0.5}$, when the normalized crack length and material ratio were varied according to condition $0.5 \leq l/a \leq 2.5$ and $20 \leq E/\sigma_y \leq 200$ respectively; in such an arrangement a wide range of brittle and elastic plastic material properties will be covered. Figure 10-12 shows a three dimensional plot of the relationship between critical *SIF*, $K_{IC}/\sigma_y a^{0.5}$and l/a values as a function of $20 \leq E/\sigma_y \leq 120$ obtained at $\theta = 90$. A non-linear surface fit model (Rational Taylor) with an iterative algorithm (Levenberg Marquardt) was employed to predict the critical *SIF* (K_{IC}) values of

Palmqvist crack system as a function of E/σ_y and l/a. Therefore, the fracture toughness of the selected material properties and crack length obtained from FEM analyses can be calculated according to the following expression Eq. 10.18 for the best fit surface area:

$$\frac{K_{IC}}{\sigma_y\sqrt{a}} = f\left(\frac{E}{\sigma_y}, \frac{l}{a}, 90^o\right) = \frac{Z_0 + A_{01}\,(l/a) + B_{01}(E/\sigma_y) + B_{02}(E/\sigma_y)^2 + C_{02}(l/a)(E/\sigma_y)}{1 + A_1(l/a) + B_1(E/\sigma_y) + A_2(l/a)^2 + B_2(E/\sigma_y)^2 + C_2(l/a)(E/\sigma_y)} \tag{10.18}$$

where the coefficients are: $Z_0 = 0.17011$, $A_{01} = -0.00616$, $B_{01} = 0.01186$, $B_{02} = -0.39932 \times 10^{-5}$, $C_{02} = -0.182 \times 10^{-2}$, $A_1 = 1.48933$, $B_1 = 0.00663$, $A_2 = 0.20925$, $B_2 = -0.71759 \times 10^{-4}$, $C_2 = 0.9617710^{-3}$

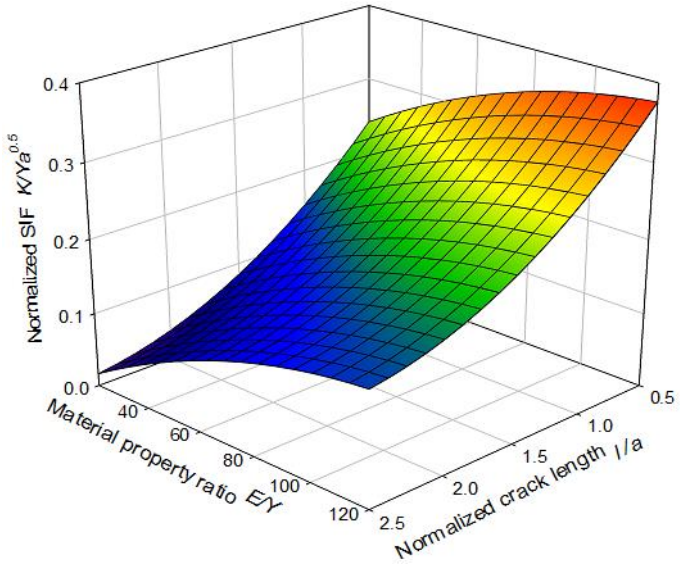

Figure 10-12 The normalized critical stress intensity factor $K_{IC}/\sigma_y a^{0.5}$, as a function of *material ratio* $\boldsymbol{E/\sigma_y}$*,and dimensionless Palmqvist crack length l/a.*

Niihara (1983) established a simple model for a Palmqvist crack when the normalized crack length is smaller than 2.5 and developed a new model Eq. (10.19) for a Palmqvist crack:

$$K_{IC} = 0.035\left(\frac{l}{a}\right)^{-0.5}\left(\frac{H_V}{E\emptyset}\right)^{-0.4}\left(\frac{H_V a^{0.5}}{E\emptyset}\right) \tag{10.19}$$

Evans and Wilshaw (1976) suggested that the constraint factor $\emptyset = H_V/\sigma_y$, and (Johnson and Johnson 1987) proposed that the H_V/E is function of E/σ_y for elastic perfectly plastic material properties. Therefore, the Niihara equation can be rewritten as:

$$\frac{K_{IC}}{\sigma_y a^{0.5}} = 0.035\left(\frac{l}{a}\right)^{-1/2}\left(\frac{E}{\sigma_y}\right)^{2/5} \qquad (10.20)$$

Figure 10-13 (a, and b) shows the comparison of normalized critical *SIF* $K_{IC}/\sigma_y a^{0.5}$calculated from the numerical analysis Eq. (10.18) with the values obtained from Niihara model Eq. (10.20) for a given material property ratio E/σ_y= (20, 30, 40, 60, 80, 100, 120, 200) and dimensionless Palmqvist crack length *l/a* =(0.5, 1, 1.5, 2, 2.5).

The results of both calculation models shows similar trends in that the fracture toughness decreases with the increasing Palmqvist crack length and also the fracture toughness increases when the material stiffness increases. It is interesting to observe that the discrepancy between the present study and the Niihara (1983) model was about 14% for material ratio range $20 \leq E/\sigma y \leq 60$, this difference increases to about 17% for material ratio range $60 \leq E/\sigma y \leq 200$ irrespective of the crack length. This may be attributed to the fact that the harder materials may be strongly influenced by the inhomogeneous stress field below the indentation impression and also the Niihara model may be relatively more appropriate for ductile material where most of the experiments used in such kinds of material properties (Niihara, Morena et al. 1982). However, the present study may be valid over a wider range for brittle and ductile materials compared with the empirical model in the literatures.

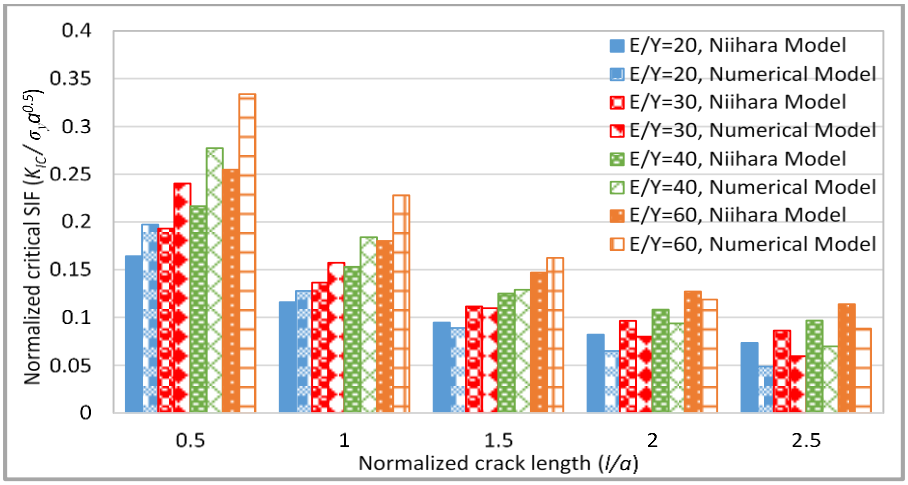

(a)

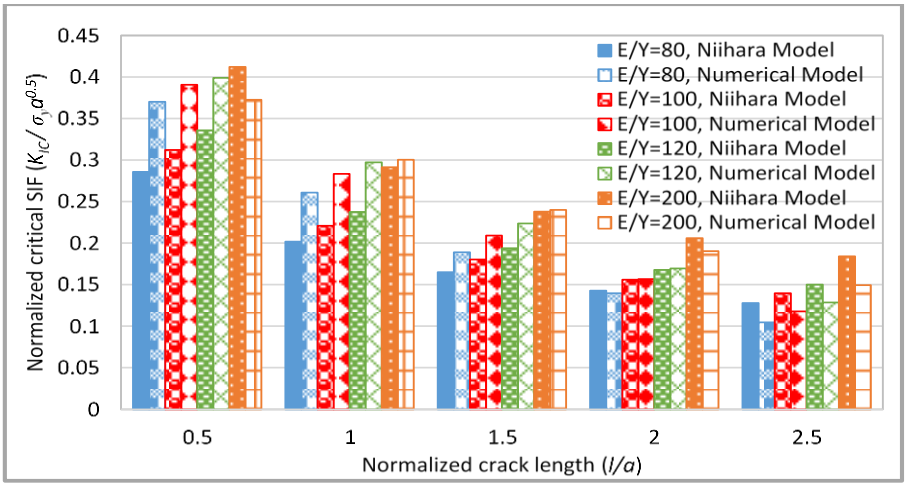

(b)

Figure 10-13 comparison of normalized fracture toughness $K_{IC}/\sigma_y a^{0.5}$ between the numerical analysis and Niihara model for a selected crack length l/a= (0.5, 1, 1.5, 2, and 2.5) and material properties: a) E/σ_y = (20, 40, 60, and 80), and b) E/σ_y = (80, 100, 120, and 200)

10.7.1.2 Numerical Stress intensity factor analysis of Median crack

The normalized *SIF* was measured at different polar coordinates angles ($0 \leq \beta \leq 90$) along the circular Median crack front for given material properties E/σ_y. Figure 10-14 shows the results of normalized *SIF* for five different normalized median crack length *c/a* values (2, 3, 4, 5, and 6) and three different material properties ratio E/σ_y (30, 60, and 120). It is clearly observed that for all cases the stress intensity factor corresponding to (mode I) can be propagated to its maximum values at the specimen surface when the polar coordinate angle β = 90 at the end of median crack length. Thus, the median surface crack can propagate to the maximum length and achieve a critical *SIF* value (fracture toughness) K_{IC} for given material properties. The normalized *SIF* increases with the increasing of material properties ratio (i:e with the increasing material ductility). The results also show that the critical *SIF* decreases with increased crack length and/or decreasing the material ratio. However, the nucleated small median crack can grow whereas its *SIF* keeps reducing because the indenter release causes a redistribution of the plastic residual stress field profile by the action of material elastic recovery until it achieves the fracture toughness value when *SIF* is equal to K_{IC} (Meneses-Amador, Campos-Silva et al. 2013).

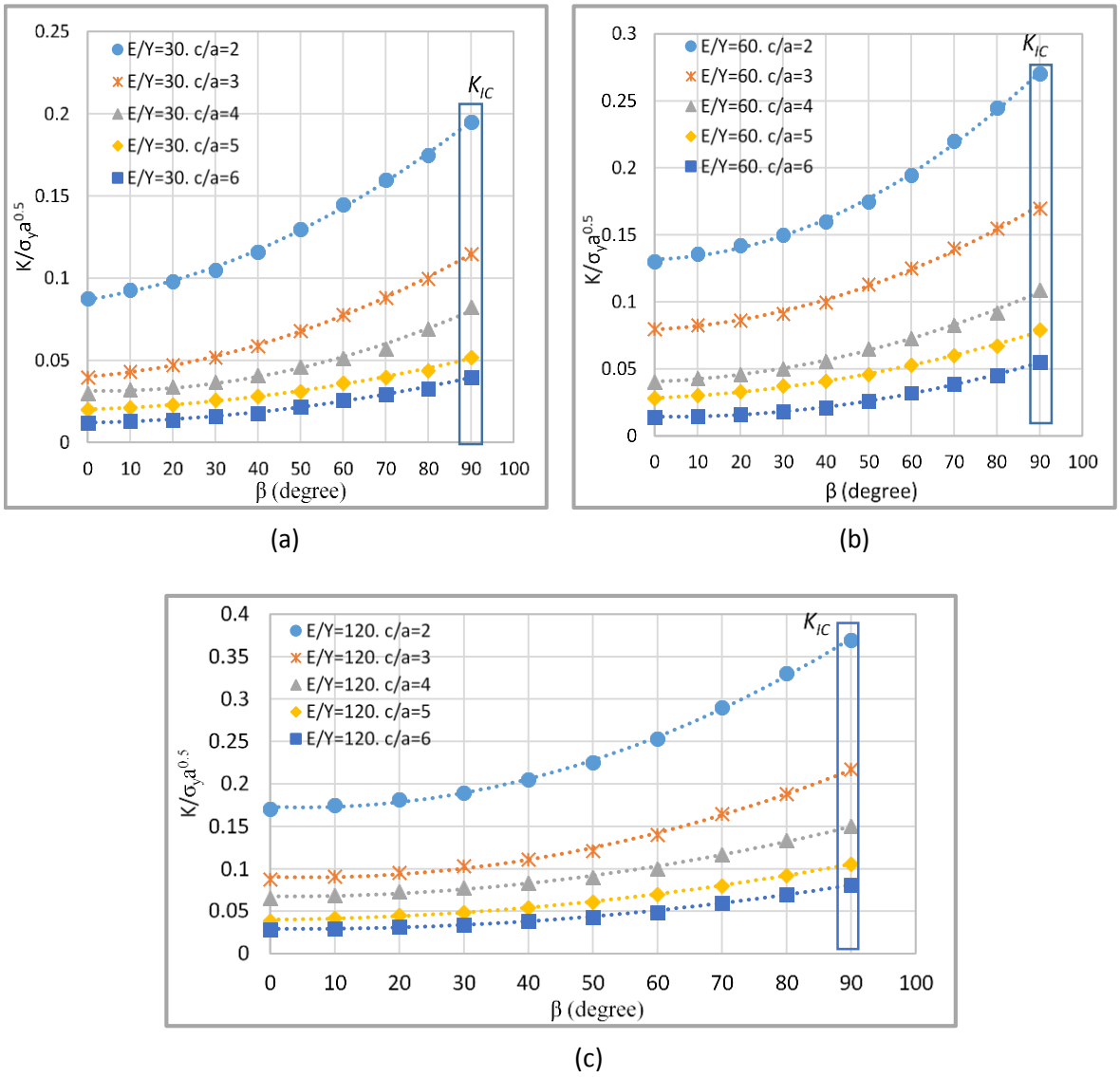

Figure 10-14 The normalized stress intensity factor $K/\sigma_y a^{0.5}$along the circular Median crack front for a selected crack length c/a= (2, 3, 4, 5, and 6) and material properties: a) E/σ_y = 30, b) E/σ_y = 60, and c) E/σ_y = 120

A series of numerical simulations were carried out using dimensionless analyses to investigate the normalized critical SIF, $K_{IC}/\sigma_y a^{0.5}$ when the normalized crack length and material ratio were varied according to condition $2 \leq c/a \leq 6$ and $20 \leq E/\sigma_y \leq 200$, respectively, in such arrangements a wide range of brittle and elastic plastic material properties will be covered. Figure 10-15 show three dimensional plot of the relationship between critical *SIF*, $K_{IC}/\sigma_y a^{0.5}$ and c/a values as a function of E/σ_y obtained at β = 90. A non-linear surface fit model (Rational Taylor) with an iterative algorithm (Levenberg Marquardt) was employed to predict the critical *SIF* K_{IC} value of median cracks as a dimensionless function of E/σ_y and c/a.

Consequently, the fracture toughness of the selected material properties and crack length obtained from FEM analyses can be calculated according to the following expression Eq. (10.21) for the best fitting surface area:

$$\frac{K_{IC}}{\sigma_y\sqrt{a}} = f\left(\frac{E}{\sigma_y}, \frac{c}{a}, 90^o\right) = \frac{Z_0 + A_{01}\,(c/a) + B_{01}(E/\sigma_y) + B_{02}(E/\sigma_y)^2 + C_{02}(c/a)(E/\sigma_y)}{1 + A_1(c/a) + B_1(E/\sigma_y) + A_2(c/a)^2 + B_2(E/\sigma_y)^2 + C_2(c/a)(E/\sigma_y)} \tag{10.21}$$

where the coefficients are: $Z_0 = -0.30447$, $A_{01} = 0.08121$, $B_{01} = 0.03375$, $B_{02} = -0.02169 \times 10^{-2}$, $C_{02} = -0.00137$, $A_1 = -1.13266$, $B_1 = 0.02756$, $A_2 = 0.89187$, $B_2 = -0.14078 \times 10^{-3}$, $C_2 = 0.0029707$

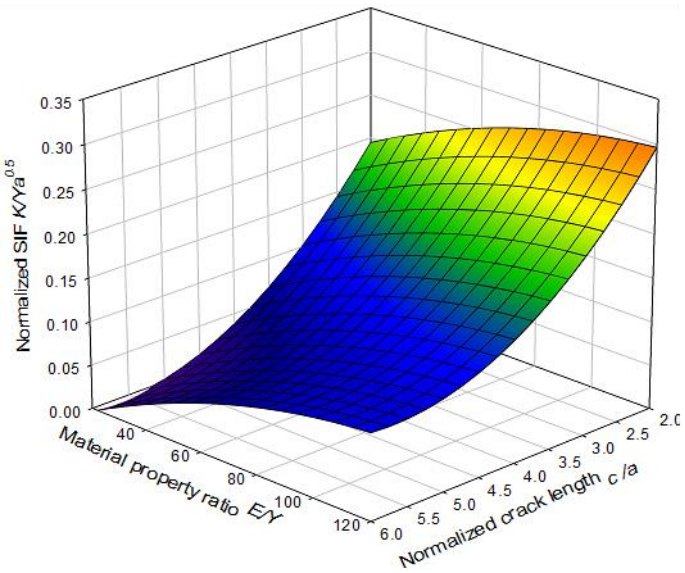

Figure 10-15 The normalized critical stress intensity factor $K_{IC}/\sigma_y a^{0.5}$, as a function of material ratio $\boldsymbol{E/\sigma_y}$, and dimensionless Median crack length *c/a*.

Evans and Charles (1976) suggested a simple relationship between median crack length and fracture toughness. Niihara (1983) developed a revised form of the Evans–Charles equation to distinguish the median crack from the Palmqvist crack based on extensive experimental results, Niihara suggested that the median crack can fit into the empirical Evans–Charles equation Eq. (10.22).

$$K_{IC} = 0.129\left(\frac{c}{a}\right)^{-3/2}\left(\frac{H_V}{E\emptyset}\right)^{-0.4}\left(\frac{H_V a^{0.5}}{E\emptyset}\right) \tag{10.22}$$

Therefore, the Evans–Charles equation can be rewritten as Eq. 23:

$$\frac{K_{IC}}{\sigma_y a^{0.5}} = 0.129 \left(\frac{c}{a}\right)^{-3/2} \left(\frac{E}{\sigma_y}\right)^{2/5} \tag{10.23}$$

Figure 10-16 (a, and b) shows the comparison of normalized critical SIF $K_{IC}/\sigma_y a^{0.5}$ calculated from the numerical analysis Eq. (10.21) with the values obtained from the Niihara model Eq. (10.23) for a given material property ratio E/σ_y= (20, 30, 40, 60, 80, 100, 120, and 200) and dimensionless Median crack length c/a =(2, 3, 4, 5, and 6).

It is clearly demonstrated that for all the range of material ratios and indentation loads, the K_{IC} values obtained from numerical analysis is in good agreement with those obtained theoretically. It is interesting to note that the numerical analysis model was anticipated to underestimate the fracture K_{IC} values of the material ratio $E/\sigma_y \leq 20$ to within 13% of their theoretical values. This may be attributed to the fact that the material ratio range employed by Niihara to derive Eq.(10.23) was $E/\sigma_y > 40$. The results also show that the numerical analysis overestimates the K_{IC} values of the material ratio range $30 \leq E/\sigma_y \leq 200$ to within 11% of their theoretical values based on the crack length dimensions. However, both models follow the same trends; the fracture toughness K_{IC} decreases with an increasing crack length and/or a decreasing material ratio. The discrepancy between the current study and Evans and Charles (1976) was fluctuating within $\mp$ 13% for all material ratios and crack lengths. Thus, the present study may be valid for a wider range of brittle materials compared with the empirical model in the literature.

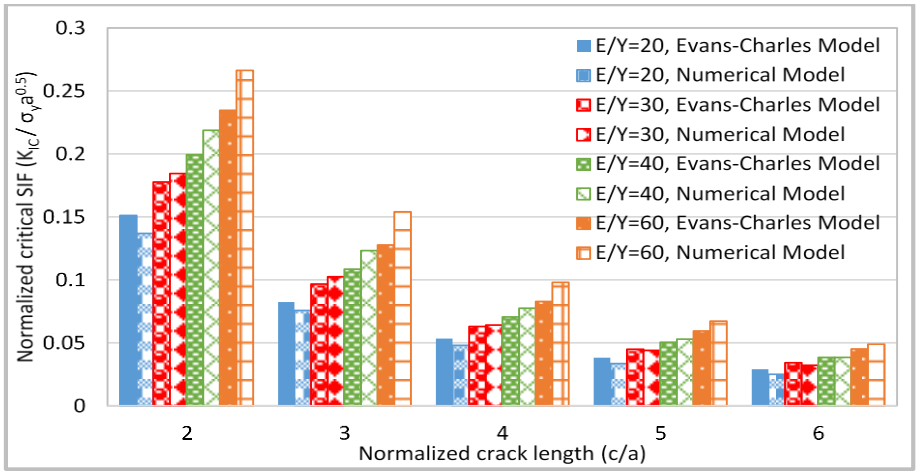

(a)

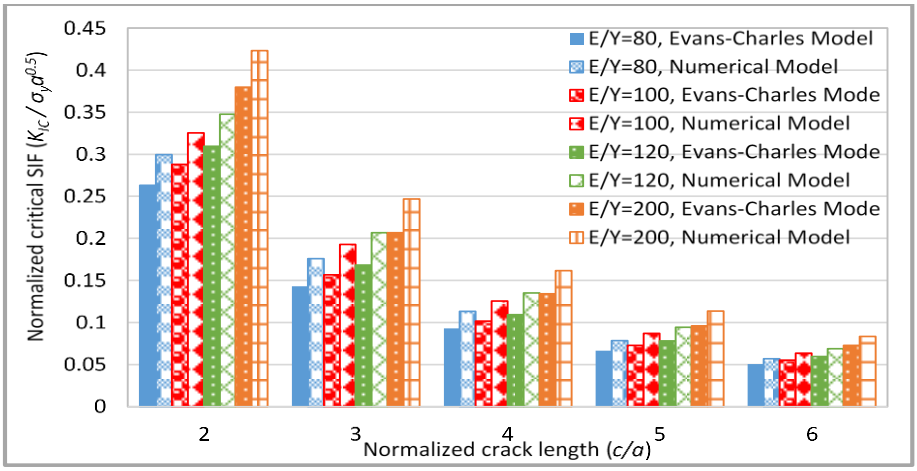

(b)

Figure 10-16 comparison of normalized fracture toughness $K_{IC}/\sigma_y a^{0.5}$ between the numerical analysis and Evans Charles model for a selected crack length c/a= (2, 3, 4, 5, and 6) and material properties: a) $\boldsymbol{E/\sigma_y}$ = (20, 40, 60, 80, and 200) and b) $\boldsymbol{E/\sigma_y}$ = 80, 100, 120, and 200

10.8 Validation of the 3-D FE cracking model against published experimental data

The Validation of the 3-D FE cracking model against published data was performed by comparing the predicted results with published experimental results. The FEM of Palmqvist and Median crack induced by the Vickers indentation test was verified by comparing the numerical models (Eq. 10.18 and Eq. (10.21) from this work with the fracture experimental results obtained by Evans and Charles (1976), Evans and Wilshaw (1976), Lankford (1982), and Niihara, Morena et al. (1982) for soda lime glass, *ZnS*, $and\ Si_3N_4$, as presented in Table 10-2.

Many researchers used double torsion techniques in the measurement of the critical stress intensity factor. In this study, various indentation loads were applied in each case, the surface Palmqvist and Median crack length (l, and c) were measured as a function of impression size a. Niihara, Morena et al. (1982) suggested that the Palmqvist and Median crack systems are likely to occure when $l/a < 2.5$, $c/a > 2.5$ respectively.

It may be difficult to identify the Palmqvist crack dimension and orientation experimentally especially for non-transparent materials. However, to simplify measurements, the assumption of uniform surface median crack length, c and the surface Palmqvist crack length, $l=c-a$ are considered. Figure 10-17 shows the comparison between predicted results obtained from developed models with published experimental results.

The comparison has been established on the relationship between the normalized fracture toughness $K_{IC}/\sigma_y a^{0.5}$and normalized Palmqvist and Median crack length (*l/a, and c/a*) with three different materials ratios E/σ_y. For the Palmqvist crack, it's interesting to note that the discrepancy between the current study Eq.(10.18) and experimental results may be attributed to the fact that the Niihara relationship Eq. (10.20) is not a universal one , thus each material follows a different straight line relationship. Niihara, (1982) proposed that if the normalized Palmqvist crack length l/a is represented by$(l/a)^{-m}$, then m is found to range $0.5 \leq m \leq 1.05$, and the difference curves diverge from one to another especially at lower l/a values. On the other hand for Median cracks better agreement has been observed between both analyses, the only notable thing is that the present model has overestimated the fracture toughness for the high material ratio $E/\sigma_y > 35$. Niihara, (1982) suggested that if the normalized Median crack length c/a is represented by$(c/a)^{-n}$, the slopes (n) of the curves are unusually similar, in the range of $1.45 \leq n \leq 1.66$ and are in a good agreement with Evans and Charles' (1976) average value of 1.5. As demonstrated, the fracture toughness obtained from the proposed model is reasonably close to the reference values, which validates the current study framework.

Table 10-2 Material properties used in published experimental results (E.Vans and Charles 1976, Evans and Wilshaw 1976, Lankford 1982, Niihara, Morena et al. 1982)

Material	E (GPa)	σ_y (GPa)	E/σ_y
soda lime glass	72	2.03	35.5
ZnS	75	0.65	115.4
$\boldsymbol{Si_3N_4}$	300	4.2	71.5

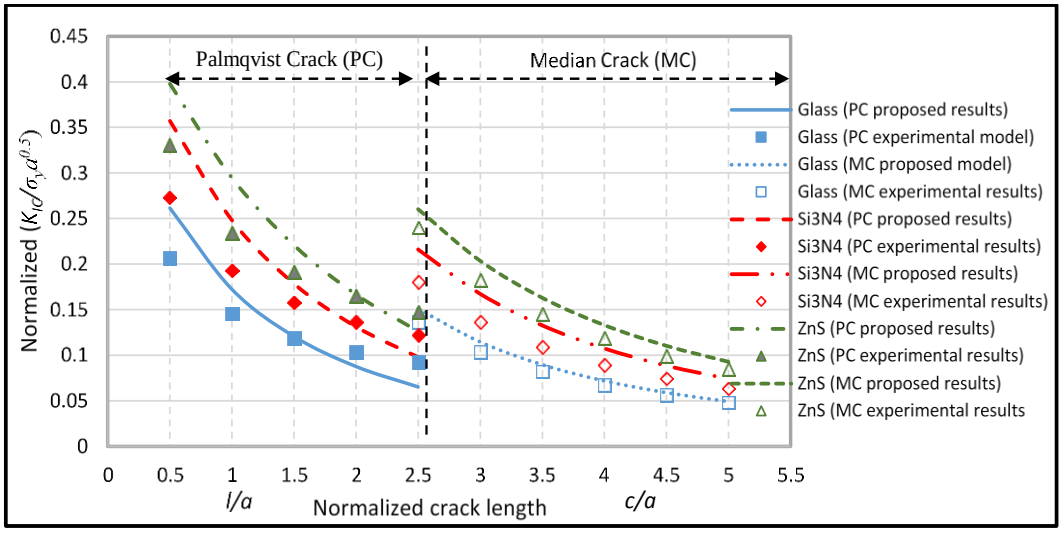

Figure 10-17 Comparison of the normalized $\boldsymbol{K_{IC}/\sigma_y a^{0.5}}$ between the predicted results from the present analysis with published experimental results (Evans and Charles 1976, Evans and Wilshaw 1976, Lankford 1982, Niihara, Morena et al. 1982)

10.9 The fracture toughness of thermally treated glass media

10.9.1 Experimental procedure

A recycled soda lime glass powder (VG+350) was subjected to heat treatment in a conventional programmable furnace. A standard firing profile was used in all firing tests with various ramp stages to the maximum temperature and holding time. The cooling rate was fixed in all firing tests at 40 min. The maximum temperature was varied from (VT-70 to VT+60)C^O, the ramp stage RT range from RT40 to RT60 min, and the holding time (VP) varied from VP-30 to VP+20 min.

The material was prepared to standard metallographic and microindentation test specification. The specimens were mounted using a cold mould thermosetting resin. The samples were ground and polished such as to reduce subsurface damages. One face of each sample was then treated by one of several standard grinding processes using a Metaserv Rotary Grinder machine which removes a particular layer from the specimen surface until the required surface roughness acceptable in the indentation microhardness and topography test is achieved. The specimen surfaces were cleaned with acetone before each test.

The microindentation tests were conducted with a Vickers indenter using a full calibrated Buehler Omnimet MHT machine at (Manufacturing technology centre, Coventry, UK). The specimens were fixed on the instrument bed to prevent any rotation about the indentation axis and measurements were taken carefully to maintain the indenter normal to the specimen surface. High power optical microscopy fitted to the microindentation instrument and also a three-dimensional optical profiler instrument were used to investigate the morphology of the specimen surface after indentation. The characteristic dimensions of the indentation imprint were measured by taking the average value over the two orthogonal radial directions. The peak contact load of 4.9 N was applied for each set of experimental conditions in order to keep to the minimum crack length requirement of the Niihara model ($c > a$) at the upper end by taking into account the specimen thickness. For a particular thermally treated glass condition, five Vickers indentation hardness readings were recorded, and both the diagonal length and Palmqvist crack lengths l starting from the edge of Vickers indentation were measured to an accuracy of $\mp 0.1\mu m$ by optical microscopy. Figure 10-18 shows the optical microscopy images of the Vickers indentation test for three different heat treatment cycle conditions (a) VT+50, VP+10, RT40 (Finishing media), (b) VT-10, VP+20, RT50 (General purpose media), and (c) VT-50, VP-20, RT50 (Cutting media).

The mean hardness and averaged normalized Palmqvist crack with diagonal impression lengths obtained after unloading stage of 4.9 N (maximum indentation load) for each set of glass media conditions were summarised in Table10-3. The material properties such as Young modulus and Yield stress for each case were determined by inverse FEM and experimental load displacement curves algorithm proposed in [Chapter 9].

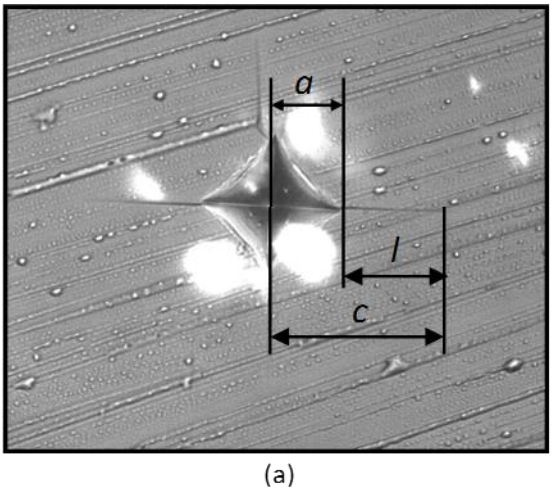

(a)

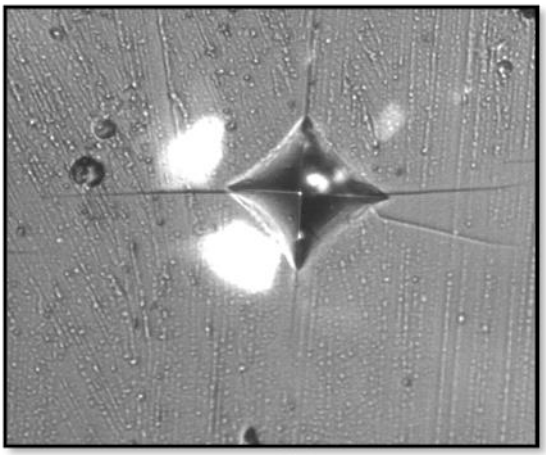

(b)

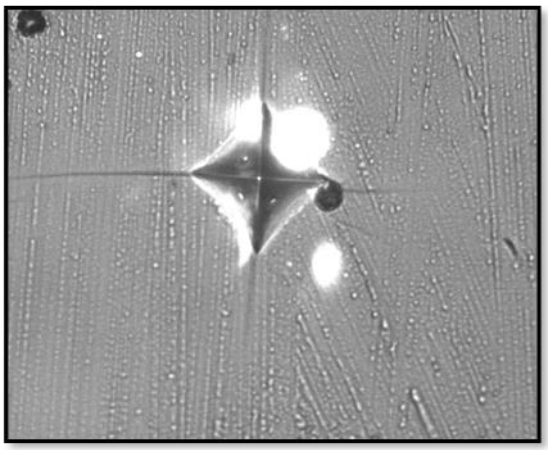

(c)

Figure 10-18 Optical microscopy images of Vickers indentation test for three different heat treatment cycle condithions (a) VT+50, VP+10, RT40, (b) VT-10, VP+20, RT50, and (c) VT-50, VP-20, RT50

Table 10-3 Vickers indentation experimental results of thermally treated glass obtained at maximum indentation load of 4.9 N.

Temperature code	Cycle time (min)	H (GPa)	E / σ_y	l/a
VT+50	140	6.5∓0.4	25.5∓0.4	0.9∓0.1
	160	6.9∓0.4	24.8∓0.2	0.8∓0.2
	180	6.7∓0.4	25.8∓0.3	0.9∓0.2
VT-10	140	5.8∓0.3	28.1∓0.4	0.9∓0.1
	160	6.2∓0.3	27.5∓0.1	0.8∓0.2
	180	6.1∓0.2	28.9∓0.3	0.8∓0.2
VT-50	140	5.6∓0.4	30.1∓0.4	0.7∓0.1
	160	5.7∓0.4	29.2∓0.4	0.8∓0.2
	180	5.8∓0.4	30.5∓0.4	0.6∓0.2

10.9.2 Results and discussion

The procedure and analyses used in previous sections were employed to determine the fracture toughness of thermally treated glass media used in the mass finishing production. The FEM of the Palmqvist crack induced by the Vickers indentation test and superposition technique was used to estimate the critical stress intensity factor (K_{IC}) of the glass media, which was examined by dimensionless analysis of the relationship between the elastic–plastic material properties and different crack lengths.

For each indentation simulation test, the assumption of the Palmqvist crack is used, to measured crack length and impression size are substituted in Eq. (10.18) along with the material properties derived from inverse FEM analysis as is shown in Table 10-3 , the measurements resulting in fracture toughness (K_{IC}) are established.

The numerical model of the fracture toughness (K_{IC}) Eq. (10.18) was compared with Palmqvist cracking model proposed by Niihara (1983) represented by Eq. (10.20) and the Ray and Dutta (1999) model was represented by Eq. (10.24) which was determined from extensive experimental results. These analyses were carried out on a range of thermally treated recycled glass media, which can be summarized in Table 10-4. Figure 10-20 shows the comparison between the numerical model and traditional curve fit experimental models (Niihara & Ray) of the relationship between the fracture toughness and absolute cycle time over three different elevated temperatures. As displayed, the fracture toughness determined from the present study is realistically close to the reference values, which validated the proposed numerical method. However during an experimental application it is recommended to use the Niihara, Morena et al. (1982) model if the crack length is relatively small. When l/a$<$ 2.5, the Palmqvist crack creation, thus the numerical solution presented by Eq. (10.18) can be employed, otherwise the numerical solution of Eq. (10.21) can be used for bigger crack length where a Median crack may form.

$$K_{IC} = 0.0515\, P/c^{3/2} \qquad (10.24)$$

The results also show logarithmic-like increases of the crack propagation resistance when the treatment cycle time increases. Moreover, exponential enhancements of the fracture toughness were observed when the absolute temperature was increased.

Table 10-4 Comparison of fracture toughness values of the thermally treated glass calculated by FEM analyses with the literature values proposed by (Niihara 1983), and (Ray and Dutta 1999)

Temperature code	Cycle time (*min*)	K_{IC} (Niihara) ($MPa\sqrt{m}$)	K_{IC} (Ray) ($MPa\sqrt{m}$)	K_{IC} (FEM) ($MPa\sqrt{m}$)
VT+50	140	0.85∓0.03	0.91∓0.03	0.96∓0.04
	160	0.83∓0.09	0.88∓0.07	0.93∓0.04
	180	0.88∓0.06	0.92∓0.04	0.95∓0.04
VT-10	140	0.87∓0.02	0.89∓0.03	0.93∓0.04
	160	0.84∓0.07	0.87∓0.06	0.91∓0.01
	180	0.88∓0.04	0.88∓0.05	0.92∓0.03
VT-50	140	0.9∓0.04	0.88∓0.02	0.92∓0.04
	160	0.88∓0.07	0.85∓0.05	0.91∓0.02
	180	0.89 ∓0.08	0.89∓0.04	0.95∓0.03

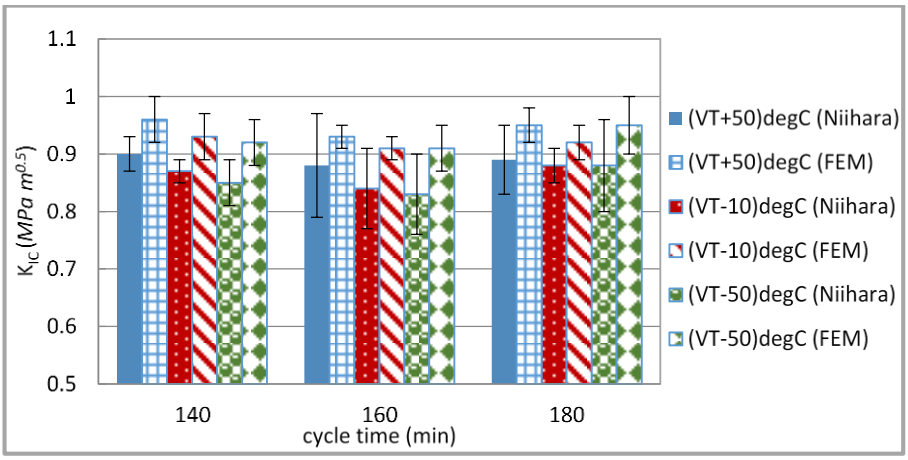

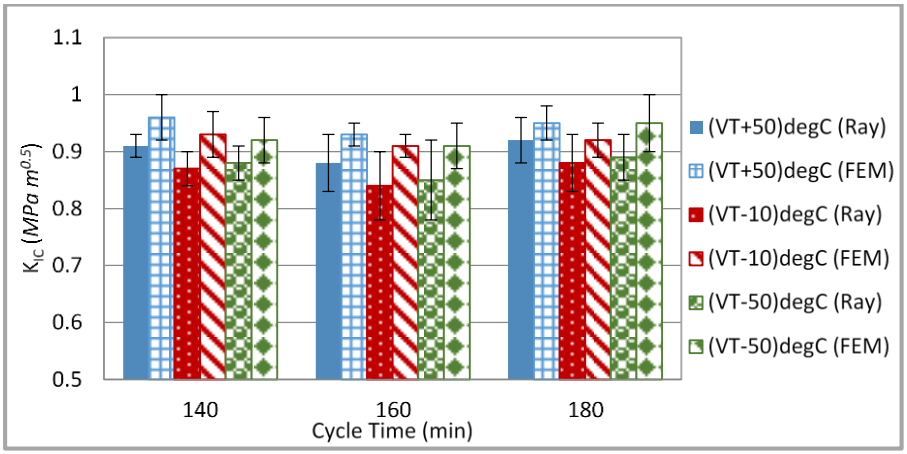

Figure 10-19 Comparison between the numerical model and traditional curve fit experimental models over three different elevated temperatures

10.10 Conclusion

In this chapter, an extensive three dimensional FEM simulation has been developed for different cracking systems induced by the Vickers indentation tests. The analysis of crack systems needs to be combined with the indentation residual stress field, which is strongly influenced by elastic plastic material properties. The superposition technique was generated to estimate the residual stress field in a particular plane using different indentation loads and it was superimposed on the surface of the Palmqvist and median cracks front plane to calculate the stress intensity factor *SIF* at different polar coordinate angles. Numerical models (Eq.10.18 for Palmqvist crack, and Eq.10.21 for median crack) were established between the critical *SIF* (fracture toughness), material properties, crack length and indentation size. However, an empirical functional form of the critical stress intensity factor was determined based on a non-linear surface fit model (Rational Taylor) with an iterative algorithm (Levenberg Marquardt).

From this function reverse algorithms were presented, which may be used to measure the fracture toughness of materials. The numerical models were validated with the experimental data proposed by many researchers over a wide range of material properties.

Moreover, Vickers indentation tests were carried out over a range of thermally treated recycled glass media and by measuring the crack length, the fracture toughness (K_{IC}) was derived throughout the Palmqvist numerical model. The results demonstrated that the K_{IC} of thermally treated recycled glass estimated from FEM is reasonably close to the values determined by the empirical models proposed by Niihara, Morena et al. (1982) and Ray and Dutta (1999). However, the proposed approach is applicable to a wide range of elastic plastic and brittle materials, through which the fracture toughness can be easily calculated from the Vickers indentation experiment which can be extended to use as a quality control method.

10.11 References

Anderson, T. L. (2005). Fracture mechanics: fundamentals and applications, CRC press.

Anstis, G., P. Chantikul, B. R. Lawn and D. Marshall (1981). "A critical evaluation of indentation techniques for measuring fracture toughness: I, direct crack measurements." Journal of the American Ceramic Society **64**(9): 533-538.

Arora, A., D. Marshall, B. Lawn and M. Swain (1979). "Indentation deformation/fracture of normal and anomalous glasses." Journal of Non-Crystalline Solids **31**(3): 415-428.

Asundi, C. I. C. Y. J. L. A. (1993). "an incremental stress-based constitutive modeling on anisotropic damaged materials." International Journal of Fracture **64**((4)): 299-319.

Barenblatt, G. I. (1996). Scaling, self-similarity, and intermediate asymptotics: dimensional analysis and intermediate asymptotics, Cambridge University Press.

Chen, X., J. W. Hutchinson and A. G. Evans (2005). "The mechanics of indentation induced lateral cracking." Journal of the American Ceramic Society **88**(5): 1233-1238.

Chen, X., N. Ogasawara, M. Zhao and N. Chiba (2007). "On the uniqueness of measuring elastoplastic properties from indentation: the indistinguishable mystical materials." Journal of the Mechanics and Physics of Solids **55**(8): 1618-1660.

Chen, X., J. Yan and A. M. Karlsson (2006). "On the determination of residual stress and mechanical properties by indentation." Materials Science and Engineering: A **416**(1): 139-149.

Chiang, S., D. Marshall and A. Evans (1982). "The response of solids to elastic/plastic indentation. I. Stresses and residual stresses." Journal of Applied Physics **53**(1): 298-311.

Cook, R. F. and G. M. Pharr (1990). "Direct observation and analysis of indentation cracking in glasses and ceramics." Journal of the American Ceramic Society **73**(4): 787-817.

Dias, A. M. d. S., P. J. Modenesi and G. C. d. Godoy (2006). "Computer simulation of stress distribution during Vickers hardness testing of WC-6Co." Materials Research **9**(1): 73-76.

Evans, A. (1979). "Fracture toughness: the role of indentation techniques." Fracture mechanics applied to brittle materials **678**: 112.

Evans, A. and T. R. Wilshaw (1976). "Quasi-static solid particle damage in brittle solids—I. Observations analysis and implications." Acta Metallurgica **24**(10): 939-956.

EVans, A. G. and E. A. Charles (1976). "Fracture toughness determinations by indentation." Journal of the American Ceramic society **59**(7-8): 371-372.

Evans, A. G. and T. R. Wilshaw (1976). "Quasi-static solid particle damage in brittle solids—I. Observations analysis and implications." Acta Metallurgica **24**(10): 939-956.

Gei, M., D. Bigoni and S. Guicciardi (2004). "Failure of silicon nitride under uniaxial compression at high temperature." Mechanics of materials **36**(4): 335-345.

Giannakopoulos, A., P.-L. Larsson and R. Vestergaard (1994). "Analysis of Vickers indentation." International journal of solids and structures **31**(19): 2679-2708.

Gong, J., J. Wang and Z. Guan (2002). "Indentation toughness of ceramics: A modified approach." Journal of materials science **37**(4): 865-869.

Hagan, J. and S. Van Der Zwaag (1984). "Plastic processes in a range of soda-lime-silica glasses." Journal of non-crystalline solids **64**(1): 249-268.

Hutchinson, J. (1968). "Singular behaviour at the end of a tensile crack in a hardening material." Journal of the Mechanics and Physics of Solids **16**(1): 13-31.

Inoue, A., W. Zhang, T. Zhang and K. Kurosaka (2001). "High-strength Cu-based bulk glassy alloys in Cu–Zr–Ti and Cu–Hf–Ti ternary systems." Acta materialia **49**(14): 2645-2652.

Jiang, W., K. Qiu, F. Liu, H. Choo and P. K. Liaw (2007). "Compressive Deformation and Fracture of a Hollow Bulk-Metallic Glass." Advanced Engineering Materials **9**(3): 147-150.

Johnson, K. (1970). "The correlation of indentation experiments." Journal of the Mechanics and Physics of Solids **18**(2): 115-126.

Johnson, K. L. and K. L. Johnson (1987). Contact mechanics, Cambridge university press.

Kobe, K. A. (1951). "The friction and lubrication of solids." Journal of Chemical Education **28**(4): 230.

Lankford, J. (1982). "Indentation microfracture in the Palmqvist crack regime: implications for fracture toughness evaluation by the indentation method." Journal of Materials Science Letters **1**(11): 493-495.

Larsson, P.-L., A. Giannakopoulos, E. Söderlund, D. Rowcliffe and R. Vestergaard (1996). "Analysis of Berkovich indentation." International Journal of Solids and Structures **33**(2): 221-248.

Laugier, M. (1987). "New formula for indentation toughness in ceramics." Journal of materials science letters **6**(3): 355-356.

Lawn, B. and A. Evans (1977). "A model for crack initiation in elastic/plastic indentation fields." Journal of Materials Science **12**(11): 2195-2199.

Lawn, B. and R. Wilshaw (1975). "Indentation fracture: principles and applications." Journal of Materials Science **10**(6): 1049-1081.

Lawn, B. R., A. Evans and D. Marshall (1980). "Elastic/plastic indentation damage in ceramics: the median/radial crack system." Journal of the American Ceramic Society **63**(9-10): 574-581.

Leonardi, A., F. Furgiuele, R. J. K. Wood and S. Syngellakis (2010). "Numerical analysis of brittle materials fractured by sharp indenters." Engineering Fracture Mechanics **77**(2): 264-276.

Meneses-Amador, A., I. Campos-Silva, J. Martínez-Trinidad, S. Panier, U. Figueroa-López and A. Torres-Hernández (2013). "An expression to determine the Vickers indentation fracture toughness obtained by the finite element method on Fe2B layers." Surface and Coatings Technology **215**(0): 285-290.

Muchtar, A., L. Lim and K. Lee (2003). "Finite element analysis of vickers indentation cracking processes in brittle solids using elements exhibiting cohesive post-failure behaviour." Journal of materials science **38**(2): 235-243.

Niihara, K. (1983). "A fracture mechanics analysis of indentation-induced Palmqvist crack in ceramics." Journal of materials science letters **2**(5): 221-223.

Niihara, K., R. Morena and D. Hasselman (1982). "Evaluation ofK Ic of brittle solids by the indentation method with low crack-to-indent ratios." Journal of Materials Science Letters **1**(1): 13-16.

Pachler, T., R. M. Souza and A. P. Tschiptschin (2007). "Finite element analysis of peak stresses developed during indentation of ceramic coated steels." Surface and Coatings Technology **202**(4–7): 1098-1102.

Perrott, C. (1977). "Elastic-plastic indentation: Hardness and fracture." Wear **45**(3): 293-309.

Ponton, C. and R. Rawlings (1989). "Vickers indentation fracture toughness test Part 2 Application and critical evaluation of standardised indentation toughness equations." Materials Science and Technology **5**(10): 961-976.

Rabier, J. and J. Demenet (2000). "Low temperature, high stress plastic deformation of semiconductors: the silicon case." physica status solidi (b) **222**(1): 63-74.

Ray, K. and A. Dutta (1999). "Comparative study on indentation fracture toughness evaluations of soda–lime–silica glass." British ceramic transactions **98**(4): 165-171.

Yan, J., A. M. Karlsson and X. Chen (2007). "Determining plastic properties of a material with residual stress by using conical indentation." International Journal of Solids and Structures **44**(11–12): 3720-3737.

Yan, J., A. M. Karlsson and X. Chen (2007). "On internal cone cracks induced by conical indentation in brittle materials." Engineering Fracture Mechanics **74**(16): 2535-2546.

Yao, K., F. Ruan, Y. Yang and N. Chen (2006). "Superductile bulk metallic glass." Applied Physics Letters **88**(12): 122106.

Yoffe, E. (1982). "Elastic stress fields caused by indenting brittle materials." Philosophical Magazine A **46**(4): 617-628.

Zeng, K., E. Söderlund, A. Giannakopoulos and D. Rowcliffe (1996). "Controlled indentation: a general approach to determine mechanical properties of brittle materials." Acta Materialia **44**(3): 1127-1141.

Zhang, L. and M. Mahdi (1996). "The plastic behaviour of silicon subjected to micro-indentation." Journal of materials science **31**(21): 5671-5676.

Zhang, W. and G. Subhash (2001). "An elastic–plastic-cracking model for finite element analysis of indentation cracking in brittle materials." International Journal of Solids and Structures **38**(34): 5893-5913.

CHAPTER ELEVEN

PERFORMANCE ANALYSIS OF THERMALLY TREATED GLASS MEDIA USING CONVENTIONAL AND ADVANCED MASS FINISHING PROCESSES

11.1 Introduction

Mass finishing, also called loose abrasive finishing, is a process used to clean and smooth surfaces for industrial use on mass by application of either loose abrasive media, which can include plastics and ceramics, or metals. It is used in various industries, with applications that range from the surface finishing of coins to titanium turbine blades (Gillespie 2006). It is commonly used to deburr large numbers of parts simultaneously; it can produce hundreds of parts per hour (Davidson 2003). As the term suggests, this is the advantage that defines mass finishing compared with other processes which do not allow deburring or surface finishing on as large a scale. The finishing of parts on mass is commonly used for their low cost processes and wide range of materials. In generally, the mass finishing operation includes edge break, edge contour, surface smoothing and improvement, tool mark blending, burnishing, polishing, super finishing, and micro finishing (Davidson 2003, Davidson 2005).

The basic process of using any traditional equipment in the mass finishing process involves the insertion of the workpiece to be finished into tubs/troughs by the action of rotation loose bonded media. This rotation creates friction between the part and the media, polishing the workpiece surface and edge (Domblesky, Cariapa et al. 2003). The media can be composed of either metal or abrasive. Metal media beats against the workpiece; abrasive media grinds away surface and edge material from workpieces, which is called the loose abrasive process. In addition to the media, water mixed with other compounds is added; the solution contains finer abrasives and soaps to achieve a smooth, clean finish.

The abrasive action can be achieved by mechanically distracting the total mass of part and media, the difference in mass causing relative movement between individual parts and contacting pieces of media. The sliding contact at the surface causes a shearing force; the results from the microscope illustrated that the amount of material removed during finishing is generally small and typically micrograms per part in the case of polishing and grams for deburring. In addition, material removal and the finishing action also results from a peening and blowing action generated during media contact (Domblesky, Cariapa et al. 2003).

The common factors that affect the mass finishing process are:

- Machine size and design (vibration amplitude, frequency, rotational speed)

- Workpiece (geometry, tolerance, surface finishes, material properties, appearance e.g. colouring, burr properties, edge tolerance)
- Media (size, shape, composition, absolute and relative amount of part per volume)
- Compounds (grain size, volume)
- Running time

Recently, academics have suggested several approaches to modified mass finishing technologies based on consolidated process to avoid power loss due to the particles' friction to increase wear resistance and provide longevity of the equipment. A better surface finish can be achieved when the active abrasive particles move in random motion. However, rotational abrasive flow finishing (RAFF) was developed by providing rotary motion to the workpiece in the case of finishing complex external and internal shapes. RAFF is the process that saves production time and cost of the final product. Sankar, Jain et al. (2009) demonstrated the effect of workpiece rotation on the conventional finishing process of abrasive flow. The results shows better surface finish and high removal rate can be achieved by applying RAFF to Al alloy and an Al alloy/SiC metal matrix composite compared with conventional abrasive flow finishing. Davidson (2007) suggested a new dry polishing technique, which is considered as a green process due to the very low pollutant wet residuals after the finishing cycle. Barletta (2006) reviewed the potential applications of the abrasive fluidized bed by developing abrasive fluidized bed assisted drag finishing. Such an arrangement provides a rapid surface finish with reduced environmental impact and increased productivity even for complex shapes or nonstandard materials.

A review of the literature shows that very little scientific research has been published with respect to mass finishing and few mathematical or process models exist. A number of trade articles and empirical studies have been published, (Zaki 1992, Brust 1997, Davidson 1997, Domblesky, Evans et al. 2004). These describe, in general terms, how surface finish and material removal are controlled, but these have only limited usefulness as they provide little insight into comparative performance of different tool materials nor do they explain fully and scientifically relationships between key process parameters.

The first area of this study included evaluation of the machining performance of the new glass media compared to that of conventional media using a vibratory mass finishing process.

A series of well-conditioned experiments were developed to embrace a wide range of process conditions including various media types such as (thermally treated recycled glass,

conventional ceramic; plastic and porcelain), work material (aluminium, brass, mild steel, stainless steel and an aerospace material – titanium alloy) and cycle time. Performance was evaluated based variously on workpiece surface roughness (Ra), cycle time, brightness, burr removal, and edge retention. Further experimental tests were completed to determine self-attrition rates.

The evaluation analyses were extended to include the on-site industry tests. A partner company engaged in the manufacture of aerospace fan blades supported the study with a production machine, components, media, compounds, and technical staff. The production of fan blades was investigated using both conventional media and glass media. Performance measures used on-site were surface roughness (Ra), brightness and cycle time. The study was extended to include the effects of other compound solutions.

The second area of this study focused on the on-site comparative analysis of advanced mass finishing processes using conventional media. A partner company supported the study with a production machine, components, media, compounds, and technical staff. A series of experiments were developed over a wide range of manufacturing process conditions including various machining process (vibratory, disc centrifuge, drag, and stream) finishing, abrasive type (conventional ceramic; plastic and porcelain), work material (CPM10, M2, EN31, and Inconel). Performance was assessed based on workpiece surface roughness (Ra) results over a range of machining parameters such as rotational speed and cycle time.

11.2 Mass Finishing System

11.2.1 Traditional mass finishing process

There are a number of different mass finishing processes in common use throughout industry. Among these are barrel, centrifugal, vibratory, and spindle finishing. Vibratory systems have become the predominant technique due to advantages inherent to the method in terms of ease of use, automation and material handling. Such systems fall into two broad categories in terms of the equipment being used: round bowl and rectangular tub designs (Davidson 2006). When first developed in the 1950s, these systems were typically modest in size, and were used for deburring and finish processing of smaller components. Being

able to process larger batch lots of various sized parts was important to competitiveness. Three commonly used processes are described in the following sections.

11.2.1.1 Round-bowl vibratory systems

Round-bowl equipment normally has a processing chamber that resembles the bottom half of a doughnut (Davidson 2006). Figure 11-1 shows the image of a Round Bowl Vibratory Deburring Machine. The vibratory motion generator on these machines is customarily a vertical shaft mounted in the centre-post area of the bowl. Adjustments related to the eccentric weights on this shaft will affect the rolling motion of the media, as well as the forward spiral motion of the media in the bowl chamber. This spiral motion promotes an even distribution and segregation of parts in the mass, thus lessening but not preventing the chance of part-on-part contact. Machines can also be configured to perform in a continuous mode with the parts being put in, then making one pass around the bowl and exiting via the internal separation deck. Equipment size vary from small bench models whose capacities are measured in quarts or gallons to veries large pieces of equipment in excess of 300 lt capacities. Water levels are critical to process success. Too much water will obstruct the vibratory motion of the mass, while too little will permit a soils / sludge build-up on the media, thereby reducing its cutting efficiency. Flow-through functions can be automated with appropriate controls and metering devices.

Figure 11-1 Round bowl vibratory deburring machine (Coating and Adhesives Group 2014)

Domblesky, Cariapa et al. (2003) developed a model to describe mass removal rate in terms of key process parameters for vibratory bowl process finishing. The predicted results

were consistent with those reported by Hashimoto and DeBra (1996) and indicated that the material removal rate remains constant over time and is governed by bowl acceleration, workpiece mass, material properties, and workpiece velocity. For the materials and geometry considered, the ratio of density to specific energy was similar. The workpiece mass and velocity were found to have a stronger influence on material removal rates than on process efficiency (measured through the specific energy)

11.2.1.2 Tub vibratory finishing equipment

Rectangular tub mass finishing is one of the vibratory equipment types that has the ability to process large parts, or even massive parts such as (2×2) m and can deal with difficult shaped of parts such as parts 10 m long or longer. Figure 11-2 show vibratory tub finishing with dividers. Generally, the vibratory tub has a U shape cross section with flat barrel ends and contains a more aggressive media action than the round bowl machine. The motion generators in this type includes rotating shafts with a range of eccentric weights attached either at the bottom of the U-shaped tub or one of the sidewalls. This equipment is usually loaded from the top of the chamber but unloaded from the release door that is located on a side panel (Benjarungroj 2012).

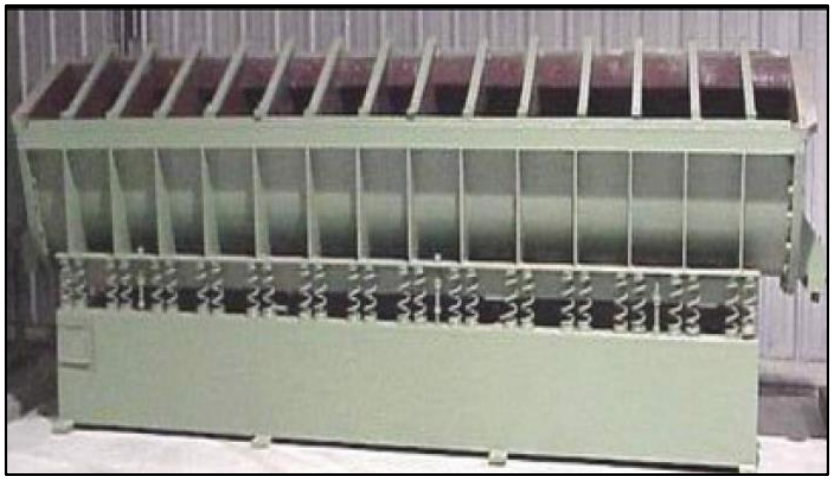

Figure 11-2 Vibratory tub finishing with dividers (metal finishing) (William 2013)

In addition, there are other shapes such as a keyhole shape, and enclosed tubular unit that can be used to enhance unrestricted mass movement. In this type, it is possible to use

removable separators in order to divide the rectangular tub into a number of sections. This operation permits the use of different types of media and processing the parts individually at the same time as shown in Figure 11.2 (Gillespie 2006).

The operation principle of the system is that the variable stroke acts like the variable speed and amplitude of a mechanical vibrator without having to change the weights. Then media action against the part will take place through the entire load. As a result, the media will rub against the part while the entire load within the container is turning over. Vibratory tub finishing has many advantages such as the capability of in-process inspection, unloading and reloading without stopping the machine and also the possibility of automating for batch or in line processing. Also in the vibratory tub it is possible to process large components such as crankshafts or aircraft wings or other long object and it is possible to have a fully automated system that continues processing for small parts

11.2.1.3 Centrifugal disk

Centrifugal disk machines were designed to combine the three dimensional action advantage of a vibratory bowl with the rapid cycle time of the centrifugal barrel. Figure 11-3 shows an image of a centrifugal disc machine (OTEC). The centrifugal force and the rotating action of the disk sends the mass outwards towards the chamber wall. The mass then slows down and returns to the center to complete the cycle (Cariapa, Park et al. 2008). Centrifugal disk machines are also used for their fast processing and cycle time (10 to 30 minutes), their capability for batch production and their control in process (Gillespie 2006). However, due to the small capacity of the chamber, the workpiece should not exceed 1 foot in length.

Figure 11-3 Centrifugal disk machine (OTEC, 2015a)

11.2.2 Fixture process

The concept of fixture method is to give motion to the part that is fixed (by dragging, rotating or developing planetary motion) and immersed in loose abrasive or polishing media. When the part edges and surfaces interact with loose media then a higher force is generated than that developed in conventional mass finishing process, where the part is placed randomly in the machine chamber and depends on the media motion to achieve surface finishing result. However, the purpose of the fixture process is to prevent contact between parts, increase the force against the part and control the cycle time in order to attain good result for the surface that is finished. Best examples of fixture processes are drag finishing and stream finishing which both give high quality results with short processing time and high reliability (Davidson 2003). In this study, the automation and optimization of fixture finishing process were developed, where the human factor can be totally neutralized

11.2.2.1 Drag finishing

Drag finishing machine technology is used for high quality and sensitive workpieces that need to be ground or polished without contact between parts and it is available in dry and wet processing. Workpieces are fixed in a special arrangement of workpiece holders.

Holders are dragged in circular motion through the container that is filled with the grinding or polishing media. The main spindle is also rotated at different speeds either clockwise or anticlockwise. Figure 11-4 shows an image of a drag finishing machine (OTEC, 2015b). The mass finishing process is significantly dependent on pressure and speed. In the drag finishing process, the intersect between high speed workpiece and media will create high pressure contact leading to the development of a high quality surface finish and precise rounding of the edge of the parts in a short time that can otherwise only be obtained by the hand polishing method. Due to the different variables that can be controlled such as depth and rotary speed, it is easier to reach rates of material removal up to 40 times higher than in conventional mass finishing and about 4 to 5 times faster than high-energy systems. In addition, the existence of a double drive system with two electric motors allows workpiece edges to be rounded uniformly, which enhances the tool life. The applications for drag finishing range from aggressive deburring and edge breaking all the way to high gloss polish of a range of parts. Drag finishing is the optimum mass finishing technique that produces a satisfactory surface finish.

Figure 11-4 Drag Finishing machine (OTEC, 2015b)

11.2.2.2 Stream finishing

Stream finishing is a method of mass finishing and also termed abrasion finishing because it is not always used for the grinding process but also for lapping and polishing that depends on the process. It is able to finish workpieces of length upto 200mm and weight of 20 kg including the holder.

Figure 11-5 shows an image of a stream finishing machine (OTEC, 2015c). The workpiece holder is rotated either clockwise or anti clockwise to allow the workpiece itself to align the direction of stream flow media. The media flow is generated through the bowl rotation at a specific speed. This configuration helps to reduce the effect of transverse force and remove the risk of the tool breaking or becoming deformed (Telljohann 2014). Stream finishing is described as short in processing time, simple in operation and has excellent reliability. However, the high processing force can generate a fine surface roughness value (Ra) less than 0.03µm. The machine is able to process six workpieces at the same time in a single holder fitted with a quick release mechanism to ensure that the workpiece is finished over the entire surface. Workpiece holders (Example: jaw chuck, drill chuck, collets and gripper) are available in different feature which rotate around their own axis at the same time. The processing time can be reduced significantly by adapting High speed rotating workpiece holders (up to 2000rpm).

Figure 11-5 Stream finishing machine (OTEC, 2015c)

11.3 Mass finishing media

There are five major materials of loose abrasive media (ceramic, plastic & synthetic, metal, precision, and micro-bite). The internal composition of conventional media is the source of the cutting action, weight, wear, and level of surface finish, all of which define the capabilities of the media. Knowing the different types of media and their application is useful for the comparative study with recycled glass media undertaken in this study

11.3.1 Shape, Size and Weight

There are approximately 15 different shapes of loose abrasive media as is shown in Figure 11-6. Each abrasive media is used for a specific application depending on the workpiece configuration. Shape is an important factor in media selection. The major considerations are that the shape of the loose abrasive media chosen should permit access to all surfaces of the workpiece – meaning any ledges, holes, or other geometric features - for the deburring or finishing operation, and it must allow an easy separation of the media from the workpiece treated at the end of the cycle. In some cases, a mixture of media shapes may be most effective.

The size of loose abrasive media is important for several reasons. It helps to keep the workpieces separate from each other. The right choice can allow the media to reach all surfaces to finish or deburr. Larger media have a faster cutting rate and produce smoother surfaces on workpieces. However, the use of small media in high-energy methods of mass finishing can improve the surface finish without increasing the cycle time. The weight of the loose abrasive media is another important factor in media selection. According to Gillespie (2006), heavier media allow faster cutting. However, heavier media apply more pressure than lighter media, which can cause thin or ductile workpieces to bend or distort.

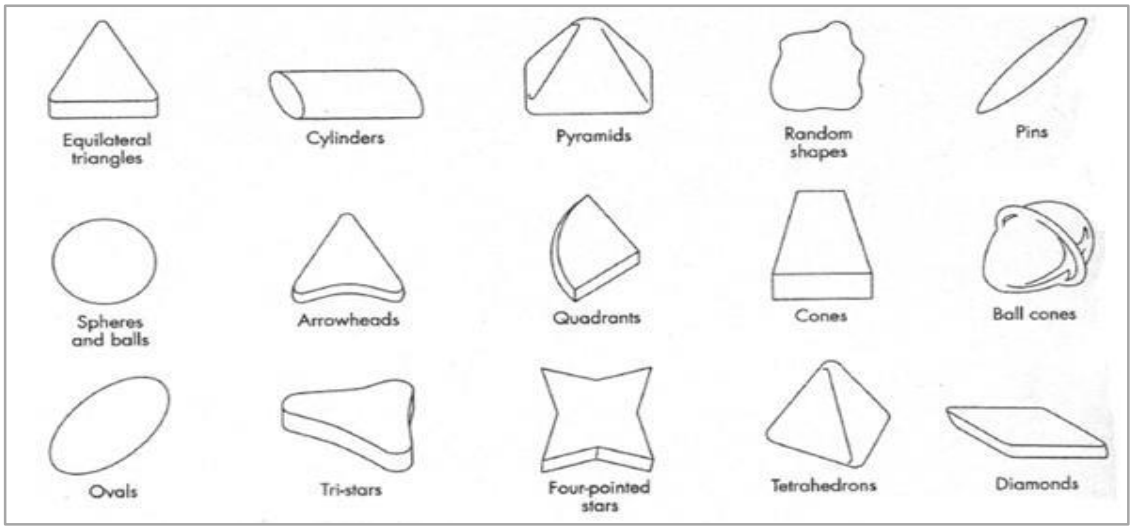

Figure 11-6 Shapes of media (Gillespie 2006)

11.3.2 Media Capability

The capability is the ability of the media to deburr corners, edges and other surface requirements with uniformity (constant performance over time). The capability of a media is principally defined by: the machining parameters; the media wear rate; media composition (cutting action, weight, wear and surface finish); the ability to finish a range of workpieces (i.e. shape, size, material); and quality of the finishing. Hard media will work longer, but softer media will cut faster. In terms of media wear, most plastic, abrasive, or ceramic media get smaller over time, which can affect the finishing operation if they are lodged in holes and other recesses, which requires removing them manually.

The efficiency of material removal is strongly determined by the sharpness, hardness and density of the abrasive cutting edges. A media with an aggressive cutting surface will result in a poor surface finish and a media with a fine cutting efficiency will result in a good surface finish. This aspect is essential to understand the capability of the media assessed in this study.

11.3.3 Grain size effect

Figure 11-7 (a) shows the abrasive grain distribution on the conical shape media to be largely independent to stock removed. A study directed by Moore (1974) investigating the relationship between the volume of abrasive wear and the mean diameter of the abrasive particles is shown in Figure 11-7 (b); by determining the ratio of media to workload, it is possible to find the most economical solution. The results of that study indicate that any change in the optimum ratio can produce a significant effect on the quality of finishing achieved (Gillespie 2006) . It can also be noted that, for a range of materials used in the study, increasing the diameter of the abrasive grain increases the volume that is removed from the workpiece (Domblesky, Cariapa et al. 2003).

Dennis V. (2002) suggested that the particle shape is not the only variable that controls the behaviour of manufactured abrasives. The relationship between particle shape and stacking behaviour needs to be understood before the former can be used to accurately predict wear-rate.

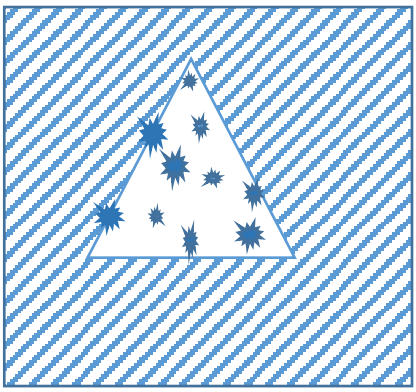

Cross section of conical shape media

(a)

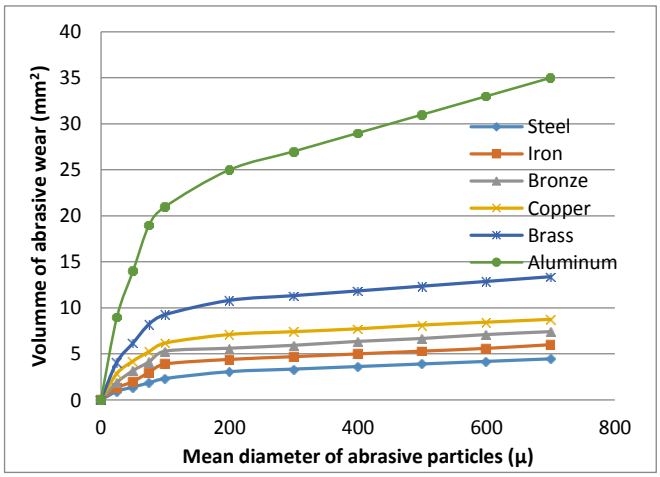

(b)

Figure 11-7 a) Abrasive grain size, b) volume wear with particle size relationship (Gillespie 2006)

11.4 Comparative study between conventional media and Vibraglaz media using vibratory mass finishing process

The surface parameter used to evaluate surface roughness in this experimental study is the average roughness (Ra), the most widely used parameter for surface texture. Surface roughness plays a vital role in determining the desired quality of a machined metal surface for today's engineering industry. Surface roughness inspection is one of the essential quality control processes carried out to ensure that manufactured parts conform to specified standards (ISO 4288, 1996)

11.4.1 Experimental procedure

A vibratory tub type finisher was used for experiments. The unit had a U-shaped cross-section chamber with a polymer liner and capacity of 10 litres. Vibration amplitude and frequency were fixed in all trials. Three grades of the thermally treated glass tools (Finishing, General purpose, and Cutting) media were used together with a conventional ceramic and a conventional plastic (also known as a 'polyester') media for comparison. All glass media were of a conical shape with average diameter of 20 mm and 15.7 mm height.

The ceramic media was triangular in shape, approximately 24.37 mm height, 22.77 mm width, and 24.91 mm length. The polyester media were of a conical shape with approximate dimensions: diameter 28 mm and height 30 mm.

Four types of workpiece material were employed in this study:- aluminium alloy (cylindrical), with diameter of 16 mm and average length of 40 mm; brass (cylindrical) with an average diameter of 16.5 mm and average length of 36.5 mm; Mild steel (cylindrical) with diameter of 17 mm and average length of 40 mm; and Stainless Steel coupons with average dimensions of 33 mm length 23 mm width and 5 mm thickness. Fluid compound was a non-foaming general purposes compound. The machining time was varied dependent on the experiment.

The surface roughness of the workpieces was inspected by tracing the surface using a Talysurf surface instrument (Diamond stylus, with M-speed 0.5 mm/s, R-speed 1mm/s, distance 5 mm) at several positions along the surface. Five surface roughness measurements were performed on each workpiece material at each time interval, the average of the group results were presented in this study. Compound was added at regular intervals to maintain a constant wet mix.

The experiments were extended to include Ti alloy coupons as a benchmarking material. In this test, the comparative study between glass Finishing media and pink polyester media was performed. The pink polyester is commonly used throughout industry (aerospace and automotive) for general purpose super-finishing. This media utilizes a wider range of abrasive types and sizes than preformed ceramics. The most popular grades are those using quartz as an abrasive. Aluminium oxide, silicon carbide and other abrasives are also used. Usually, low-cost polyester resins are employed as the binder and the various shapes are produced by casting. Five surface roughness measurements at three fixed points on the each side of the workpiece in a two-dimensional axis (horizontal and vertical) were performed. The averages of the group results were presented in this study. Compound was added at regular intervals to maintain a constant wet mix. A super-finishing agent (paste) was added at the beginning to aid in super-finishing during certain experiments (identified in the results).

11.4.2 Results and discussions

11.4.2.1 Comparison of machining performance between Vibraglaz and conventional media on (aluminium, brass, mild steel, and stainless steel) workpiece materials

Figure 11-8 shows the comparison of average surface roughness of aluminium workpiece material (HRC 30-35) as a function of time using Vibraglaz media (Finishing media, G-Purpose media, and Cutting media), and conventional media (ceramic, and plastic). As presented, all media excepting plastic, act aggressively on the surface of the material. Aluminium is a soft material, and in general, surface finishing would be achieved with a relatively light media or polisher. In the case of thermally treated glass and ceramic media, the surface roughness increases significantly for the first 15 minutes of the machining process. This may be attributed to the soft surface material being comprised largely of ceramic and glass wear debris from the media (aluminium with abrasive) which increases at the first stage of machining. It is also noted that the surface roughness was stabilized for all kinds of media after 50 min, due to the decreased wear of the media. However, the glass media only roughen up the surface for 15 minutes while the ceramic media still aggressively performed further. Thus, all kinds of thermally treated glass may prove a useful tool in this context and aid both in edge smoothing and in surface finish better than ceramic media. The results from conventional media agree with results proposed by Hashimoto (1996).

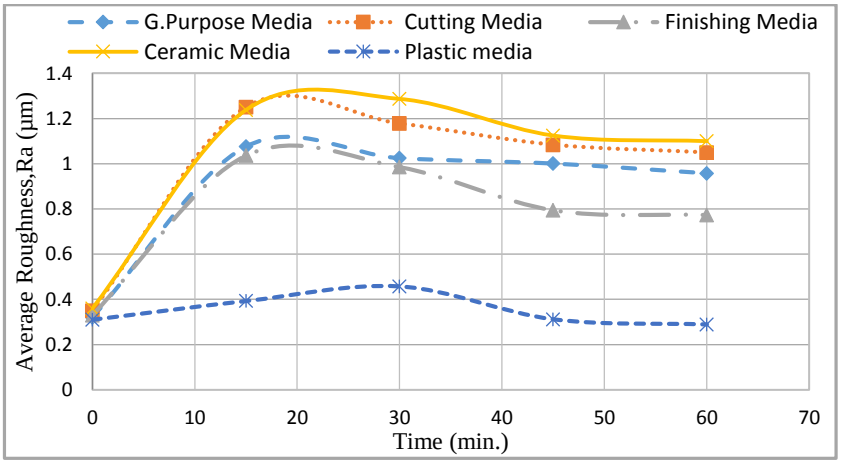

Figure 11-8 Comparison of average surface roughness of aluminium workpiece material as a function of time using Cutting media, Finishing media, G. Purpose media, Ceramic media, and Plastic media.

Figure 11-9 shows the comparison of average surface roughness of Brass workpiece material (HRC 33-38) as a function of time using Vibraglaz media (Finishing media, G-Purpose media, and Cutting media), and conventional media (ceramic, and plastic). As displayed all media other than plastic are too hard for the purpose of improving the surface finish of Brass. Again as brass is considerably soft material, the material surface is more likely to be comprised of ceramic and glass wear debris from the media. This is expected and a finishing media is usually employed in this case. However, it does show clearly that the mass of the thermally treated glass media lies someway between that of plastic and ceramic.

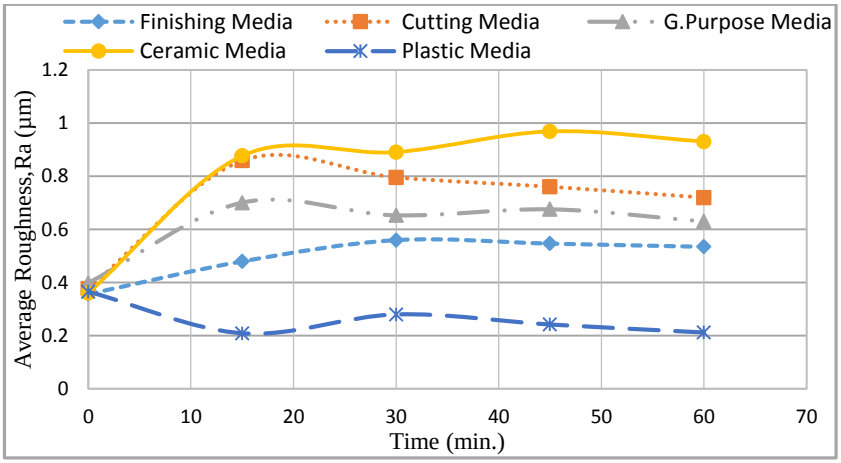

Figure 11-9 Comparison of average surface roughness of Brass workpiece material as a function of time using Cutting media, Finishing media, G. Purpose media, Ceramic media, and Plastic media.

Figure 11-10 shows the average roughness comparison of mild steel workpiece material (HRC 40-45) as a function of time using vibraglaz and conventional media. It is clearly noticed that the glass media achieved better Ra than did the conventional media. This improved performance was most significant for the Finishing media. The performance of all glass media matched that of the plastic media with this material. This informs us that the hardness and cutting ability of the recycled glass media are suited to the application. It was also observed during the experiment that the wear rate of the glass media was minimal and no dulling of the surface occurred. The outcome is consistent with results from the grinding process where it is well established that harder materials result in better surface finish compared with softer materials (Shaw 1996)

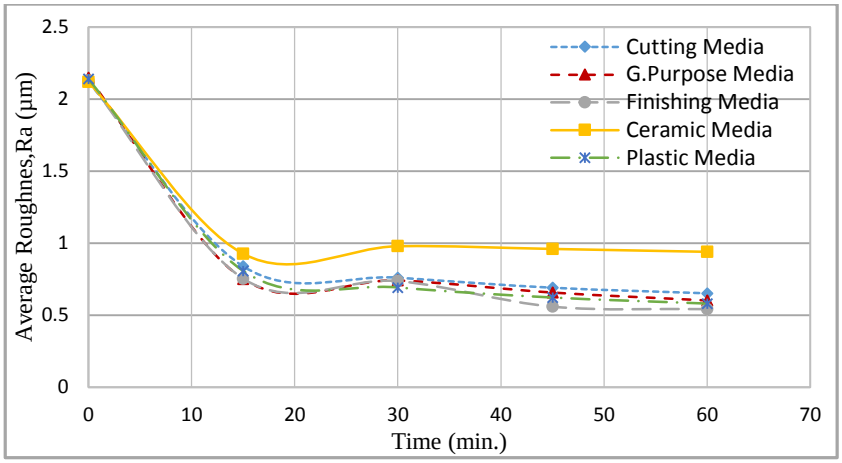

Figure 11-10 Comparison of average surface roughness of Mild Steel workpiece material as a function of time using Cutting media, Finishing media, G. Purpose media, Ceramic media, and Plastic media.

Figure 11-11 shows the average roughness comparison of stainless steel workpiece material (HRC 47-55) as a function of time using vibraglaz and conventional media. The results suggested that the surface roughness improved continuously in the case of Finishing media. The results also show that the final surface roughness produced by ceramic media was similar to the results from cutting media, while plastic media matched the G. Purpose media. This suggests, that the Finishing media is more suitable for stainless steel applications.

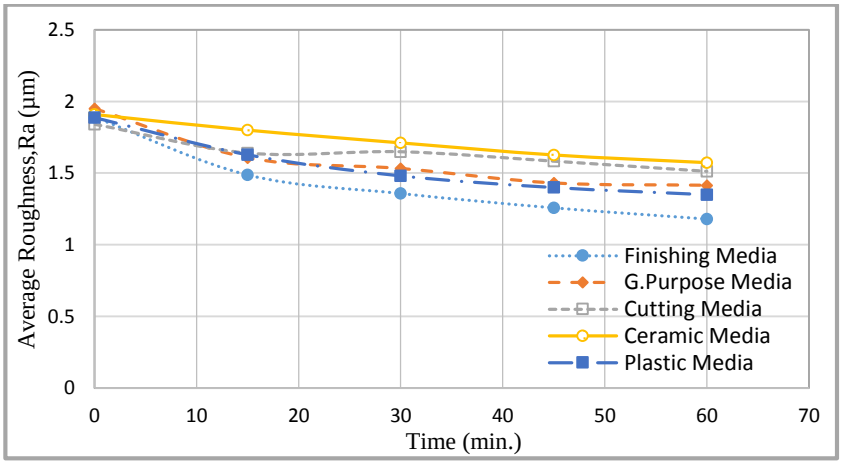

Figure 11-11 Comparison of average surface roughness of stainless steel workpiece material as a function of time using Cutting media, Finishing media, G. Purpose media, Ceramic media, and Plastic media.

Conventional ceramic media, is normally employed in processes that require an aggressive tool action, for example cutting and deburring. The number and size of active grains will have a strong impact on cutting performance and rapid cutting may be achieved. However, a consequence of using large grains is a higher surface roughness and a more dull and matte surface brightness. These effects were observed from the results reported for vibratory finishing aluminium alloy, brass and mild.

In the case of plastic media, only a few grains were distributed about the surface, giving an indication that it was designed for softer, less aggressive machining processes. Additionally, the bond resin, commonly polyester or urea-formaldehyde, creates a media of lower density than ceramic, and one that acts more softly. However, due to the weaker bond strength of the resin compared with the vitrified bond of the ceramic, complete grain detachment is more likely with plastic and wear rates subsequently affected. However overall wear rates will also be influenced by self-attrition and machining parameters.

The density of thermally treated glass media lies somewhere between that of ceramic and the plastic allowing it to be used as either a cutter or polisher tool. However, the composition of the glass media is 100 per cent devitrified glass. The cutting edge density is therefore considerably higher than that of ceramic and plastic media. Secondly, the surface is of a consistent 'roughness' in that no binder or other material is present i.e. no individual grains interrupt the general surface profile. As observed from the experiments, the performance of glass media was comparable and in some cases better, than the other media. Furthermore, it is able to brighten the surface of work materials to the same visual condition as the plastic media. However, control of kiln temperature and cycle time is key to whether one produces a cutter or polisher.

The work material, its hardness and the surface finish specification also influence the type of media that may be required. It was identified within this study that the glass media, in the variant supplied by the company, were too aggressive on selected work materials including brass and aluminium. This was also the case with the ceramic media, which is consistent with its application in industry. Similarly, it was identified within this study that conventional plastic media is inadequate to machine the stainless steel work material.

11.4.2.2 Comparison experiments between glass Finishing media and plastic media performance on titanium alloy workpiece.

The objective of this study is concerned with the machining performance of thermally treated recycled glass in vibratory mass finishing of Ti Alloy aerospace material. The surface finish generated with the glass was compared to that achieved using conventional polyester media under different lubrication conditions.

Figure 11-12 shows the vertical and horizontal surface roughness values of the Ti alloy coupon (Front side) using conventional plastic media and glass finishing media. Figure 11-13 shows the vertical and horizontal surface roughness values of the Ti alloy coupon (Rear side) using conventional plastic media and glass finishing media. ARF fluid compound was used in all experiments. The Ra measurements shown in the figures are the averages of three measurements taken on the same coordinate on the part surface as illustrated in Figure 11.14 (a). The results demonstrate that the surface roughness achieved with the glass media is comparable to that of the polyester bonded media and in fact, it achieved the lowest of all measured values in the horizontal plane shown in Figure 11-12 b. In general, the performance of the glass media matched that of the polyester bonded media with Ti Alloy material (Mike Morgan 2012) .This suggested that the hardness and cutting ability of the glass are suitable to this application. It was also observed throughout the experiments that the resulting part brightness (visual assessment) matched that of the polyester media as is shown in Figure 11-14 (b, and c). It is clearly noticed that the addition of paste (Keramo) in the finishing process by Finishing glass media had a deleterious effect on surface roughness, use of paste also impaired brightness. The rate at which the surface roughness improved (i.e. material removal and/or flattening of surface asperities) was similar for both abrasives; this suggests that the glass would be suitable as a super-polishing media for Ti Alloy aerospace material.

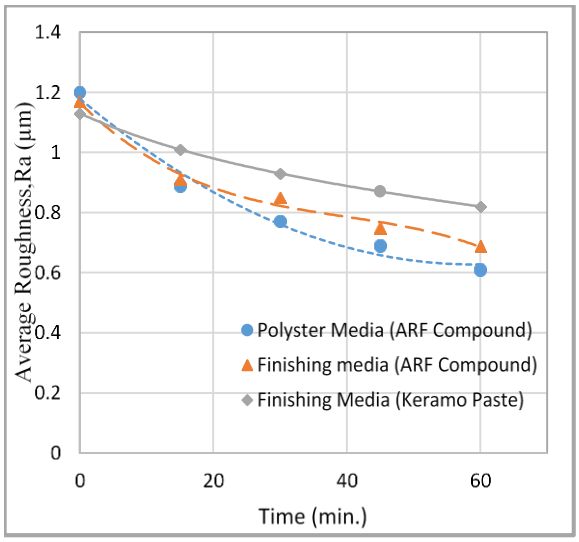

(a)

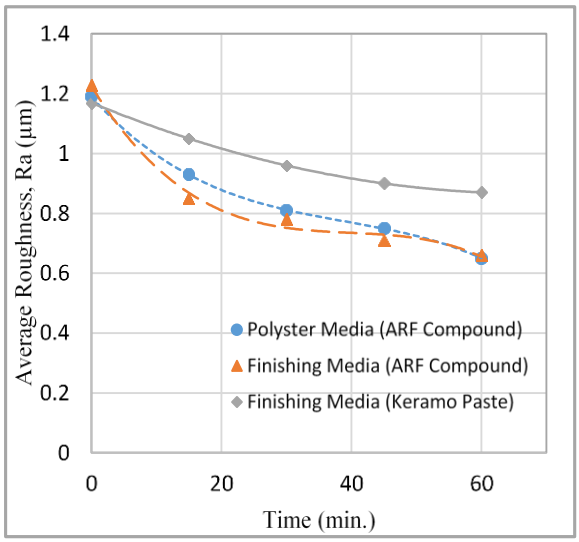

(b)

Figure 11-12 Surface roughness values of the Ti alloy coupon (front side) using glass Finishing and coventional polyster media measured on a) Vertical coordinate, b) Horizontal coordinate

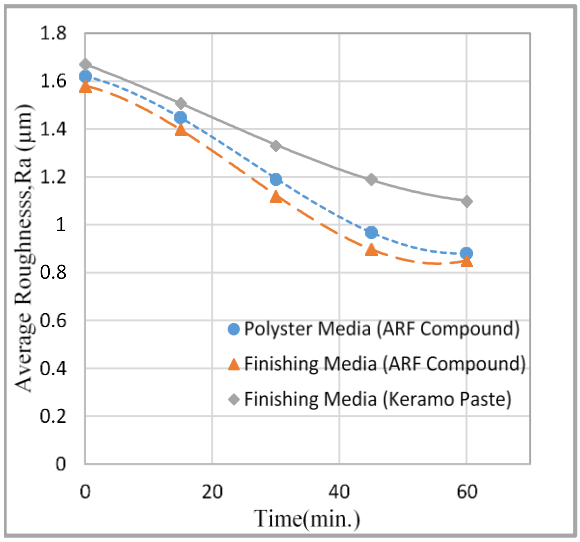

(a)

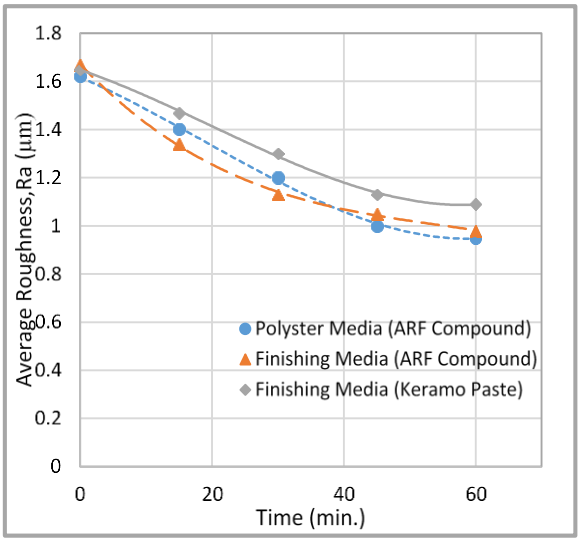

(b)

Figure 11-13 Surface roughness values of the Ti alloy coupon (rear side) using glass Finishing and coventional polyster media measured on a) Vertical coordinate, b) Horizontal coordinate

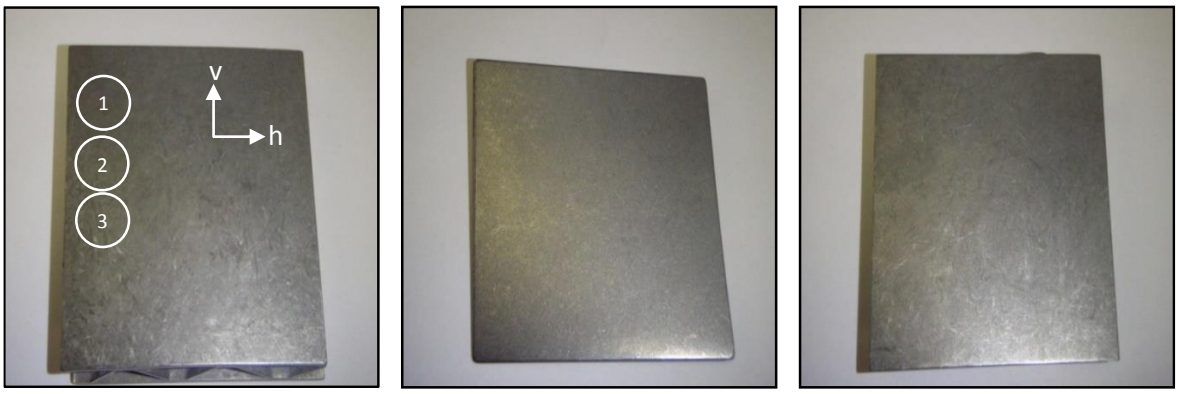

(a) (b) (c)

Figure 11-14 Observation of brightness of titanium alloy coupon a) Without machining, b) Machining for 60 min. with glass finishing media, C) Machining for 60 min. with conventional polyester media.

11.5 Comparison results from on-site simulated production test (Rolls Royce) of vibratory super-finishing process using thermally treated glass (Finishing media) and conventional (Plastic media)

The performance of media was established in laboratory tests, and further tests on a 'real' application were agreed. The industrial partner for these tests was Rolls Royce. The selected application was turbine blade (FAN) production. Rolls Royce annexed a machine tool for this study and provided media, components, compound, metrology, and technical support to help undertake the tests. The components provided were actual FAN blades and production replicated that currently in practice.

11.5.1 Experimental procedure

On-site production tests were completed on a suite of fan blades (A6R2500) using the Vibraglaz Finishing media. The on-site facility provided a vibratory twin motor trough (2 compartments). The two blades were housed in polyurethane coated jigs (one jig per compartment). Machine parameters (vibration amplitude and frequency) were fixed as per common production practice. Two fluid compound types were employed: First compound was Walther Trowal A6RF35 at a dosing rate of 1 per cent and second compound was Rosler FC120 at dosing rate of 3 per cent. The resulting brightness of blades from each fluid type was visually assessed. The glass media was pre-conditioned for a period of 36 hours in the test machine prior to start of tests.

The total machining cycle setup is (120 min.). The blades were measured off-line at 30 min. intervals using the metrology instrument currently used for this purpose in production (referred to in these tests as Taylor-Hobson) and by the Mitutoyo Surftest SJ401 instrument (employed in previous benchmarking test) having a 2µm radius diamond stylus (60 deg. angle). As average of five surface roughness measurements were taken on the same coordinate, toward the aerodynamic flow (horizontal tracing) which is considered as a critical measurements and perpendicular to the aerodynamic flow (vertical tracing) on the convex surface of the blade at points approximately 100 mm from the leading blade edge and 75 mm in from the side (as per conventional practice). A single blade from each compartment was measured. Both blades were separately identified as: Blade S5-1 and Blade S5-2. Blade S5-1 was super-polished using ARF compound and Blade S5-2 was super-polished using FC120 compound.

11.5.2 Results and discussion

Figure 11-15 shows the horizontal surface roughness measurements by means of Taylor-Hobson and Mitutoyo Surftest SJ401of fan blade (S5-1) processed by glass finishing media. Figure 11-16 shows the horizontal surface roughness measurements by means of Taylor-Hobson and Mitutoyo Surftest SJ401of fan blade S5-2 processed by glass finishing media. The error bar presented in each measurement explains the surface roughness boundary at this point. The results of surface roughness in both cases demonstrated that the ARF compound was more suitable in the super-polishing process with glass media, the Ra reduces to 0.43µm and 0.55 µm with ARF, and FC120, respectively within 120min of processing cycle.

The glass media is shown to reduce the roughness value Ra from the start value of approximately 1.5 µm to a value of approximately 1.00 µm in the period between 30 and 60 minutes in almost all cases using either measurement instrument. In the case of one fan blade a value of Ra = 0.42 µm was obtained after 60 minutes using Mitutoyo Surftest SJ401. This is the only measurement in tolerance up to this time and the distribution of results was consequently relatively wide.

After 90 minutes of polishing one third of measurements from the Mitutoyo instrument are within tolerance and the remaining values close to that threshold. The measurements from the Taylor Hobson hand held are not as close to the target value. This infers that the glass media is reducing surface peak heights more readily than is suggested by the Taylor Hobson instrument.

After a period of 120 minutes, all measurements from the Mitutoyo instrument were within target tolerance. No measurements within tolerance were recorded with the Taylor Hobson instrument. In many cases, the latter results obtained with the Taylor Hobson hand held had a wider distribution than those obtained from the Mitutoyo.

Calibration of each instrument was undertaken. A further comparative measurement was taken using a metrology 'Standard'. Each instrument was determined to be measuring and functioning correctly. It is important to note that the calibration 'Standard' was an engineered flat unlike the convex surface the Taylor Hobson instrument is challenged to measure. The Mitutoyo is designed to measure all types of surface (flat or curved) using compensatory software (skid bias). No discernible difference in visual appearance or process performance was identified for either of the fluid compounds.

Figure 11-17 shows a comparison of horizontal surface roughness measurements (Mitutoyo Surftest SJ401) of fan blade S5-1 using Finishing media, and Plastic media. As displayed, the thermally treated recycled glass (Finishing media) has a demonstrated efficiency in delivering target performance in super-polishing of fan blades.

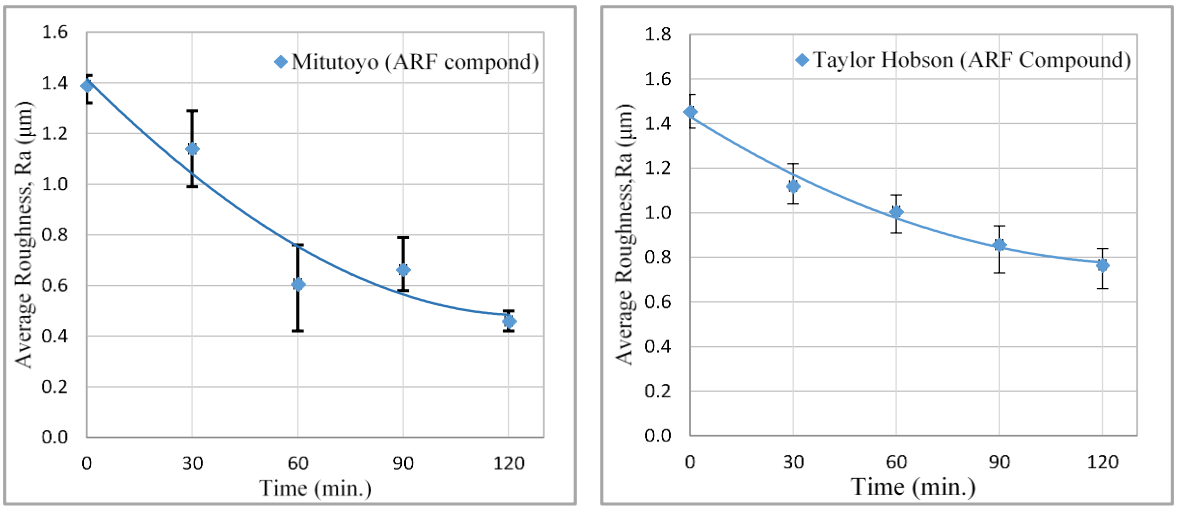

(a) (b)

Figure 11-15 Horizontal surface roughness measurements of fan blades S5-1 using a) Mitutoyo Surftest SJ401 and b) Taylor-Hobson instruments

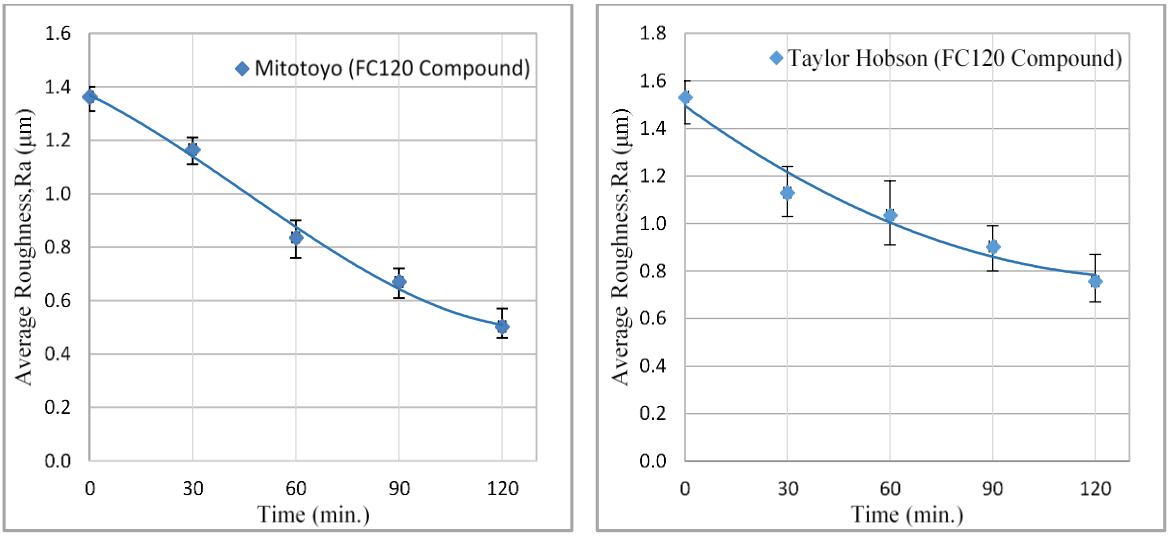

(a) (b)

Figure 11-16 Horizontal surface roughness measurements of fan blades S5-2 using a) Mitutoyo Surftest SJ401 and b) Taylor-Hobson instruments

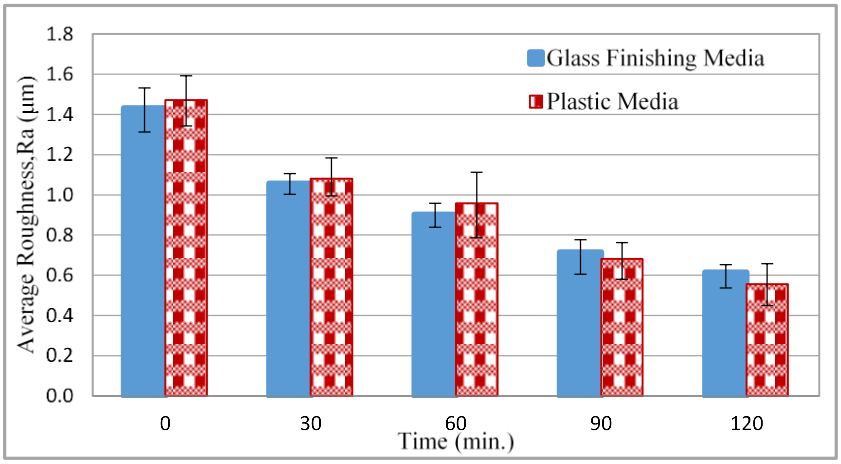

Figure 11-17 Comparison of horizontal surface roughness measurements (Mitutoyo Surftest SJ401) of fan blade S5-1 using Finishing media, and Plastic media

11.6 Environmental credentials of glass media

Beyond the scope of these tests are issues associated with environmental / sustainable technologies and process economics. The environmental credentials of plastic media and its user friendliness are not as strong as for glass, as it produces unpleasant odour and a flocculated foam-like waste that is difficult to treat and separate machined metals form. It also has a tendency to put a thin film on the media, machine tool, and equipment. Figure 11-18 shows a series of photographs of the resin foam.

The environmental credentials of the glass media are very much more favourable than plastic or ceramic bonded media. It is a wholly recycled product and the waste is in itself again recyclable, a further benefit identified by users during the experimental work related to the effluent. The effluent is essentially the dosed compound (3 per cent with water) and machined material. In the case of glass the effluent settled after a short period, typically, 2 to 3 minutes, and the residues were observed to settle and sink to the bottom of the container. This allowed for the ready separation of the compound for re-use. Analysis of the compound following separation in this manner identified that the dilution remained constant, the fluid was re-usable, and lubrication properties were unaffected.

Liquid effluent (plastic media)

effluent (plastic media)

dry solid from effluent

Effluent produced from glass media

Figure 11-18 Photographs of the resin foam (Effluent) observed during on site trials at Vibraglaz

11.7 Comparison results from on-site production test (Finishing Technique Ltd.) of spindle finishing (Drag, and Stream) and Centrifugal disk finishing processes using conventional abrasive granulate (Plastic and Ceramic) media.

The experimental analyses were carried out on the comparison between different spindle finishing techniques (drag and stream) and centrifugal disc finishing processes. Automotive workpiece parts materials (CK 60) were used in this investigation. The liquid compound SC15 was used for the tests. The proposed techniques were compared according to better surface finish achievable at constant processing time interval (0, 5, 10, 20 and 30) min. The experimental parameters were summarized in Table 11-1. Two different media were used during the finishing process plastic (OTEC DS) and ceramic (OTEC KM10 and KXMA24). The finishing process involved preloading media inside the chambers. The experimental tests that involves drag finishing were performed by setting the head speed at 50 rpm, and varying the spindle speed over the values of 20, 40, and 80 rpm. In the case of stream finishing, the experimental tests were performed by setting the spindle speed at 30 rpm, and changing bowl speed over the values of 20,40,60 rpm. The position of the workpiece in the bowl was selected carefully at the maximum stream flow region. In both cases full immersion of the workpieces were employed to ensure better performance results. Based on the workpiece geometry, the angled head was selected to be zero in all operation processes in order to ensure optimal contact between the media and workpiece.

The experimental tests related to the centrifugal disc finishing, were performed by varying the rotating speed within the values of (150, 200, 250) rpm. The surface roughness of the workpieces was inspected by tracing the surface using a Talysurf surface instrument at several positions along the surface before and after finishing processes. Three surface roughness measurements were performed on the workpiece surface at each time interval, the average of the group results were presented in this study.

Table 11-1 Overall machining parameters

Drag Finishing	
Main head speed (rpm)	50
Spindle speed (rpm)	20, 40, 80
Processing time (min)	5, 10, 20, 30
Immersion depth (mm)	300 / full immersion depth
Angled head (degree)	0
Media	Plastic KM10, Ceramic KXMA24
Compound	SC15
Dosing (%)	3.9
Stream Finishing	
Spindle speed (rpm)	30
Bowl speed (rpm)	20, 40, 60
Processing time (min)	5, 10, 20, 30
Immersion depth (mm)	300 / full immersion depth
Angled head (degree)	0
Media	Plastic KM10, Ceramic KXMA24
Compound	SC15
Dosing (%)	3.9
Centrifugal Finishing	
Disc speed (rpm)	150, 200, 250
Processing time (min)	5, 10, 20, 30
Media	Plastic KM10, Ceramic KXMA24
Compound	SC15
Dosing (%)	1

11.7.1 Surface roughness results and discussion

The results of comparative evaluation between three advanced finishing process techniques (drag, stream, and centrifugal) were summarized in Figures 11-19, 11-20, and 11-21, which provides the surface roughness values in different steps of the manufacturing process.

The finishing processes improved the starting workpiece morphology by progressively cutting the peaks and obtaining a smooth surface based on the setting of the operational parameters. The surface roughness profile shows that the valley surfaces remains not

influenced by the finishing process, this may be attributed to the media size, which cannot reach these regions.

Figure 11-19 (a, b) shows the comparison of surface roughness as a function of the processing time of the drag finishing process over a range of spindle speeds using plastic and ceramic media, respectively. It is clearly noticed, the increased spindle head speed reduces the average surface roughness over the processing time regardless of the abrasive tool. In the case of plastic abrasive media, the Ra decreases to 0.64 μm after 30min. of the machining process using spindle speed rotation of 20 rpm and to approximately (0.39, and 0.19) μm for the spindle speed rotation of (40, and 80) rpm, respectively. The ceramic media follow the same scenario that the Ra decreases to about 0.88 μm after 30min. of the machining process using spindle speed rotation of 20 rpm and to approximately (0.76, and 0.54) by means of the spindle speed rotation of (40, and 80) rpm, respectively.

These results also show that the type of the abrasive granulate (media) influences the performance of the drag finishing technology. The ceramic media reduces the Ra value to 30% relative to the initial surface roughness after 5min machining process with 40 rpm spindle rotation speed, while plastic media reduces the value to about 23%. This observation suggested that the ceramic media can be used as pre-finishing tool (cutting tool) after that plastic media will employed for the super finishing process.

Figure 11-20 (a, b) shows the comparison of surface roughness as a function of the processing time of the stream finishing process over a range of bowl speeds and constant spindle speed using plastic and ceramic media, respectively.

The results demonstrated that the increased bowl speed reduces the average surface roughness over the processing time. Using the plastic media, Ra decreases to about 0.98 μm after 30min. of the machining process using bowl speed rotation of 20 rpm and to approximately 0.49 μm, and 0.35 μm for the bowl speed rotation of 40 rpm, and 60 rpm, respectively. In contrast, the ceramic media bring down the Ra to about (1.13, 1.04, and 0.97) μm by means of the bowl speed rotation of (20, 40, 60) rpm, respectively. In the stream finishing process, the results suggested that the plastic media is the more powerful finishing tool in all steps of the manufacturing process compared with ceramic media.

The outcomes from the drag and stream finishing processes suggested that the higher the pressure exerted by the media on the parts resulting from increases in rotational speed, the faster the media polishes the parts, the faster the desired finishing surface results can be

achieved. A multi-stage finishing process after machining is required to achieve design surface roughness starting with aggressive surface grinding using ceramic media, surface smoothing and high-gloss polishing with plastic media.

The centrifugal disc finishing process shows lowest performance capability in terms of finishing surfaces compared with the drag and stream finishing processes. Figure 11-21 (a, b) shows the comparison of surface roughness as a function of the processing time of the centrifugal disc finishing process over a range of disc speeds using plastic and ceramic media, respectively. After 30 min processing time, the plastic media decreases the Ra to about (1.3, 1.19, and 1.03) µm using the rotation speed of (150, 200, 250) rpm respectively, while the ceramic media decreases Ra to about (1.35, 1.25, and 1.17) µm values by mean of (150, 200, 250) rpm rotation speed. The results also shows inconsistency and non-repeatable over machining process. This may attributed to the fact that the parts are free-floating in the media, which increases the opportunity of part-on-part contact and, therefore increased nicking or marring of the finish surface. However, the results suggested that the drag finishing process is more efficient by enhancing the surface roughness followed by stream finishing and then centrifugal disc finishing process.

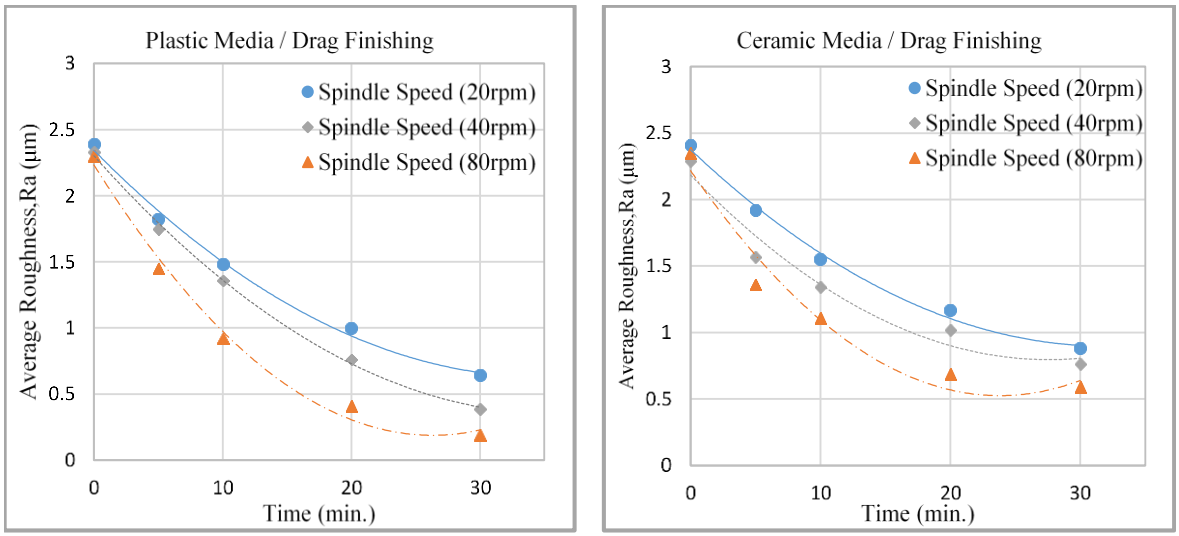

Figure 11-19 Comparison of surface roughness as a function of processing time of drag finishing process over a range of spindle speed using a) Plastic Media, b) Ceramic Media

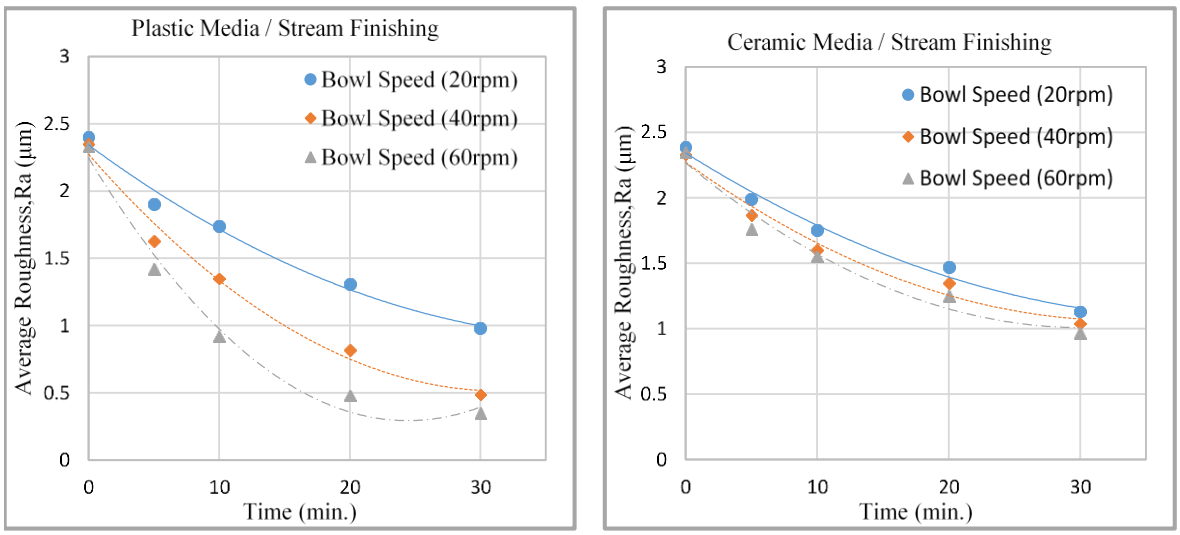

Figure 11-20 Comparison of surface roughness as a function of processing time of stream finishing process over a range of bowl speed using a) Plastic Media, b) Ceramic Media

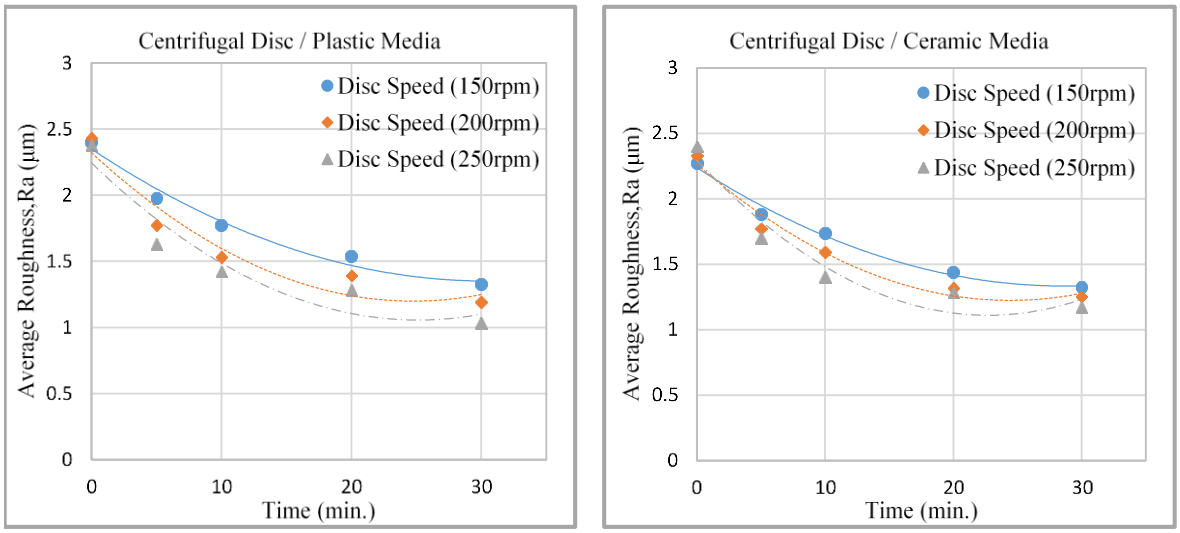

Figure 11-21 Comparison of surface roughness as a function of processing time of centrifugal disc finishing process over a range of disc speed using a) Plastic Media, b) Ceramic Media

11.8 Comparison results from on-site production test (Finishing Technique Ltd.) of Drag and Stream finishing processes using advanced workpiece material systems (M2, CPM10V, EN31, and Inconel 718).

Performance analyses were carried out on the comparison between drag, and stream super-finishing processes of advanced material systems such as M2 (Molybdenum High Speed Tool Steel) , CPM10V (Powder Metal Tool Steel**)**, EN31 (High Carbon Alloy tool steel) , and Inconel 718.

Such material systems are difficult to ground with a conventional grinding wheel because of the high degree of hardness with compressive strength and high wear with abrasion resistance .The experiments were performed at constant processing time intervals (0, 10, 20, and 30) min. to measure the percentage decreases in the average surface roughness. Plastic media (OTEC DS) and liquid compound FC120 were used in the tests. The experimental tests that involved drag finishing were performed by setting the main head speed at 50 rpm, and spindle speed at 60 rpm. In the case of stream finishing, the experimental tests were performed by setting the spindle speed at 20 rpm and bowl speed at 60 rpm. The workpieces were positioned at maximum immersion depth with zero angled head.

The surface roughness of the workpieces was inspected by tracing the surface using a Talysurf surface instrument at several positions along the surface before and after the finishing processes. Three surface roughness measurements were performed on each workpiece material at each time interval, the bar codes show the average of the group results were presented in this study.

Figure 11-22 shows the comparison of the percentage decrease in surface roughness relative to the initial surface roughness as a function of the cycle time of the drag finishing process over four material systems (M2, CPM10V, EN31, and Inconel 718). The percentage decrease in the surface roughness for a set of material systems does not linearly depend on initial workpiece surface roughness and processing time. The results proposed that the percentage decrease in surface roughness increases with processing time but at different rates. The percentage decreases in surface roughness relative to the initial surface roughness of M2, CPM10V, EN31, and Inconel 718 at the maximum processing time of 30 min. were 85.7, 78.9, 95.5, and 90.6, respectively. Figure 11-23 shows the comparison of the percentage decrease in surface roughness relative to the initial surface roughness as a function of the processing time of the stream finishing process over four material systems (M2, CPM10V, EN31, and Inconel 718). The percentage decreases in surface roughness relative to the initial surface roughness of M2, CPM10V, EN31, and Inconel 718 at the maximum processing time of 30 min. were 86.5, 75, 87.4, and 88.8, respectively. It is clearly noticed that the rate at which surface roughness decreases at the maximum cycle time is related to the material hardness and abrasion resistance. A three-dimensional optical profiler instrument (Bruker) was used to investigate the morphology of the specimen before and after the machining process.

The (Bruker) is a good tool for characterizing surface height variations and quantifying the amplitude of peaks and valleys (roughness profile) resulting from the machining process. Figure 11-24 shows an example of the 2-D, and 3-D evaluation maps of (CPM10V) workpiece morphology (which is considered as a harder material among the selected material systems) using the drag finishing process. Figure 11-25 shows an example of the 2-D, and 3-D maps assessment of (CPM10V) workpiece morphology using the stream finishing process. The 3-D maps were performed before and after 30 min of finishing processes. The results demonstrated that, after 10 min. the scratches grooves of the workpieces processed (M2, CPM10V, EN31, and Inconel 718) using drag and stream finishing are very thin and completely disappear after 30min. These results agreed with the results in Figures 11-22, and 11-23. This suggests that, the drag and stream finishing process is a suitable finishing process for high abrasion resistance materials. However, low energy requirements and rapid operation processes make these technologies industrially sustainable and promising in several manufacturing domains where the highest quality and performance are critical requirements.

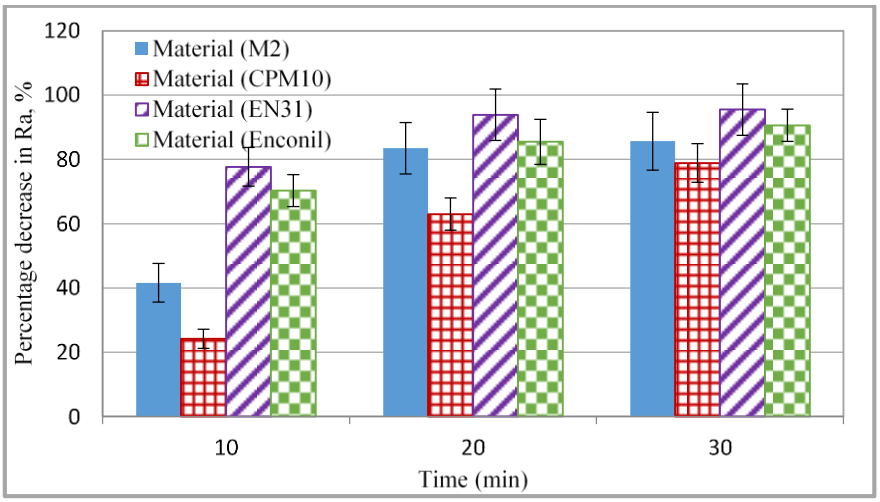

Figure 11-22 Comparison of percentage decrease in average surface roughness relative to the initial surface roughness of drag finishing process

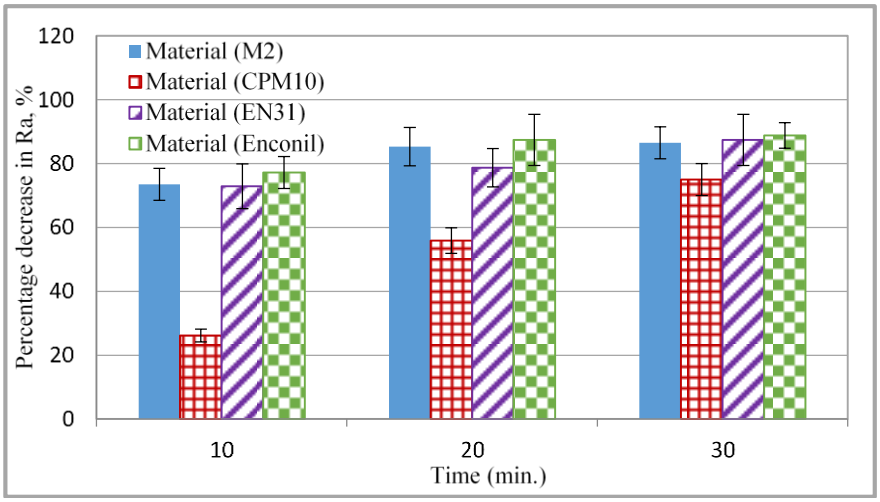

Figure 11-23 Comparison of percentage decrease in average surface roughness relative to the initial surface roughness of stream finishing process

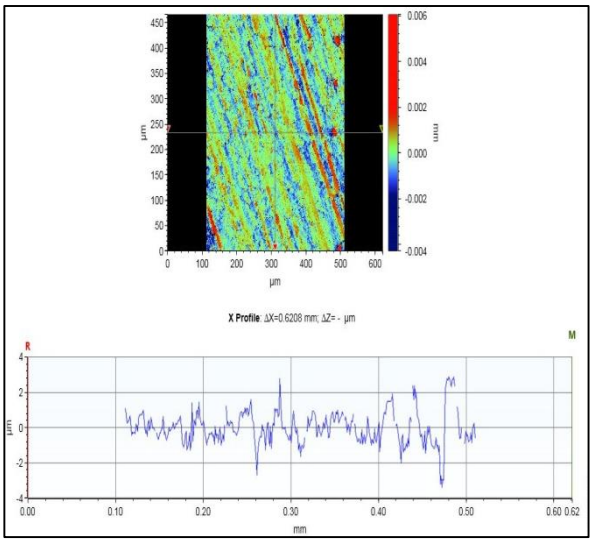

2-D map and roughness profile before finishig process

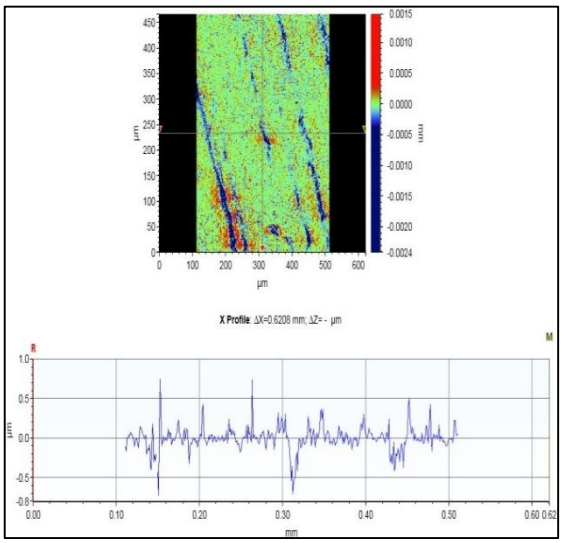

2-D map and roughness profile after 30 min of processing

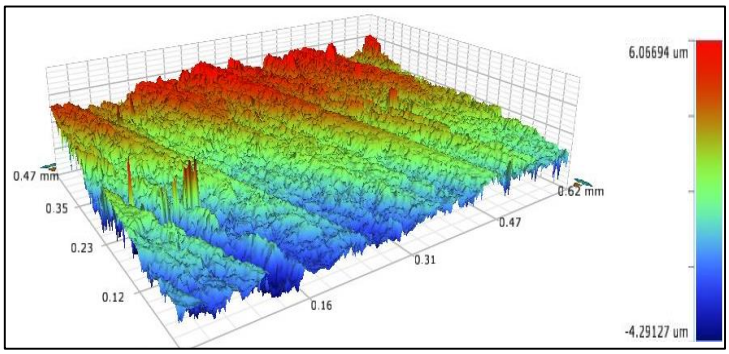

3-D map before finishing process

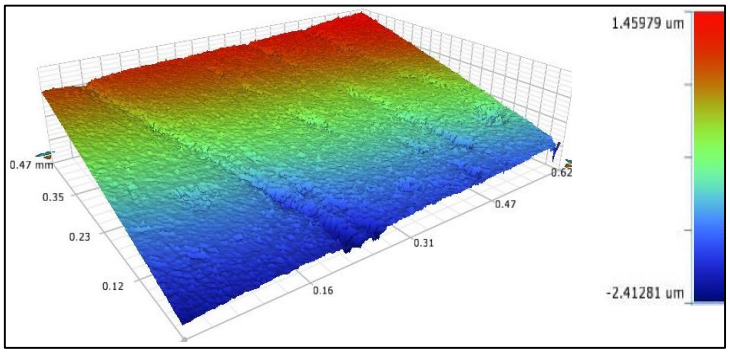

3-D map after 30 min of processing time

Figure 11-24 2-D, and 3-D maps assessment of (CPM10V) workpiece morphology using drag finishing process.

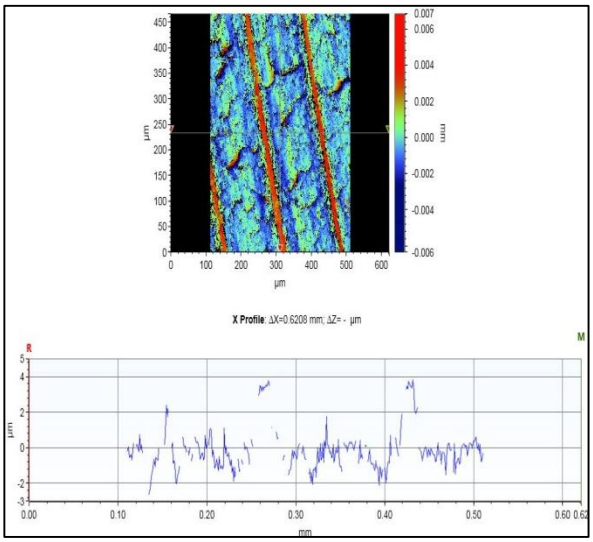

2-D map and roughness profile before finishig process

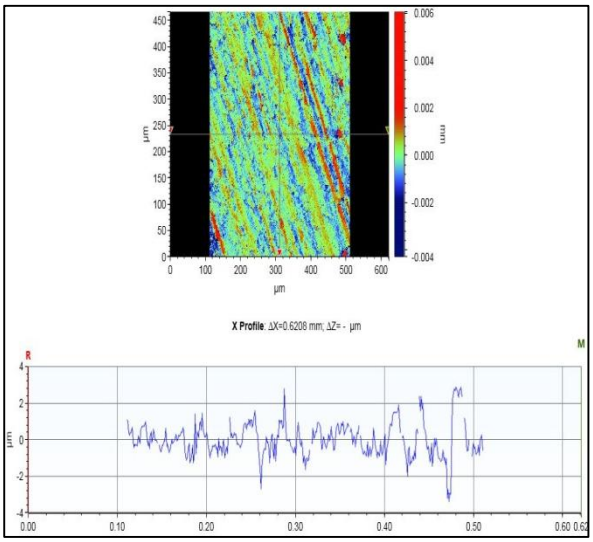

2-D map and roughness profile after 30 min of processing time

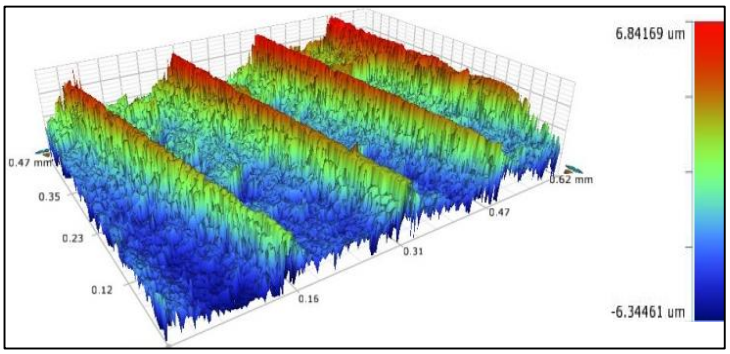

3-D map before finishing process

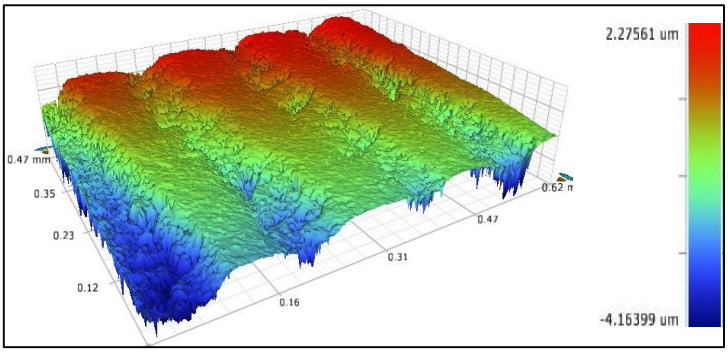

3-D map after 30 min of processing time

Figure 11-25 2-D, and 3-D maps assessment of (CPM10V) workpiece morphology using stream finishing process.

11.9 Concluding Discussion

The performance of the newly developed thermally treated glass as a vibratory mass finishing media were investigated. Machining tests compared the new media against benchmark media, namely conventional plastic (polymer) and ceramic.

It is noted from the results that the thermally treated glass media (referred to as: Finishing media, General purpose media and Cutting media) performed well on most occasions. The results displayed promising evidence that the thermally treated glass media has capability as an environmentally positive new choice as a vibratory deburring media. The glass cutting media and glass finishing media demonstrate their competitive potential to outperform their predecessors. In the case of comparable study of the glass media against conventional polyester bonded media (pink plastic media) the performance of the glass media matched that of the polyester bonded media with the stated work material. This informs us that the hardness and cutting ability of the glass are suited to the application. It was observed throughout the experiments that the resulting part brightness (visual assessment) matched that of the polyester bonded media.

The performance test from on-site simulated production tests (Rolls Royce) of the vibratory super-finishing process using thermally treated glass (Finishing media) and conventional (Plastic media) on turbine fan blades has been established. The thermally treated recycled glass (Finishing media) has demonstrated efficiency in delivering target performance in super-polishing of fan blades.

Furthermore, the described function of the plastic media make it more suited to pre-plated, super-finishing, polishing and smoothing applications, and also for usage on soft materials and fragile parts. However, the environmental credentials of plastic media and its user friendliness are not as strong as those for glass, as it produces unpleasant odour and a flocculated foam-like waste that is difficult to treat and separate machined metals from. It also has a tendency to put a thin film on the media, machine tool and equipment. The environmental credentials of the glass media are very much more favourable than those of the plastic or ceramic bonded media. It is a wholly recycled product and the waste is in itself again recyclable.

Due to the brittle behaviour of the glass media, there may be a few challengs using the thermally treated glass media with heavy load work material. The load may crush some media underneath it and may break those media leaving some shards and introduce them into the system. These shards when introduced and rotated together with media/ workpiece, could cause undesired damage on the surface of the workpiece. As consequence, a new design of work holding (jig arrangement) was performed in [CHAPTER 12] for the vibratory mass finishing system in order to hold the part in free rotation within the media whilst reducing or removing the risk of shard generation.

The comparison results from on-site production test (Finishing Technique Ltd.) of spindle finishing (Drag, and Stream) and Centrifugal disk finishing processes using conventional abrasive granulate (Plastic and Ceramic) media on the auotomative workpiece were established. The results suggested that the drag finishing process is more efficient by enhancing the surface roughness followed by stream finishing and then centrifugal disc finishing process.

The abrasion potential of the drag and stream finishing processes is high, especially when operated at the fastest spindle speed 80 rpm and bowl speed 60 rpm, respectively. This may be attributed to the different hydrodynamic behaviours of the abrasive media in the processing medium. The impacts with abrasive media take place at high speed, which is generated from the difference between the workpiece rotating speed and the quasi-static abrasive media for the drag finishing process and from the difference between the workpiece rotation speed and abrasive media rotation flow for the stream finishing process. In the centrifugal finishing process, the workpiece is immersed into the abrasive media.

The difference in the size, shape, and density of the abrasive media and the workpiece generates the relative motion between them. Hashimoto and DeBra (1996) proposed that, despite the high rotation speed of the disc in the centrifugal finishing process 250 rpm, the relative speeds between the abrasive media and the workpiece are expected to be lower because it only comes from the resultant difference in the system force acting on the abrasive medium and on the heavier and larger workpiece. However, the impact speed together with the mass of abrasive media developed kinetic energy which is released onto the workpiece surface. Based on the abrasive media type, the abrasion potential of different technologies is controlled by the impact speeds between the abrasive media and the workpiece. Thus, higher impact speeds result in higher energy releases after each impact of the abrasive media onto the workpiece. This higher energy should be accurately controlled to avoid problems such as the over-finishing of the workpiece surface. This over-finising may cause a failure of the workpiece due to the massive surface erosion.

The comparison results from the on-site production test (Finishing Technique Ltd.) of the Drag and Stream finishing proceses using advanced workpiece material systems (M2, CPM10V, EN31, and Inconel 718) were established. The results demonstrated that, the drag and stream finishing processes are suitable finishing processes for high abrasion resistance materials. The energy of such kind of finishing process which is converted to strain energy once impacted on the workpiece surface, is the key to the mass finishing process. However, the strain energy release must be high enough in order to achieve a critical value equal to the resistancce of crack growth, thus givinig increase the surface plastic deformations by micro-cutting.

In conclusion, lack of residual after machining , low energy requirements, and quick finishing process make the Fixture process industrially sustainable and promissing in different manufacturing areas where the high quality and performance are crucial requirements.

11.10 References

Barletta, M. (2006). "A new technology in surface finishing: fluidized bed machining (FBM) of aluminium alloys." Journal of materials processing technology **173**(2): 157-165.

Benjarungroj, P. (2012). Investigation of Sustainable Recycled/Recycable Materials for Application in Mass Finishing and Appriasive Processes. MPhil Thesis, Liverpool John Moores University.

Brust, P. C. (1997). "Surface improvement by vibratory cascade finishing process." Transactions-north american manufacturing research institution of sme: 93-98.

Cariapa, V., H. Park, J. Kim, C. Cheng and A. Evaristo (2008). "Development of a metal removal model using spherical ceramic media in a centrifugal disk mass finishing machine." The International Journal of Advanced Manufacturing Technology **39**(1-2): 92-106.

Coating and Adhesives Group. (2014). "Round bowl vibrotary deburring machine , http://www.partsfinishing.com/index.php " Retrieved 16/07, 2014.

Davidson, D. (1997). "Mass finishing processes." Metal Finishing(USA) **95**(1): 105-106.

Davidson, D. (2003). Developments in Mass Finishing Technology. Metal Finishing, DeburringlSurface Finishing Specialist.

Davidson, D. A. (2003). "Developments in mass finishing technology." Metal finishing **101**(7): 49-56.

Davidson, D. A. (2005). "Surface finishing reaches new heights: Mass media finishing techniques can improve aircraft part performance and service life." Metal finishing **103**(3): 25-28.

Davidson, D. A. (2006). "Precision finishing processes in centrifugal barrel equipment: methods promise faster cycling in select applications." Metal finishing **104**(7): 65-67.

Davidson, D. A. (2007). "Green mass finishing with dry abrasive and polishing media: novel finishing process allows refined surface edge effects while avoiding conventional wet-waste discharge." Metal finishing **105**(5): 45-48.

Dennis V. De Pellegrin∗, Gwidon W. Stachowiak (2002). “Assessing the role of particle shape and scale in abrasion using ‘sharpness analysis’Part II. Technique evaluation”. Wear 253 1026–1034

Domblesky, J., V. Cariapa and R. Evans (2003). "Investigation of vibratory bowl finishing." International journal of production research **41**(16): 3943-3953.

Domblesky, J., R. Evans and V. Cariapa (2004). "Material removal model for vibratory finishing." International journal of production research **42**(5): 1029-1041.

Gillespie, L. (2006). Mass finishing handbook, Industrial Press.

Gillespie, L. (2006). Mass Finishing Handbook New York, Industerial Press Inc.

Hashimoto, F. and D. DeBra (1996). "Modelling and optimization of vibratory finishing process." CIRP Annals-Manufacturing Technology **45**(1): 303-306.

Mike Morgan, M. J., Benjiarungroj P., Steve Vaughan. (2012). "Vibratory superpolishing of a ti alloy aerospace material with thermally treated recycled glass media." MANUFACTURING TECHNOLOGY **12**(12).

Moore M. A., Douthwaite R. M. (1976). "Plastic deformation below worn surfaces." Metallurgical Transactions A. 7(12):1833-1839.

Sankar, M. R., V. Jain and J. Ramkumar (2009). "Experimental investigations into rotating workpiece abrasive flow finishing." Wear **267**(1): 43-51.

Shaw, M. C. (1996). Principles of abrasive processing, Oxford University Press.

Telljohann, D. (2014). "Stream Finishing Process and Application, http://www.otec.de/ " Retrieved 10/07, 2014.

William, N. (2013). "Considerations Regarding the Proper Loading of Vibratory Finishing Bowls for Optimal Quality, Performance and Throughput Efficiency." NASF Surface Technology White Papers **78**(1): 1-13.

Zaki, N. (1992). "Mass finishing considerations for optimum productivity." Metal finishing **90**(7): 50-54.

CHAPTER TWELVE

JIG ARRANGEMENT ASSISTED VIBRATORY MASS FINISHING PROCESS

12.1 Introduction

This chapter is focussed on the vibratory trough process. In this process, work and abrasive media are free to vibrate in the chamber of the machine and variation in the cycle can be achieved through modification of vibration frequency or amplitude. This is generally achieved through varying spring stiffness or adjustment of weights supporting the central chamber. In the vibratory trough process, the media has been observed to follow an identifiable trajectory determined by process parameters and mass of media and parts. This implies variation in media velocity throughout its path and hence implicitly a variation in abrasive performance. The trough therefore has areas more efficient than others in terms of abrasive performance. However, given that parts are carried through these regions, many times it is reasonable to assume an average abrasive performance for a process cycle and this results in a finish that is similar about the entire part surface.

In the case of a heavy part, this arrangement is somewhat less effective due to the part not rotating as freely in the trough as a lighter part; or it may lodge or have motion that restrains it from free rotation. In addition, if the media used is aggressive, i.e. a cutting media as opposed to a polishing media, than the action of the machine vibration will serve to crush the part against the media and to hammer it against the wall of the trough. In the case of glass, this situation will produce small shards that may scratch or impair a fine surface finish (contribute against Ra).

As a consequence, a new design of work holding for the mass finishing system is proposed in order to hold the part in free rotation within the media whilst reducing or removing the risk of shard generation. This design has been developed to provide a readily constructed portable and low-cost solution in order to carry the parts horizontally within the trough while allowing for variation in immersion depth and variation in position throughout the longitudinal or transverse directions in the vibratory trough machine. This approach is suggested to be used with a jig arrangement for large components, especially for those parts used in the aerospace and automotive industries. It is also hypothesised that work holding will result in improved process efficiency and this is to be evaluated as part of the work.

12.2 Product design specification

The product design specification (PDS) is a statement of what the product is intended to do; it differs from the design brief as it goes further than just defining major goals and constraints. The PDS outlines precise limits for the full set of requirements in the product being designed, or in this case optimised. The following PDS requirements were taken into account during design of jig arrangement system:

1. Performance: A high-performance jig arrangement is the main objective. The system must be designed from high-quality material and that gives the opportunity for a long life warranty against manufacturing defects or wear.
2. Competitors: Product design should satisfy the requirements of competition, higher performance, and higher specification which costs less; these are extremely desirable attributes.
3. Environment: The environmental conditions such as temperature, humidity, and risk of corrosion vary depending on where the product will be used. Consideration should be given to the potential working environment.
4. Size: Sizes of all the fixtures shall comply with the Standards. System elements, which are designed to be a specific size, should comply with workpiece selection size.
5. Weight: Weight of the system should comply with desirable material, i.e. alloy steel, to prevent fatigue after long periods of use.
6. Materials: The jig arrangement system was manufactured from alloy steel material (DIN1.2714) , which has great hardness and strength. It provides high quality with lower cost. Its composition consists of elements that help to reduce wear; therefore, it is considered the appropriate material for the system.
7. Appearance: The appearance of the jig arrangement system should be acceptable and comply with the vibratory trough process in order to make sure that this system is capable of adapting in to different vibratory trough sizes.
8. Safety: The safety of the final product is the most important factor that engineering should focus on. The new design should be free from rough surfaces and harmless, safe in loading and unloading parts, and should be fit to meet the design purpose.
9. Quantity and manufacture: System assembly should be limited as much as possible so as to provide a cheaper and less complex system. The created system should be easy to manufacture by using simple operation techniques.

10. Design time constraints: The design time constraints are limited. A period has been assigned to carry out an analysis from initial the idea to solving existing problems up to production final design. Considerations such as time reduction in the system assembly with the vibratory mass finishing machine, loading and unloading workpiece should be considered in the engineering design.

12.3 Jig arrangement design

A vibratory trough machine and workpieces, such as a crankshaft, were identified for the new system. Selection of jig arrangement dimension depends on the height and width of the tub vibratory machine as well as workpiece dimensions. The 3-D jig arrangement design was performed using SolidWork. Figure 12-1 shows the jig arrangement system assembly fixed on the vibratory machine bed. As illustrated, the jig arrangement assembly consists of many sub-assemblies such as mainframe, workpiece-holding frame, adjustable frame, and adjustable block.

Figure 12-2 shows the jig arrangement components. As illustrated in the whole assembly system, the main frame 12-2 (a) is fixed on the machine bed through four legs. Figure 12-2 (b) shows the arrangement for the holding frame, which allows for the positioning of the workpiece horizontally and gives the free rotation by aid of bulk media circulation. This arrangement also provides the flexibility to change the immersion depth within the vibratory tub using equally spaced holes along the vertical direction of the workpiece holding arm as is shown in Figure 12-2 (c). This frame is bolted with two adjustable blocks Figure 12-2 (e), which gives the transverse movement for the workpiece within the tub along the adjustable frame as it shown in Figure 12-2 (d). Consequently, the workpiece can be located wherever necessary using an equally spaced hole along the transverse direction. The position of the workpiece in the longitudinal direction can be controlled by relocating the adjustable frame. The final stage is about bolting the adjustable frame with the mainframe using equally spaced holes along the longitudinal direction. Based on such design, the workpiece position can be adjusted in X, Y, and Z direction to achieve better performance results.

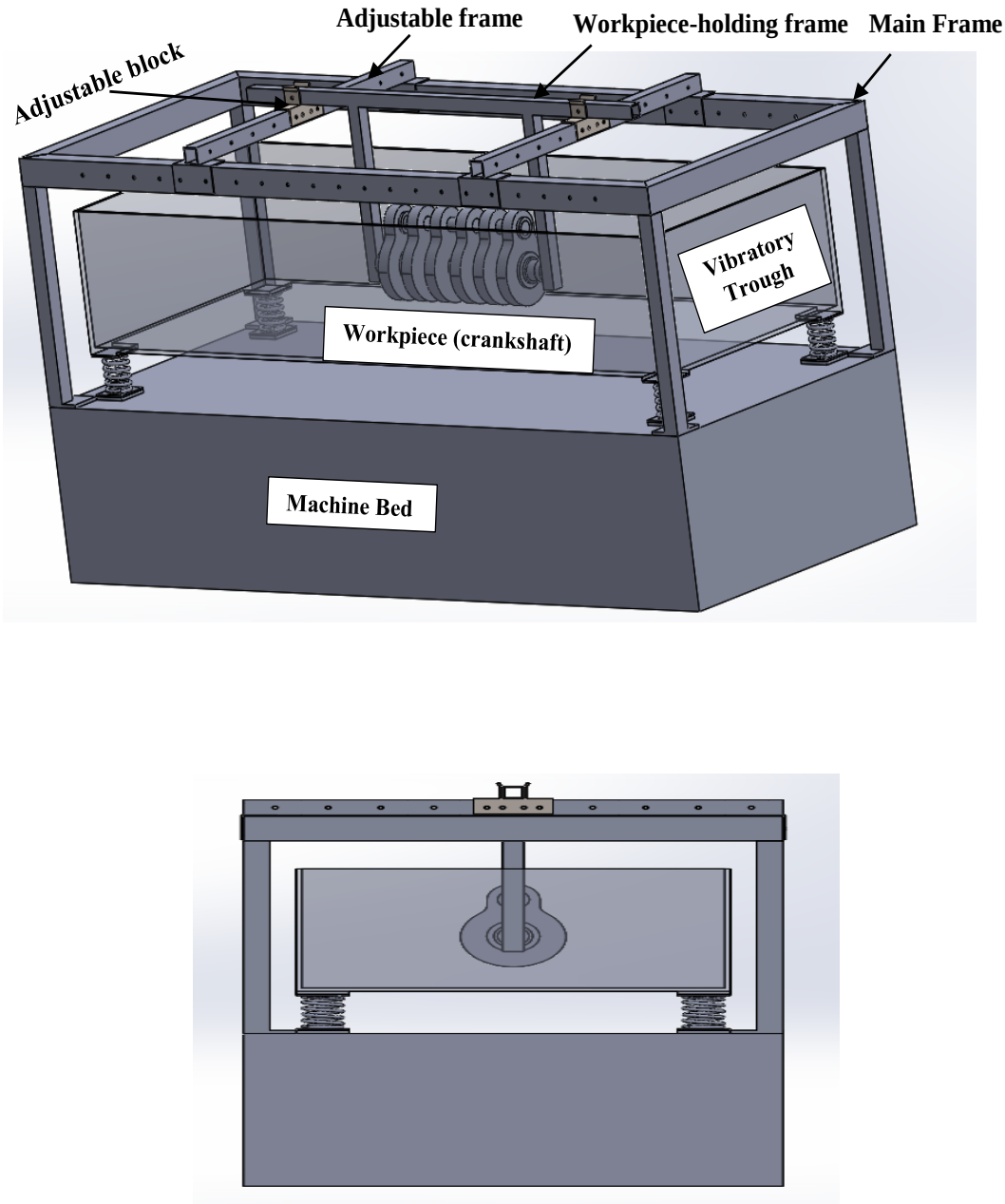

Figure 12-1 Jig arrangement system assembly fixed on the vibratory machine bed

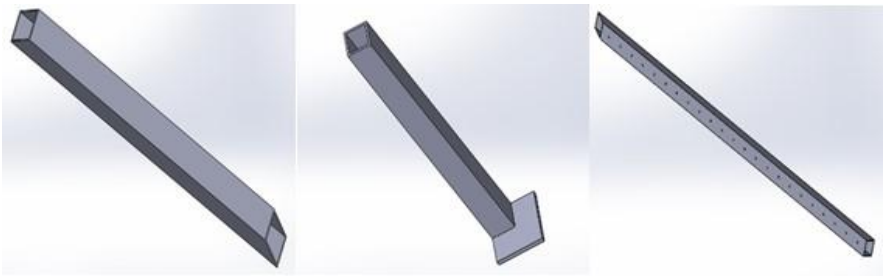

(a)
Main frame components

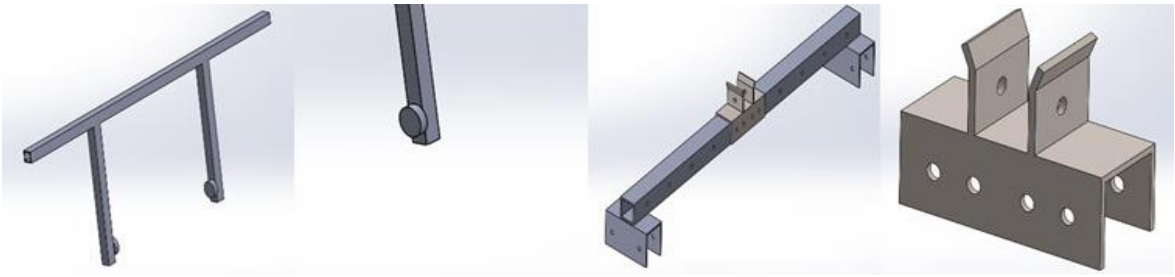

(b) Workpiece holding frame | (c) Holding arm | (d) Adjustable frame | (e) Adjustable block

Figure 12-2 Jig arrangement sub-assembly components

12.4 Structural analysis using SolidWork FEM

Finite Element Modelling was employed using SolidWork to analyse structural failure and to determine design modifications to satisfy new requirements. Structural analysis is the most common application in FEM and is frequently applied to the analysis of bridges, buildings, and mechanical structures and components such as: machine parts, tools and structures. By using FEM it is easy to predict failure due to unknown stress by identifying the areas with high stress concentration as a result of external load. This method helps in finding the linear stress analysis for engineers to validate the design product in quality, performance, and safety measures. Consequently, the SolidWorks simulations help in reducing the need for reworks, delays, saving time as well as development costs.

FEM simulation of the jig arrangement was employed to compute stresses and deformation under three basic assumptions: Firstly, the parts and /or assembly is subjected to load, which causes deformation by means of rotation and displacement. Secondly, the system loading in the numerical simulation is static which ignores the inertia and remains constant

all the time. Thirdly, the numerical simulation follows Hookes law, which maintains the stress strain relationship.

The stress and deformation analyses simulations consist of two stages, pre-processing and post-processing. In the pre-processing stage, the material properties of Alloy Steel were assigned to the jig arrangement parts. The boundary condition of a rigid fixed body was applied on the mainframe legs as is shown in Figure 12-3. The predicted stress and deformation analyses were evaluated based on two numerical simulations: Firstly, an external normal force was applied to the workpiece body (crankshaft; DIN 1.2343, HRC 45), in this case a parametric study of five different forces (20, 30,40,50,60) N was employed to investigate the performance of the jig arrangement over various loads on the workpiece. Secondly, a rotational speed was applied to the workpiece (crankshaft) and keeping the whole assembly in a stationary position, in this case a parametric study of five different rotational speeds (5,10,20,30,40) rpm was employed to simulate different media circulatory bulk flows generated from various vibratory machining parameters (frequency and amplitude) and workpiece size.

FEM simulation of the jig arrangement was employed with a complex system of nodes, which make a grid called a mesh. A mesh is a programme consisting of material and structural properties, which shows how a structure responds to certain loading conditions. Nodes are located at a certain density through the workpiece and that depends on the stress level of the specific region. The regions that received a large amount of stress had high node density compared with other regions without stress. Figure 12-3 shows the mesh density distribution on the jig arrangement system. As displayed coarser mesh densities were applied during the first simulation run in order to identify the critical area, then the mesh densities were modified to fine mesh accordingly.

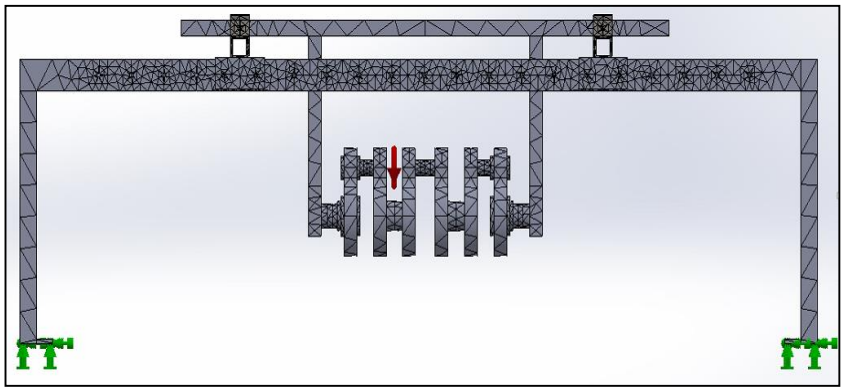

Figure 12-3 Mesh density distribution

12.5 Stress and deformation results

In this study, all frames were manufactured from square hollow section of 80×60×4 mm. This section was assumed to have uniform density with constant cross-section extrusion similar to that of the actual model. The resulting centre of mass is located at the centre of the cross section at the midway point of the square hollow block. 3-D stresses and strains build up in the jig arrangement body in many directions. The common way to explain multi-directional stresses is by summarizing them in an Equivalent stress, also known as the Von-Mises stress induced in the frame. The 3-D solid has six stress components of all sides. Sometimes, uniaxial stress test of material can be found experimentally. In that case, the combination of the six stress components can be summarized by a single equivalent stress corresponding to the real stress system. The safety factor is related to the mechanical properties of the structure parts. This factor can be calculated by the ratio of the maximum allowable stress (Yield strength) to the equivalent stress (Von Mises) under maximum load. The system deformation is the amount of displacement that the part undergoes due to the loading. In this study, the maximum allowable deflection was 10mm.

12.5.1 Stress and deflection generated from normal force

Figure 12-4 shows the Von Mises stress plot distribution of 30N force applied on the crankshaft (on all cam faces) which is represented by arrows in the horizontal direction. It is clearly noticed that the Von Mises stress increases in the holding frame structure. This may be attributed to the fact that this part works like a cantilever beam, loaded by two weights (crankshaft and holding arm) and also withstands the horizontal force on the crankshaft which represents the force action produced by media flow. The parametric study shows that increased force will lead to increasing stress of the holding frame structure. At the high force of 60N, high stress spots were most noticeable in the adjustable block at the section connected with the holding frame. Finer mesh was applied in these regions to investigate the stress level. The results demonstrated that no change in the Von Mises stresses were recognized. However, the parametric study over a series of numerical simulations proposed that the equivalent stress was below the allowable stress which suggested that the model is safe over a wide range of loads.

Figure 12-5 shows the maximum Von Mises stress obtained from the parametric study of different loads applied to the workpiece. As illustrated when the applied load increases, the maximum Von Mises stress increases. The predicted stress suggested that the maximum Von Mises stress was 30MPa at 20N force, this stress increased to 160MPa at 60N.

Figure 12-6 shows the strain rate distribution of 30N force applied on the workpiece. The strain rate measures the rate at which the distances of adjacent nodes change during the time in the neighbourhood of that point. It includes both the rate at which the material system is expanded or shrunk (expansion rate) and also the rate at which it is being deformed by shearing without changing its volume (shear rate). As displayed, the maximum strain rate of $5.100e^{-003}$ was observed in the region of holding frame. The parametric study shows that increased forces will lead to increasing the strain rates of the holding frame structure. In such cases the frame body nodes are slightly expanding but still in a rigid state.

Figure 12-7 shows the displacement plot distribution of 30N force applied on the workpiece. As illustrated in this plot, the maximum displacement of 0.065 mm was observed at the crankshaft near the points of applied force and slight displacement on the holding arm. This displacement is too small for the plastic deformation occurrence due to the high hardness property of the frame. The parametric study shows that increased forces will lead to increasing displacement of the crankshaft. However, the maximum displacement observed at maximum force was 8.5 mm, which is less than the maximum design deformation limit (10 mm).

Figure 12-8 show the maximum deflections obtained from the parametric study at different load. As illustrated when the applied load increases the maximum deflection increases. The numerical simulation suggested that the maximum deflection value is 1.5mm at 20N force; this value increases to 8.5mm at 60N. However, the parametric study suggested that the maximum deflection was below the design deflection which suggested that the model is safe over a wide range of loads

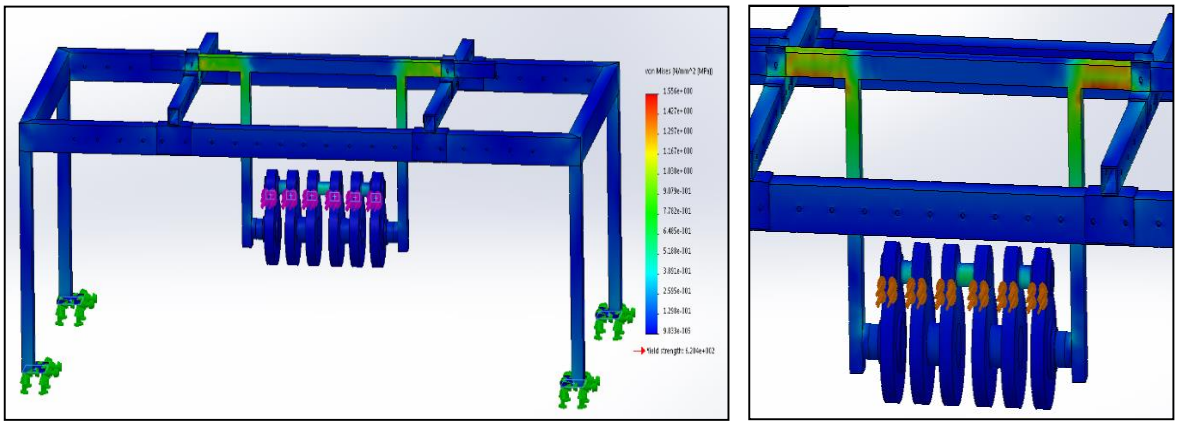

Figure 12-4 Von Mises Stress distribution of 30N force simulation

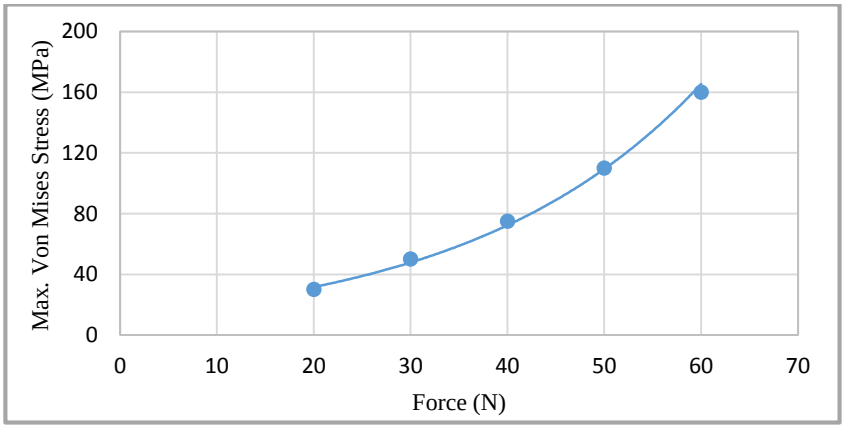

Figure 12-5 Relationship between maximum Von Mises stress and maximum force applied to the jig arrangement system

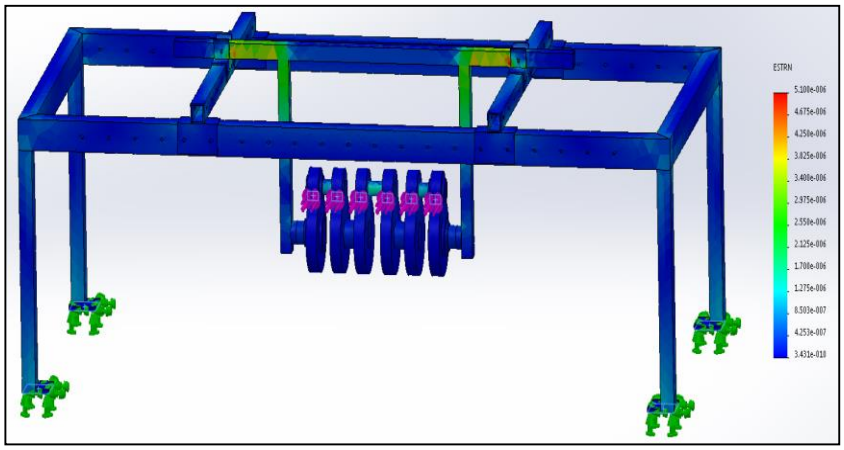

Figure 12-6 Strain distribution of 30N force simulation

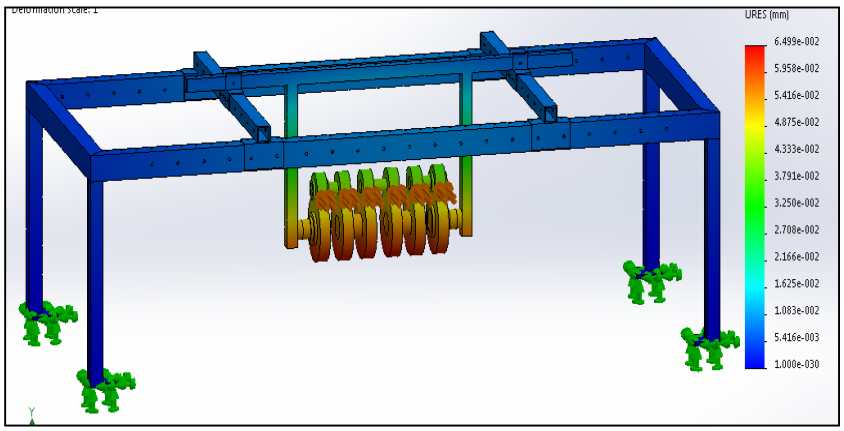

Figure 12-7 Displacement distribution of 30N force simulation

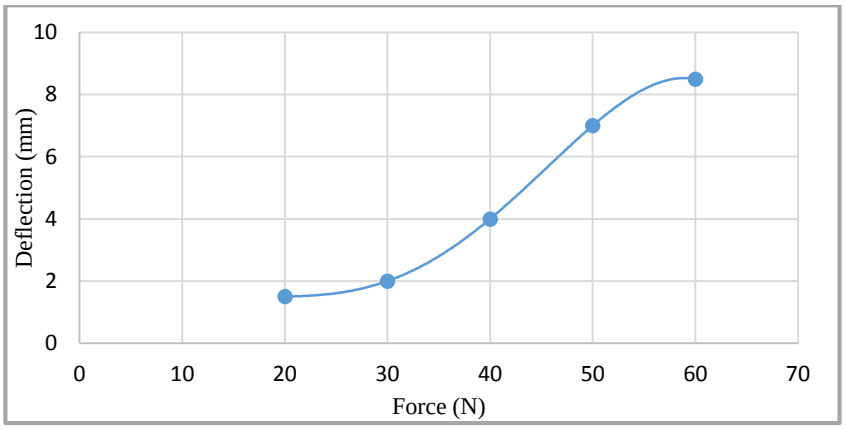

Figure 12-8 Relationship between maximum deflection and force applied on. the jig arrangement system

12.5.2 Stress and deflection generated from rotational force

Figure 12-9 shows the Von Mises stress plot distribution of 5 rad/sec rotational speed applied on the crankshaft. As displayed, the Von Mises stress increases in the holding frame structure. Lower stresses were observed on the main and adjustable frames. This may be attributed to the system vibration which was noticed during the rotational speed of heavy weight workpiece samples such as a crankshaft. Damping rubber bearings were used beneath the adjustable block to control and reduce the shock vibration and noise. The parametric study shows that increased forces will lead to increasing stresses of the holding and main frame structures.

Figure 12-10 shows the maximum Von Mises stress obtained from the parametric study of different specimen's rotational speed. As presented, this slightly increases of the predicted stress value of rotational speed between 5 to 20 rad/sec, this value increases significantly for rotational speed between 20 to 50 rad/sec.

Figure 12-11 shows the displacement plot distribution of 5 rad/sec rotational speed applied on the workpiece. As demonstrated in this plot, the maximum displacement of 1.24 mm was observed at the crankshaft and slight displacement of 0.66 mm on the holding arm and mainframe. The occurrence of such displacement did not produce plastic deformation due to the high hardness property of the frame. The parametric study shows that increased rotational speed will lead to increasing displacement of the main frame. However, maximum displacement achieved at maximum force was 6.6 mm.

Figure 12-12 shows the maximum deflections obtained at different rotational speeds. As illustrated, the applied rotational speed increases the maximum deflection. The numerical simulation suggested that the maximum deflection value is 1.24mm at 5 rad/sec force; this value increases to 7.98 mm at 50 rad/sec, which is still below the maximum deflection allowable of 10mm

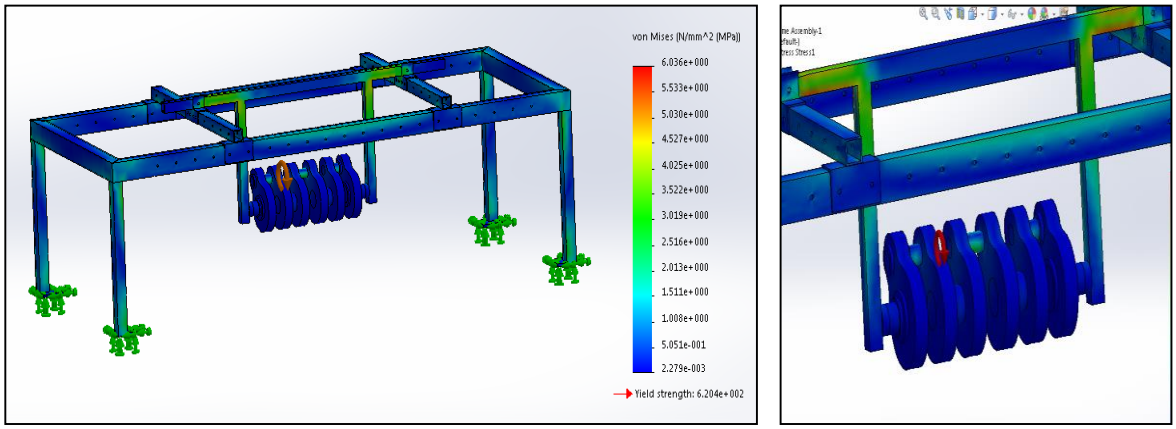

Figure 12-9 Von Mises Stress distribution of 5 rad/sec rotational speed simulation

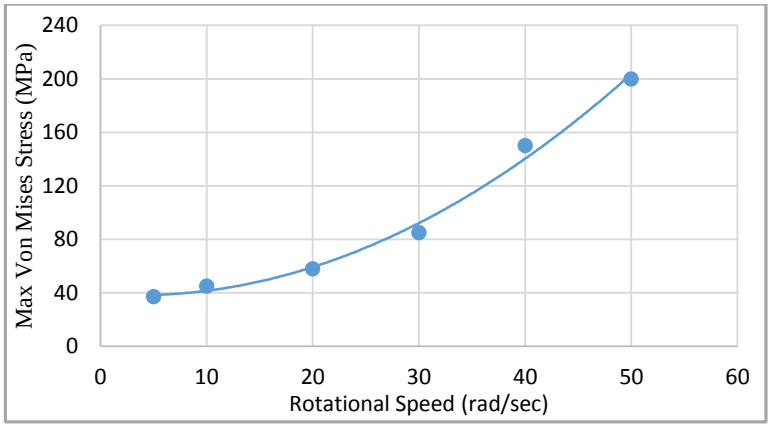

Figure 12-10 Relationship between maximum Von Mises stress and workpiece rotational speed of jig arrangement system

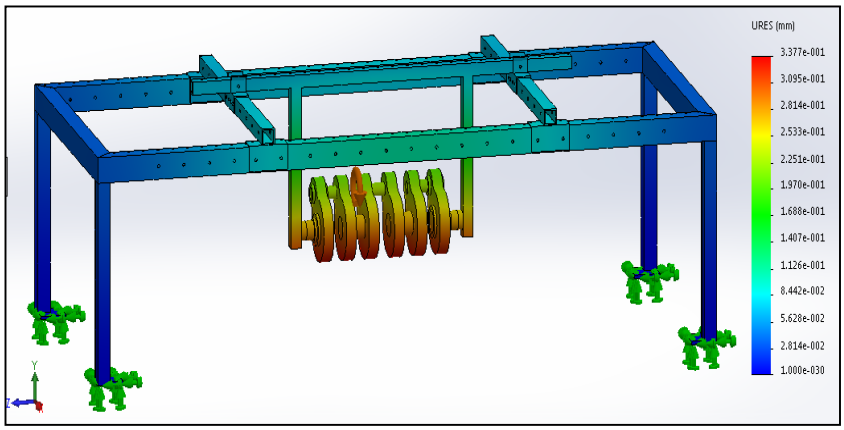

Figure 12-11 Displacement distribution of 5 rad/sec rotational speed simulation

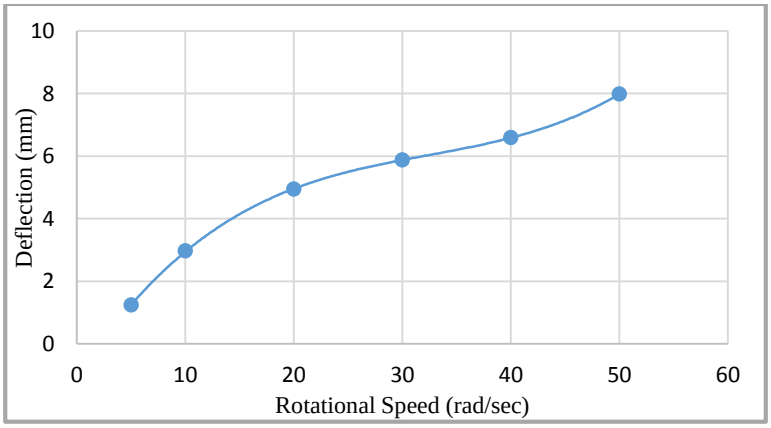

Figure 12-12 Relationship between maximum deflection and rotational speed of jig arrangement system

12.6 Comparison results from on-site production test of jigged and non-jigged vibratory super-finishing process using thermally treated glass (Finishing media) and conventional (Plastic media)

The jig arrangement design was made using a simple manufacturing process, thus fewer and cheaper machine parts are required. The dimensions of all the parts have been kept as simple as possible to ensure that the product design can be manufactured using simple processes such as cutting, turning, milling, etc. In addition, tolerance has been established to ensure all the parts and sub assembly units have the correct fit to simplify the assembly process and also to allow the new system to be suitable for a range of workpieces dimensions. A full set of engineering drawings were generated to facilitate manufacturing. The final jig arrangement system to assist the vibratory mass finishing process was manufactured at Vibraglaz Ltd. LJMU technical support and supervision was given during the fabrication process. Figure 12-13 shows the photographs of the jig arrangement system fixed on the vibratory mass finishing bed.

Figure 12-13 Jig arrangement system assists vibratory mass finishing process

On-site production tests were completed using a Vibraglaz vibratory trough machine. 750 Kg of conventional porcelain media with Rostler Keramo paste and liquid compound FC120 at dosing rate of 3 per cent were used for the tests. Machine parameters (vibration amplitude and frequency) were fixed as per common production practice. Two experiments were carried out on the crankshaft workpieces under the same environment, the first test was without jigging (freely rotation workpiece), and the second test was with the jig arrangement system.

The surface roughness of the workpieces was inspected by tracing the surface using a Talysurf surface instrument (Diamond stylus, with M-speed 0.5 mm/s, R-speed 1mm/s, distance 5 mm) at several positions along the surface. Three surface roughness measurements were performed at different time intervals, the average of the group results are presented in this study.

Figure 12-14 shows the average roughness comparison of jigged and non-jigged vibratory finishing process as a function of time using porcelain conventional media. The results demonstrated that the surface roughness improved continuously in both cases. The results shows that 25% improvement in Ra after (3.5 hrs.) with the non-jigged machining process, while 44.5% improvement in Ra after (3.5 hrs.) with the jigged machining process. Full machining cycles shows, 38.5% improvement in Ra after (7 hrs.) with the non-jigged process, whereas 62% improvement in Ra after (7 hrs.) with the jigged process. This suggested that the jigging process was successfully enhancing the machining performance by improving the surface roughness value.

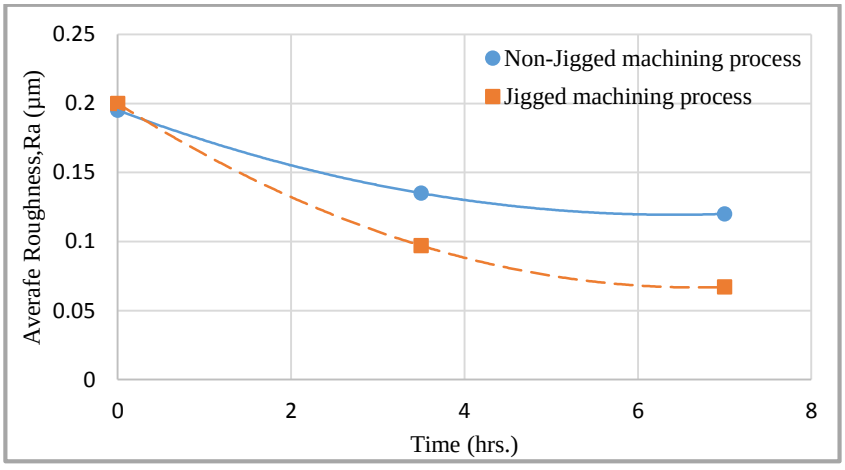

Figure 12-14 Comparison of average surface roughness of jigged and non-jigged assisted vibration finishing process as a function of time using conventional media

The on-site experiments were extended to complete the comparative study using Vibraglaz finishing media and conventional plastic media in the jigged vibration finishing process. The plastic media is commonly used throughout industry (aerospace and automotive) for general-purpose super-finishing processes. In this test, a liquid compound FC120 at dosing rate of 3 per cent was used. A cylindrical workpiece EN40B (45HRC) was employed. Three surface roughness measurements were taken at five different distances from the edge (40, 45, 50, 55, and 60) mm before and after machining at a particular time interval. The average of the group results are presented in this study. The total machining cycle setup is (120 min.). The workpieces were measured off-line at 30 min. time intervals. Figure 12-15 shows the average roughness comparison of the jigged vibration finishing process as a function of time using Vibraglaz finishing media and conventional polyester media. As displayed, the Vibraglaz finishing media achieved better surface roughness compared with plastic media. This suggested that the thermally treated recycled glass (Finishing media) has demonstrated good efficiency in delivering target performance using the jig arrangement assisted vibratory super-polishing process.

Figure 12-16 illustrates the comparison of the percentage decrease in average surface roughness Ra relative to the initial surface roughness of the jigged vibration finishing process using glass finishing media. The finishing process comparison was established with and without Vibraglaz accelerant paste made of commercially available abrasive powders. The percentage decrease in Ra for a given machining process does not linearly depend on initial average surface roughness. The results also show that the reduction in Ra of finishing process with accelerant paste enhanced by 62.9% of 120min., while the finishing process without paste improved by 54.1% at full cycle time. This suggests that the Vibraglaz accelerant agent was successfully enhancing the machining performance by improving the surface roughness value.

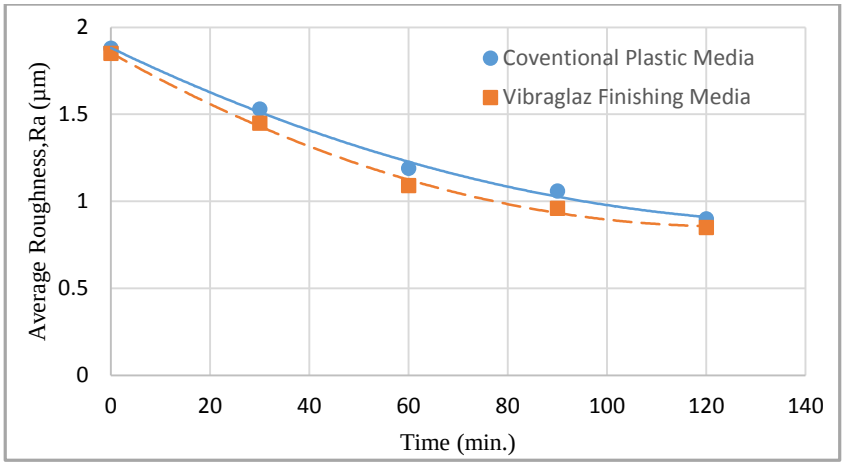

Figure 12-15 Average roughness comparison of jigged vibration finishing process as a function of time using Vibraglaz finishing media and conventional polyester media

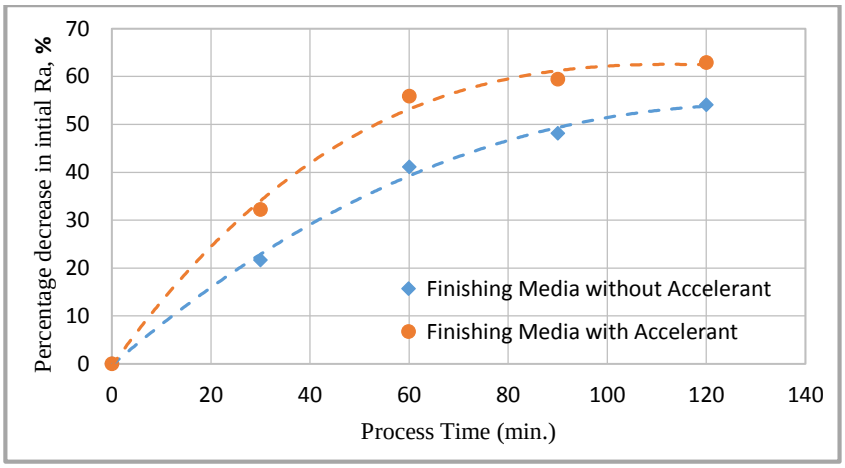

Figure 12-16 percentage reduction in average surface roughness relative to initial surface roughness of jig assisted vibratory mass finishing process.

12.7 Conclusion

The design, fabrication and evaluation of a new jig arrangement system for vibratory mass finishing has been completed. This study includes the FEM structural analyses of the new system. The performance analysis of the new jig arrangement system was also performed using conventional and thermally treated glass media. Critical analysis has been conducted, which illustrated that the design is able to overcome the load to which it was subjected due to the part weight, vibration, and media motion resulting from rotating the shaft with eccentric weight in the trough. Stress-strain, and displacement were calculated and the results showed that shear stress is less than the yield strength of the selected material, which means the design is safe and satisfies target capability.

The jig arrangement is designed to hold the part in the horizontal position and allow free rotation with the media in the vibratory mass finishing, which provides a solution to the challenges associated with thermally treated glass media. Glass media has the same performance as other media and it is inexpensive but, due to the brittleness of glass, there is a risk of shard generation when used with heavy workpieces such as those used in the aerospace industry. Fracturing of glass media with heavy parts and the introduction of shards affects its performance and leads to poor results of surface finishing, finally leading to damage of the workpiece surface.

Therefore, introducing a jig arrangement system can contribute to removing or reducing the risk of damage from large components. The jig arrangement is designed to hold the workpiece in a horizontal position whilst allowing free rotation by fixing the two ends with ball groove bearings. The system has the ability to move up and down in the vertical at increments in the trough of the machine. This operation allows the workpiece to have full abrasion with thermally treated glass media without applying any load or pressure on it that would lead to shard generation, and eventually delivers a result of finishing large components with enhanced process efficiency. The new arrangement provides about 25% improvement in Ra after 7hr. machining with conventional (porcelain) media. The results also show that the reduction in Ra for glass media and accelerant paste (developed by Vibraglaz UK Ltd.) was enhanced by 62.9% at 120min., while the finishing process without paste improved by 54.1% at full cycle time

CHAPTER THIRTEEN

DISCRETE ELEMENT MODELLING OF NON-SPHERICAL GLASS MASS FINISHING MEDIA FLOW UNDER VIBRATIONAL EXCITATION

13.1 Modelling vibrated granular flow

Vibratory Mass finishing processes continue to gain widespread acceptance in manufacturing industries, primarily as a technology for reducing the costs of producing edge and surface finishes. The process may also be used for blending in surface irregularities from machining or fabricating operations, producing reflective surfaces with non-abrasive burnishing media, refining surfaces, and developing super-finish or micro-finish equivalent surface profiles.

The vibratory mass finishing processes utilize a bonded abrasive material, loaded within a container or chamber. Energy is imparted to the abrasive mass by a variety of excitation modes, this imparts motion into the media and causes abrasion of the surfaces of a component. The previous work on the vibratory mass finishing process has been focused on the material erosion and edge rounding (Baghbanan, Yabuki et al. 2003) (Mohajerani and Spelt 2010), and also on the kinematics of the process such as media flow, impact velocities, and forces. Baghbanan, Yabuki et al. (2003), and Ciampini, Papini et al. (2007) characterized the impact wear mechanisms in vibratory-bowl finishers by three principle modes as is shown in Figure 13-1. The figure illustrated free impact, rolling of isolated media on the part, and stationary media on the part surface while adjacent media roll over it. The largest normal impact forces were identified to be associated with the first mode. The normal and tangential contact forces encountered by the part were measured in process using a strain-gauge based sensor embedded in a freely moving workpiece. The work also emphasized that most media in the dry condition do not slide on the workpiece.

Wang, Timsit et al. (2000) investigated the effect of wet and dry media on surface finish and hardness using an aluminium workpiece. The customized force transducer and a miniature video camera were mounted inside a cylindrical workpiece. Wang et al. measured normal loads and contact duration during collisions between the workpiece and surrounding media on the surfaces. Although the force data were limited to the normal direction and did not distinguish between individual media effects, they did provide some insight into contact conditions at the workpiece surface. Yabuki, Baghbanan et al. (2002) measured the normal forces corresponding to tangential forces using the same technique presented by Wang, Timsit et al. (2000) .The magnitude of the normal forces were approximately ten times greater than tangential forces in both wet and dry conditions.

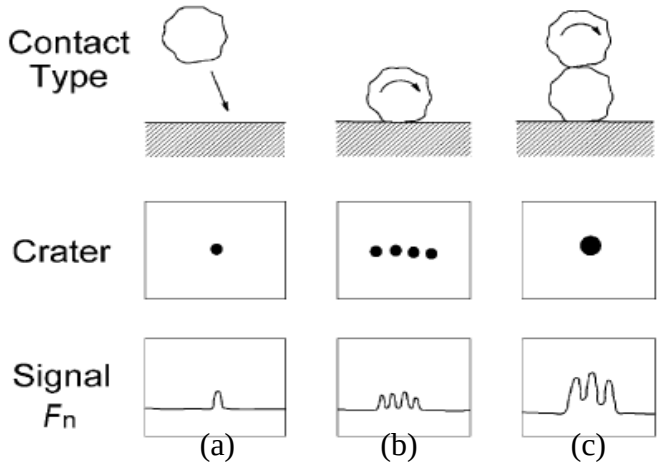

Figure 13-1 Schematic diagram of three contact modes representing by crater and normal force signal: (a) free impact; (b) rolling of individual piece of media; (c) stationary piece of media with adjacent media rolling over it (Yabuki, Baghbanan et al. 2002).

Baghbanan, Yabuki et al. (2003) evaluated the performance of a vibratory tub finisher on aluminium workpieces and corroborated the earlier results obtained by Wang, Timsit et al. (2000) and Yabuki, Baghbanan et al. (2002). The results suggested that the normal and tangential forces and the changes in the aluminium surface properties in the proposed vibratory tub finisher were similar to those in the vibratory bowl finisher. This suggested that the vibratory finishing data could be generalized regardless of vibration parameters and machine type.

It has been noted in various studies that the maximum force magnitudes exhibited by media on free surfaces due to the mass finishing process are 1N for water wet condition and 1.5N for dry condition. Figure 13-2 shows the effect of lubrication on the force magnitude of media across all the three principle impact modes presented by Baghbanan, Yabuki et al. (2003). The results demonstrated that the granular media in dry conditions normally impacted the workpiece in the normal direction while in wet condition there was an evidence of increased tangential impact across the workpieces due to the sliding phenomena presented. Thus, the dry condition exhibits a more aggressive metal removal rate (MRR). On further examination of figure 13-2, it is clearly noticed that the total numbers of impacts in the dry condition are approximately double those in the wet condition.

Ciampini, Papini et al. (2007) developed a piezoelectric impact force sensor placed in a vibratory tub finisher to measure force magnitude in carefully selected areas of a stationary plate submerged within the media.

Impact sensors were placed in small pockets and only the normal contact was registered which gave infrequent responses, with exposure time extended, the data was quantitative enough to draw suitable conclusions from the media effect. With the infrequent force impacts, they are named "bursts," these bursts occur periodically corresponding with the vibration frequencies (however this is implied by the cyclic nature of the process). The normal impact forces as detailed in this research are recorded at magnitudes of ten times greater than a tangential impact, this conclusion of frequency and impact magnitude was noted as similar to that found by Yabuki, Baghbanan et al. (2002). However, Ciampini, Papini et al. (2007) present two significant modes of impact: non-impact contact showing media being pressed onto the sensor by surrounding media, and media impact with velocity, v.

The development of the vibratory finishing process requires knowledge of the media circulation flow and its impact velocities against a workpiece surface. Herrmann and Luding (1998) reported that three numerical approaches are used for modelling granular media flow; statistical modelling, continuum modelling, and discrete element modelling. In the case of statistical modelling, Sommerfeld (2001) described the particle flow motions as a stochastic process (random process). The stochastic process involves a sequence of random variables and time associated with these variables. In the continuum modelling technique, a continuous model can be constructed with adequate average accuracy using finite element method, or powder modelling. Talu, Tardos et al. (2000). Cariapa, Park et al. (2008) developed pseudo fluid to simulate the flow of the disc centrifugal mass finishing process using the continuum approach.

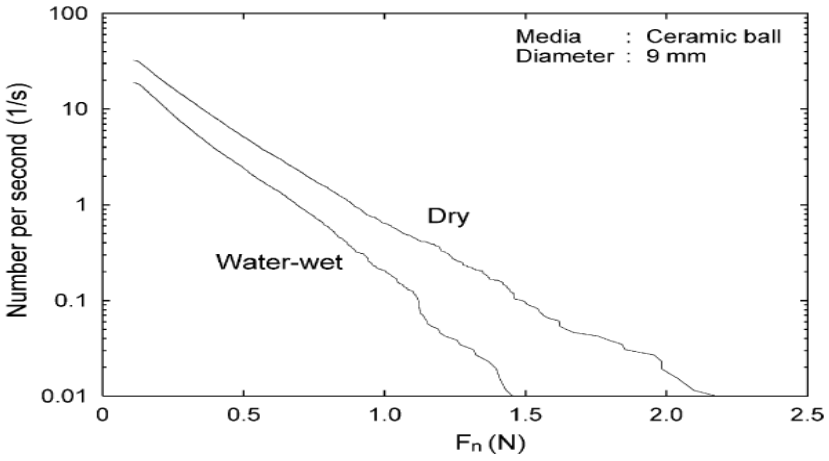

Figure 13-2 Number of impact per second as a function of normal force during wet and dry conditions (Yabuki, Baghbanan et al. 2002) .

The Discrete element modelling (DEM) is frequently used to simulate a collision between particles and flow pattern in granular systems (Sitharam 2000) (Hogue and Newland 1994). Kawaguchi, Tanaka et al. (1998) investigate the effect of boundaries on particle motion driven by an airflow using the discrete element method (DEM). Asmar, Langston et al. (2006), and Zeilstra, Collignon et al. (2008) found this approach to be a useful tool in modelling vibrated granular media to predict flow distribution and energy dissipation within a particulate media mixture. An, Li et al. (2009) developed a DEM model to analyse bed expansion in one-dimensional vibration.

The kinematics of the process are generally well understood and a number of technical papers and books have reported on studies in this the area. This knowledge base will be used to progress this study and to provide insight into the interactions of the media elements with the workpiece. This study seeks to develop a new modelling system that will provide improved understanding and insight into the movement and impact modes occurring within the process and permits fundamental analysis of the wear behaviour using DEM analysis. The predicted data will be compared to physical studies and ultimately used to aid development of monitoring and control strategies.

This chapter is on the development and optimization of the discrete element method (DEM) of bulk flow of thermally treated conical glass media in a two-dimensional vibratory finishing process. The predicted results are compared with experimental measurements of average flow velocity, bulk expansion and vertical and horizontal velocity distributions along the horizontal axis of the vibratory finishing machine. The individual particle velocity measurements in the bulk flow were determined by using particle image velocimetry adapted with MATLAB code (PIVLab). The optimization procedure was developed by means of a parametric study to enhance the predicted contact parameters through determining the best fit of the numerical results with the experimental measurements of media velocity vector at different locations in the flow. Figure 13-3 shows the flow chart of DEM and experimental steps sequence to predict and optimize contact parameters of the vibratory tub finishing process.

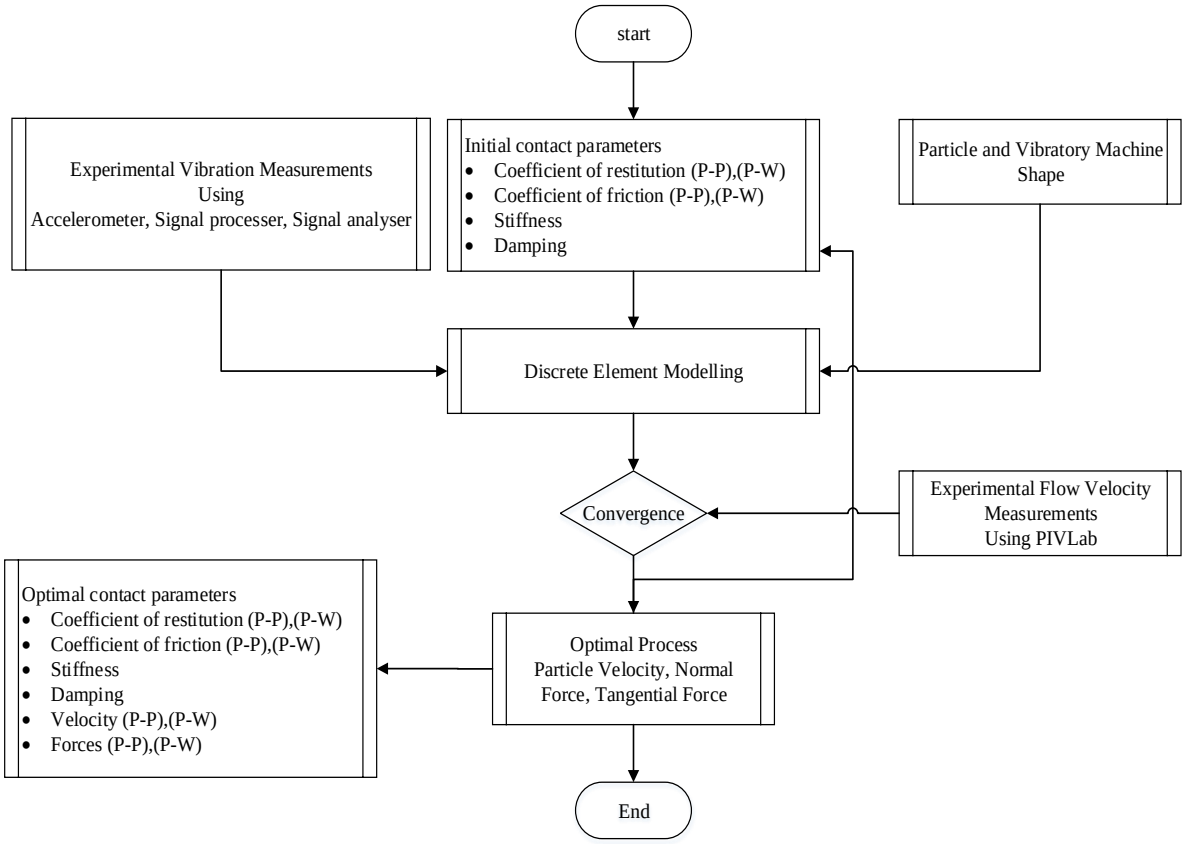

Figure 13-3 Flow chart of DEM and experimental steps sequence of contact parameters optimization of vibratory finishing process

13.2 The DEM theory

The discrete element method (D.E.M.) is a numerical method of solving bulk particle effects through their inter-particle relationships to give a solution in either 2 or 3 dimensions. The DEM has been primarily used in granular or discontinuous materials such as powders, rocks, soil, etc. Typically, the solutions requiring use of the DEM are in materials of varying degrees of consistency where conventional computational fluid dynamics or finite element solutions to be unacceptable.

In the DEM of granular flow, the inter-particle contact law determines the net force and moment on each grain. A number of contact force models are available in literature to describe inter collisional dynamics in various extents. Cundall and Strack (1979) developed the linear spring and dashpot model, where the magnitude of the normal force between two particles is the sum of spring force and damping force.

This model has been widely used in different applications such as the model of granular media motion in hoppers (Yabuki, Baghbanan et al. 2002), and modelling of vibrating granular motion in gas flow (Tatemoto, Mawatari et al. 2004). Several other models have been developed by other researchers such as: particle adhesion models (Johnson, Kendall et al. 1971), inelastic frictional particle-particle interaction model , and soft-sphere and hard-sphere force model (Schafer *et al.*, 1996). However, in this study the (Hertz 1881) contact theory to model the normal force components, and the Mindlin and Deresiewica (2014) model for tangential force components were employed. In order to simulate the DEM modelling of the vibratory finishing machine, the key areas of the DEM methodology are explored in the following subsections:

13.2.1 Motion

DEM elements are free to move in 6 degrees of freedom (in a 3 dimensional workspace), three translational and three rotational which all move in a coordinated system computationally solved by matrices. The motion of DEM elements can be described by Euler's equations for the motion of a rigid particle. Figure 13-4 illustrates the six degrees of freedom motion of conical glass media. The translation and rotation motions are given by Eq.(13-1), and Eq.(13-2) respectively, (Cundall, 1988).

$$\ddot{x}_i + \alpha \dot{x}_i = \frac{F_i}{m} + g_i \tag{13.1}$$

where $\ddot{x}_i$ is the velocity of the particle at its central node; α is the mass-proportional damping constant; F_i is the sum of all contacts and external loads applied to the elements node, g_i is the acceleration due to gravity.

$$\left.\begin{aligned} I_1\dot{\omega}_1 + (I_3 - I_2)\omega_3\omega_2 &= M_1 \\ I_2\dot{\omega}_2 + (I_1 - I_3)\omega_1\omega_3 &= M_2 \\ I_3\dot{\omega}_3 + (I_2 - I_1)\omega_2\omega_1 &= M_3 \end{aligned}\right| \tag{13.2}$$

where I_1, I_2 and I_3 are the principle moments of inertia of the block; ω_1, ω_2, ω_3, are the angular velocities about the principle axes; and M_1, M_2, M_3 are the components of the torque applied to the block referred to the principle axes.

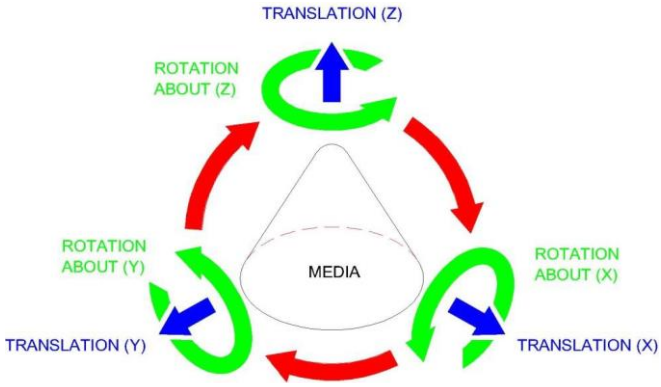

Figure 13-4 six degrees of freedom with typical glass media shape shown at centre

13.2.2 Contact

The definition of contacts within a DEM particle system is calculated by two components, firstly by Newton's second law of motion and a force-displacement law at the contact point. Newton's second law states that the forces acting on particles resulting in particle motion, whereas the force displacement is used to extract the forces from displacements. These forces were calculated at the end of each time step during the free particle flow. Particle deformation is not required to define the mechanical nature of the granular material. The particle overlap is proportional to the contact force magnitude to simulate the deformation of individual particles. Wassgren (1997) suggested that the maximum permitted overlap should be within 1% of particles average diameter. Cundall and Strack (1979) proposed a diagrammatical example of the contact modes operating within a DE, as is shown in Figure 13-5. This example illustrates two weightless discs, x and y tightly held between two rigid walls with no force applied, they are touching with no contact forces in the first image (far left). Later, (at the middle image) the walls have moved inwards over a distance $v\Delta t_1$, the positions stay the same as the time step value is 1, at the third image (far right) after 2 time steps overlaps exist at the contacts and the walls. At this step, the force displacement law is used based on the following form Eq. (13-3).

$$\Delta F_n = K_n(\Delta n)_{t1} = K_n v \Delta t \tag{13.3}$$

where *kn*, is the normal stiffness and ΔFn represents the increment in normal force.

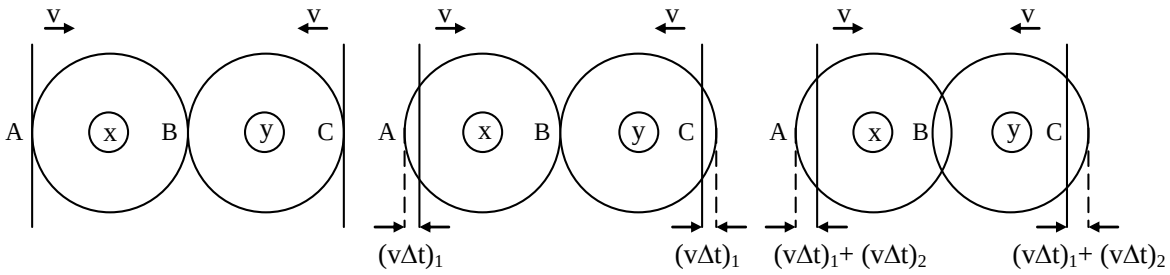

Figure 13-5 Two discs compressed between rigid walls (overlaps are exaggerated) (modified image from (Cundall and Strack 1979)

The forces calculated from this equation are then used to find the accelerations to complete the calculation of Newton's second law. The use of Newton's second law allows the calculation of the displacement increments between contacts A, B and C, this process is repeated to model contacts in all directions and calculate the resultant force on the particle. The general motion of the granular material is calculated using the force displacement model, this model essentially sets boundaries to define contacts. Assume two discs are in direct contact with each other, contact only occurs when the distance between their centres is less than the sum of the radii of the discs. When this condition is satisfied, the displacement is calculated at the contact point using the relative velocities and other factors including damping.

13.2.3 Damping

Damping is a process of reducing the effect of contacts within a DEM particle system whether linearly in the form of a correction factor or proportionally in-line with particle velocity or kinetic energy for numerical stability. Damping is a key component of the DEM solution as it affects the inter element contacts to adequately simulate a steady state solution. In the case of granular mechanics solved through DEMs, adaptive viscous damping is introduced to the model, as a constant rate of change of kinetic energy is observed; as the kinetic energy tends to zero, the damping power also tends to zero. For the DEM analysis, damping is added to the contact mechanism in two modes, as contact damping and as global damping.

Contact damping operates in conjunction with the element velocities in the normal and shear directions of the contacts, it does not operate when the particle velocity results in sliding (tangential contact) and friction damping alone operates.

Global damping is applied to the absolute velocities of the elements and is introduced in the calculations of motion; it is applied to both the velocity vectors and the rotational velocity of the elements.

Cundall and Strack (1979) used a "Nine disc test" to approximate the use of damping within a DEM system by employed nine elements within a defined area with rigid walls and calculating the perpendicular force magnitude on neighbouring elements with no damping (1) and (2) mass and stiffness damping. The test illustration is displayed in Figure 13-6. It is clearly observed that the damping of contacts is critical to the DEMs ability to provide a suitable stable numerical solution taking into account the elements prescribed radius, density, cohesion, inter-particle friction co-efficient, shear stiffness and normal stiffness. However, the damping will reduce the calculation cycles to reach the equilibrium value (Feq).

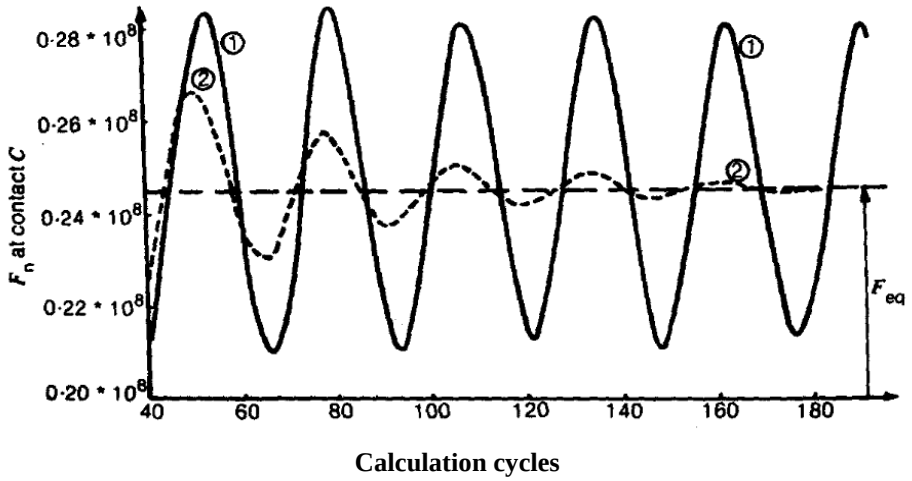

Figure 13-6 Nine-disc test, curve 1, no damping, and curve 2, mass and stiffness damping (Cundall and Strack 1979)

13.3 Hertz-Mindlin contact model

Granular materials are modelled by representing their particles' geometry as a random assembly of elastic spheres. The contact force-displacement law is related to the contact force acting between two spherical particles to their relative displacement (Elata and

Berryman 1996). The Hertz (Hertz 1881) contact model assumes that the granular material is isotropic and elastic. The overlap between two contacting particles is small compared to the radius of the un-deformed bodies.

The Cundall and Strack (1979) contact force-displacement law is based on the linear spring and dashpot model while the Hertz-Mindlin is a nonlinear elastic model with path dependence due to slip motion and neglecting the relative roll and torsion between the contact particles. Figure 13-7 shows the contact mechanism between two discrete spherical particles.

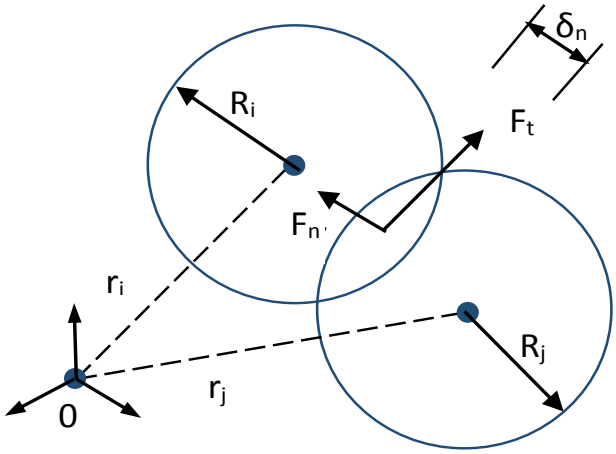

Figure 13-7 contact mechanism between two discrete particles

The elastic contact between two spherical particles allows for strikethrough overlapping by measureable amount of δ_n , the normal overlap is given by Eq. (13.4):

$$\delta_n = R_i + R_j - |r_i - r_j| \tag{13.4}$$

where R_i and R_j are the radius of particles i , j, and $r_i and\, r_j$ are position vectors of their centre of mass, respectively. The normal overlap represents the contact position in the DEM application. The normal vector r_n of the contact position is defined by Eq. (13.5)

$$r_n = \frac{r_j - r_i}{|r_j - r_i|} \tag{13.5}$$

The Newton's second law suggested that the two particles are in contact resulting in force at the contact point. Thus, the normal force of the Hertz model by means of normal vector is given by Eq. (13.6)

$$F_n = \frac{4}{3} E^* \sqrt{R^*}\, \delta_n^{3/2} \tag{13.6}$$

where E^* is the equivalent Young's Modulus between two particles in terms of Poisson's ratio of particles in contact given by Eq. (13.7), R^* represents the equivalent radius given by Eq. (13.8)

$$\frac{1}{E^*} = \frac{1-v_i^2}{E_i} + \frac{1-v_j^2}{E_j} \tag{13.7}$$

$$\frac{1}{R^*} = \frac{1}{R_i} + \frac{1}{R_j} \tag{13.8}$$

Young Modulus can be expressed in terms of shear modulus *G* given by Eq. (13.9)

$$E_i = 2G_i(1+v_i) \tag{13.9}$$

The normal damping force F_n^d is defined by Eq. (13.10) (DEM Solutions, 2011)

$$F_n^d = -2\sqrt{5/6}\,\Upsilon \mathrm{v}_n^r \sqrt{k_n m^*} \tag{13.10}$$

where v_n^r is the normal component of relative velocity, k_n is the normal stifness given by Eq. (13.11), Υ is factor related to the coefficient of restitution e_r which can be expressed by Eq. (13.12), and m^* is the equivalent mass of contacting particles given by Eq. (13.13).

$$k_n = 2E^*\sqrt{R^*\delta_n} \tag{13.11}$$

$$\Upsilon = \frac{\ln(e_r)}{\sqrt{\ln(e_r).\ln(e_r)+\pi^2}} \tag{13.12}$$

$$\frac{1}{m^*} = \frac{1}{m_i} + \frac{1}{m_j} \tag{13.13}$$

The tangential deformation at the point of contact is defined by the tangential overlap δ_t and can be determined by integrating the trajectory of relative velocity of particle i and j over the time (Pournin and Liebling 2009). Mindlin and Deresiewica (2014) developed a model for the tangential contact force F_t between two overlapping particles. The tangential force is given by means of a tangential overlap vector and tangential stiffness k_t as expressed in Eq. (13.14):

$$F_t = -\delta_t\, k_t \tag{13.14}$$

The tangential stiffness and equivalent shear modulus are given by Eq. (13.15), and Eq. (13.16), respectively:

$$k_t = 8G^*\sqrt{R^*\delta_n} \tag{13.15}$$

$$G^* = \frac{1 - v_i}{G_i} + \frac{1 - v_j}{G_j} \tag{13.16}$$

The tangential damping force F_t^d is given by means tangential component of relative velocity which can be expressed by eq. (13.17)

$$F_t^d = -2\sqrt{5/6}\,\Upsilon \mathrm{v}_t^r \sqrt{k_t m^*} \tag{3.17}$$

The tangential force is defined by means of Coulomb friction because of sliding one particle surface over the other. However, one of the two regimes given in Eq. (13.18) defines the tangential force value.

$$\left.\begin{aligned} F_t &= F_t && if\ |F_t| \le \mu\ F_n \\ F_t &= \frac{F_t}{|F_t|}\,\mu\ F_n && if\ |F_t| > \mu\ F_n \end{aligned}\right\} \tag{13.18}$$

The resultant contact force F_{ij} of particle i and j is the vector addition of normal and tangential forces given by Eq. (13.19)

$$F_{ij} = F_n + F_t \tag{13.19}$$

The rolling friction is calculated by applying torques between particles surfaces and given by Eq. (13.20)

$$\tau_r = -\mu_r F_n R_i \omega_i \tag{13.20}$$

where μ_r is the coefficient of rolling friction, and ω_i is the angular velocity vector of the particles at the contact point

Cundall's contact model suggested a linear parallel configuration of a spring and a dashpot in each time step to describe the behaviour of contact forces in the normal and tangential directions. Thus, the model calculated the variation in normal and tangential contact forces (ΔF_t, ΔF_n) at the beginning of each time step from the particle position and velocity assigned to the beginning of the interval.

$$\Delta F_n = k_n d_n + c_n \mathrm{v}_n^r \tag{13.21}$$

$$\Delta F_t = k_t d_t + c_t \mathrm{v}_t^r \tag{13.22}$$

where d_n and d_t are relative displacement along the normal and tangential directions during time interval respectively. c_n and c_t are normal and tangential damping coefficient.

The properties of both contacting bodies ($k_n, k_t, c_n, c_t,\ and\ \mu$) contribute to the impact behaviour, since the impact parameters of bodies A, and B are interact with each other, then the effective normal impact parameters, and tangential impact parameters are given by Eqs. (13.23), and (12.24), (13.25), and (13.26), respectively.

$$k_n = k_{n,A}\, k_{n,B}/(k_{n,A} + k_{n,B}) \tag{13.23}$$

$$c_{n,A} = c_{n,A}\, c_{n,B}/(c_{n,A} + c_{n,B}) \tag{13.24}$$

$$k_t = k_{t,A}\, k_{t,B}/(k_{t,A} + k_{t,B}) \tag{13.25}$$

$$c_{t,A} = c_{t,A}\, c_{t,B}/(c_{t,A} + c_{t,B}) \tag{13.26}$$

13.4 Modelling non-spherical particles

Cundall and Strack (1979) proposed that the DEM of granular particles was modelled as a disc in 2-D simulation and as a sphere in 3-D simulation. The circular shape has a better tendency to roll which reduces interlocking resistance. Different approaches have been developed with varying degrees of success in modelling non-spherical particles. Ting and Rowell (1995) proposed a 2-D simulation of ellipse shape particles and Lin and Ng (1997) introduced ellipsoid shape particles for a 3-D simulation. The ellipses and ellipsoid particles were modelled by elongated particles throughout changing the aspect ratio, these particles have fewer tendencies to rotate and do not closely represent the actual particle shapes. Favier, Abbaspour-Fard et al. (2001) proposed an axisymmetric particle shape, this technique can model various particle shapes. Jensen, Bosscher et al. (1999) introduced a clustering particles technique by joining spherical or disc shaped elements in a semi rigid configuration. In this case, any number of elements constructing the cluster arrangement will rotate and translate as a rigid body. The particles' contacts within the cluster were assumed linear elastic with high stiffness. Thomas and Bray (1999) developed a new technique of clustering by introducing kinematics restrictions on elements within clusters to prevent relative translations and rotations. Although these techniques were enhancing the early methods, the simulated cluster configuration was not similar to the actual model. Furthermore, a significant increase in the computational time was developed due to the high contact stiffness required within the cluster.

However, to overcome this problem Ashmawy, Sukumaran et al. (2003) proposed the Overlapping Rigid Clusters (ORC) technique to accurately simulate angular particle shapes.

This technique allows for permanent rigid boundaries between elements within the cluster without detecting contacts or calculating contact forces, thus increasing the computational efficiency. The ORC method depends on joining a number of overlapping discs or spheres; with such an arrangement, the resulting outline of simulated particle coincides with and is almost identical to the actual particle's outline. A digital microscope or scanner was employed to determine the actual particle outline. Figure 13-8 shows the ORC technique presented by Ashmawy, Sukumaran et al. (2003) to inscribe circles within the outline of actual particles.

However, the density of each disc within the cluster configuration must be scaled to ensure particles remain proportional to the area at whatever number of discs or degree of overlapping structure. An approximate method to scale the density is given by Eq. (13.27)

$$\rho_d = \frac{A_p}{\sum A_d}\rho_p \tag{13.27}$$

where ρ_d is the density of the disk elements, A_p is the area of the particle, $\sum A_d$ is the sum of the areas of the disk elements, and ρ_p is the density of the soil particle.

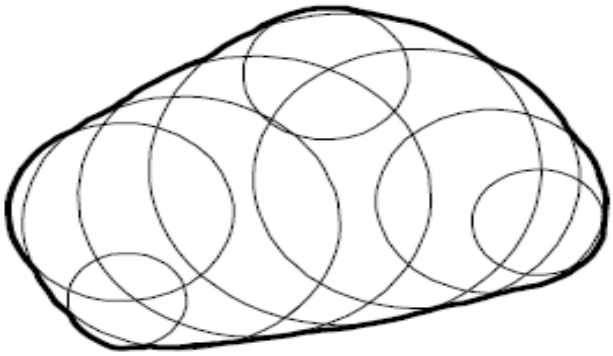

Figure 13-8 ORC of disc elements inscribed within a particle outline (Ashmawy, Sukumaran et al. 2003)

ORC technique doesn't guarantee the similarity between the created and actual particle associated to the moment of inertia or centre of gravity. Such a discrepancy will lead to the development of unsteady state particle flow causing difficulties in achieving convergence with the actual flow state. A modified ORC method has been developed by Ashmawy, Sukumaran et al. (2003) to ensure identical inertial properties for the actual and simulated particles. This method suggested determining the outline of particles by digital microscopy.

The outline is then divided into equal interval X-Y coordinates from a reference point. Thus, the area, mass, centre of gravity, and moment of inertia along the normal axis to the centre of gravity were determined. Figure 13-9 shows the sequence of implementing disc elements for Michigan sand particles. The first disc is located in the particle centre, the next disc then added to minimize the uncovered area. The addition of the following discs follows the same criterion to satisfying minimum uncovered area condition. The approach of checked area ratio after the addition of every disc or sphere within the particle cluster should be considered. The area ratio relationship is defined by Eq. (13.28).

$$A_r = \left(1 - \frac{A_{unc}}{A_t}\right) \times 100 \tag{13.28}$$

where A_r is the area ratio, A_{unc} is uncovered area, and A_t is the total area

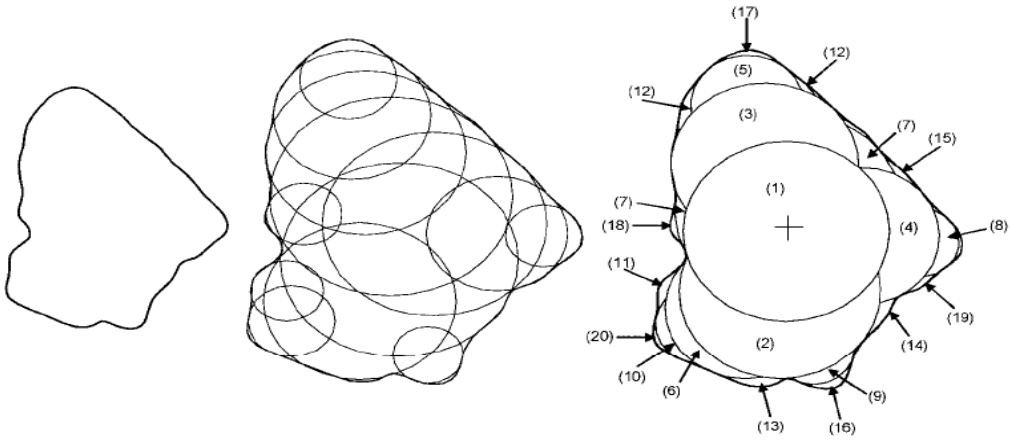

Figure 13-9 Sand particle, a) particle outline by digital microscope, b) particle generated using ORC method, c) particle generated using modified ORC method (Ashmawy, Sukumaran et al. 2003).

13.5 Thermally treated glass media particle shape

A modified ORC technique was employed to create the 3-D conical shape of thermally treated glass media (Vibraglaz) that is used for DEM simulation purposes. The average outline of ten glass media particles was determined using SEM analysis. The spheres added within the measurable outline were established by aid of the SolidWork tool. The spheres were fitted within the particle outline using the criterion described in the modified ORC method of minimizing uncovered area. The simulated cone geometry was constructed from

56 spheres to capture the design outline and provide the best fit of volume, mass, centre of gravity and moment of inertia with the actual particle. The following relationships were used to compute the conical particle centre of gravity and moment of inertia.

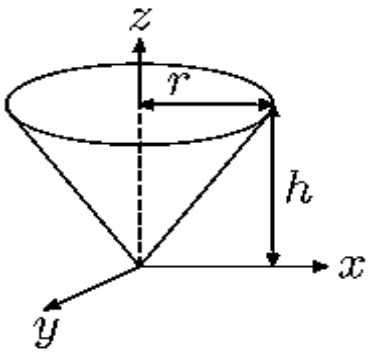

Schematic of conical shape

The conical volume

$$V = \frac{1}{3}\pi r^2 h$$

Centre of mass

Ideal is $\frac{1}{4}$ from the base of the cone. $COM = (0,0,h - \frac{h}{4})$

Moment of inertia

Ideal tensor for principal axes

$$I = \begin{pmatrix} \frac{3}{5}mh^2 + \frac{3}{20}mr^2 & 0 & 0 \\ 0 & \frac{3}{5}mh^2 + \frac{3}{20}mr^2 & 0 \\ 0 & 0 & \frac{1}{5}mr^2 \end{pmatrix}$$

Table 13-1 presented the volume, mass, centre of gravity, and moment of inertia of actual and modified ORC model. The results show that the centre of gravity of the simulated cone is within 2% of the actual cone. The result indicates that the errors are small. This may be attributed to the fact that the sphere elements are added in a uniform spatial distribution, thus the centre of gravity coincides with that of the actual particle. However, the moment of inertia result shows less agreement with the actual particle due to the clustering arrangement effect which tends to concentrate the mass at the centre of the particle while increasing the probability of sphere overlap occurrence. Figure 13-10 shows the final design of 3-D conical glass media for DEM simulation.

Table 13-1 Comparison between actual and modified OCR conical glass media for DEM simulation

Parameter	Actual	Modified OCR model
Volume	$1.78 \times 10^{-06} m^3$	$1.58 \times 10^{-06} m^3$
Mass	$4.504 \times 10^{-03} Kg$	$4.214 \times 10^{-03} Kg$
COM	$(0,0,1.275 \times 10^{-02}) m$	$(1.89 \times 10^{-08}, 3.26 \times 10^{-07}, 1.25 \times 10^{-02}) m$
Moment of Inertia about Principal Axes	$\begin{pmatrix} 8.49 \times 10^{-07} & 0 & 0 \\ 0 & 8.49 \times 10^{-07} & 0 \\ 0 & 0 & 9.00 \times 10^{-08} \end{pmatrix} Kg\, m^2$	$\begin{pmatrix} 6.17 \times 10^{-07} & 0 & 0 \\ 0 & 4.06 \times 10^{-07} & 0 \\ 0 & 0 & 5.062 \times 10^{-08} \end{pmatrix} Kg\, m^2$

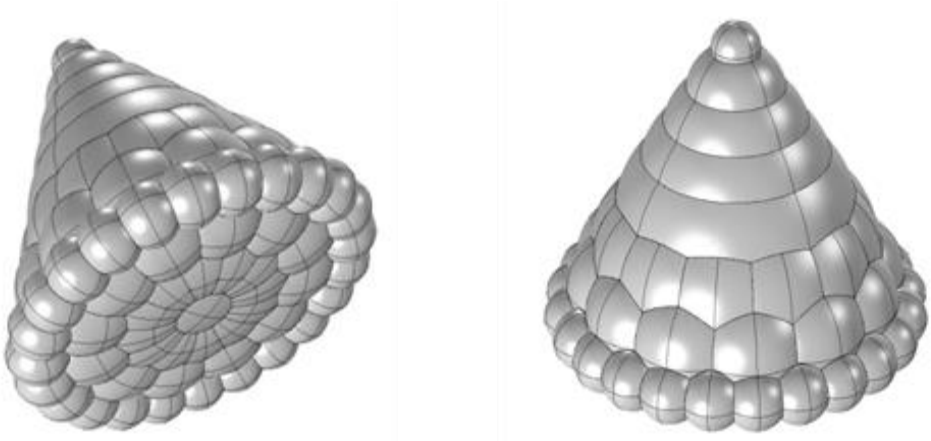

Figure 13-10 3-D conical glass media for DEM simulation.

13.5.1 Experimental setup

A vibratory tub type finisher was used for experiments. The unit had a U-shaped cross-section chamber with a polymer liner and capacity of 10 litres. Vibration amplitude and frequency were fixed during the tests. The experiments used thermally treated glass media (Vibragalz Finishing media).

The DEM simulation is based on a 2-dimensional system, thus the experimental test must adequately support this link by limiting the media's ability to move in the z-axis direction throughout circulation flow. The trough was partitioned to allow a single row of media flow in the machine by arranging 2-off Perspex panels (10mm thick) shaped to suit the profile of the trough and fixed by 3-off bolts to a prescribed inside dimension as is shown in Figure 13-11. Figure 13-11 (a) illustrated that the media gap was set to 25mm, this was chosen as the space required for media particles to freely translate and rotate in order for

the full effect of the vibration parameters to adequately perform on the layer of media. The two linked Perspex panels were then clamped to the trough liner by use of a 3-plate system outlined in Figure 13-11 (b).

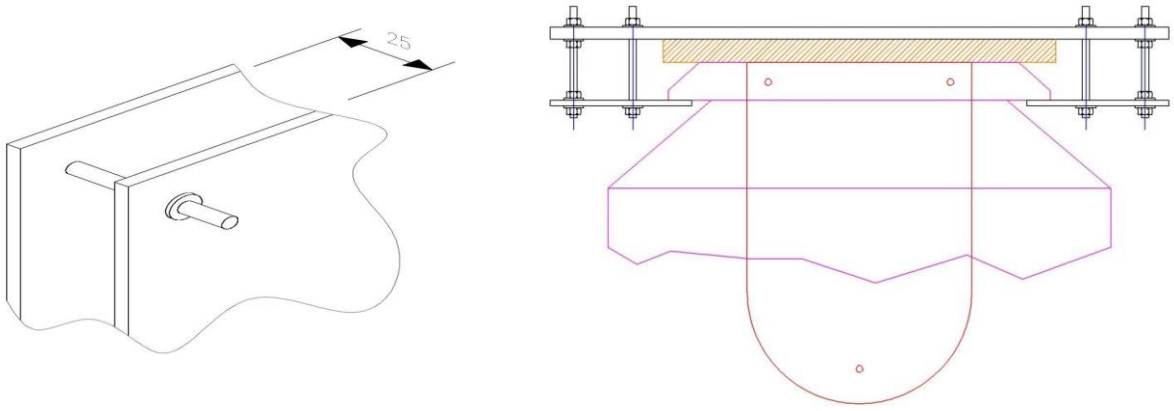

(a) (b)

Figure 13-11 Schematic of 2-D experimental setup by clamping arrangement: a) Perspex clamping and media gap, b) Perspex clamping jig attached to trough liner.

Figure 13-12 shows the gap between the Perspex panels was filled with finishing glass media giving 100mm headroom between the media and the clamping arrangement (matching the DEM setup). The Perspex panels were clamped at one end of the trough and a video taken of the movement displayed by the media under vibration as is shown in Figure 13-13. The flow motion of media was recorded using an image acquisition system. This system consisted of a CCD video camera (IDT Motion Pro X2 with 6 GB RAM) with a 50 mm lens. A 450W tungsten halogen light was used as a light source. Every image of the media flow motion was converted to grey levels, ranging from 0 to 255 based on the colour difference between the background and white tracer particles. The digital video of 60-second duration was then transferred to PC computer and saved for further analysis. The digital video converted to 1000 frames with an image resolution of 960 rows and 1024 columns were taken at a frame rate of 225fps. The view window of the CCD video camera was set to cover a region of 190 mm width equivalent to 960 pixels. This arrangement setup provides a scaling factor of 0.198 mm/pixel. These frames were then transferred to MATLAB tool (PIVLab) for the investigation of bulk flow velocity, bulk expansion, and vertical and horizontal velocity. The bulk flow velocity is defined as the average flow velocity over a specific point within the bulk flow. The flow velocity over a measurement field of 3.5×3.5 cm was determined as the average result for 4 cones.

The bulk expansion also recorded when the vibration is introduced to the machine bed, the average space between media increases. The bulk expansion was determined under a steady state vibration condition by the ratio of increased bulk volume (bulk expansion surface) to the initial volume (initial surface). This can be quantified by the mean of the PIVLab tool by identifying the bulk expansion over a set of video images during the experimental test and DEM simulations. Figure 13-14 shows the initial surface at stationary state without vibration and the bulk expansion surface after steady state vibration and the direction of media flow. As displayed the initial surface can be determined by drawing an approximate line over the video image. The same line will be drawn after vibration running and achieving steady state condition. Then the ratio of increased bulk volume to the initial volume was established through the data exploration tool. A similar procedure was following on the corresponding DEM system.

The horizontal and vertical velocity distributions were investigated on different levels of rows from the bottom wall by means of PIVLab. This results in the understanding of process performance by obtaining the orientation of the high impact flow energy within the vibratory trough. Figure 13-15 shows the sequence of the rows level from the bottom surface. The average horizontal and vertical velocities at a measurable field of over 3× 3 cm were quantified at equal interval locations along the selected row.

Figure 13-12 Finishing glass media between the two Perspex plates.

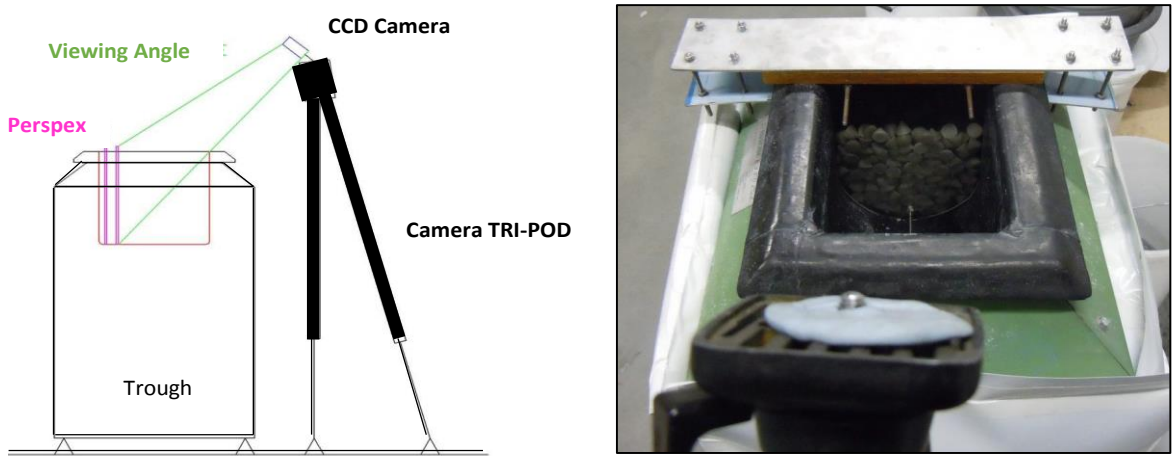

Figure 13-13 Schematic of video recording setup, and view from real camera position with clamp and media

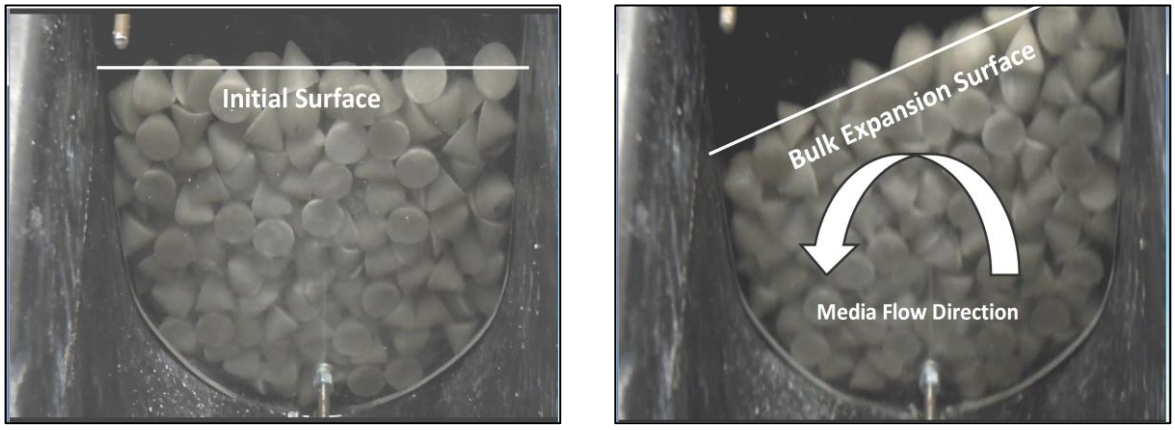

Figure 13-14 Images of vibratory tube finisher state, a) initial surface before vibration, and b) bulk flow expansion after steady state vibration and direction of media flow.

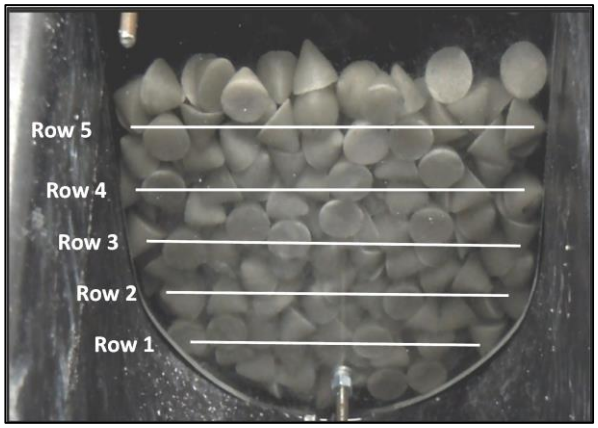

Figure 13-15 Sequence of the rows level from the bottom for horizontal and vertical velocity measurements

13.6 PIVLab technique applied to vibratory mass finishing process.

PIV, particle image velocimetry depends on investigative images in sequence to determine particle movement. A number of research articles deal with the implementation and optimization of the PIV technique (Adrian 1991, Buchhave 1992, Lourenco 1994, Prasad 2000, and Adrian and Westerweel 2011). However, PIVLab uses a technique called window deformation to track particle movement from one image to the next in order to generate velocity field vectors. PIVLab is a tool written specially for MATLAB by Thielicke and Stamhuis (2010). The suggested tool can be run through the MATLAB for high professional users or it also includes a graphical use interface GUI system that makes the programme easy for use. The PIVLab is adequately for investigating the velocity field of material or fluid based on the image processing technique. In this study the PIVLab tool was applied on the granular material in the vibration process to investigate the velocity field, bulk expansion and velocity profile in horizontal and vertical directions. Figure 13-16 shows the analysis of digital images used to obtain the velocity information by mean of PIVLab (Thielicke and Stamhuis 2010). In this process, the two images taken at a small partial time separation t_0, and $t_0+\Delta t$ were considered. Each interrogation region generated over an intensity map, I(x, y*)*. The intensity maps are the Fourier transformed using an FFT tool and cross correlation. these tasks were performed in Fourier space. The cross correlation plane, C(x, y) is then calculated throughout an inverse transformer (Kim, Swarup et al. 1961). The intensity peak in the correlation plan is equivalent to the mean displacement between two intensity maps. Finally, the pixel displacement is converted to a velocity vector using the displacement between two images and time separation of the frames.

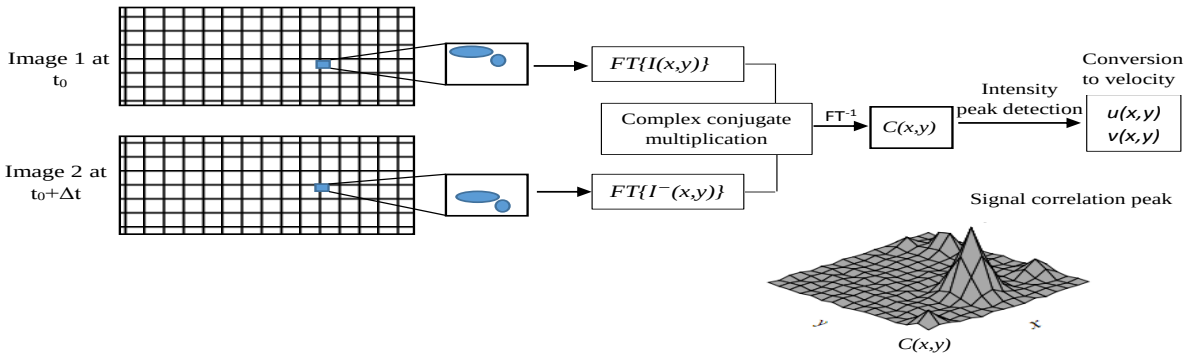

Figure 13-16 Analysis of digital images to obtain the velocity information by mean of PIVLab (Thielicke and Stamhuis 2010).

The PIVLab programme allows us to calculate the intensity peaks of the particles from various images based on the cross correlation technique. Thus the velocity vectors are generated accordingly. Many PIV techniques used the optimization method to describe the cross correlation function as given by Eq. 23 (Kim, Swarup et al. 1961).

$$max_a = \int_A^{\infty} f_1(x)\, f_2(x)(x+a)dx^2 \qquad (13.23)$$

where a is the displacement vector, and A is the correlation domain. The intensity functions $f(x)$ is defined at times t_1, and t_2 and specified by $f_1(x)$ and $f_2(x)$y respectively. Willert and Gharib (1991) suggested that the cross correlation function describes the intensity peaks for a given interrogation area and adequately finds the location of displaced intensity peaks (particle movement). There are two approaches to calculate Eq. (13.23). The direct cross correlation approach is to estimate the correlation function in the spatial domain (Okamoto, Nishio et al. 2000). The second approach is to estimate the correlation function in the frequency domain (Discrete Fourier Transformer, DFT) using Fast Fourier Transformer (FFT) (Soria 1996). Both approaches are available in the PIVLab tool.

13.7 PIVLab implementation

The PIVLab analysis consists of five main steps (import images, image pre-processing, image evaluation, and post-processing and data exploration) as is shown in the workflow chart in Figure 13-17. All set up parameters are accessible from the GUI of PIVLab. The steps in the workflow chart starting with image input as is shown in print screen GUI image Figure 13-18 (a). The imported images are grouped into appropriate pairs of either 1-2, 2-3 or 1-2, 3-4. Figure 13-18 (b) shows the print screen GUI image of the analysis setting step. In this step it is possible to set up the interrogation area and the interrogation offset for particle tracking. The user is able to set up multiple pass options to increase the accuracy of measurements. The setting option for selecting region of interest (ROI) and exclusion mask are also available in this step. Figure 13-18 (c) shows the print screen GUI image of the analysis step. In this step, the numbers of frames are setup for analysis. Figure 13-18 (d) shows the GUI image of the post processing step. This step allows the user to set up the velocity field limit and standard deviation filter. This filter will try to eliminate noise by removing vectors on how many standard deviations they are away from the mean value.

There are other options of manually deleting unwanted velocity vectors and interpolating missing data. Figure 13-18 (e) shows the GUI image of the calibration setup. In this step, the calibration tool is available to convert the Pixel/Frame into the metric unit based on the actual dimensions from the experimental setup. Figure 13-18 (f) shows the GUI image of the data exploration step, which contains the control on the presented data. It is possible to change scale, thickness and colour of the velocity vectors. This allows the user to analyse an image set with a high degree of precision. It is also possible to create shear, vortices and an average velocity fields over a complete sequence of images.

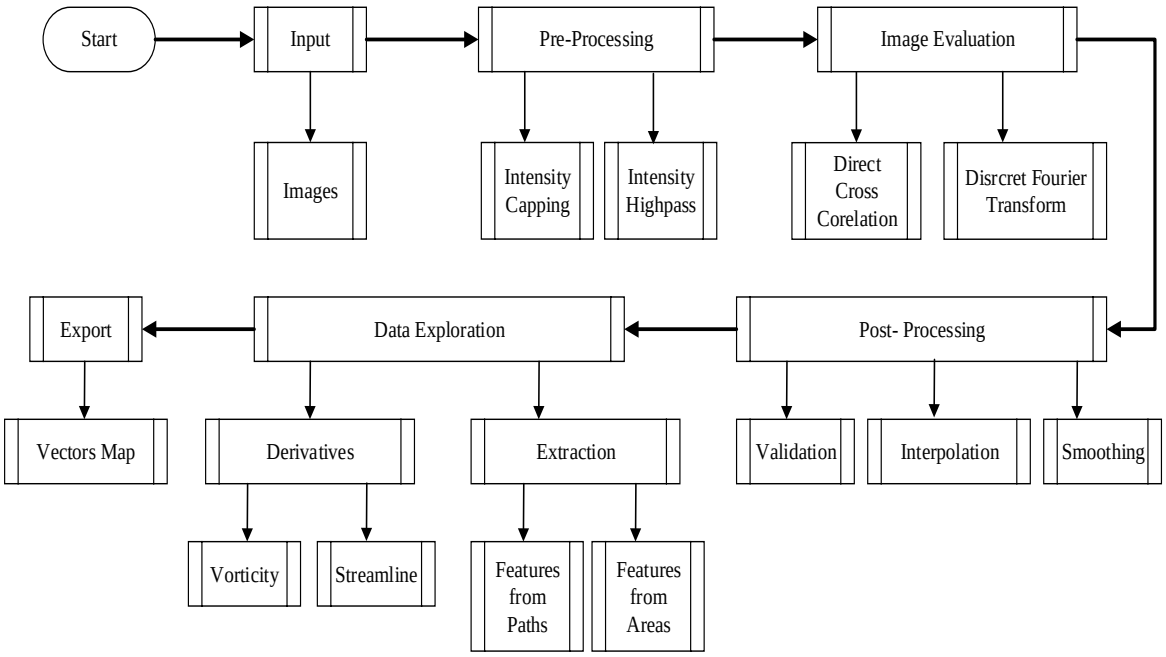

Figure 13-17 Workflow chart of PIVLab analysis

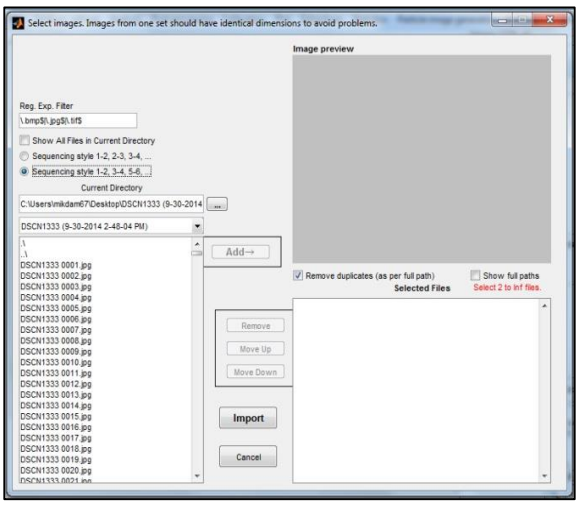

(a)

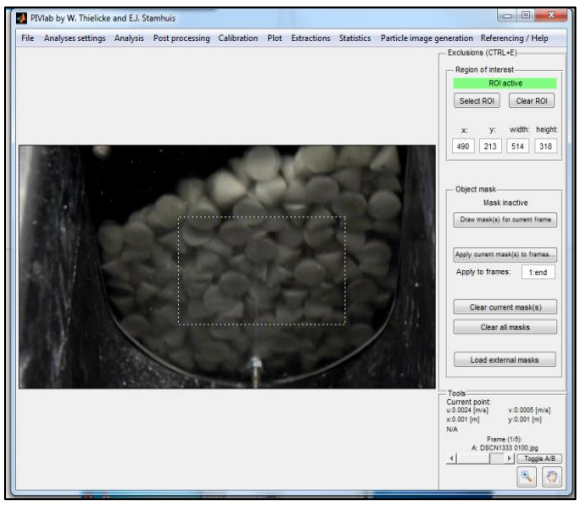

(b)

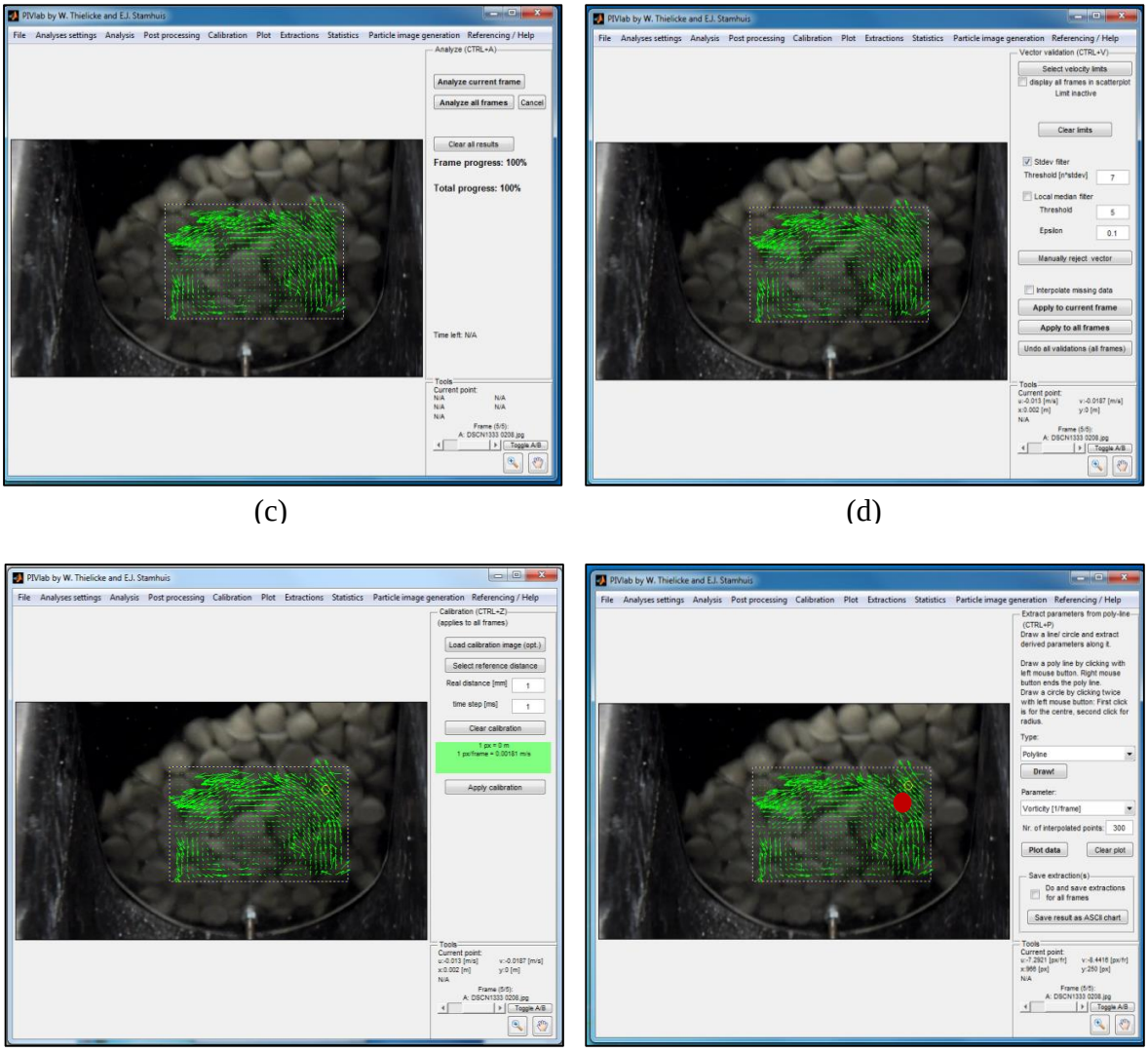

(c) (d)

(e) (f)

Figure 13-18 GUI sequence of PIVLab analysis

13.8 Vibration measurements of tub finisher

Vibration measurements of the tub finisher were determined in order to define the motion of the tube within the DEM simulation. Figure 13-19 shows the vibration measurements setup. Two Dytran Model No 3293A tri-axial accelerometers were fixed to the vibratory machine at each end. Thus the frequency and amplitude of vibration were recorded in three orthogonal axes x, y and z. The vibration measurements were estimated in three loading states, unloaded (without finishing media), partially loaded (10 kg of glass finishing media) and fully loaded (14kg of glass finishing media). The accelerometers were connected to the Abacus signal-processing unit.

The data was then transferred to Data Physics SignalCalc dynamic (signal-analyzing software) associated with the FFT (Fast-Fourier-Transform) analysis tool. In order to avoid noise, the frequency and amplitude data were recorded under a steady state vibration condition strikethrough over 16 sec.

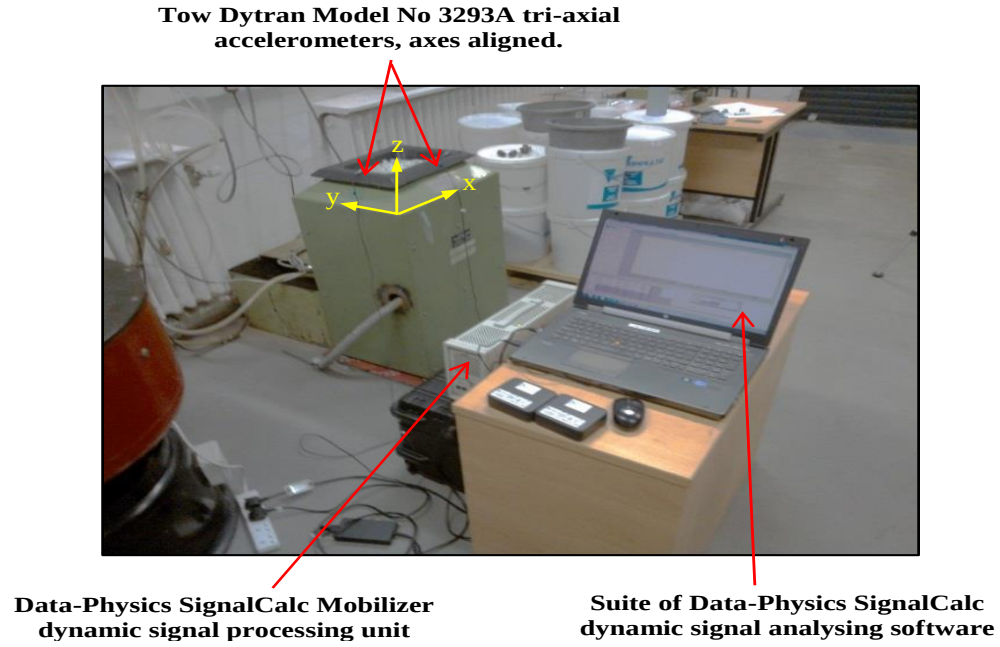

Figure 13-19 Vibration measurements setup

13.8.1 Frequency of vibration

The experiments were carried out to record the data in the time domain and the same data was represented in the frequency domain of (x, y, and z) axes using three different vibratory machine loads (no load, partial load, and full load). Figure 13-20 shows the time domain results of recorded acceleration (g) as a function of two-second time using the partially loaded vibration condition. Figure 13-21 shows the frequency domain results of recorded acceleration (g) as a function of frequency using the partially loaded vibration condition. Presenting data in the frequency domain form allows the frequency of vibration and associated amplitude to the easily displayed. The results demonstrated that the frequency of vibration for the recorded axes were consistently 49.5 Hz in all load state conditions.

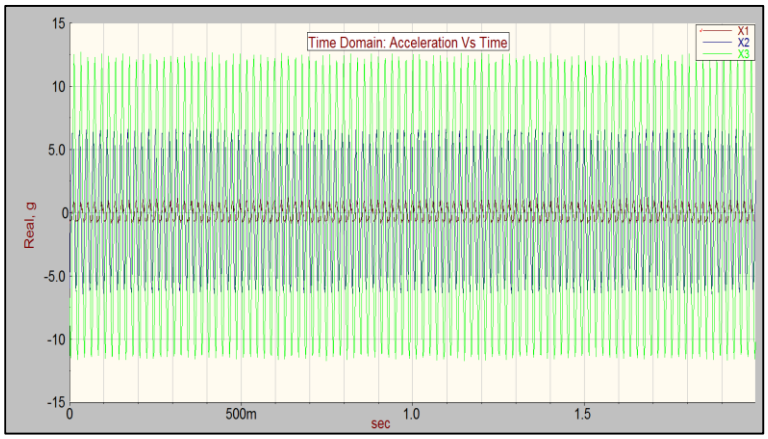

Figure 13-20 Time domain of (x, y and z) axes recorded over 2-second using a partial loaded vibration

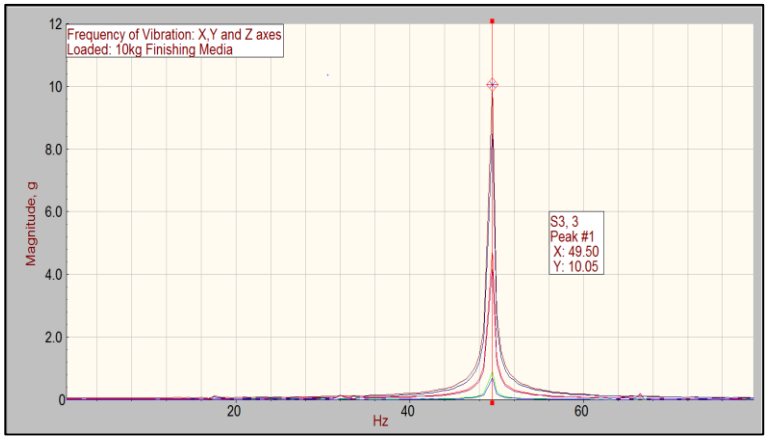

Figure 13-21 Frequency domain of (x, y and z) axes using partial loaded vibration

13.8.2 Amplitude of Vibration

The vibration amplitudes for a given loading condition were determined by extracting zero-peak amplitude of a particular axis from the respective frequency domain plots. Table 13-2 displays the measured zero-peak amplitudes of vibration axes for given loading conditions at 49.5 HZ. Figure 13-22 shows the vibration amplitude of (x, y, and z) axes using the partially loaded condition at 49.5 HZ (vibration frequency). The amplitude of vibration is greatest in the z-axis and smallest in the x-axis. The effect of loading conditions on the amplitude of vibration appears to be negligible in the y and z-axes but has a more significant effect in the x-axis. This may be attributed to the position of the driving shaft with eccentric mass within the mass finishing machine.

Table 13-2Vibration Amplitude under different loading conditions

Axis	Unloaded mm	Partial Load mm	Full Load mm
X	0.066	0.072	0.12
Y	0.537	0.488	0.521
Z	1.037	1.019	1.151

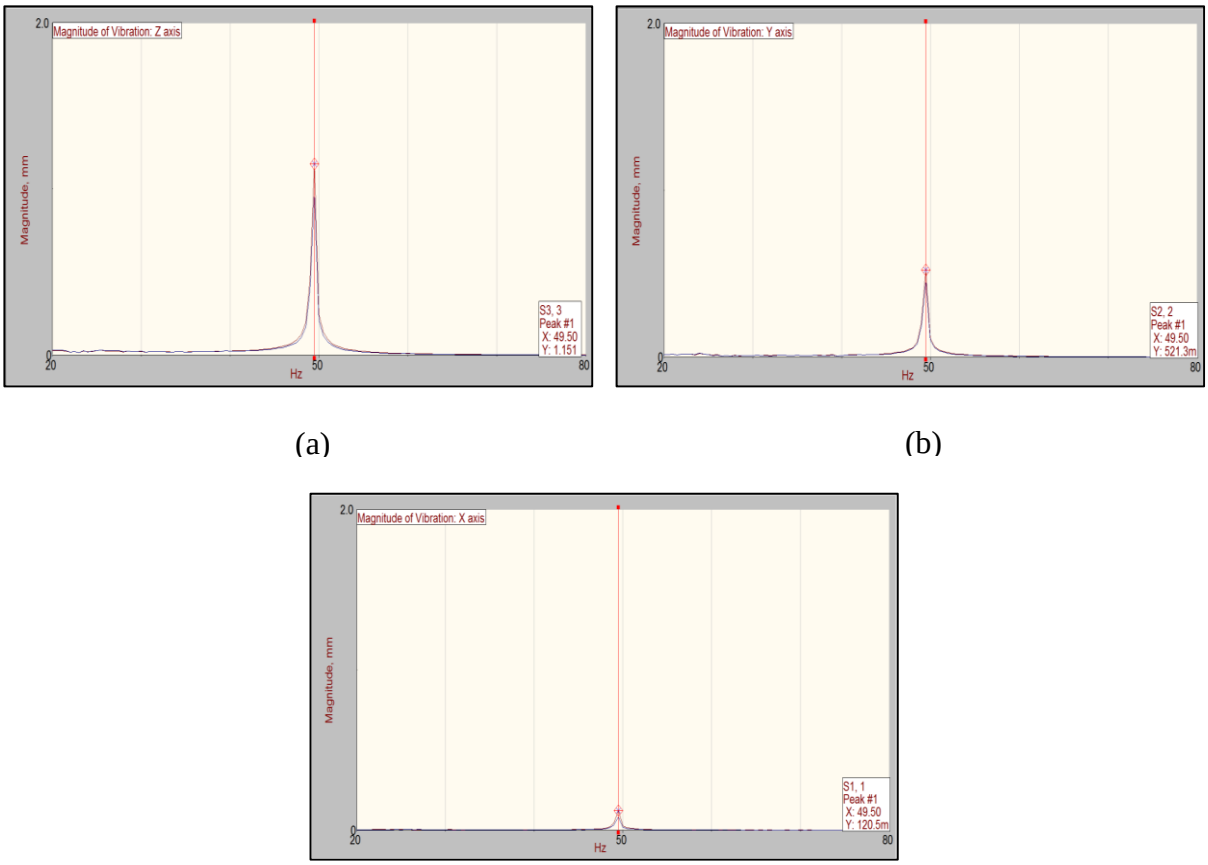

(a) (b)

(c)

Figure 13-22 Vibration amplitude using partial loaded condition at 49.5 HZ: a) Z-axis, b) Y-axis, and c) X-axis

13.8.3 Relative axial motion and displacement

Figure 13-23 shows a time domain plot that recorded acceleration as a function of time to encompass three full harmonics oscillations. The results are used to determine the relative motion of the vibration within a particular axis and phase angle φ (rad) between different axial traces. Based on the frequency, peak amplitude and phase angle between axial trace values, three equations of displacement in x, y and z-axes as a function of time can be derived as is shown by Eq. (13.24), Eq. (13.25), and Eq. (13.26), respectively.

These equations can be used as an input data to the DEM simulation to describe the motion of the vibratory tub finisher over time. Figure 13-24 illustrates the relative axial displacement of the vibrating tub finisher in the x, y and z axes as a function of time measured over three full harmonics oscillations.

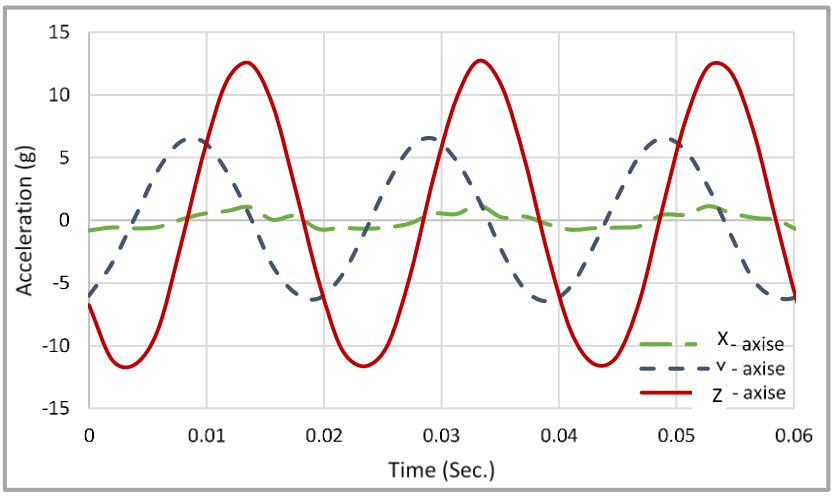

Figure 13-23 Time domain of (x, y, and z) axes in Figure 13-19 recorded over three full harmonics oscillations using partially loaded vibration

Equation of motion for displacement in Y

$$Y = A\,sin\omega t \tag{13.24}$$

where Y is the displacement in the y axis, A is the maximum amplitude in the Y direction, ω is the circular frequency (rad/s) and t is time (s)

Equation of motion for displacement in x

$$x = B\ \sin(\omega t + \varphi_1) \tag{13.25}$$

where B is the maximum amplitude in x, *and* φ_1 is the phase angle between the x and y traces.

Equation of motion for displacement in z

$$z = C\ \sin(\omega t + \varphi_2) \tag{13.26}$$

where C is the maximum amplitude in z, and φ_2 is the phase angle between the z and y traces.

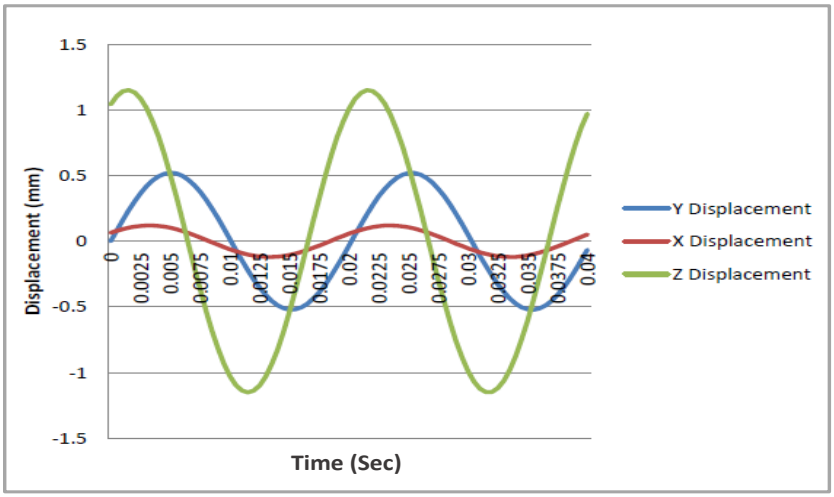

Figure 13-24 Axial displacements in x, y, and z axes in Figure 13-19 as a function of time

13.9 DEM analysis

The two dimensional discrete element method (2-D DEM) was performed using LIGGGHTS (Kloss and Goniva 2010) particle simulation code. The DEM was developed to simulate the flow motion of conical thermally treated glass media (Finishing media) between two Perspex plates in the vibratory finishing machine using the Hertz-Mindlin contact and Cundall's model. Thus, the conical glass media bed was simulated as a single layer of particles with collisions and motion assumed to occur in the *y* and *z* plane. The DEM simulations were started by allowing the conical glass media to settle at low energy state (stationary stage). Figure 13-25 show the DEM simulations of vibratory finishing tube at stationary stage of partially and full loading conditions.

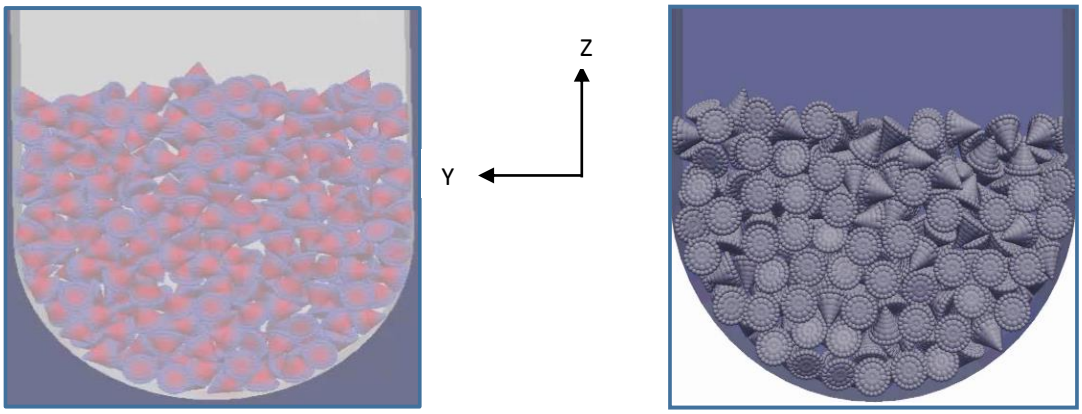

Figure 13-25 DEM simulations of vibratory finishing tub at stationary stage of a) full loading condition, b) partially loading condition

13.9.1 DEM contact parameters

The parameters used in the DEM simulations are classified into two categories based on the method in which they are chosen. The first category is for the parameters that extracted directly from experiments. The numerical parameters are imported directly from the experimental works include vibration cycle frequency (*f*), vibration acceleration amplitude (*A*) , tube finisher dimensions, load condition (partial, and full) , particle geometry, particle physical and mechanical properties (Mass *m*, Moment of inertia *I*, Density ρ, Modulus of elasticity *E*, Poisson's ratio *v*, and Shear modulus *G*). The mechanical properties of thermally treated glass media (Finishing media, [Chapter 9] were employed in the DEM simulations. The second category is for the contact model. The initial contact parameters were estimated according to the published experimental data, which includes particle-particle coefficient of restitution ($e_{p\text{-}p}$), particle- wall coefficient of restitution ($e_{p\text{-}w}$), particle-particle friction coefficient ($\mu_{p\text{-}p}$), and particle-wall friction coefficient ($\mu_{p\text{-}w}$). The particles in the simulated system were assumed to have a uniform geometry.

The DEM in this study was employed linear Hertz-Mindlin contact parameters using Cundall's model. The set of parameters that are based on the contact model described in section (13.3) include normal stiffness (k_n), tangential stiffness (k_t), normal damping c_n , tangential damping c_t. The normal stiffness was determined from maximum overlap of particles. The maximum overlap is dependent on particle mass, coefficient of restitution e_r, and maximum relative velocity. The coefficient of restitution is equal to relative velocity after collision divided by the velocity before collision; however, the assumption of constant e_r should be valid when the relative impact velocities of particles have a similar magnitude. Wassgren (1997) suggested that the particles collision causes energy to be lost due to the plastic deformation. Consequently, coefficient of restitution decreases with increasing collision particle velocity.

Wassgren (1997) suggested that the maximum overlap between two particles in a vibratory finisher should be less than 1% of the particles' radius estimated at maximum contact velocity. Cundall and Strack (1979) proposed that the tangential stiffness coefficient can be estimated by means of normal contact stiffness given by Eq. (13.27). The results also demonstrated that for a small value of the friction coefficient μ, the ratio of k_t/k_n did not change the DEM simulation performance.

However, when μ increases, the relative damping coefficient β is active for long duration resulting in k_t/k_n becomes more critical.

$$\frac{2}{3} \leq \frac{k_t}{k_n} \leq 1, thus \ \ \frac{c_t}{c_n} = \frac{k_t}{k_n} \tag{13.27}$$

$$\beta = \frac{c}{c_{cr}} \tag{13.28}$$

$$c_{cr} = 2\sqrt{km} \tag{13.29}$$

where β is the critical damping coefficient, and k and c is the stiffness and damping, respectively, in either the normal or tangential directions.

The initial contact parameters were estimated according to published relationships and values. The parametric study was then employed to optimize contact parameters using the best fit between the predicted and experimental bulk flow velocity measurements at different locations within the two-dimensional flow field using different load conditions. Figure 13-26 shows the schematic diagram of the tub finisher with the locations of velocity measurements.

The initial contact parameters are presented in table 13-3 The initial coefficients of restitution, $e_{p\text{-}p,}$ and $e_{p\text{-}w}$ for glass particles was estimated to be 0.5 (Stronge 2004). The parametric study of coefficients of restitution were selected to be in the range 0.2≤ er≤ 0.9. A value of 0.5 was selected for the friction coefficient between glass particles, $\mu_{p\text{-}p}$, and 0.4 for the friction coefficient between glass particle and wall, $\mu_{p\text{-}w,}$ (Wassgren 1997). The parametric study of friction coefficients was chosen within range 0.2≤ μ ≤0.9. The Normal stiffness and damping coefficients were calculated from conventional DE formulae (Cundall and Strack 1979) assuming a maximum particle overlap equal to 1% of the particle diameter at the maximum velocity measured in a similar tub finisher (Wassgren 1997). The Normal stiffness and damping coefficients parametric study was estimated to be within range ($2 \leq k \leq 8$) KN/m, and $0.05 \leq \beta \leq 2$, respectively. In the present study, the ratio of k_t/k_n=1, and c_t/c_n =1, was employed in the DEM simulations.

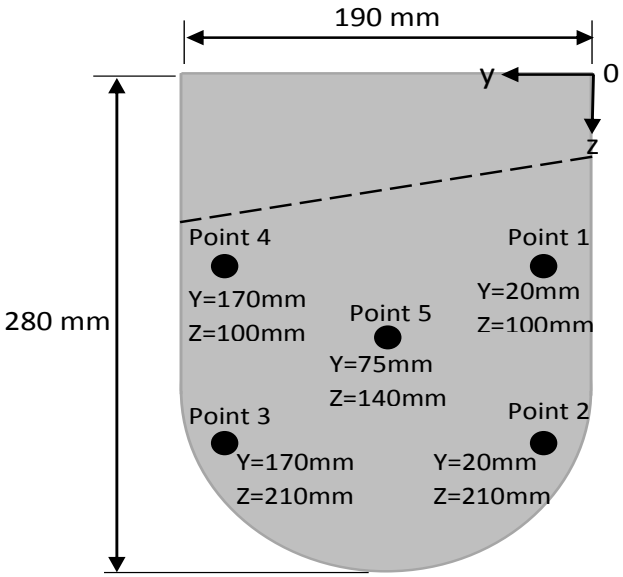

Figure 13-26 Schematic diagram of tub finisher layout with the locations of velocity measurements

Table 13-3 Contact parameters used in the DEM simulations of the flow of conical finishing glass media.

Contact Parameter	Finishing Glass Media	Optimization Range
Relative damping, $\boldsymbol{\beta}$	0.16	$0.05 \leq \beta \leq 2$
Coefficient of restitution, $e_{p\text{-}p}$, $e_{p\text{-}w}$	0.5	$0.2 \leq e_r \leq 0.9$
Stiffness, $\boldsymbol{k_n}$, $\boldsymbol{k_t}$ (KN/m)	4.5	$2 \leq k \leq 8$
Particle - Particle Friction, $\mu_{p\text{-}p}$	0.5	$0.2 \leq \mu \leq 0.9$
Particle-Wall Friction, $\mu_{p\text{-}w}$	0.4	$0.2 \leq \mu \leq 0.9$

13.9.2 DEM results of single layer circulation

The mechanics of single layer circulation during DEM simulations of a 2-D inclined vibratory tube finisher were investigated. Figure 13-27, and Figure 13-28 show the 2-D DEM simulation under inclined vibration amplitude of A_Z*=1.25mm*, and A_y*=0.55mm* with fully and partially media loaded at different time intervals. The supplement shows the direction of vibratory tub motion, direction of bulk flow velocity, and bulk expansion surface.

The observation during the first half of the inclined vibration cycle demonstrated that when the tub finisher accelerated upward A_Z*, and* A_y *>0,* shear forces will be generated over the sidewalls and tub bottom wall by the action of moving the conical glass media up.

However, the media next to the left wall are separated from the wall, since this wall is moving away from the conical media. Thus, the net shear force reduces significantly over this wall. In this case, the media velocity vectors tend to move toward the right wall. Since, the tub finisher starts moving back during the second half of the inclined vibration cycle A_Z, *and* $A_y < 0$ both tub sidewalls try to drive the conical media downward. In this part of the motion, the reaction on the right wall is smaller because the nearby media are not packed together. During the second part of vibration cycle, shear force reduces significantly due to the change in direction. Thus, the averaged resultant forces over the sidewalls and bottom surface enables the media circulation flow. The PIVLab analysis demonstrated that the predicted circulation flow is in a good agreement with experimental results of the 2-D inclined vibratory tub finisher.

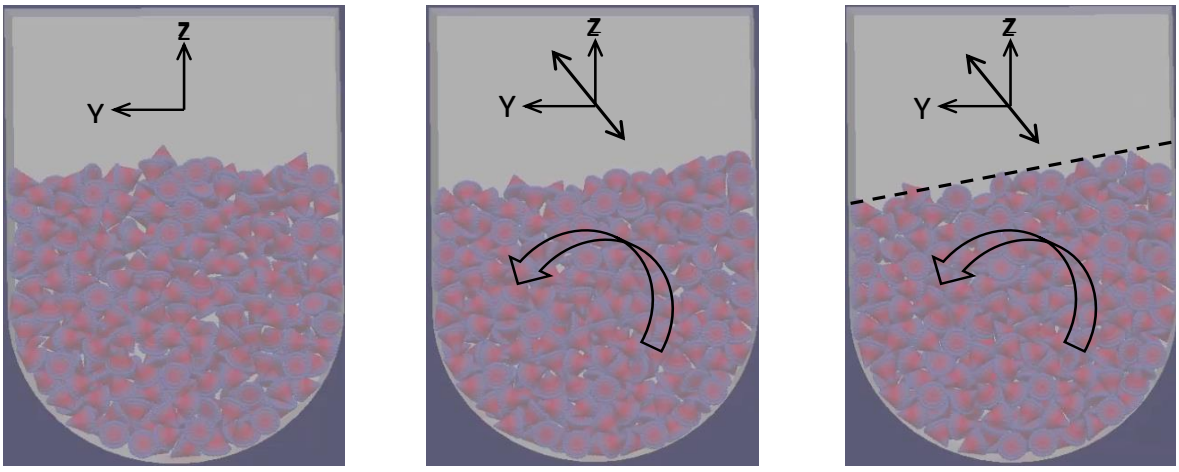

. 0 Sec. 1 Sec. 2 Sec.

Figure 13-27 DEM simulations of 2-D inclined vibratory tub finisher with full media loaded at different time intervals

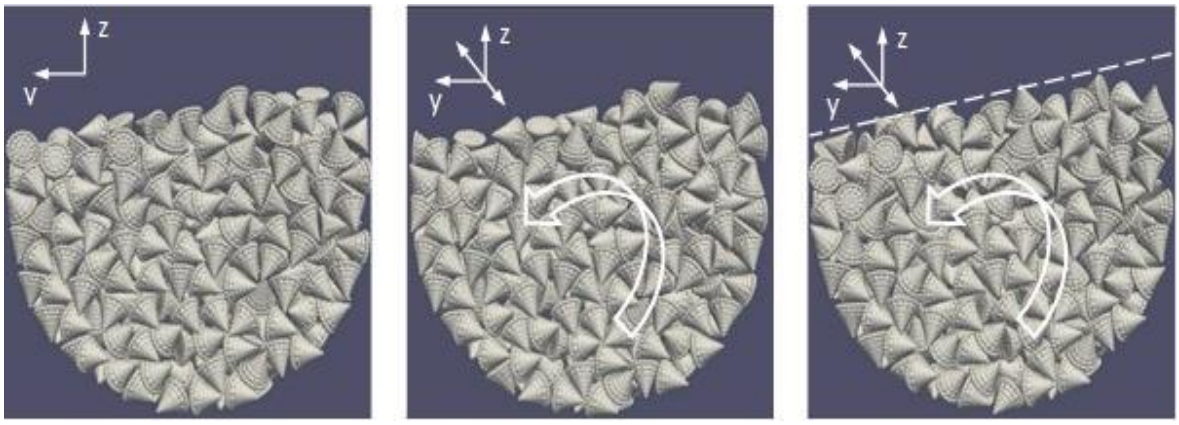

0 sec. 1 sec. 2 sec.

Figure 13-28 DEM simulations of 2-D inclined vibratory tub finisher with partially media loaded at different time intervals

13.10 DEM and experimental results

The average flow velocity of the optimal DEM simulations were compared with the equivalent experimental results at five different measurable field locations using partial and full conical media load conditions as is shown in Figure 13-29. The optimal contact parameters were determined for both loaded conditions corresponding to experimental measurements. The PIVLab technique was employed to determine the bulk flow velocity from experiments and DEM simulations. The accuracy and repeatability of measurements were investigated by repeating the experiments and DEM simulations three times at each location. The error bars present the average results of three repeated measurements. The location points were different for the partial and full loads of conical media, however, these locations were estimated to represent the same positions on the z-axis relative to bulk expansion surface in both cases. It is clearly noticed that the DEM results underestimate the bulk flow velocity in contrast with the experimental data. In the case of the partially loaded media condition, the average error in the bulk flow velocity at five locations between the experimental results and DEM simulations was 17%, whereas for the fully loaded media condition the average error in the bulk flow velocity was 14%. This suggested that the optimized contact parameters can produce good agreement with two different flow fields. It is also seen that the bulk flow velocity increases with the increasing numbers of conical particles. As a consequence, the resulting shear force and the strength of media circulation increases. This suggestion agrees with the mechanics of particle circulation in the DEM simulation that the circulation can be enhanced associated with driving shear forces at the tube walls.

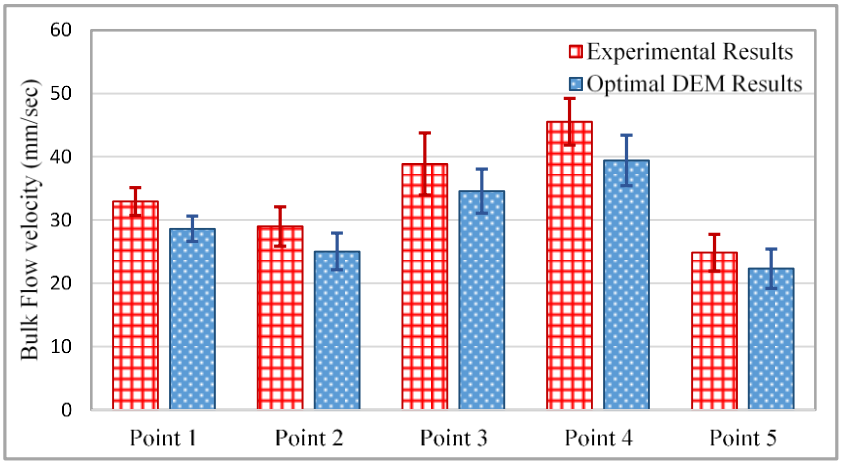

(a)

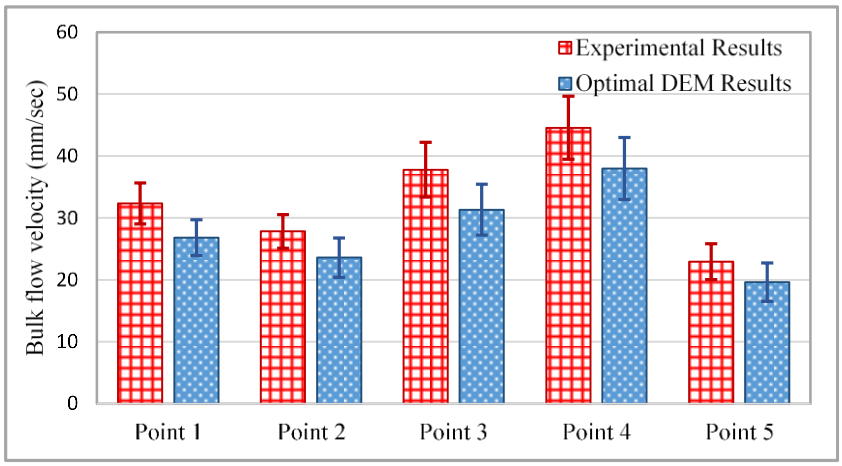

(b)

Figure 13-29 Comparison between experimental and DEM average flow velocity at different locations in the tub finisher: a) full media loaded, and b) partial media loaded

The bulk expansion of the inclined vibration tub finisher with different load conditions (partial and full media load) was measured at steady state conditions. The DEM predicted bulk expansion values were estimated at optimal contact parameters condition. For repeatability the measurements of total bulk flow were investigated by repeating the experiments and DEM simulations three times at different load conditions.

Figure 13-30 shows the partially loaded tube experiment and DEM images of bulk expansion at optimized condition. The total bulk expansion in the tub with full load of conical media was measured to be 14% (∓4%) , while the DEM simulations predicted value was 9% (∓2%). In the tub with the partially loaded condition, the measured bulk expansion increases to 17% (∓4%), while the DEM simulations predicted value increases to 13% (∓3%). The increases in the total bulk expansion as the number of conical particle decreases may be attributed to the reduction in the hydrostatic pressure that causes increasing particle motion.

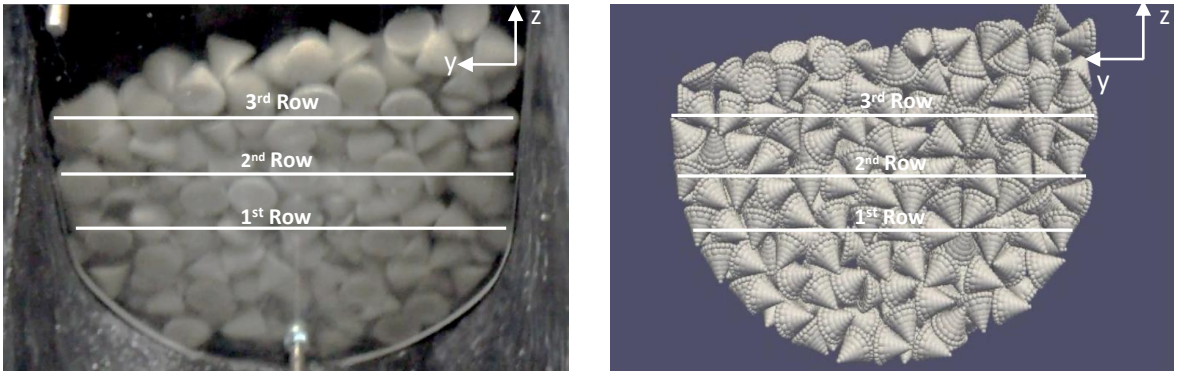

Figure 13-30 Partially loaded tub experiment and DEM images of bulk expansion and velocity distribution along horizontal direction at different row locations from the tub bottom

The experimental and numerical horizontal and vertical velocities distributions in particular field locations along the horizontal direction of the partially loaded tub finisher were measured at different levels of rows from the bottom wall. The DEM predicted values of horizontal and vertical velocities distributions were estimated at optimal contact parameters condition. The accuracy and repeatability of measurements were investigated by repeating the experiments and DEM simulations three times. The same numbers of conical particles were selected in experimental and numerical analysis. The row levels within the tub finisher were estimated carefully to represent the same positions on the z-axis relative to the bottom wall surface in both cases (experimental and numerical). Figure 13-30 shows that the average velocities were measured at six equal interval field positions along the horizontal direction on each row of the vibrated tub finisher, and the same orientation points were selected on each row in the DEM simulation.

Figure 13-31 shows the experimental results of average vertical and horizontal velocities components distributions over measurable fields along the horizontal direction of 1st, 2nd, and 3rd rows from the bottom wall. Figure 13-31 (a) shows that the average vertical velocities components distributions along the left wall of the tub finisher were significantly increased toward positive direction. These velocities dramatically reduce to the lower values in the central part, while the average vertical velocities along the right wall reversed and become a negative. This indicates that the flow was upward and downward increases along the left and right walls, respectively.

The maximum vertical velocities near the left side wall were (33.98, 29.83, and 25.45) mm/sec, over a quantified fields on 1st ,2nd , and 3rd rows, respectively. Whereas the maximum vertical velocities near the right side wall were (-35.34, -20.76, -13.15) mm/sec, over a measured fields on 1st ,2nd, and 3rd rows, respectively.

Figure 13-31 (b) shows that the average horizontal velocities components along the left wall of the tube finisher were increased toward a positive direction. These velocities reduced to the lower values in the central part, while the average horizontal velocities along the right wall reversed and become a negative. The maximum horizontal velocities near the left side wall were (29.63, 25.34, and 20.39) mm/sec, over a quantified fields on 1st ,2nd, and 3rd rows, respectively. Whereas the maximum horizontal velocities near the right side wall were (-24.48, -18.47, -15.98) mm/sec, over a measured fields on 1st ,2nd, and 3rd rows, respectively.

Figure 13-32 shows the optimal DEM results of average vertical and horizontal velocities components distributions over measurable fields along the horizontal direction of 1st ,2nd, and 3rd rows from the bottom wall. Figure 13-32 (a) illustrated that the maximum vertical velocities near the left side wall were (27.18, 23.21, and 20.61) mm/sec, over a quantified fields on 1st ,2nd, and 3rd rows, respectively. Whereas the maximum vertical velocities near the right side wall were (-27.56, -16.4, -12.09) mm/sec, over a measured fields on 1st ,2nd, and 3rd rows, respectively. Figure 13-32 (b) illustrated that the maximum horizontal velocities near the left side wall were (22.56, 20.01, and 17.31) mm/sec, over a quantified fields on 1st ,2nd, and 3rd rows, respectively. Whereas the maximum horizontal velocities near the right side wall were (-22.05, -16.43, and -10.76) mm/sec, over a measured fields on 1st ,2nd, and 3rd rows, respectively.

In this kind of inclined vibration mode, the horizontal velocity accompanying the vertical velocity in same phase causes the tub finisher to follow a closed vibration path. Thus, a single-cell circulation is observed in the present media flow, where the left wall tends to push the media upward in the direction of the right wall while the right wall pushes the media downward in the direction of the left wall. The resultant velocities along the bottom wall of the tub finisher also contribute in changing media direction from right wall to the left wall. It is clearly noticed that the average vertical and horizontal velocities distribution reached their maximum values near the location of 1st row. However, the circulation flow obtained in this study is in good agreement with the result obtained by (Naeini 2011) .

As displayed the velocities distribution follows the same trend of experimental results. The vertical and horizontal velocities along the left and right wall increases toward positive and negative directions, respectively. These velocities drop to the lower values in the central part. It is clearly noticed that the DEM results underestimate the experimental vertical and horizontal components of velocities in all row levels and measurable field positions. This may be attributed to the fact that in the DEM simulation, the linear Hertz-Mindlin model limits shear forces to the friction of normal forces known by the coefficient of friction. In almost all particle-wall contacts, the tangential velocity is large enough to achieve this limitation. However, in a few cases of inclined vibration, the particles impact the bottom wall in a vertical component of velocity, thus the tangential velocity can be significantly below this threshold, and the particles are predicted to slide over the bottom wall.

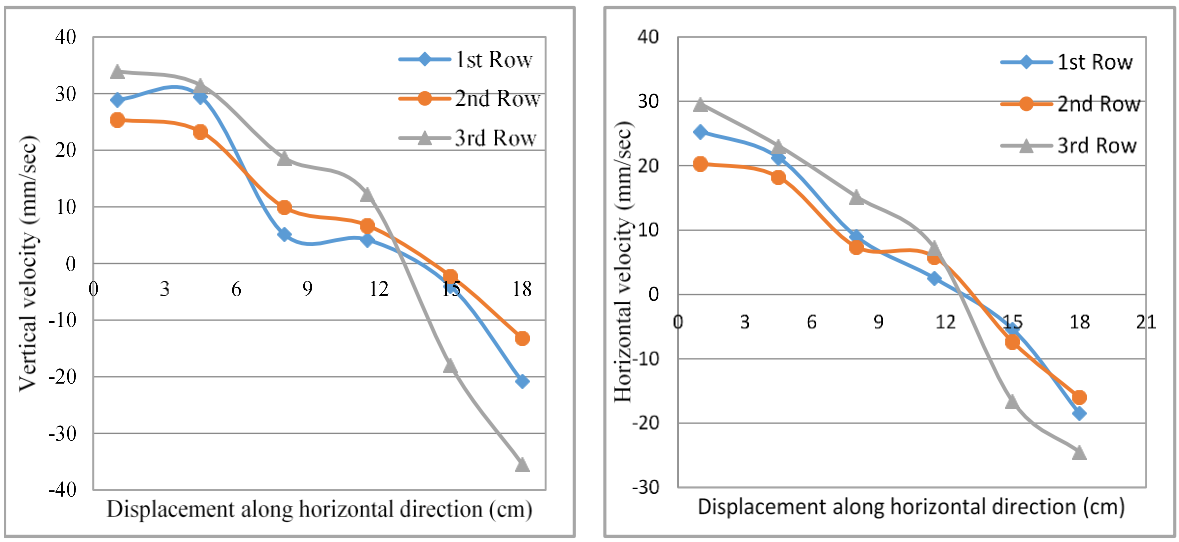

(a) (b)

Figure 13-31 Experimental vertical and horizontal velocities components distribution on 1st, 2nd , and 3rd rows from the bottom wall at: a) Vertical velocity component, and b) Horizontal velocity component

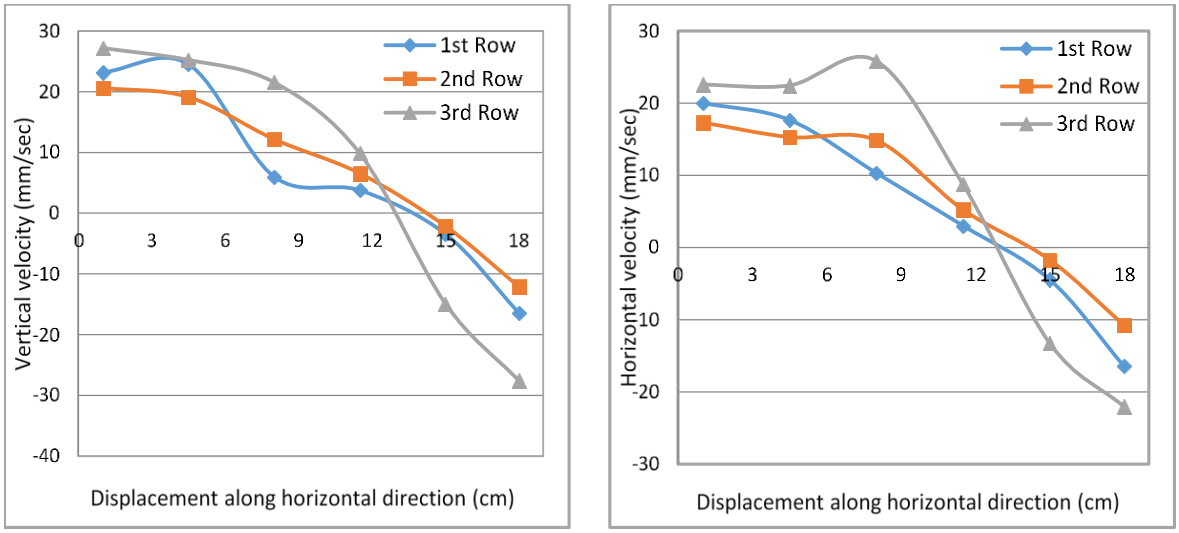

(a) (b)

Figure 13-32 Numerical (DEM) vertical and horizontal velocities components distribution at 1st, 2nd, and 3rd rows from the tub bottom at: a) Vertical velocity component, and b) Horizontal velocity component

13.11 Conclusion

A 2-dimensional flow of thermally treated conical glass media with two different load (partial media load, and full media load) conditions was modelled using the discrete element method DEM. Optimal contact parameters were determined using an optimization method by distinguishing the DEM and experimental bulk flow velocities results by means of PIVLab technique. The PIVLab technique was successfully employed to predict the velocity vectors within the experimental flow of conical media and DEM simulation. The developed technique is shown to have the capability to determine more precisely the velocity field vectors of non-spherical particulate systems.

Using optimal contact parameters, the DEM simulated bulk velocities at five locations of partially and fully loaded conditions were on average within 17%, and 14% of the measured values, respectively. The results suggested that the bulk flow velocity increases with the increasing the numbers of particles. As a consequence, the resulting shear force and the strength of media circulation increases.

The bulk expansions of the inclined vibration tub finisher with different load conditions were determined at steady state conditions. The total bulk expansion in the tube with full loaded of conical media was measured to be 14% (∓4%) , while the DEM simulations predicted value was 9% (∓2%).

The tube with partially loaded condition, the measured bulk expansion increases to 17% (∓4%), while the DEM simulations predicted value increases to 13% (∓3%). The optimal contact parameters that were determined by the optimization method to fit the experimental bulk velocity had a relatively small influence on the predicted bulk expansion.

The experimental and numerical horizontal and vertical velocities distributions in particular field locations along the horizontal direction of the partially loaded tub finisher were determined at different levels of rows from the bottom wall. Both experimental and DEM observations confirmed that the vertical and horizontal velocities distributions change with the depth of media in the tub finisher. Consequently, there are strong relationships between the strength of circulation that depends on the horizontal and vertical velocities distributions and the total shear force along the tub finisher walls. However, bulk circulation increased significantly in the positive and negative direction near the left and right tub walls, respectively. Therefore, the pressure and forces at the tub finisher walls and between media were increased accordingly. It is clearly noticed that the bulk circulations reached their maximum values near the location of the 1^{st} row followed by the 3^{rd} row.

It was hypothesized that the larger values of the vertical velocity create larger impact intensities and residual stress within the material, while increasing the tangential velocity to the specimen results in more abrasive processing of the specimen and a smoother surface. In absolute terms, the DEM predicted results were consistently smaller than the experimental values. The maximum discrepancy between numerical and experimental vertical components of velocities were 20%, 19%, and 17% along the horizontal direction of 1^{st} ,2^{nd}, and 3^{rd} rows, respectively. While the maximum difference between numerical and experimental horizontal velocities components were 22%, 18%, and 19% along the horizontal direction of 1^{st} ,2^{nd}, and 3^{rd} rows, respectively.

13.12 References

Adrian, R. J. (1991). "Particle-imaging techniques for experimental fluid mechanics." Annual review of fluid mechanics **23**(1): 261-304.

Adrian, R. J. and J. Westerweel (2011). Particle image velocimetry, Cambridge University Press.

An, X., C. Li, R. Yang, R. Zou and A. Yu (2009). "Experimental study of the packing of mono-sized spheres subjected to one-dimensional vibration." Powder Technology **196**(1): 50-55.

Ashmawy, A. K., B. Sukumaran and V. V. Hoang (2003). Evaluating the influence of particle shape on liquefaction behavior using discrete element modeling. Proc. Offshore and Polar Engineering Conference.

Asmar, B., P. Langston, J. Walters, A. Matchett and T. Yanagida (2006). "Distinct element model of energy dissipation in vibrated binary particulate mixtures." Particulate science and technology **24**(4): 395-409.

Baghbanan, M. R., A. Yabuki, R. S. Timsit and J. K. Spelt (2003). "Tribological behavior of aluminum alloys in a vibratory finishing process." Wear **255**(7): 1369-1379.

Buchhave, P. (1992). "Particle image velocimetry—status and trends." Experimental Thermal and Fluid Science **5**(5): 586-604.

Cariapa, V., H. Park, J. Kim, C. Cheng and A. Evaristo (2008). "Development of a metal removal model using spherical ceramic media in a centrifugal disk mass finishing machine." The International Journal of Advanced Manufacturing Technology **39**(1-2): 92-106.

Ciampini, D., M. Papini and J. Spelt (2007). "Impact velocity measurement of media in a vibratory finisher." Journal of materials processing technology **183**(2): 347-357.

Cundall, P. A. and O. D. Strack (1979). "A discrete numerical model for granular assemblies." Geotechnique **29**(1): 47-65.

Elata, D. and J. G. Berryman (1996). "Contact force-displacement laws and the mechanical behavior of random packs of identical spheres." Mechanics of Materials **24**(3): 229-240.

Favier, J., M. Abbaspour-Fard and M. Kremmer (2001). "Modeling nonspherical particles using multisphere discrete elements." Journal of Engineering Mechanics **127**(10): 971-977.

Herrmann, H. and S. Luding (1998). "Modeling granular media on the computer." Continuum Mechanics and Thermodynamics **10**(4): 189-231.

Hertz, H. (1881). "On the contact of elastic solids." J. reine angew. Math **92**(156-171): 110.

Hogue, C. and D. Newland (1994). "Efficient computer simulation of moving granular particles." Powder Technology **78**(1): 51-66.

Jensen, R. P., P. J. Bosscher, M. E. Plesha and T. B. Edil (1999). "DEM simulation of granular media—structure interface: effects of surface roughness and particle shape." International Journal for Numerical and Analytical Methods in Geomechanics **23**(6): 531-547.

Johnson, K., K. Kendall and A. Roberts (1971). Surface energy and the contact of elastic solids. Proceedings of the Royal Society of London A: Mathematical, Physical and Engineering Sciences, The Royal Society.

Kawaguchi, T., T. Tanaka and Y. Tsuji (1998). "Numerical simulation of two-dimensional fluidized beds using the discrete element method (comparison between the two-and three-dimensional models)." Powder technology **96**(2): 129-138.

Kim, B. J., C. Swarup and H. J. Sung (1961). "Interpolation for image deformation in PIV." Appl. Csi. Res. A **6**: 114.

Kloss, C. and C. Goniva (2010). LIGGGHTS: a new open source discrete element simulation software. Proceedings of The Fifth International Conference on Discrete Element Methods, London, UK.

Lin, X. and T.-T. Ng (1997). "A three-dimensional discrete element model using arrays of ellipsoids." Geotechnique **47**(2): 319-329.

Lourenco, L. (1994). "Particle image velocimetry."

Mindlin, R. D. and H. Deresiewica (2014). "Elastic spheres in contact under varying oblique forces." Journal of applied mechanics **20**.

Mohajerani, A. and J. Spelt (2010). "Numerical modeling of the edge rounding of brittle materials by vibratory finishing." Wear **268**(7): 1002-1012.

Naeini, M. S. E. (2011). Discrete Element Modeling of Granular Flows in Vibrationally-Fluidized Beds, University of Toronto.

Okamoto, K., S. Nishio, T. Saga and T. Kobayashi (2000). "Standard images for particle-image velocimetry." Measurement Science and Technology **11**(6): 685.

Pournin, L. and T. M. Liebling (2009). From spheres to spheropolyhedra: generalized distinct element methodology and algorithm analysis. Research trends in combinatorial optimization, Springer**:** 347-363.

Prasad, A. K. (2000). "Particle image velocimetry." Current science-bangalore- **79**(1): 51-60.

Sitharam, T. G. (2000). "Numerical simulation of particulate materials using discrete element modelling." Current Science **78**(7): 876-886.

Sommerfeld, M. (2001). "Validation of a stochastic Lagrangian modelling approach for inter-particle collisions in homogeneous isotropic turbulence." International Journal of Multiphase Flow **27**(10): 1829-1858.

Soria, J. (1996). "An investigation of the near wake of a circular cylinder using a video-based digital cross-correlation particle image velocimetry technique." Experimental Thermal and Fluid Science **12**(2): 221-233.

Stronge, W. J. (2004). Impact mechanics, Cambridge university press.

Talu, I., G. I. Tardos and M. I. Khan (2000). "Computer simulation of wet granulation." Powder Technology **110**(1): 59-75.

Tatemoto, Y., Y. Mawatari, T. Yasukawa and K. Noda (2004). "Numerical simulation of particle motion in vibrated fluidized bed." Chemical engineering science **59**(2): 437-447.

Thielicke, W. and E. J. Stamhuis (2010). "PIVlab-time-resolved digital particle image velocimetry tool for matlab." Published under the BSD license, programmed with MATLAB **7**(0.246): R14.

Thomas, P. A. and J. D. Bray (1999). "Capturing nonspherical shape of granular media with disk clusters." Journal of Geotechnical and Geoenvironmental Engineering **125**(3): 169-178.

Ting, J. M. and J. D. Rowell (1995). ELlipse-based Discrete Element Model for Granular Materials: Validation Testing. Engineering Mechanics (1995), ASCE.

Wang, S., R. Timsit and J. Spelt (2000). "Experimental investigation of vibratory finishing of aluminum." Wear **243**(1): 147-156.

Wassgren, C. R. (1997). Vibration of granular materials, California Institute of Technology.

Willert, C. E. and M. Gharib (1991). "Digital particle image velocimetry." Experiments in fluids **10**(4): 181-193.

Yabuki, A., M. Baghbanan and J. Spelt (2002). "Contact forces and mechanisms in a vibratory finisher." Wear **252**(7): 635-643.

Zeilstra, C., J. Collignon, M. Van der Hoef, N. Deen and J. Kuipers (2008). "Experimental and numerical study of wall-induced granular convection." Powder Technology **184**(2): 166-176.

CHAPTER FOURTEEN

PROCESS OPTIMISATION SYSTEM

14.1 Introduction

The optimisation of a machining process or of processes that have a wide range of variables is very challenging and is rarely achieved without extensive experimental and production testing and the knowledge contributions from process experts. It is also the case that optimised parameters are frequently overtaken by developments within the field. These results in inefficient production and a consequent higher cost per part. It is also deleterious in respect of environmental impact. There is no quick and easy method to achieve optimal machining and much research has been completed / is ongoing in this area. Importantly, there are very few methods, if any, able to inform the user that optimal conditions have in fact been achieved. It is generally the domain of the operator to advise the process planner / designer how parameters may be modified in an effort to improve productivity without increased risk to part quality. This situation, clearly unsatisfactory and not-sustainable, has been a key driver in the research of more advanced machining control system technologies / systems. Methods to deliver optimal machining are most commonly based on adaptive control (A/C) techniques. In such cases continual process monitoring is undertaken and machining parameters automatically modified when a target threshold is breached or approached. The most advanced A/C techniques may also be supported with intelligent systems that employ strategies to manage historical data in an efficient and intelligent manner. However, and similarly, strategies for optimisation and process control are prone to redundancy due to advances in the technology; by higher quality demands or by the more practical challenges met in attempting to introduce and implement an A/C system (operator reluctance, software engineering and others).

It was within this context that an ambitious programme of research was initiated to develop a process optimisation method for application in the fast emerging and increasingly important area of mass finishing process (MF) such as drag finishing and stream finishing. MF typically requires a large number of parameters to be set prior to cycle start.

Despite the widespread application of mass finishing processes, the fundamentals of this process have not yet been rigorously researched. The majority of publications on vibratory finishing come from an industrial source, the choice of values for the parameters are presently based on experience and expert knowledge, and lack basic scientific standards.

There are no measurements available to inform the user of production parameters needed to achieve target criteria of surface roughness e.g. (Hashimoto and DeBra 1996, Arvin 2002, Davidson 2008). More articles have been published on empirical studies of applications of vibratory mass finishing process, which has led to some understanding about the influence of vibration amplitude, frequency, cycle time, and abrasive media on the metal removal rate and surface roughness (Matsunaga 1967, Wang, Timsit et al. 2000, Takahashi, Kataoka et al. 2005, Sangid, Stori et al. 2011) . However, most of them are not valid for generic vibratory finishing processes

The most significant generic findings are given by: Domblesky, Cariapa et al. (2003), and Domblesky, Evans et al. (2004); the authors state that the metal removal rate per unit time is constant and a function of velocity, bowl acceleration, workpiece material, and specific energy. Cariapa, Park et al. (2008) developed a metal removal model combined with a model for the media movement for a centrifugal disk mass finishing process. Uhlmann, Dethlefs et al. (2014) developed a model that combines machining process parameters and metal removal mechanisms validated with an empirical process model that can be used to predict surface roughness of material for given parameters. DEM simulation was also performed to investigate the contact between media and workpiece.

Up to now, no analysis of the drag and stream finishing process is available. A comprehensive process model is currently being developed by Barletta, Rubino et al. (2014). The experimental practice has allowed an increase in the knowledge of the modelling of fluidized bed assisted drag finishing. However, the comprehensive basic mechanism involved during MF process and a theoretical model concerning the surface roughness and metal removal are still missing. Barletta, Gisario et al. (2014) established a comparative study of fluidized bed assisted drag finishing and centrifugal disc finishing. The results showed that the fluidized bed assisted drag finishing was more efficient than centrifugal disc finishing in both achievable surface roughness quality and reduced processing time.

To lessen such uncertainty in knowledge of efficiency, cost and in achievable quality, we have now developed a software tool that is able to predict cycle efficiency over a wide range of parameters and identify an optimal set of parameters one should employ to deliver any stated target criteria. This information can then readily be extrapolated to give production cost. Additionally, the system will also predict cost and efficiency when parameters are modified in any way and predict the consequence on achievable quality.

In this study, the core of the system is based on readily available and well-understood proprietary statistical and mathematical software packages. The tools used are ANOVA, The Taguchi experimental methodology and the Response surface methodology (RSM) coupled with a MATLAB - Graphical User Interface (GUI) code to develop a surface roughness prediction model of advanced mass finishing technology (drag and stream finishing processes) under various machining parameters conditions. This model can be used to estimate process parameters needed to achieve a desired roughness of a workpiece.

The usefulness of the system is not restricted to optimisation in the production context. It can also be used as design tool or as a production planning aid. As a design tool it can provide optimal parameter sets for materials new to the process or not in common use, and as a planning tool to plan production cycles to match related operations and to avoid misalignment of outputs with other processes, or to ensure maximum machine utilisation or indeed both. Further, it has potential to be of great benefit to machine tool 'systems' salespersons and production engineers in the field.

14.2 Process under investigation

The latest development of mass finishing technologies of drag and stream finishing processes was investigated. The stream finishing machine Figure 14-1 (a) is a completely new concept which features short processing times, easy automation and excellent reliability. It produces a good mirror finish even inside the channels. In this process, the workpieces are held by special jig arrangements and then immersed in fast flowing and circulating grinding or polishing medium. The process times are tremendously short compared with traditional mass finishing process. For example in workpieces made of aluminium, the roughness of Ra 0.9 µm can be reduced to Ra 0.05 µm in minutes through a single step dry finishing process.

In the drag finishing process Figure 14-1 (b), workpieces are mounted on special holders. These are dragged in a circular motion at high speed through a container filled with grinding or polishing media. The circular motion creates high contact pressures between the workpieces and the media, producing good results in short time in the form of high-precision rounding of the edges or high finish in a quality that can otherwise only be obtained through hand polishing.

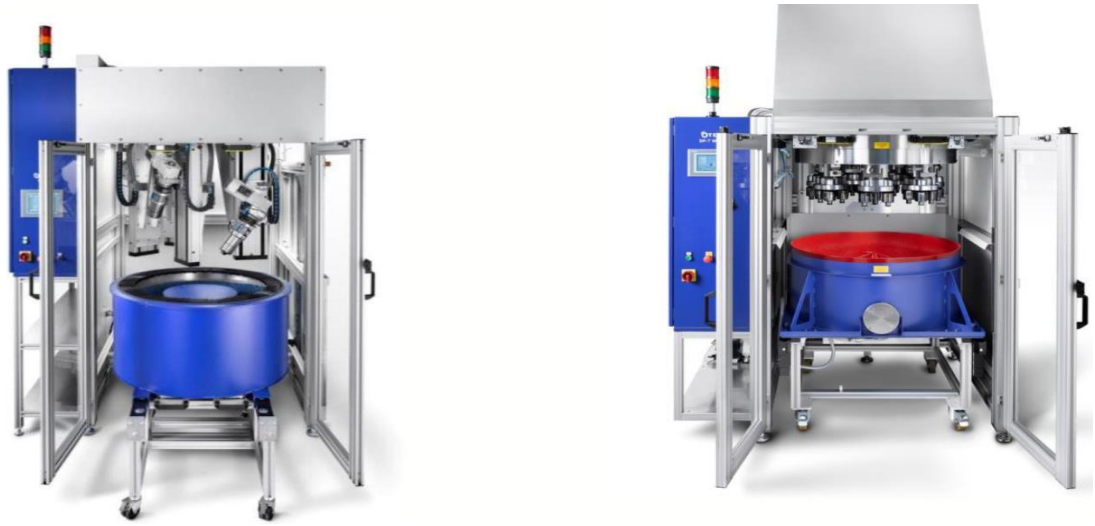

(a) (b)

Figure 14-1 Advanced mass finishing techniques a) Stream finishing process, b) drag finishing process (OTEC)

14.2.1 Drag finishing in comparison with Stream finishing

Stream Finishing process	Drag Finishing process
The applications of stream finishing process are : deburring, edge honing, the smoothing and polishing is 5-10 times faster than drag finishing process due to the generation of additional centrifugal forces.	The application of drag finishing process are : deburring, edge honing, smoothing and polishing
Number of processing per batch: - up to 5 processing stations, in manual operation up to 5 tools per batch, easy to automate process.	Number of processing per batch:- up to 60 tools per batch for manual charging.
Targeted and / or focused localized surface finish processing.	Required low operation effort.
Suitable for processing of long tools, due to the deep container	Not suitable for long tools processing

14.3 Statistical software package

Minitab 17 is a statistical software package for analysing data in a statistical environment that allows the user to determine accurate and reliable results by selecting design of experiment (DOE) strategy. Design of Experiment is one of the important statistical techniques to study the effect of multiple parameters simultaneously that includes a sequence of steps which must be followed by a certain experiment in order to enhanced understanding of process performance (Roy, Paul et al. 2009) . DOEs require a certain number of combinations of factors and levels to be examined in order to observe the results of those test conditions.

Minitab also consists of many statistical analysis methods in one software package, including ANOVA, regression analysis, response surface methodology, Taguchi method, Factorial method, , quality and reliability tool, control multiple design process, etc. The user can calculate, and verify the results using different methods in this package.

14.3.1 Taguchi method

Taguchi is a statistical experimental tool designed to calculate a single or multiple groups of data (variable) to find the optimal and regularity in the operating environment (response) (Taguchi and Konishi). It also used to identify the controllable and un-controllable factors in order to minimize the effect of noise factors. The Taguchi method is also used to estimate the effect of each factor within the orthogonal array relative to the means and variance. The orthogonal array matrix is designed to investigate the effect of each factor independently from others in order to reduce time and cost. The main objective is to identify the ranks of each factor that affect the mean response. However, the limited orthogonal array design in the Taguchi method fails to deal with the interaction effect between important factors.

The Taguchi method employed a statistical evaluation of performance called signal-to-noise (*S/N*) ratio approach to measure the quality characteristic deviation from the design value. The *S/N* ratio can be used instead of the average value for the evaluation characteristic in the optimum variable analysis (Phadke, Kackar et al. 1983, Pignatiello JR 1988, Pease 1993).

The *S/N* ratio approach can be divided into three quality tools: the smaller the better, the nominal the better, and the higher the better when characterizing the response quality for engineering process. In this study, the smaller the better of the surface roughness was considered in investigating the influence of machining variables in drag and stream finishing process. The *S/N* ratio of smaller the better quality characteristics can be defined by Eq. (14.1).

$$\frac{S}{N} = -10 \log \left[\sum_{i=1}^{n} \frac{Y^2}{n} \right] \tag{14.1}$$

where $(Y^2)/n$, is the mean square of measured data at i test, and n is the number of repetitions

14.3.2 Analysis of variance method (ANOVA)

ANOVA is a statistical method to identify the differences between two or more independent groups of variables. The variance results are explained in their degree of freedom (DF), the mean square (MS), and total sum of square (SS). The ANOVA will calculate also the F-statistic and p-values, which are used to determine whether the factor is significant/dominant, related to the response.

The ANOVA is used to test the availability of the surface roughness model in the process optimization of drag and stream finishing processes. F-statistics and p-value were applied on each term of both models to investigate the significant variables. The effect is considered statistically significant wherever the p-value is less than 0.05 due to the test set up condition being at the 5% level of significance or 95% confidence. The "lack of fit value" result represents the variation of actual experimental data around the predicted model. If the "lack of fit" is not significant, it indicates that the model fits the data. The R^2 value is used to indicate the acceptability of a fitted least square model which estimates the variance around the mean values, and the adjusted R^2 value is a measure of the variation around the mean of adjusted model terms (Reisgen 2012). The accuracy of the model is defined by the difference between R^2 and adjusted R^2. A small difference indicates a good model.

14.3.3 Response Surface Methodology (RSM)

Response Surface Methodology (RSM) is the useful statistical analysis tool used to investigate the relationship between response and a set of quantitative experimental factors at different levels. Shi, Zhang et al. (2014) proposed that the RSM performs better statistical analysis compared with other techniques when a large number of experiments are not possible. RSM is a statistical method based on least squares theory founded on the linear, linear with interactions and quadratic polynomial equations between input factors at different levels and responses. Then, these equations will aim to determine the appropriate range of process parameters.

The independent variables $x_{1,}\, x_{2\ldots}x_n$ are assumed continuous which can be controlled with negligible errors ($\mp\epsilon$). The response Y, is supposed to be a random variable. In general test conditions, it is possible to characterize the independent variables in a quantitative form that has a functional relationship with the response Y. This can be expressed in Eq.(14.2) (Montgomery 2008).

$$Y = f(\, x_1, x_2, \ldots x_n) \mp \epsilon \tag{14.2}$$

In this study, the quantitative form of the relationship between the response variable and independent variables is given by Eq. (14.3), and Eq.(14.4) of drag and stream finishing processes, respectively.

$$R_a = f(\, DSS, DHS, DID\,) \mp \epsilon \tag{14.3}$$

$$R_a = f(\, SHS, SBS, SID) \mp \epsilon \tag{14.4}$$

where DSS is drag spindle speed and DHS is drag head speed and DID is the drag immersion depth. SHS is stream head speed, SBS is stream bowl speed and SID is the stream finisher immersion depth.

The main advantage of RSM is the capability to exhibit the factor contributions from the coefficients in the regression analysis model. This capability is a powerful tool to classify the insignificant factors, insignificant interactions, or insignificant quadratic terms in the design model, thus the complexity and difficulties of the problem can be overcome.

However, the functional relationship between a response and process parameters is illustrated by a second order polynomial response surface that can be fitted by Eq. (14.5) (Montgomery 2008).

$$Y = \beta_0 + \sum_{i=1}^{n} \beta_i x_i + \sum_{i=1}^{n} \beta_{ii} x_i^2 + \sum_{i}^{n} \sum_{j}^{n} \beta_{ij} x_i x_j + \epsilon \qquad (14.5)$$

Where β are the coefficients, which are calculated by appropriate least square method.

14.4 Experimental design and setup

On-site experimental investigations were carried out at Finishing Technique Ltd. using drag and stream finishing OTEC machines as is shown in the experimental set-up Figure 14-2. Aerospace turbine blades were used in the experiments with average surface roughness values of 1.9 µm (∓ 0.1µm). Liquid compound SC15 at a constant dosing rate of 3%, and plastic media KM10 were employed in the tests. All experiments were performed at a constant processing time of 20min. The machining parameters were selected as follows: The experimental tests that involve drag finishing were performed with variable spindle speed, DSS within range $(10 \leq DSS \leq 80)$ rpm, the head speed, DHS various within range $(10 \leq DHS \leq 60)$rpm and the immersion depth $, ID$ various within range$(300 \leq DID \leq 380)$ mm. In the case of stream finishing, the experimental tests were performed with high power head speed SHS, which varies within the range $(40 \leq SHS \leq 1500)$ rpm, the bowl speed, SBS various within range $(20 \leq SBS \leq 60)$ rpm, and the immersion depth $, SID$varies within range $(100 \leq SID \leq 300)$ mm. Another important parameter that should be considered in the drag and stream finisher is the angled head of the workpiece. Due to the shape of the turbine blade, the angled head was selected to be zero in all tests using a special holding arrangement to ensure continuous flow of media on the workpiece surface during operation. The positions of workpieces in the stream finisher were selected to be the same for all experiments, 10 cm away from the bowl wall which provided the best media flow according to (OTEC 2013).

The surface roughness tests were carried out by tracing the surface using a Tylor Hobson surface instrument at several positions along the workpiece surface before and after finishing processes as is shown in Figure 14-3.

Three surface roughness measurements were performed on each workpiece material, the average of the group results are presented in this study. The process optimization system (POSY) of Taguchi, ANOVA, and Surface response methodologies were conducted to develop a mathematical model used to predict the surface roughness of an aerospace component. In general, POSY is based on 10-steps of planning, performing and evaluating results of matrix experiments to determine the performance levels of control parameters. Figure 14-4 illustrate a schema of the Process Optimization System. Those ten steps are given as follows:

- The pre-experiment step, which consists of identifying the performance characteristics (responses) to optimize and process parameters to control (test).
- Select the number of levels required for each of the tested parameters.
- Select an appropriate orthogonal array Based on the problem complexity, and then assign each parameter into the orthogonal array.
- Conduct an experiment based on the random arrangement of the orthogonal array.
- Statistical analysis data were obtained for each combination of the tested parameters based on Taguchi, ANOVA, and RSM.
- Evaluate the experimental result and determine the optimal level for each of the process parameters.
- The mathematical model established for each set of process parameters.
- POSY developed within MATLAB code using GUI system.

Figure 14-2 Experimental set up a) Drag finishing process, b) Stream finishing process

Figure 14-3 Tylor Hobson surface roughness measurement of aerospace turbine blade

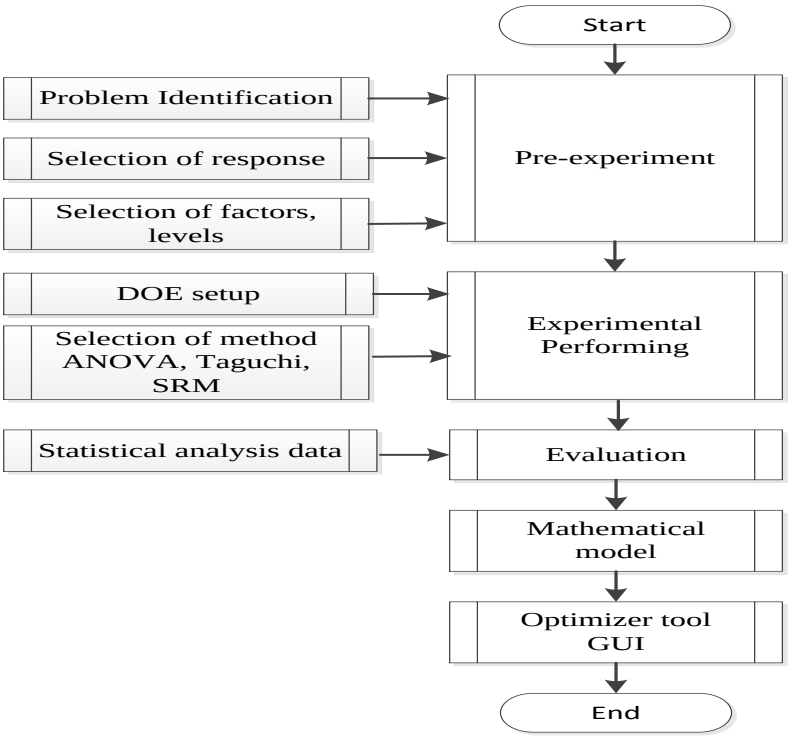

Figure 14-4 A schema of the Process Optimization System

14.5 Results and discussions

14.5.1 Analysis of the signal-to-noise (S/N) ratio (Taguchi method)

The S/N number represents the ratio between desirable and non-desirable values. The process parameter with the highest value causes the most significant effect on the optimization process (Phadke 1995). In this study, the Taguchi optimization process was selected for six degree of freedom, three factors and three levels. The process parameters and their levels in drag and stream finishing processes were presented in Table 14-1, and Table 14-2, respectively.

The process variables and their levels were set up over a wide range of parameters in order to cover a comprehensive performance capability of THE finishing processes. A set of experiments were conducted on drag and stream finishers using the L9 orthogonal array with nine experiments. Table 14-3, and Table 14-4 shows the DOE layout and results of drag and stream finishing processes, respectively. Due to different units within the process parameters, each factor need to be coded with three levels -1, 0, 1. The influence of interaction between variables is neglected in the Taguchi method. Regardless of the machining process characteristics, a greater S/N value is related to a better performance. Therefore, the optimal level of the machining parameters is responding to the greatest S/N value. Based on the S/N ratio analysis, the optimal drag finisher performance for better surface roughness was obtained at 80 rpm spindle speed (level 3), 10 rpm head speed (level 1) , and 380 mm immersion depth (level 3). While the optimal stream finisher performance was obtained at 60 rpm bowl speed (level 3), 1500 rpm head speed (level 3), and 300 mm immersion depth (level 3). Optimal finishing conditions for drag and stream finishing processes are shown in Table 14-5, and Table 14-6, respectively. Table 14-5 illustrates that the rank 1 indicates that spindle speed factor has the strongest effect on the finishing process followed by rank 2 the head speed, while rank 3, the immersion depth has the minimum effect on the process. Table 14-6 shows that the rank 1 indicates that the immersion depth factor has the strongest effect on the finishing process followed by rank 2 the head speed, whereas rank 3 the bowl speed has the minimum effect on the process.

Figure 14-5 shows the main effects plots for *S/N* ratio. The strongest influence of the factor on the finishing process is measured by differences values. The factor contributes with higher difference in the mean S/N ratio over the selected design control factor, the more significant impact. Optimal finishing conditions of design control factors of drag and stream finishing processes can be determined from the *S/N* response graphs in Figure 14-5 (a, and b) respectively. The lower the better S/N ratios was assigned to determine the influence of (DSS,DHS, and DID) factors of drag finisher and also the effect of (SHS,SBS, and SID) factors of stream finisher on the surface roughness values of the turbine blades. As displayed, the spindle speed shows the higher slope of the S/N ratio, which identifies the significant impact on the finishing process. It is also noticed that the immersion depth has a remarkably significant effect on the stream finishing process.

However, the results demonstrated that the surface roughness decreases with the increasing drag spindle speed, and stream head speed. The S/N ratios for the other factors had less influenced between the three levels.

Table 14-1 Drag finishing process parameters and their levels

Process parameter	Level 1	Level 2	Level 3
Spindle speed (DSS)	20	40	80
Head speed (DHS)	10	30	50
Immersion depth (DID)	300	340	380

Table 14-2 Stream finishing process parameters and their levels

Process parameter	Level 1	Level 2	Level 3
Bowl speed (SBS)	20	40	60
Head speed (SHS)	500	1000	1500
Immersion depth (SID)	100	200	300

Table 14-3 DOE lay out and drag finishing results using Taguchi method

No.	DSS	DHS	DID	Ra	S/N
1	-1	-1	-1	1.69	-4.558
2	-1	0	0	1.12	-0.984
3	-1	1	1	0.6	4.437
4	0	-1	0	1.75	-4.861
5	0	0	1	1.22	-1.727
6	0	1	-1	0.65	3.742
7	1	-1	1	1.71	-4.660
8	1	0	-1	1.48	-3.405
9	1	1	0	0.84	1.514

Table 14-4 DOE lay out and stream finishing results using Taguchi method

No.	*DSS*	*DHS*	*DID*	Ra	S/N
1	-1	-1	-1	0.78	2.158
2	-1	0	0	0.63	4.013
3	-1	1	1	0.31	10.458
4	0	-1	0	0.63	4.013
5	0	0	1	0.48	6.375
6	0	1	-1	0.57	4.883
7	1	-1	1	0.67	3.479
8	1	0	-1	0.51	5.849
9	1	1	0	0.35	9.119

Table 14-5 S/N Ratios for surface roughness using drag finisher

Level	Head Speed (rpm)	Spindle Speed (rpm)	Immersion Depth (mm)
1	1.0660	1.6800	1.2980
2	1.2533	1.2933	1.2673
3	1.3480	0.6940	1.1020
Delta	0.2820	0.9860	0.1960
Rank	2	1	3

Table 14-6 S/N Ratios for surface roughness using stream finisher

Level	Bowl Speed (rpm)	Head Speed (rpm)	Immersion Depth (mm)
1	0.6076	0.6553	0.7013
2	0.5804	0.6049	0.6049
3	0.4893	0.4601	0.4232
Delta	0.1183	0.1952	0.2781
Rank	3	2	1

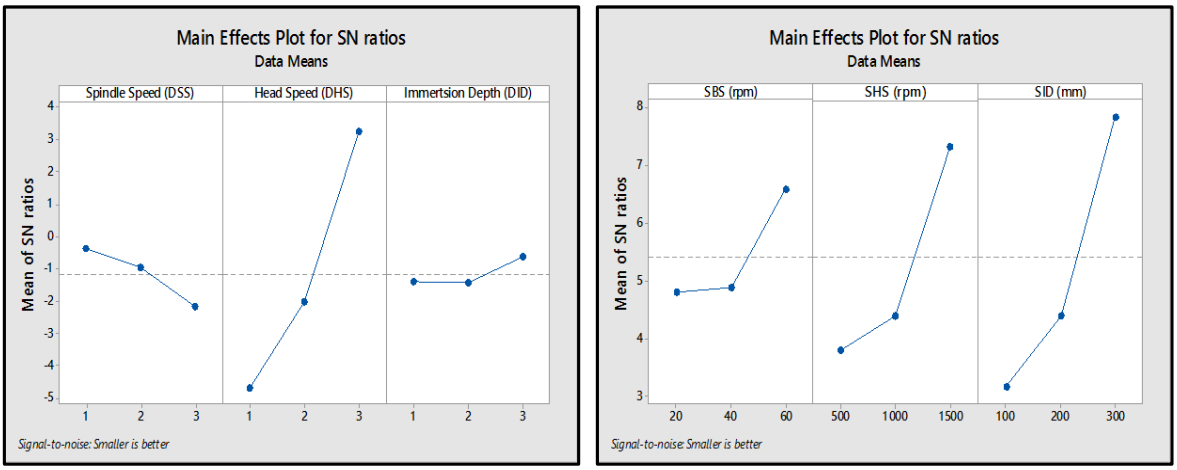

(a) (b)

Figure 14-5 Effect of process parameters on surface roughness by a) Drag finisher, b) Stream finisher

14.5.2 Development of Response Surface Model

The statistical analysis using the Taguchi method presented in section (14.5.1) is an analysis only for the main factors that affect surface roughness without any consideration of correlation and interaction between control factors. Therefore, response surface methodology RSM was employed to predict the surface roughness of aerospace components in drag and stream finishing processes.

The essential data required for developing the RSM have been collected by design of experiments based on central composites design (CCD) arrangement. CCD is a second order polynomial design, which was introduced by Box and Wilson, and graphically can be represented as a cube consisting of factorial or fractional factorial design with axial and centre points. The CCD of the three-factor design includes 8- factorial points, 6- axial points, and 6- central points in the cube. In this study, the DOE system used for RSM consisted of 20 experiments of three factors with three levels each. Full replication was used to analyse and optimize the main effects and interaction of process parameters of drag and stream finishing techniques. The process factors and their levels in drag and stream finishing processes were presented in Table 14-1, and Table 14-2, respectively, the three level design of each coded factor given as -1, 0, 1. Table 14-7 and Table 14-9 shows the DOE layout and results of drag and stream finishing processes, respectively.

Based on three independent control factors and their levels, the statistical models were formalized into second order polynomial mathematical relationships (quadratic model) to explain the effect of parameters with interaction given by Equations (14.6), and (14.7) for drag and stream finishers, respectively. The models' coefficients were obtained using a multiple regression analysis (MINITAB 17).

$$R_a(DF) = 0.85 - 3.83 \times 10^{-2}DSS + 7.4 \times 10^{-3}DHS + 1.09 \times 10^{-2}DID + 7.6 \times 10^{-3}(DSS)^2 - 8 \times 10^{-3}(DHS)^2 - 2.4 \times 10^{-5}(DID)^2 - 9.7 \times 10^{-5}(DSS)(DHS) + 5 \times 10^{-5}5(DSS)(DID) + 1.4 \times 10^{-5}(DHS)(DID) \quad (14.6)$$

$$R_a(SF) = 0.726 + 1.03 \times 10^{-3}SBS + 4.65 \times 10^{-4}SHS - 1.14 \times 10^{-3}SID - 1.33 \times 10^{-4}(SBS)^2 + 1.1 \times 10^{-6}(SHS)(SBS) - 1.2 \times 10^{-6}(SHS)(SID) + 3.11 \times 10^{-6}(SBS)(SID) \quad (14.7)$$

14.6 Models accuracy and fitness analyses

The analysis of variance (ANOVA) was applied to calculate the significance of the coefficients and suitability of models in determining the mathematical relationships between the response (surface roughness) and the machining parameters in the drag and stream finishing processes. Tables 14-8, and Table 14-10 show the ANOVA results for surface roughness obtained by the drag and stream finishing processes. In the case of the drag finishing process, the presented ANOVA result shows that the model F value was 86.94, which demonstrated it is significant. The significance was proved by the value of P < 0.05 (i:e $\alpha = 0.05, \text{or } 95\%$ confidence), this indicates that the model terms are significant. The significance of the first order parameters can be clearly observed Head speed, (DHS), spindle speed (DSS), and immersion depth, (DID) in the quadratic model. The interactions between$(DSS \,\&DHS)$,and$(DSS\&DID)$ were also found to be significant. The insignificant terms of the second order parameters $(DSS)^2$, $(DHS)^2, and\ (DID)^2$and interaction $(DHS\&DID)$ were eliminated (model reduction) to simplify and improve the surface roughness model.

The R^2 value of 98.43% is close to unity, which indicates a good agreement between the predicted model and actual experimental data. The adjusted R^2 value of 97.6% is close to the R^2 value, indicating the good fitness of the experimental data to the predicted quadratic model. The ANOVA shows that the adequate precession value was 23.35, which is greater than 4, and indicates the predicted model was significant. The lack to fit value of 0.094 represents an insignificant effect, which indicates the model fits with experimental data. However, the created model proposed a higher determination of R^2 value and adequate precision can be considered as significant in fitting and predicted responses, authorising usage of the model to predict the response values within the DOE space (Gopalakannan and Senthilvelan 2013). From previous analysis, removing the insignificant variables $(DSS)^2$,$(DHS)^2$, $(DID)^2$, and $(DHS\&DID)$ gave the final mathematical model of the drag finishing process in terms of more significant factors given by Eq. (14.8).

$$R_a(DF) = 0.85 - 3.83 \times 10^{-2} DSS + 7.4 \times 10^{-3} DHS + 1.09 \times 10^{-2} DID - 9.7 \times 10^{-5} (DSS)(DHS) + 5 \times 10^{-5} 5 (DSS)(DID) \quad (14.8)$$

The ANOVA stream finishing process is given in Table 14-10. The model F value of 17.43 suggests that the model is significant. The P value less than 0.05 implies the model terms are significant. In this case, bowl speed (SBS), head speed (SHS), immersion depth (SID), interaction between (SBS&SID), and interaction between (SHS&SID) are considered as significant model terms. These values represent sufficient variables from the model, and they can be used to predict the response values within the DOE space. The R^2 value of 94.63% is close to the adjusted R^2 of 92.12%. The lack to fit value of 0.071 represents an insignificant effect, which indicates the model fits with experimental data. The adequate precision value that measures the signal to noise ratio was 19.73. The determination of R^2 value and adequate precision measurement suggested the significance of the model in predicting and fitting the response, which allowed usage of the model to predict the surface roughness values within the DOE space. However, the final mathematical model of the stream finishing process in terms of significant factors after eliminating the insignificant factors is given by Eq. (14.9).

$$R_a(SF) = 0.726 + 1.03 \times 10^{-3} SBS + 4.65 \times 10^{-4} SHS - 1.14 \times 10^{-3} SID - 1.2 \times 10^{-6} (SHS)(SID) + 3.11 \times 10^{-6} (SBS)(SHS) \quad (14.9)$$

14.7 Models validation for statistical analysis

The capability of models for statistical analyses has been investigated by the examination of residuals using normal probability plots and the plots of the residuals versus the predicted response. The residual is the measure of the differences between the experimental and predicted values of response. The statistical model is validated when the normal distribution keeps the mean value in zero. A Least square regression method was employed to determine the normality; the straight-line distribution indicates no abnormalities (Khan, Romoli et al. 2012). Figure 14-6 (a, and b) shows the normal probability plot of residual of surface roughness determined by drag and stream finishing processes. As displayed the residuals are distributed fairly close to a straight line suggesting that the errors are normally disseminated and the regression model fitted well with the experimental values, which indicates the models are effective.

On the other hand, the data points distribution in the plots of the residuals versus the predicted response should be of non-obvious pattern (less structure). Figure 14-7 (a, and b) shows the plot of residual against fitted surface roughness values of drag and stream finishing processes, respectively. As illustrated, they have no obvious pattern and rare structure. This suggests that the models proposed are adequate and there is no reason for independence or constant variance assumption (Suresh, Rao et al. 2002) .

Table 14-7 DOE lay out and results of drag finishing process using Response Surface method

Exp. No.	$DHS\ (rpm)$	$DSS\ (rpm)$	$DID\ (mm)$	Ra (μm)	Residual
1	1	1	1	1.69	-0.006
2	2	1	1	1.99	0.049
3	1	3	1	0.66	-0.013
4	3	3	1	0.84	0.067
5	1	1	3	1.26	0.037
6	3	1	3	1.71	-0.003
7	1	3	3	0.6	-0.030
8	3	3	3	0.72	0.016
9	1	2	2	1.12	-0.059
10	3	2	2	1.48	-0.039
11	2	1	2	1.75	-0.077
12	2	3	2	0.65	0.040
13	2	2	1	1.31	0.037
14	2	2	3	1.22	-0.032
15	2	2	2	1.31	0.017
16	2	2	2	1.3	-0.023
17	2	2	2	1.34	0.033
18	2	2	2	1.36	0.042
19	2	2	2	1.32	-0.073
20	2	2	2	1.39	0.019

Table 14-8 ANOVA for surface roughness obtained by drag finisher

Source	DF	Adj SS	Adj MS	F-Value	P-Value
Model	9	2.87089	0.31899	86.94	0.000
Linear	3	2.70531	0.90177	245.78	0.000
DHS	1	0.18700	0.18700	50.97	0.000
DSS	1	2.43049	2.43049	662.44	0.000
DID	1	0.08782	0.08782	23.94	0.001
Square	3	0.01124	0.00375	1.02	0.424
DHS*DHS	1	0.00003	0.00003	0.01	0.932
DSS*DSS	1	0.00998	0.00998	2.72	0.130
DID*DID	1	0.00401	0.00401	1.09	0.320
2-Way Interaction	3	0.05864	0.01955	5.33	0.019
DHS*DSS	1	0.02771	0.02771	7.55	0.021
DHS*DID	1	0.00101	0.00101	0.28	0.611
DSS*DID	1	0.02992	0.02992	8.16	0.017
Error	10	0.03669	0.00367		
Lack-of-Fit	5	0.03096	0.00619	5.40	0.094
Pure Error	5	0.00573	0.00115		
Total	19	2.90758			

Table 14-9 DOE lay out and results of stream finishing process using Response Surface method

Exp. No.	$DHS\ (rpm)$	$DSS\ (rpm)$	$DID\ (mm)$	Ra (μm)	Residual
1	1	1	1	0.838	0.062
2	2	1	1	0.711	0.006
3	1	3	1	0.723	-0.035
4	3	3	1	0.571	0.035
5	1	1	3	0.520	-0.035
6	3	1	3	0.590	0.035
7	1	3	3	0.306	0.002
8	3	3	3	0.270	-0.061
9	1	2	2	0.651	0.006
10	3	2	2	0.526	-0.009
11	2	1	2	0.636	-0.069
12	2	3	2	0.430	0.059
13	2	2	1	0.690	0.047
14	2	2	3	0.660	0.017
15	2	2	2	0.610	-0.033
16	2	2	2	0.650	0.007
17	2	2	2	0.640	-0.003
18	2	2	2	0.630	-0.013
19	2	2	2	0.620	-0.023
20	2	2	2	0.650	0.007

Table 14-10 ANOVA for surface roughness obtained by stream finisher

Source	DF	Adj SS	Adj MS	F-Value	P-Value
Model	8	0.318995	0.039874	17.43	0.000
Linear	3	0.209283	0.069761	30.50	0.000
SBS	1	0.023341	0.023341	10.20	0.009
SHS	1	0.032034	0.032034	14.01	0.003
SID	1	0.099368	0.099368	43.44	0.000
Square	2	0.034164	0.017082	7.47	0.009
SBS*SBS	1	0.007465	0.007465	3.26	0.098
SHS*SHS	1	0.007266	0.007266	3.18	0.102
2-Way Interaction	3	0.040088	0.013363	5.84	0.012
SBS*SHS	1	0.000239	0.000239	0.10	0.752
SBS*SID	1	0.022113	0.022113	9.67	0.010
SHS*SID	1	0.024222	0.024222	10.59	0.008
Error	11	0.025160	0.002287		
Lack-of-Fit	3	0.017979	0.005993	6.68	0.071
Pure Error	8	0.007180	0.000898		
Total	19	0.344155			

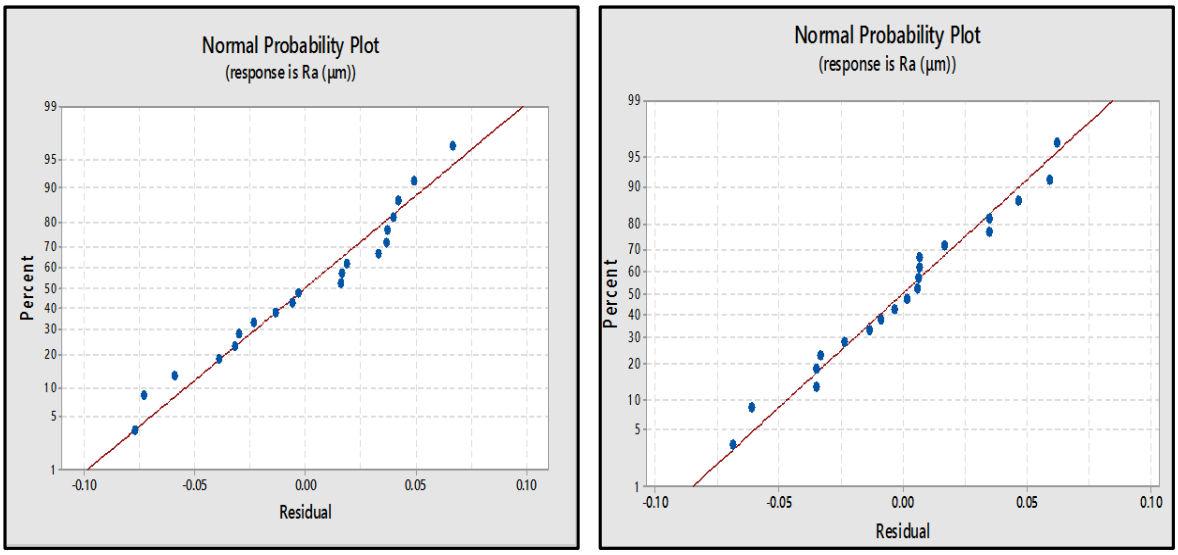

(a) (b)

Figure 14-6 Normal probability of residuals plot for surface roughness determined by a) drag and b) stream finishing process

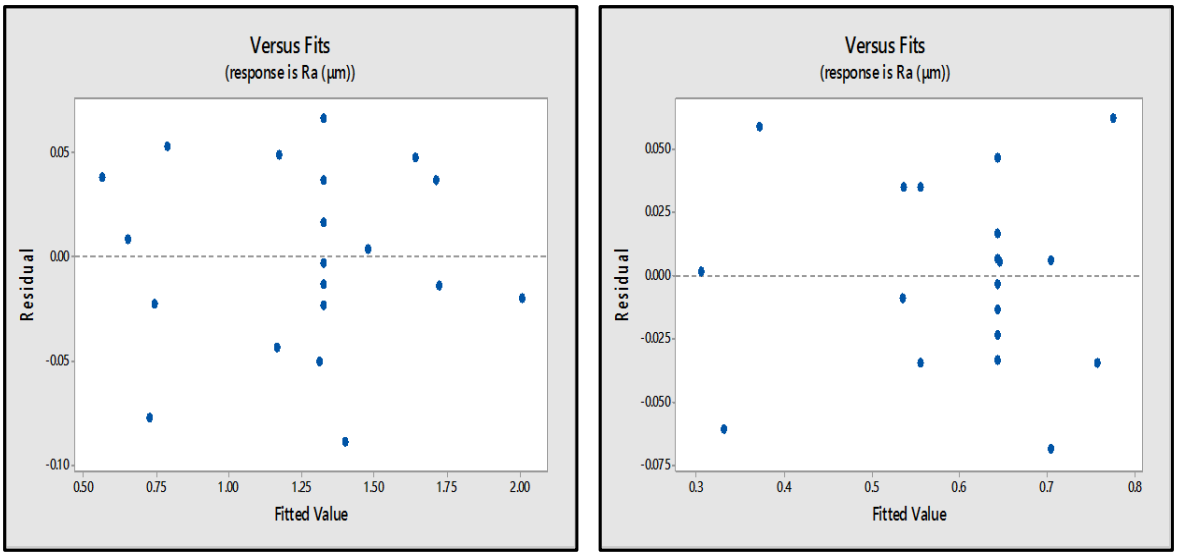

(a) (b)

Figure 14-7 Plot of residual against fitted surface roughness values.

14.8 Effect of finishing parameters on response

The effect of drag and stream fishing parameters on the surface roughness was investigated using the mathematical models developed by (Eq. 14.8) and Eq. (14.9) by means of response surface methodology. Figure 14-8 shows contours and 3-D surface roughness plots developed with various combinations of input drag finishing parameters a) head speed (DHS) and immersion depth (DID), b) spindle speed (DSS) and immersion depth (DID), and c) spindle speed (DSS) and head speed (DHS). These response contours and surface plots can help in the prediction of the Ra at any region in the experimental domain. It is clearly noticed from the 3-D surface plot Figure 14-8 (a) that the surface roughness decreases with the decreasing head speed and increasing immersion depth. The counter plot illustrated that for a given value of spindle speed, better surface roughness of 0.9 to 1.0 µm can be achieved within range of input parameters, 10-15 rpm head speed and 300-380 mm immersion depth. Referring to Figure 14-8 (b) the 3-D surface plot shows that the surface roughness decreases with the increasing spindle speed and head speed has no significant effect. The counter plot analysis for a given immersion depth demonstrated that lower surface roughness of 0.8 to 1.0 µm was attained within a range of 65-80 rpm spindle speed and 10-50 rpm head speed. The analysis of the 3-D surface plot shown in Figure 14-8 (c) suggested that the surface roughness decreases with the increasing spindle speed but no significant effect has been observed in the immersion depth.

However, for holding head speed value of 30 rpm, the contour plot illustrated that range of 0.8 -1.0 µm surface roughness was achieved through various input parameters within, 70-80 rpm spindle speed and 300-380 mm immersion depth.

Figure 14-.9 shows the contour and 3-D surface roughness plots developed with various combinations of stream finishing parameters a) head speed (SHS) and immersion depth (SID), b) bowl speed (SBS) and immersion depth (SID), and c) bowl speed (SBS) and head speed (SHS). The 3-D surface plot shown in Figure 14-9 (a) suggested that the surface roughness decreases with the increasing head speed and immersion depth. The counter plot displayed the range of input parameters for a given bowl speed, 1200-1500 rpm head speed and 220-300 immersion depth were anticipated for enhanced response of Ra $<$ 0.4µm. The 3-D surface plot shown in Figure 14-9 (b) illustrated that the surface roughness decreases with increasing bowl speed and immersion depth for a given head speed value of 1000. It is clearly shown that the surface roughness can be enhanced to minimum values of 0.5 to 0.6 µm using immersion depth of 250 to 300 mm and bowl speed has no significant effect. The analysis of the 3-D surface plot shown in Figure 14-9 (c) suggested that for a given immersion depth of 200 mm, surface roughness decreases with the increasing bowl speed and spindle speed. The counter plot analysis confirmed that a very small range of input parameters can satisfy the minimum surface roughness values of 0.45 to 0.55 µm. on the other hand, the Ra value significantly changes when the bowl speed decreases and becomes worst with head speed range of 500 to 1000 rpm.

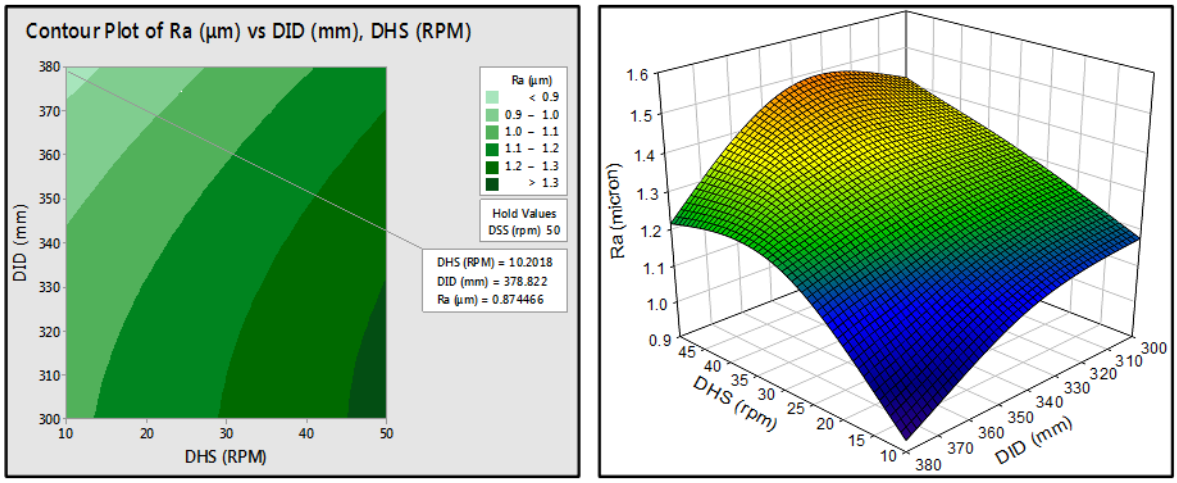

(a)

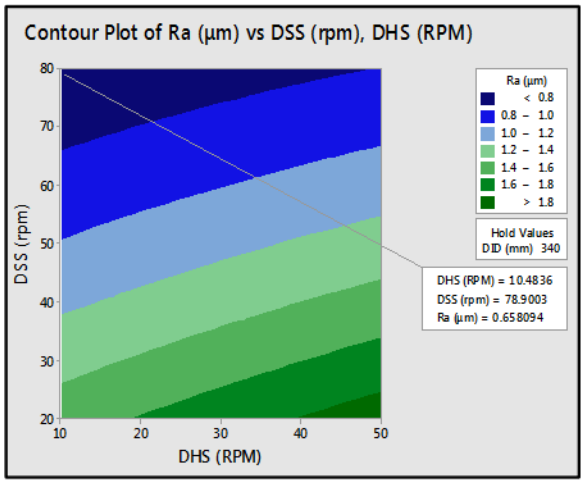

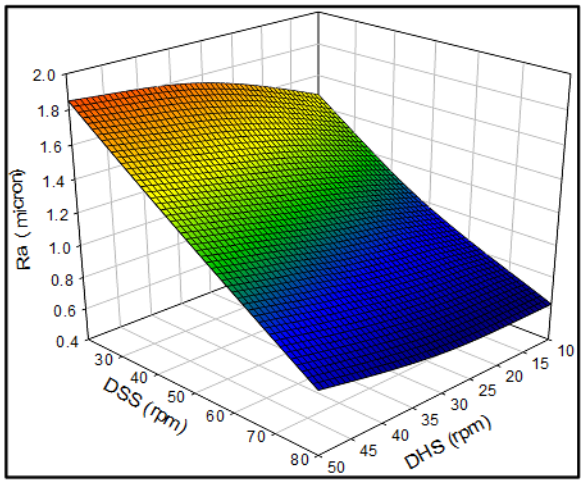

(b)

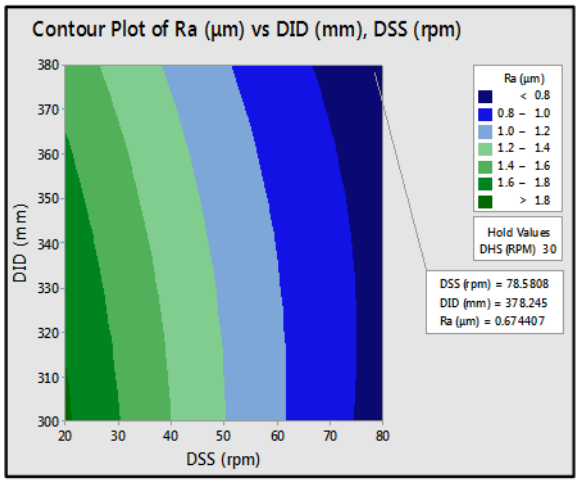

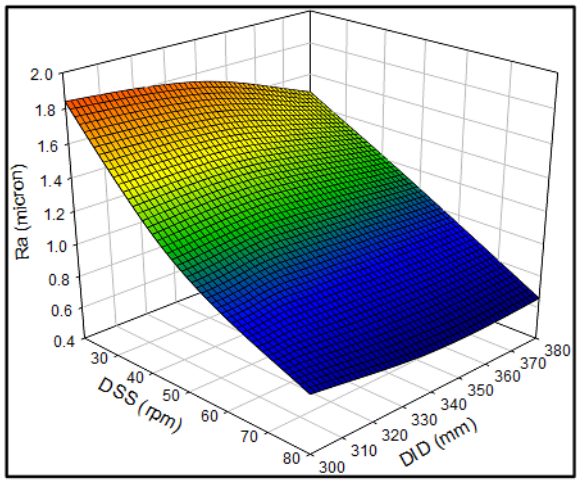

(c)

Figure 14-8 Contour and 3-D surface roughness plots developed with various combinations of drag finishing parameters a) head speed (DHS) and immersion depth (DID), b) spindle speed (DSS) and immersion depth (DID), and c) spindle speed (DSS) and head speed (DHS).

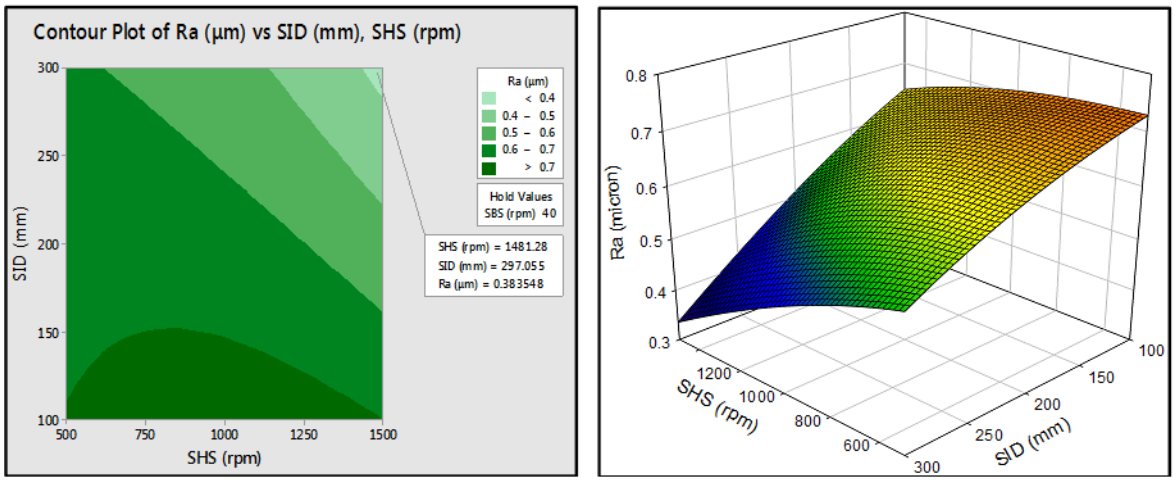

(a)

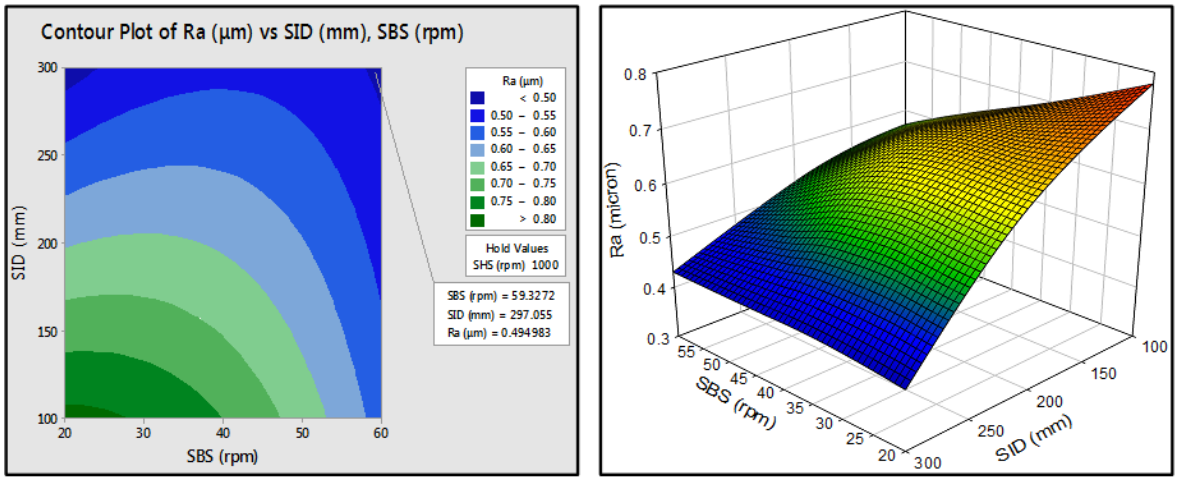

(b)

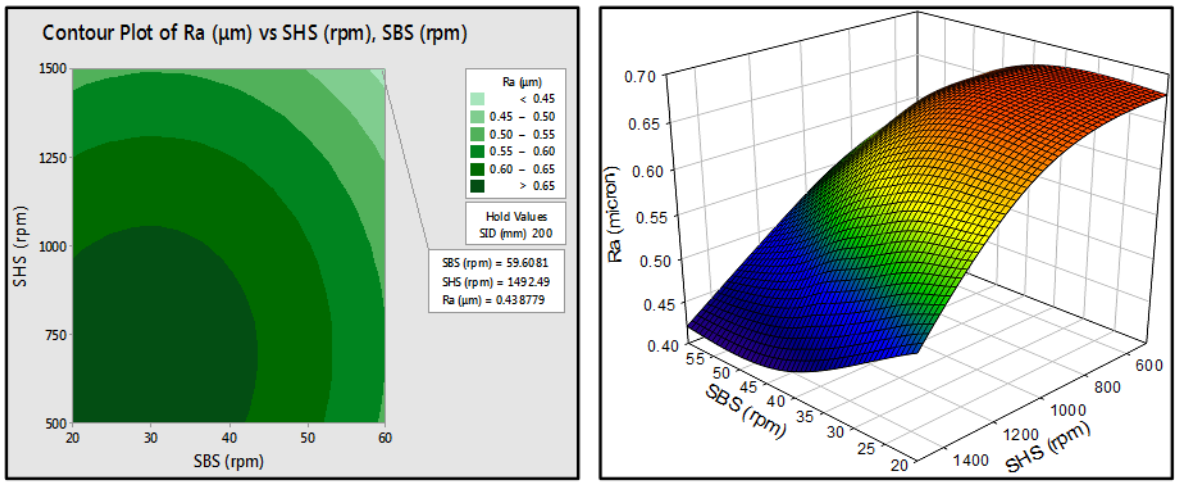

(c)

Figure 14-9 Contour and 3-D surface roughness plots developed with various combinations of stream finishing parameters a) head speed (SHS) and immersion depth (SID), b) bowl speed (SBS) and immersion depth (SID), and c) bowl speed (SBS) and head speed (SHS)

14.9 Interaction between factors

Figures 14-10 and 14-11 show the interaction factor plots relative to the surface roughness using the drag and stream finishing processes, respectively. The interactions plot represents a plot of means for each level of a factor with the level of a second factor kept constant. The importance of the interaction plot is on the understanding of the relation between each factor of interaction (Minitab 17). This interaction plot is in balanced design when the uses of two types of factor are identical. Interaction is present when the response at a factor level depends on the levels of other factors. Parallel lines in an interactions plot indicate no interaction. The greater the deviation of the lines from the parallel condition, the higher the degree of interaction state. In this study, the quality control is surface roughness Ra, thus the smaller the better response was investigated throughout interaction factors analyses.

Figure 14-10 shows the drag finishing interaction plot between factors of head speed (DHS), spindle speed (DSS), and immersion depth (DID) relative to surface roughness. The ANOVA demonstrated that interaction between (DHS & DSS), and (DSS & DID) were the most significant 2-way interaction factors. In the first case, surface roughness at minimum mean value of 0.62 µm, the head speed needs to be 10 rpm, and the spindle speed is 80 rpm. In the second case, surface roughness can be enhanced to minimum mean value of 0.66 µm throughout 80-rpm spindle speed and 380 mm immersion depth. However, the result of interaction in both cases agrees well with the Taguchi analysis in Table 14-5 and surface response methodology in Table 14-8, with regard to the significant factor with the highest impact on response. The interaction factors DHS & DID have no significant effect on the finishing process response.

Figure 14-11 shows the stream finishing interaction plot between factors of bowl speed (SBS), head speed (SHS), immersion depth (SID) relative to surface roughness. When these parameters were examined, the ANOVA suggested that the interaction between (SBS & SID) and (SHS & SID) were the most significant 2-way interaction factors. The first interaction result plot has been observed at the Ra value of 0.42 µm when the bowl speed is 60 rpm and the immersion depth is 300 mm. The second group was observed at the Ra value of 0.35 µm given by head speed of 1500 rpm, and immersion depth of 300 mm. The interaction factors agree well with the Taguchi and response surface methodology presented in Table 14-6, and Table 14-10, respectively.

However, the stream finishing interaction plot suggested that the (SHS&SID) was the most significant interaction factor on the finishing process. The remaining interaction factors SBS & SHS have no significant effect on the process response.

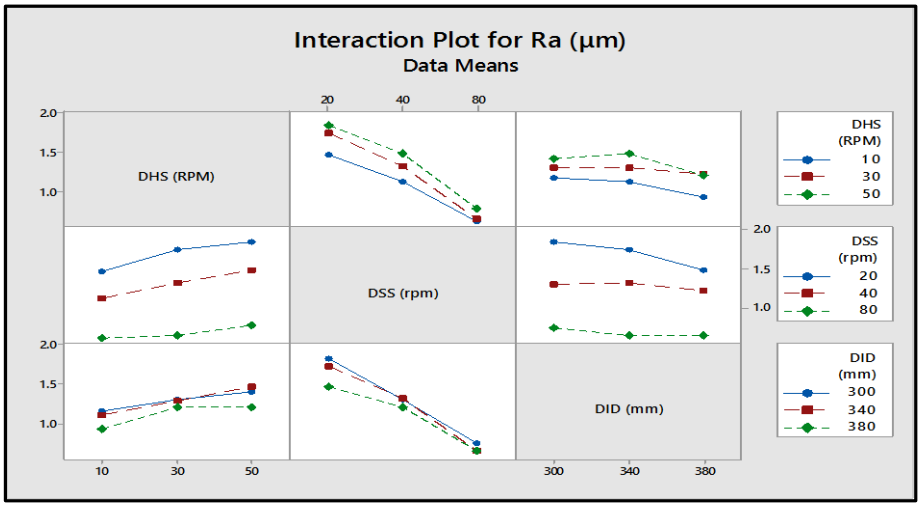

Figure 14-10 Drag finishing interaction plot for surface roughness

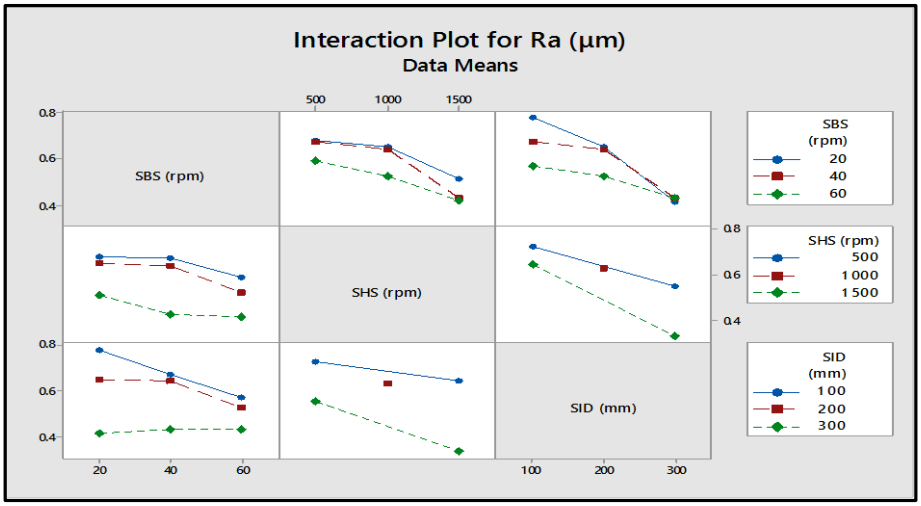

Figure 14-11 Stream finishing interaction plot for surface roughness

14.10 Response surface optimization

The most important aims of experiments related to the mass finishing process is to achieve the desired surface roughness by the optimal finishing parameters. The response surface optimization is a perfect method for characterising the best process parameters of the mass finishing operation. In this study, the goal from process optimization is to minimise surface roughness within the design requirement.

However, this response should be accurately controlled to avoid major problems such as over-finishing of the workpiece surface. The larger the better desirability was used for the calculated surface roughness. The desirability measure is how well a combination of factors can satisfy the response target. Desirability measurement has a range of zero to one. One represents the ideal predicted response. Zero indicates that the response is outside the acceptable limit.

Figure 14-12 shows response surface optimization results of drag finishing parameters. Optimum parameter levels were identified at larger desirability numbers as follows: head speed (DHS) of 10 rpm, spindle speed (DSS) of 80 rpm, immersion depth (DID) of 380 mm. The optimized surface roughness parameter was 0.561µm with a desirability number of 1, which indicates that the set parameters achieved the favourable result of response.

Figure 14-13 show response surface optimization results of stream finishing parameters. Optimal setting parameter levels were identified as follows: bowl speed (SBS) of 20 rpm, head speed (SHS) of 1500 rpm, immersion depth (DID) of 300 mm. The optimized surface roughness parameter was 0.3 µm with a desirability number of 0.93. The desirability result verified that the set variables achieved the desired response.

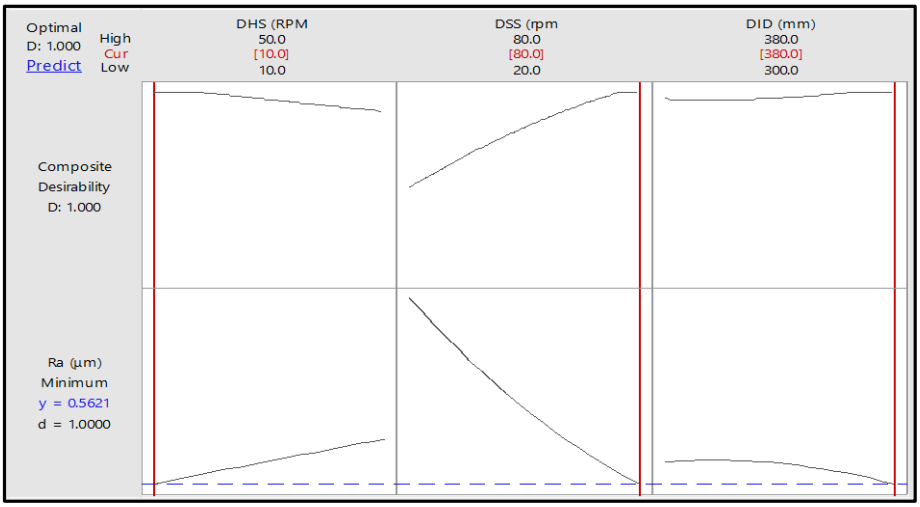

Figure 14-12 Drag finishing process optimization tool

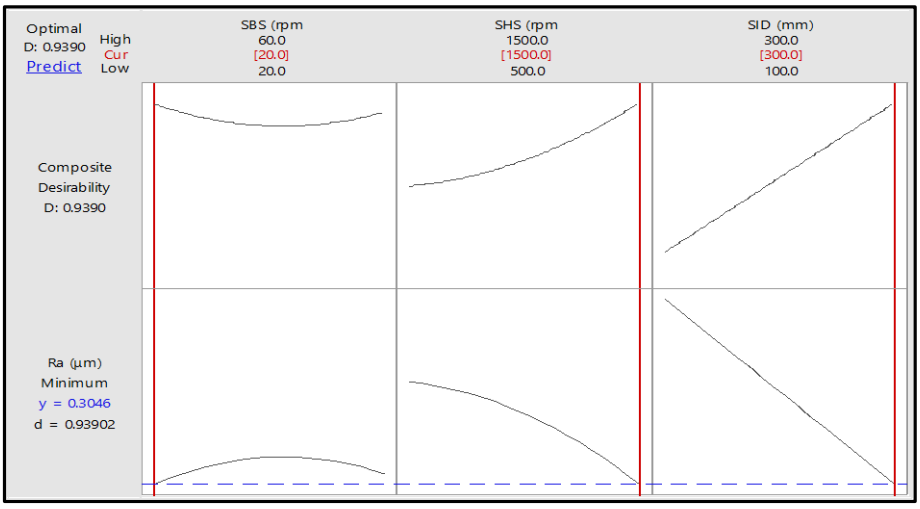

Figure 14-13 Stream finishing process optimization tool

14.11 Confirmation test

The plots of predicted values using the reduction model (Eq. 14.8, and Eq. 14.9) against the actual values of surface roughness were displayed in Figure 14-14 for the drag and stream finishing processes. The data points falls close to the diagonal line, which indicates a good agreement between predicted values and the actual data points. However, in order to validate the accuracy of the proposed model, a confirmation test was established. The test conditions for the confirmation trials were also selected within the range of levels defined by the DOE array. An aerospace turbine blade was employed in the confirmation tests with average surface roughness values of 1.9 µm ($\mp$0.1µm). Combinations of finishing parameters were chosen randomly for the experimental trials, and the responses obtained were compared with those calculated by the developed models. Table 14-11, and Table 14-12 show three confirmation trials were performed by the drag and stream finishing processes, respectively. The error percentage is within the allowable limits. Thus, the proposed models can be used to successfully predict the surface roughness values of any combination of drag and stream finishing parameters within the range of the experimentation performed.

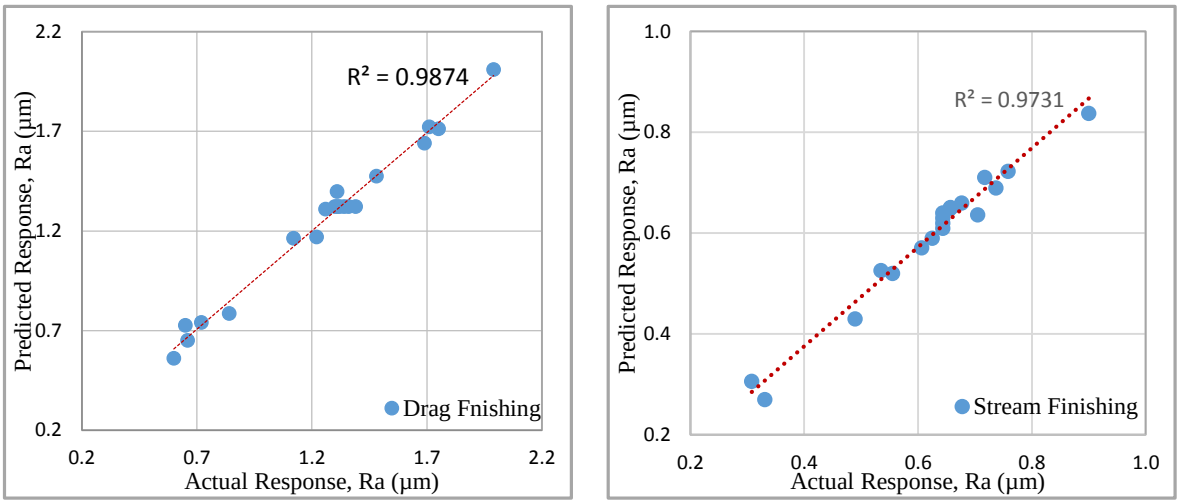

Figure 14-14 Comparison of predicted with actual values of surface roughness using drag and stream finishing process

Table 14-11Confirmation tests of drag finishing process

Exp.No.	DHS (rpm)	DSS (rpm)	DID (mm)	Actual Ra (µm)	Predicted Ra (µm)	Residual	Error (%)
1	50	70	320	1.01	0.95	0.06	6.32
2	25	30	340	1.51	1.46	0.05	3.42
3	40	50	300	1.23	1.27	0.04	3.25

Table 14-12 Confirmation tests of stream finishing process

Exp.No.	SBS (rpm)	SHS (rpm)	SID (mm)	Actual Ra (µm)	Predicted Ra (µm)	Residual	Error (%)
1	30	650	150	0.81	0.75	0.06	8
2	50	900	200	0.68	0.64	0.03	6.25
3	40	1200	300	0.44	0.48	0.04	9.1

14.12 Sensitivity Analysis

Sensitivity analysis is one the most important assessments in the optimization process because it provides information about the increases or decreases tendencies of the optimization function with the design parameters.

This method categorizes the significant parameters and ranks them by their order of importance (Sarıgül and Secgin 2004). The sensitivity analysis of a design optimization model can be stated by a mathematical model of a partial derivative of the response with respect to its variables. The sensitivity analyses were carried out to differentiate response surface optimization models developed by means of drag finishing parameters of interest Eq.(14.6) and stream finishing parameters Eq.(14.7). Sensitivity models given by Eq. (14.10), Eq. (14.11), and Eq. (14.12) represents the sensitivity of surface roughness determined by the drag finishing process with respect to head speed (DHS), spindle speed (DSS), and immersion depth (DID), respectively. Similarly, the sensitivity models given by Eq. (14.13), Eq. (14.14) and Eq. (14.15) represent the sensitivity of surface roughness determined by the stream finishing process by means of bowl speed (SBS), head speed (SHS), and immersion depth (SID), respectively.

$$\frac{\partial R_a(DF)}{\partial DSS} = -3.83 \times 10^{-2} + 15.2 \times 10^{-3}(DSS) - 9.7 \times 10^{-5}(DHS) + 5 \times 10^{-5}5(DID) \quad (14.10)$$

$$\frac{\partial R_a(DF)}{\partial DHS} = 7.4 \times 10^{-3} - 16 \times 10^{-3}(DHS) - 9.7 \times 10^{-5}(DSS) + 1.4 \times 10^{-5}(DID) \quad (14.11)$$

$$\frac{\partial R_a(DF)}{\partial DID} = 1.09 \times 10^{-2} - 4.8 \times 10^{-5}(DID) + 5 \times 10^{-5}5(DSS) + 1.4 \times 10^{-5}(DHS) \quad (14.12)$$

$$\frac{\partial R_a(SF)}{\partial SBS} = 1.03 \times 10^{-3} - 2.7 \times 10^{-4}(SBS) + 1.1 \times 10^{-6}(SHS) + 3.1 \times 10^{-6}(SID) \quad (14.13)$$

$$\frac{\partial R_a(SF)}{\partial SHS} = 4.65 \times 10^{-4} - 1.3 \times 10^{-6}(SHS) + 1.1 \times 10^{-6}(SBS) - 1.2 \times 10^{-6}(SID) \quad (14.14)$$

$$\frac{\partial R_a(SF)}{\partial SID} = -1.14 \times 10^{-3} - 1.2 \times 10^{-6}(SHS) + 3.11 \times 10^{-6}(SBS) \quad (14.15)$$

The sensitivity study was aimed to predict the tendency of surface roughness due to change in drag and stream finishing parameters. The calculated sensitivity of surface roughness with respect to DSS, DHS, and DID in (14.10), (14.11), and (14.12), was shown in Figure 14-15 (a, b, and c) respectively. The results of DSS sensitivity indicates that as the spindle speed increases, surface roughness decreases 14-15 (a), whereas the DHS sensitivity demonstrated that as the DHS increases, surface roughness increases Figure 14-15 (b). The immersion depth has no significant effect on the surface roughness sensitivity Figure 14-15 (c). These results reveal that the surface roughness is more sensitive to DSS and DHS than immersion depth DID. Generally, the sensitivity values of the spindle speed DSS are higher than head speed DHS and immersion depth DID. Thus, the DSS affects surface roughness more strongly than DHS, and DID.

The sensitivity analysis of the stream finishing process determined by Eq. (14.13), Eq. (14.14), and Eq. (14.15), was shown in Figure 13.16 (a, b, and c) respectively. It is clearly noticed that all parameters follow the same trend of surface roughness decreasing with the increases of SBS, SHS and SID. However, the rate of influence on the surface roughness changed with various parameters. Sensitivity values of head speed shows the most important effect on the surface roughness followed by immersion depth, the bowl speed has ranked the lowest influence on the response.

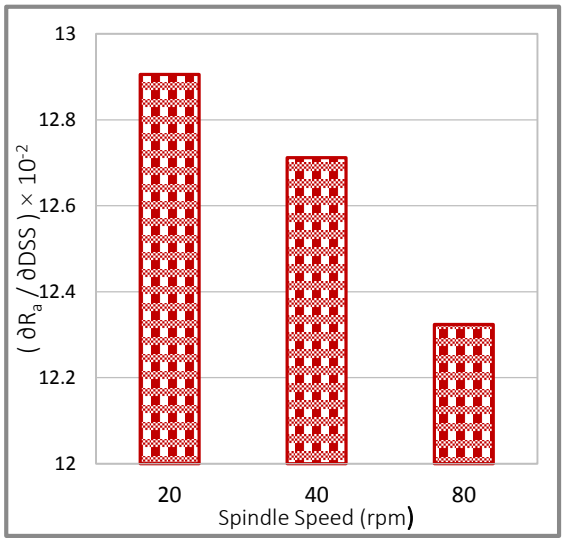

(a)

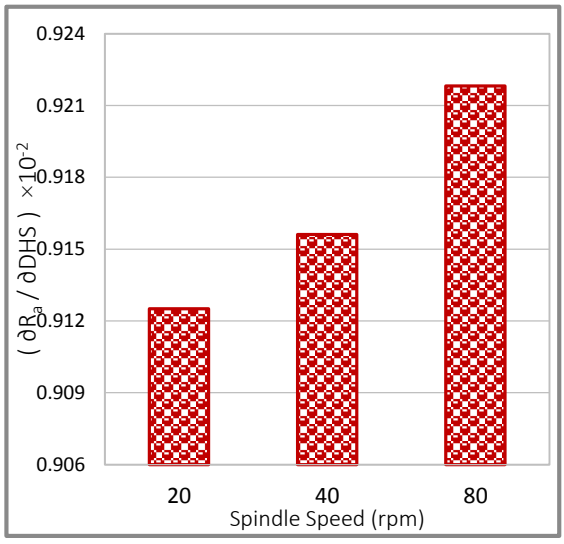

(b)

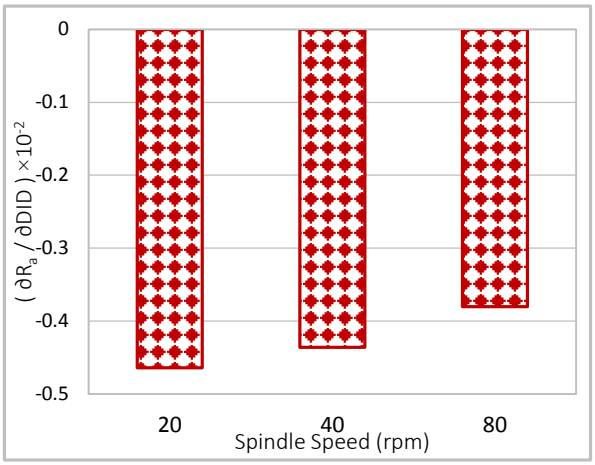

(c)

Figure 14-15 Sensitivity analysis results of drag finishing parameters of a) spindle speed, b) head speed, and c) immersion depth

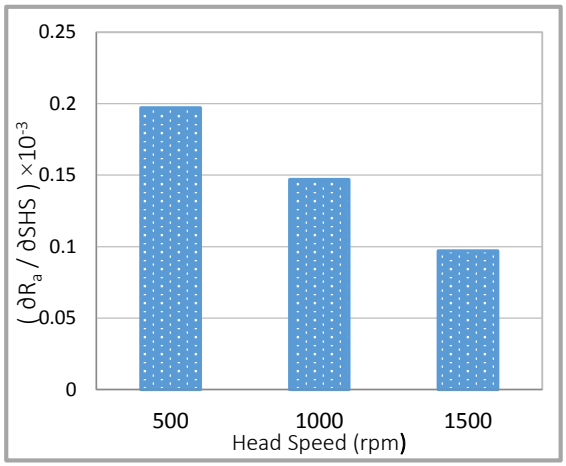

(a)

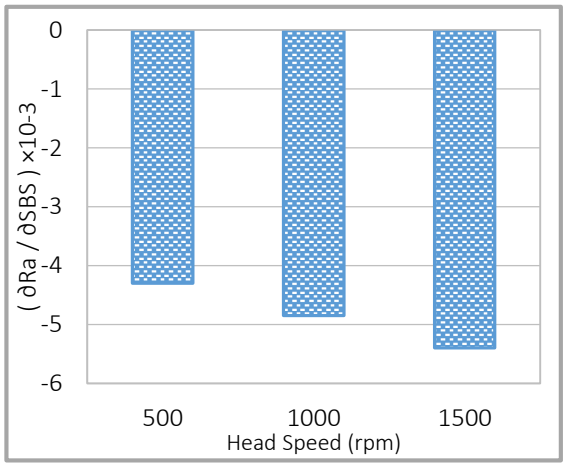

(b)

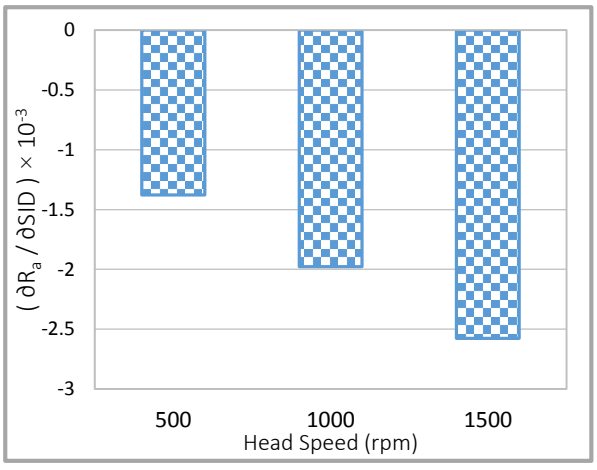

(c)

Figure 14-16 Sensitivity analysis results of stream finishing parameters of a) head speed, b) bowl speed, and c) immersion depth.

14.13 Conclusion

In this study, the experimental investigation with statistical analysis to determine the effect of spindle speed DSS, head speed DHS and immersion depth DID in the drag finishing process, and also the effect of bowl speed SBS, head speed SHS, and immersion depth SID in the stream finishing process on the surface roughness values of aerospace components has been established using the principles of Taguchi, ANOVA, and Response surface methods. Taguchi analysis is responsible for investigating the rank and the level of factors that have a significant effect on the response. The best fit between the developed models and the experimental data were further evaluated through ANOVA, F-statistical and P-value tests to determine whether the factors are significantly related to the response. The interaction plots were also used to compare the effects across the control factors when changes in response between levels of one factor are not the same as the changes in response at the same levels of a second factor. The proposed methods predict surface roughness to within 95% confidence level. Sensitivity analysis has been investigated to determine the efficiency of processing parameters on the optimization models developed by statistical regression analysis. The following conclusions are established:

- Taguchi statistical analysis of the drag finishing process suggested that the optimal control factors which minimize the surface roughness were DSS (level 3), DHS (level 1), and DID (level 3). The DSS had the greatest effect and its contribution was 89%, followed by the DHS and its contribution was 7.2 % and the DID had a lower effect, its contribution was 3.8 % on quality characteristics. The stream finishing process proposed that the optimal control factors were SBS (level 3), SHS (level 3), and SID (level 3) which contribute to minimizing the surface roughness by 52.8 %, 40.3 %, and 6.9 %, respectively.
- The significant factors and the rank of variables were examined and there is a good agreement between the observations.
- 3D surface and counter plots are useful tools in determining the optimum parameters condition for specific values of surface roughness at any region in the experimental domain. The plots also illustrated that the Ra decreases with increasing DSS and DID, and Ra increases with increasing DHS. In the case of the stream finishing process, Ra decreases with increasing control factors (SHS, SBS, and SID).

- Confirmation experiments suggested that the predicted quadratic models were successful in predicting surface roughness in the drag and stream finishing process within 6 %, and 9 % error, respectively.
- The interaction investigation of the drag finishing process demonstrated that the (DHS & DSS), and (DSS & DID) had the most significant effect on response, while (SBS & SID) and (SHS & SID) had the most significant effect in the stream finishing process.
- The ANOVA results with the confirmation trials have proved that the quadratic mathematical models of the process variables were fit and predicted the recorded experimental value with a 95% confidence interval.
- The optimization tool was employed to determine the design surface roughness with high desirability at various process conditions. The results obtained from this tool were in good agreement with the verification trials.
- The sensitivity analyses of the drag finishing process showed that the DSS affects surface roughness more strongly than DHS, and DID. Sensitivity values of SHS show the most important effect on the surface roughness followed by SID; the SBS factor has the lowest effect on the surface roughness.
- RSM has the potential for more complicated sensitivity analysis and may be used for optimal parameter determination of various mathematical models.

Finally, this study demonstrated that the proposed methods can be successfully applied for optimizing surface roughness of the advanced mass finishing process at an industrial scale and that it is an economical way of obtaining the maximum amount of information in a short period of time and with the lowest number of experiments.

14.14 References

Arvin, J. (2002). The effect of chemically accelerated vibratory finishing on gear metrology, AGMA.

Barletta, M., A. Gisario, S. Venettacci and G. Rubino (2014). "A comparative evaluation of fluidized bed assisted drag finishing and centrifugal disk dry finishing." Engineering Science and Technology, an International Journal **17**(2): 63-72.

Barletta, M., G. Rubino and P. Valentini (2014). "Experimental investigation and modeling of fluidized bed assisted drag finishing according to the theory of localization of plastic deformation and energy absorption." The International Journal of Advanced Manufacturing Technology: 1-16.

Cariapa, V., H. Park, J. Kim, C. Cheng and A. Evaristo (2008). "Development of a metal removal model using spherical ceramic media in a centrifugal disk mass finishing machine." The International Journal of Advanced Manufacturing Technology **39**(1-2): 92-106.

Davidson, D. A. (2008). "Vibratory finishing: Versatile, effective, and reliable." Metal Finishing **106**(5): 30-34.

Domblesky, J., V. Cariapa and R. Evans (2003). "Investigation of vibratory bowl finishing." International journal of production research **41**(16): 3943-3953.

Domblesky, J., R. Evans and V. Cariapa (2004). "Material removal model for vibratory finishing." International journal of production research **42**(5): 1029-1041.

Gopalakannan, S. and T. Senthilvelan (2013). "Application of response surface method on machining of Al–SiC nano-composites." Measurement **46**(8): 2705-2715.

Hashimoto, F. and D. DeBra (1996). "Modelling and optimization of vibratory finishing process." CIRP Annals-Manufacturing Technology **45**(1): 303-306.

Khan, M., L. Romoli, M. Fiaschi, G. Dini and F. Sarri (2012). "Multiresponse optimization of laser welding of stainless steels in a constrained fillet joint configuration using RSM." The International Journal of Advanced Manufacturing Technology **62**(5-8): 587-603.

Matsunaga, M. (1967). "Theory and experiments on centrifugal barrel finishing." The International Journal of Production Research **5**(4): 275-287.

Montgomery, D. C. (2008). Design and analysis of experiments, John Wiley & Sons.

Pease, G. (1993). Taguchi Methods: A Hands-on Approach to Quality Engineering, Addison Wesley, New York.

Phadke, M. S. (1995). Quality engineering using robust design, Prentice Hall PTR.

Phadke, M. S., R. N. Kackar, D. V. Speeney and M. J. Grieco (1983). "Off-line quality control in integrated circuit fabrication using experimental design." Bell System Technical Journal, The **62**(5): 1273-1309.

PIGNATIELLO JR, J. J. (1988). "An overview of the strategy and tactics of Taguchi." IIE transactions **20**(3): 247-254.

Reisgen U, Schleser M, Mokrov O, Ahmed E (2012). "Statistical modeling of laser welding of DP/TRIP steel sheets". Opt Laser Technol **44**(1):92–101.

Roy, A., S. Paul, A. Shamsuzzaman and M. I. Raza (2009). Design of an optimum antenna system for maximum power transfer using statistical design of experiment approach. PIERS Proceedings.

Sangid, M. D., J. A. Stori and P. M. Ferriera (2011). "Process characterization of vibrostrengthening and application to fatigue enhancement of aluminum aerospace components—part I. Experimental study of process parameters." The International Journal of Advanced Manufacturing Technology **53**(5-8): 545-560.

Sarıgül, A. and A. Secgin (2004). "A study on the applications of the acoustic design sensitivity analysis of vibrating bodies." Applied acoustics **65**(11): 1037-1056.

Shi, H., K. Zhang, Z. Xu, T. Huang, L. Fan and W. Bao (2014). "Applying statistical models optimize the process of multi-pass narrow-gap laser welding with filler wire." The International Journal of Advanced Manufacturing Technology **75**(1-4): 279-291.

Suresh, P., P. V. Rao and S. Deshmukh (2002). "A genetic algorithmic approach for optimization of surface roughness prediction model." International Journal of Machine Tools and Manufacture **42**(6): 675-680.

Taguchi, G. and S. Konishi "Taguchi methods, orthogonal arrays and linear graphs, tools for quality engineering, 1987." Dearborn, Mich: American Supplier Institute.

Takahashi, Y., M. Kataoka, M. Uekusa and Y. Terumichi (2005). "Behavior of three kinds of particles in rotary barrel with planetary rotation." Multibody System Dynamics **13**(2): 195-209.

Uhlmann, E., A. Dethlefs and A. Eulitz (2014). "Investigation of material removal and surface topography formation in vibratory finishing." Procedia CIRP **14**: 25-30.

Wang, S., R. Timsit and J. Spelt (2000). "Experimental investigation of vibratory finishing of aluminum." Wear **243**(1): 147-156.

CHAPTER FIFTEEN

GENERAL CONCLUSIONS AND RECOMMENDATIONS FOR FUTURE WORK

15.1 General conclusion

A study of the newly developed mass finishing media, referred to as 'thermally treated recycled glass' has been completed. The first part of the study, as presented in chapter 3 , various powder characterization methods were successfully employed to determine the morphology, granularity, and flow and packing properties of soda lime recycled glass. This chapter addressed deviation of powder physical and chemical properties across a range of glass particle size batches. It was clearly observed from the morphology analysis, the glass particles exist in irregular and elongated particle shapes. As a result, various size distribution was recognized in the same particle size batch, the smallest particle size, the highest distribution width span. This chapter also addressed the flowability and packing properties through a series of traditional and advanced techniques. It was clearly noticed that with the increase of particle size, the better flowability and also increasing the apparent and tab density (packing properties). The study concluded that the particle sizes VG+350, and VG+150 would be the recommended recycled glass sample in terms of flow and packing characteristics (manual and automatic mould filling).

In chapter 4 thermal analyses were successfully employed to determine the optimal glass powder size in term of crystallinity. DTA analysis suggested that when the particle size increases the intensity of crystallization decreases and the temperature for crystallization increases. However the particle size VG+350 provides the best solution for glass media production in terms of decomposition, nucleation and crystallization growth, flow-ability and packing characteristics. This chapter also assessed various types of mould materials in terms of thermal conductivity and sticking behaviour. The heat transfer and sticking results suggested that the silicon carbide was the more appropriate material among the moulds.

In addition, in chapter 4, it is proposed throughout the SEM and XRD analyses that by controlling the TTT relationship, it is possible to consistently produce abrasive media possessing particular mechanical and physical properties such that they deliver targeted mass finishing performance**.** The change in temperature and time leads to a change in the rate of crystallinity. The lower temperature, in general, will generate a higher number of smaller crystals, and thus impact positively on the number of crystal edges on the surface of the media (cutting edges). The TTT diagram suggested that the full crystalline state could be achieved at 40 minutes holding time and VT-30ºC. At or above VT+10ºC, full crystallisation is reached with a very short heating time of 30 minutes. As consequence, the

surface roughness decreases with the increasing firing temperature and this could be associated with the large crystal grain propagation. However, the X-Ray tomography analysis confirmed that the rate of inclusion and voids defects could be reduced by increasing the sintering temperature due to the diffusion phenomena.

The residual stress developed in the final product was addressed in chapter 5. In this chapter the residual stresses of various glass media products were obtained using numerical simulations through uncoupled thermo-mechanical solidification and elastic-viscoplastic material dependent temperature analysis. The optimal HTC that's provided the best fit to numerical and experimental thermal history was successfully established for one kind of media (cutting media) through use of a parametric study. The numerical solidification criteria was then employed as an external force by means of a quasi-static mechanical analysis and the numerical residual stresses were obtained. The validation of numerical solidification result at optimal HTC present reasonable agreement for the purpose of this validation, which is measured at the same node position (edge node).

The experimental residual stress of cutting media was determined by X-ray diffraction analysis ($sin^2\psi$ method). The thermal histories and the residual stresses were compared with the experiment data obtained by the X-ray diffraction technique. The results show that the numerical FE code is suitable for prediction residual stresses from thermally treated recycled glass. Some differences were observed in the residual stress calculations between numerical and experimental results. However, the results in both measurements follows similar trends indicating that the residual stress become compressive near the media edges, these stresses reduced gradually toward the media center and convert to a tensile stress at the end of the solidification process to room temperature. The residual stress analysis demonstrated that the finishing media exhibits the highest compression and tensile residual stress concentration followed by general purpose media and then cutting media. This explains the strengthening effect of the quenching process. The knowledge of the transient and residual stress state will help to optimize the media shape and geometry according to planned use, allows understanding of the influence of residual stress on defects such as cracks and helps evaluate the lifetime of glass media.

Chapter 6 presents a method to determine the area function of the Berkovich indenter used in nanoindentation hardness tests. A simulation of the nanoindentation hardness test system is developed using finite element modelling (FEM) methods. Solutions for a range of load

indentation curves obtained from experiment with fused silica are determined from best fit analyses using the root mean square error objective function (RMSE). A linear regression method is subsequently developed and used to estimate the area function. A parametric study of simulation and experimental results has been completed to verify the FEM and to assess the influence of varying tip curvature on force-displacement response during the loading and unloading stages and is summarily reported. A new method of analysis for determination of area function is proposed for use with numerical based simulations, which for the first time, accommodates variation in tip geometry and which is shown to deliver improved agreement with nanoindentation experimental results.

In chapter 7, the results of a study concerned with the tip geometry of the Vickers micro-indenter are presented. It is important to have knowledge of the tip geometry as this affects the correctness of the value of contact area parameter used to determine the mechanical properties such as Hardness and Young's modulus of elasticity. Results from experiment are compared with results from published works and also the most current accepted analytical models. A new method is proposed for the determination of contact area based on residual imprint measurements using 3-D optical profilometry supported by Vision 64 and Gwyddion software for image processing and analysis. The outcomes show that by measuring contact area with the new method improves the overall relative error in the obtained mechanical properties. It is also concluded that the contact area obtained from experimental and numerical load displacement curves is more accurate than the contact area measured by the assumption of perfect indenter geometry developed by Oliver Pharr method. The results demonstrated that the proposed method could achieve an accurate determination of indenter tip radius without a pre knowledge for the material property of the specimen. The dimensional analysis suggested that the applicability of the proposed procedures are not limited for a certain type of material property.

In Chapter 8, the influence of sample size, tip geometry, frictional condition, mesh density and material properties on the numerical force displacement curves during the loading and unloading stages of various contact geometries of (Berkovich, Vickers, spherical, and conical) were investigated using a parametric study. The study clearly defined a new set of criteria for converged FE 2- dimensional (axisymmetric) geometry at condition: specimen dimension ratio (workpiece radius to the workpiece height) $rw:hw$ = unity; and depth ratio (workpiece height to the maximum indentation depth) $hw/hm \geq 100$.

The result of optimal mesh density of various contact geometry were achieved, both computational time and variation in predicted Force is minimised. It is also the value at which indentation depth correlates most accurately with the convergence value associated with higher element numbers. The sensitivity analysis were carried out through parametric study, the numerical simulations confirmed that the indentation curvatures increases with the increasing of elastic plastic material properties σ_y, and E regardless of the of contact geometry. The Poisson's ratio has a only minor effect on the indentation result. No significant differences can be found in the load displacement curves when varying coefficient of friction, except the von Mises stress distributions after unloading stage, which are noticeably different between frictional and frictionless contact surfaces. The magnitude of the frictional surface after unloading is less than that of the frictionless one.

The load increases with the increasing tip radius. A greater tip radius leads to a slightly deeper indentation surface profile and residual surface profile along the straight surface in direction opposite to the mid plane. However, it results in less residual surface profile around the region of the tip radius. A greater elastic recovery and a lesser residual von Mises stress after unloading agree with these findings.

The ability of various 3-D FE indentation models to predict the experimental results has been examined by a validation of the numerical results against published data. Good agreement has been observed of hardness, elastic modulus, and the indentation depth ratio between the predicted and published data for the three different indenter geometries. This suggest that the models are accurate and valid for material characterization. A parametric study has been successfully employed to optimize the inclination angle of 2-D axisymmetric model to determine the best fit data with the 3-D model.

In chapter 9, a non-linear least square curve fitting function (LSQNONLIN) within the optimization toolbox of MATLAB was developed in order to extract the mechanical properties of unknown materials follows various range of material constitutive law (elastic plastic and Drucker-Prager) using single and dual target load displacement curves. The developed algorithm automatically feeds the input material properties data to ABAQUS software and automatically runs the simulations to establish a convergence between the numerical loading unloading curve and the target data. In previous work associated with material characterization by the indentation process suggested that dual indenters are required to predict a unique set of material properties. However, the optimization algorithm

developed in this study demonstrates that a single indentation approach is able to converge the input data to the target values to within 3% error with high iteration numbers compared with dual indentation method which converges data to the target properties within 1% error with less iteration numbers but more computational time, despite using various initial guess values. It is interesting to note that the convergence criteria is dependent on how far the initial guess parameters vary from the target value and indenter geometry. Furthermore, it is shown that the optimisation algorithms produce good accuracy for different indenter geometries; Conical, Vickers, Berkovich, and Spherical.

The sensitivity analysis suggested that the results achieved by dual Spherical and Berkovich (*S&B*) approach are significantly better than other single and dual indentation methods. As a result a small deviation in the predicted elastic plastic mechanical properties (σ_y , E , and n) and pressure-sensitive plastic material properties (E, σ_{yc}, β) produces a very limited material range with identical load displacement curves (same objective function), such behaviour reflects the uniqueness of the method in solving a complex material systems.

The proposed algorithms have also been applied to a real life target loading unloading curves from a range of thermally treated recycled glass materials to determine the unknown four material parameters (σ_y , E , v, n). For more accurate results, the predicted residual stress from Chapter 5 has been implemented into the numerical simulations prior to the material characterization process. The results show that accurate values of Young modulus, Yield stress, and strain hardening were obtained compared with the traditional technique of Oliver & Pharr based on experimental load displacement curve analysis.

In conclusion, this study has shown that a robust optimization method based on a non-linear least-squares curve fitting function (LSQNONLIN) within MATLAB and ABAQUS can be used to accurately predict a unique set of elastic plastic material properties (σ_y , E , v, n) and Drucker-Prager (E,σ_{yc}, β) material properties.

In chapter 10, the indentation cracking mechanism is shown to be an effective solution for measuring the material fracture toughness, and the Palmqvist and Median cracks are the most common independent crack systems. The determination of these crack systems needs to be combined with the indentation stress field, which strongly depends on material elastic plastic properties. In this study, a series of 3-D FEM analyses were performed, the indentation stress field was determined and applied by superposition technique to given

crack geometries (the Palmqvist cracks and Median cracks) to compute the *SIF*. Based on dimensionless analyses, a non-linear surface fit model was employed to predict the *SIF*. The relationship (equations (10.18), and (10.21) for Palmqvist and Median crack, respectively) were established between the critical SIF (fracture toughness), crack geometry, material properties, indentation size, and polar coordinate angles. The empirical relationships were validated over a wide range of material properties from Vickers indentation experimental data of previous works. By measuring the surface crack length the material fracture toughness is then derived. As demonstrated, the fracture toughness obtained from the proposed model is reasonably close to the reference values, which validates the framework of this study. It is clearly noticed for a given material properties the Palmqvist crack is associated to lower load, while the median crack is more likely propagated at higher indentation load.

The proposed procedure has also been applied to real life Vickers indentation tests over a range of thermally treated recycled glass materials and by measuring the crack length, the fracture toughness (K_{IC}) was derived throughout the Palmqvist numerical model. The compared results suggest that the K_{IC} of glass media estimated from equation (10.18), is reasonably close to the values determined from theoretical models proposed by (Niihara, Morena et al. 1982) and (Ray and Dutta 1999). However, the proposed method is expected to be applicable to compute the fracture toughness of a wide range of brittle materials.

In chapter 11, The study included investigation of the experimental programme concerned with the performance of various glass media samples compared with conventional ceramic and polyester bonded media (-pink plastic media) on different types of work material including a titanium alloy (coupon and aerospace turbine blade). Performance measures were surface roughness (Ra), brightness and compound consumption.

The thermally treated recycled glass media has a demonstrated efficiency in delivering target performance in super-polishing of turbine blades. The glass media was studied in on-site tests and shown to perform at least as well as the currently used polyester bonded media (pink plastic media) through achievement of target finish at reduced cycle times. The results of the comparative performance study provide promising evidence that the thermally treated glass media has a process capability and performance comparable to that of currently used media. Key performance indicators: surface roughness, brightness and self-attrition rate all matched or exceeded those obtained with benchmark media

The opportunity for cleaner machining was evidenced through the effluent. Glass media resulted in very little 'dirty' effluent and after separation the compound is able to be reused. Effluent resulting from use of plastic media was 'dirty', difficult to manage and was sent to landfill following extraction of work material.

Overall, the thermally treated recycled glass media has demonstrated a strong potential as an environmentally positive new choice in vibratory finishing operations.

The comparison results from on-site production test (Finishing Technique Ltd.) of spindle finishing (Drag, and Stream) and Centrifugal disk finishing processes using conventional abrasive granulate (Plastic and Ceramic) media on the auotomative workpiece were established. The results suggested that the drag finishing process is more efficient in enhancing the surface roughness followed by stream finishing and then the centrifugal disc finishing process.

The performance analyses were extended to include various spindle finishing techniques (drag, and stream) and centrifugal disc finishing processes using conventional plastic and ceramic media. The spindle finishing techniques show better surface finishing results and cycle times compared with centrifugal finishing because it is possible to control abrasion and they are inherently higher energy processes. The energy of the abrasive medium, is converted to strain energy during the impact with the workpiece surface. This energy should be sufficiently high to overcome the critical strain of material under investigation. However, the spindle finishing process delivers such opportunity in increasing the local plastic deformations and subsequent erosion by micro cutting. This is clearly noticed from the performance analyses of materials exhibiting high wear and abrasion resistance

In chapter 12, a novel design and fabrication jig arrangement system for vibratory mass finishing has been completed. The jig arrangement is designed to hold the part in horizontal position which allows free rotation of the workpiece with the media flow in the vibratory mass finishing operation. This provides a solution to the challenges associated with thermally treated glass media fracture due to the impact with a heavy workpiece. This design has been developed to carry the parts horizontally within the trough while allowing for variation in immersion depth and variation in position throughout the longitudinal or transverse directions in the vibratory trough machine. It also allows the workpiece to have full abrasion with thermally treated glass media without applying any load or pressure that would lead to shard generation and provides a facility to re-position the workpiece in order

to achieve optimal abrasivity performance. The new arrangement system was successfully used to deliver better performance results with both the conventional and thermally treated recycled glass media.

In chapter 13, DEM was developed to investigate different aspects of granular bulk flow of conical shaped thermally treated glass media in a vibratory finishing machine having both vertical and horizontal components of motion. An optimization procedure was developed by means of a parametric study to enhance the predicted contact parameters throughout the process of determining the best fit of numerical results with the experimental measurements of media velocity vector at different locations in the flow. The conical shape of media was successfully implemented into the DEM simulation using a modified Overlapping Rigid Clusters (ORC) technique developed by (Ashmawy, Sukumaran et al. 2003). The velocity vector measurements in the bulk flow were determined using particle image velocimetry adapted with MATLAB code (PIVLab). The average flow velocity of the optimal DEM simulations were compared with the equivalent experimental results at five different measurable field locations using partial and full conical media load conditions. The DEM results always underestimated the bulk flow velocity in contrast with experimental data. The average error in the bulk flow velocity at five different locations between the experiments and DEM simulations was 17%, and 14%, for partial and full loaded conditions, respectively. This suggested that the optimized contact parameters can produce reasonable agreement with two different flow fields. It was also clearly noticed that the bulk flow velocity increased with an increase in particle number, as a result shear forces and the strength of media circulation increases.

The DEM was then used to investigate the bulk expansion of a single cell circulation in the vibrating tub and its relation to the different load conditions. A physical model was also developed to describe the behaviour of the system at the steady state condition and the trend was found to follow the results predicted by DEM simulations. The average numerical bulk expansion results underestimated the experimental values of partially and fully loaded conditions on average by 4%, and 5%, respectively. The results also show that the bulk flow expansion increases with partially loaded condition due to a reduction in hydrostatic pressure, which results in an increase in the particles motion.

In addition, in chapter 13, the experimental and numerical horizontal and vertical velocity components in specific field locations along the horizontal direction of a partially loaded

tub finisher were measured at different levels from the bottom wall. Both experiments and DEM observations followed the same trend and confirmed that the vertical and horizontal velocity components changed with the depth of media in the tube finisher. Consequently, there is a strong relationship between the strength of circulation and the total shear force along the tub finisher walls. However, bulk circulation increases significantly near the left and right side tub walls. These average velocities drop to the lower values in the central part.

Therefore, the pressure and forces at the tub finisher walls and between the media were increased accordingly. It is clearly noticed that the average vertical and horizontal velocity distributions reached maximum values when the bed depth increased. However, it is proposed that as the vertical velocity increases, there is an increase of residual stress on the material surface. While increases in the horizontal velocity can enhance the abrasive processing and produce smoother surfaces.

In general, the predicted velocities from DEM were consistently smaller than the experimental values. The predicted horizontal velocities of conical glass media were about 20% and 17% less than the experiment measurements for the highest and lowest rows respectively, while the vertical velocity component shows the discrepancy in results up to about 22%, and 19% for the highest and lowest rows, respectively.

In chapter 14, a process optimization system was developed based on readily available and well-understood statistical and mathematical software packages. The tools used were ANOVA, Taguchi experimental methodology and the Response Surface Methodology (RSM) coupled with a MATLAB - Graphical User Interface (GUI) code, developed to give a surface roughness prediction model for advanced mass finishing technologies such as (drag and stream finishing processes) under various machining parameters conditions. The predicted model can be used to estimate process parameters needed to achieve a desired roughness of a workpiece. The proposed empirical model predicts surface roughness to within 95% confidence level.

The process optimization and the relationships between factors and levels from the trial experiments and prediction models agree well using the regression, ANOVA, Taguchi and Response surface methodology. Furthermore, the proposed method provides a useful tool to determine the optimum parameters condition for specific values of surface roughness at any region in the experimental domain. A statistical analyses of the drag finishing process

demonstrated that the Ra decreases with increasing spindle speed DSS and immersion depth DID, and Ra increases with increasing head speed DHS. In the case of the stream finishing process, Ra decreases with increasing control factors head speed SHS, bowl speed SBS, and immersion depth SID. The interaction investigation shows that the (DHS & DSS), and (DSS & DID) were the most significant effects on the response of the drag finishing process, while (SBS & SID) and (SHS & SID) were the most significant effects in the stream finishing process.

Confirmation experiments suggested that the predicted quadratic models were successfully used to predict surface roughness in drag and stream finishing process within 6 %, and 9 % error, respectively.

With the information gathered and presented, there are possible ways to choose the machine quality and quantity of products by following the guidelines presented in this chapter.

15.2 Recommendations for future work

Finally, this chapter provides ideas for possible ways to extend the research field presented in this thesis in order to secure and deliver to industry the further scientific grounding required to advance and exploit the mass finishing process.

- Design experiment methodologies for the determination of media element velocities, trajectories and impact behaviour over a defined range of machining and lubrication conditions. Design methodologies for measurement of impact frequencies, impact power per unit area and individual surface-normal impacts. Determine and quantify machining performance over a defined range of machining and lubrication conditions (performance measures: cycle time, surface finish/MMR, lustre; attrition rates; compound consumption).
- As discussed, the heat treatment processes create high residual stresses in the components. Future research can be performed to investigate different mould material, release agent and cooling rate for decreasing the residual stresses. Further research can be carried out to predict the residual stresses by including the feeding system into the FEA for simulating the glass media or other industrial components.

Residual stress optimizations can be made in the FEA by implementing a Graphical User Interface (GUI) system in user defined subroutines.

- A means to improve the fatigue life of the products can be attained by use of an optimization tool delivered by the proposed GUI system. This can be achieved by controlling a large number of process variables related to the manufacturing process, including: media (shape, grit material, size), compound solution (flow rate, composition), workpiece material (hardness, composition) and bowl characteristics (capacity, shape, acceleration, frequency. and amplitude).
- Development of a GUI system (automated algorithm system) can help in estimation of non-linear time-dependent mechanical characteristics from indentation measurement data with greater efficiency and accuracy and it may enhance the robustness of the current optimization algorithm.
- Establish a mechanistic and tribological founded abrasion model that relates process parameters to machining performance and surface finish condition for a selected range of materials. This model could be used to validate outputs from the simulation system and to aid process / cycle design and optimisation
- Fully characterise vibratory-fluidized flows for the major cases of mass finishing using advanced 3-D DEM. Develop DEM capability for simulation of media and work interactions to aid understanding of surface evolution phenomenon in mass finishing to include the cases of free-to-flow and fixed workpiece arrangements. Contact forces, impact nature, and particle and workpiece attrition (MMR) predicted from the model could be correlated with outcomes from the abrasion model and experimental studies. A workpiece of stated geometry and size could be introduced and the system response evaluated for varied workpiece orientation, location and fixing.
- Evaluate and validate theoretical and simulation outcomes via experiment and on-site trials